C474

NANODESIGNING OF HIERARCHICAL
MULTIFUNCTIONAL CERAMICS

AFOSR No. F49620-93-1-0259

ILHAN A. AKSAY

Department of Chemical Engineering and
Princeton Materials Institute, Princeton University
Princeton, New Jersey 08544

July 31, 1996

Princeton Materials Institute

P R I N C E T O N   U N I V E R S I T Y

NANODESIGNING OF HIERARCHICAL
MULTIFUNCTIONAL CERAMICS

AFOSR No. F49620-93-1-0259

ILHAN A. AKSAY
Department of Chemical Engineering and
Princeton Materials Institute, Princeton University
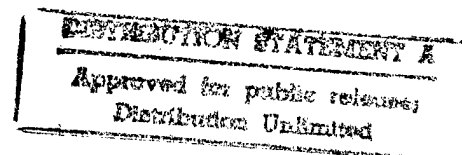Princeton, New Jersey 08544

July 31, 1996

19961015 041

DISCLAIMER NOTICE

UNCLASSIFIED

Technical Report
distributed by

DEFENSE
TECHNICAL
INFORMATION
CENTER

DTIC Acquiring Information-
Imparting Knowledge

Cameron Station
Alexandria, Virginia 22304-6145

UNCLASSIFIED

THIS DOCUMENT IS BEST
QUALITY AVAILABLE. THE
COPY FURNISHED TO DTIC
CONTAINED A SIGNIFICANT
NUMBER OF PAGES WHICH DO
NOT REPRODUCE LEGIBLY.

REPORT DOCUMENTATION PAGE

1. AGENCY USE ONLY *(Leave blank)*	2. REPORT DATE 31 July 1996	3. REPORT TYPE AND DATES COVERED Final Technical Report, 940901 - 951231

4. TITLE AND SUBTITLE

Nanodesigning of Multifunctional Ceramics

5. FUNDING NUMBERS

AFOSR F49620-93-1-0259

6. AUTHOR(S)

Ilhan A. Aksay

7. PERFORMING ORGANIZATION NAMES(S) AND ADDRESS(ES)

Department of Chemical Engineering and Princeton Materials Institute
Princeton University
Princeton, NJ 08544

8. PERFORMING ORGANIZATION REPORT NUMBER

9. SPONSORING/MONITORING AGENCY NAME(S) AND ADDRESS(ES) *NA*

Air Force Office of Scientific Research, Chemistry and Materials Sciences
110 Duncan Ave., Suite B115, Bolling AFB
Washington DC 20332-0001

10. SPONSORING/MONITORING AGENCY REPORT NUMBER

93-1-0259

11. SUPPLEMENTARY NOTES

The views, opinions, and/or findings contained in this report are those of the author(s) and should not be construed as an official Department of the Air Force position, policy, or decision, unless so designated by other documentation.

12a. DISTRIBUTION/AVAILABILITY STATEMENT

Approved for public release; distribution unlimited.

12b. DISTRIBUTION CODE

13. ABSTRACT *(Maximum 200 words)*

The work presented in this report details the activities of the Ceramic Materials Laboratory at Princeton University during the period 1992 through 1995. The goals of the project were to develop methods for processing ceramic composites at the nanometer scale using a variety of processing methodologies. Materials systems included high (>1000°C) and low (<1000°C) materials (ceramic/ceramic and ceramic/metal composites respectively) and multifunctional ceramics. Several different approaches were used for the nanodesigning of materials: (i) reaction sintering, (ii) exsolution, and (iii) coassembly; two classes of materials were used as model systems for these processing methods: (i) structural ceramics and (ii) functional ceramics. Shape forming research emphasized field assisted patterning, gel-casting, osmotic consolidation, and coassembly. Modeling efforts continued on (i) the interaction between inorganic materials and organic surfactants in the coassembly of particles an mesoporous matrices and (ii) the sintering of nanosized particles. In general, our studies demonstrated that nanometer scale inclusions in oxide and non-oxide ceramic matrices can be achieved by any one of several different routes. Different materials systems require different methods of processing in order to achieve the level of control desired for the manufacture of nanocomposites.

14. SUBJECT TERMS	15. NUMBER OF PAGES 164
ceramics, multifunctional, hierarchical design, nanometer scale	16. PRICE CODE

17. SECURITY CLASSIFICATION OF REPORT UNCLASSIFIED	18. SECURITY CLASSIFICATION OF THIS PAGE UNCLASSIFIED	19. SECURITY CLASSIFICATION OF ABSTRACT UNCLASSIFIED	20. LIMITATION OF ABSTRACT UNLIMITED

Nanodesigning of Hierarchical Multifunctional Ceramics

I. A. Aksay, Principal Investigator

September 1, 1992 through December 31, 1995

Department of Chemical Engineering and
Princeton Materials Institute
Princeton University
Princeton, New Jersey   08544-5263

Table of Contents

List of Figures

NANODESIGNING OF HIERARCHICAL MULTIFUNCTIONAL CERAMICS

Ilhan A. Aksay

Executive Summary

This is the final technical report for AFOSR grant number F49620-93-1-0259, covering the period September 1, 1992, through December 31, 1995, describing the final segment of the project *"Nanodesigning of Hierarchical Multifunctional Ceramics"* that began October 1, 1990 at the University of Washington, Seattle, which in turn extended the preceding AFOSR-sponsored project *"Microdesigning of Lightweight/High Strength Ceramic Materials"* (Grant Nos. AFOSR-83-0375, 1 October 1983 to 30 November 1986, and AFOSR-87-0114, 1 December 1986 to 28 February 1991). On September 1, 1992, our project on nanodesigning was transferred from the University of Washington to Princeton University.

The principal focus of our earlier AFOSR-sponsored projects during 1983 to 1991 was to establish guidelines for processing low density (< 3.0 g/cc) and high strength (> 800 MPa) ceramic matrix composite materials for structural applications. The achievements of the first six years of the research program led to the development of improved ceramic fabrication processes involving the use of colloidal dispersion and consolidation methods. Although significant gains in understanding the processing of dense ceramic matrix composites resulted from that work, it became apparent that our understanding of the structural and optoelectronic properties of composite materials failed as we approached length scales between 1 to 100 nm. Within this size range our knowledge of materials synthesis and processing by deliberate design is the weakest, yet we came to understand that nanometer-scale interactions strongly determine the macroscopic properties of materials. In response, our work over the preceding past four years shifted to address issues related to the *nanodesigning* of ceramic matrix composites using colloidal dispersions and molecular precursors.

The overall goal of our work has been to demonstrate the practical advantages of applying the concept of hierarchy to developing superior macroscopic properties in ceramic matrix materials. To this end, we seek to design materials with predictable properties, requiring that structural development be closely controlled at each step during processing, beginning with mixing (at the nanometer scale) and continuing through the densification of the constituent phases (at the micron and larger scales). For example, ceramic/ceramic nanocomposites have been reported to have significantly improved mechanical properties (§1.2) yet it is also claimed that these observations are merely the result of poor sample preparation. We have developed reproducible methods for synthesizing nanocomposite powders to be used to fabricate test specimens for mechanical testing. A model describing the effect of nanometer-sized inclusions in a continuous matrix has been proposed.

The research projects summarized in the following sections were all selected to meet the goal of designing multifunctional ceramics for structural and functional applications with a starting point at the atomic and nanometer level, recognizing that modeling of physical phenomena is a requisite part of any integrated materials research group. A colloidal approach to processing has been taken in the most part, stemming from our recognition that this will be the most feasible approach for the production of large scale devices and components. Tasks within the program are categorized into three areas: (i) applications (§1.), (ii) functional ceramics (§2.),

and (iii) model systems (§3.). In the first task area the research projects are concerned primarily with the fabrication of monoliths, built up from nanoscale structures. In the second task area the key emphasis is on the application of fundamental concepts generated in our previous projects to produce novel composites that can be utilized in novel optoelectronic applications. Finally, model experiments are designed to (i) provide guiding principles for applications and functional ceramics and (ii) develop new concepts in materials processing.

Copies of a selection of manuscripts completed within the reporting period are included in the Appendices.

1. Applications

In this portion of our project the emphasis is on basic issues in the processing of hierarchical materials. We choose to work at the nanometer scale as this holds the most promise for fabricating multifunctional materials with the desired properties. Proper fabrication of applied materials involves controlling each step of manufacture, from the synthesis of the starting materials to the production of the final monolith, making this area the most wide-ranging of the three task areas described above. Grouped within the study of applications are task areas on (i) processing methods (§1.1), (ii) ceramic/ceramic composites (§1.2), and (iii) low and high temperature ceramic/metal composites (§§1.3, 1.4).

1.1. Processing Methods
Investigators: Matt Trau, Fatih Dogan, John Mellowes, James S. Vartuli, Dudley A. Saville, and Ilhan A. Aksay

Processing methods for the production of nanocomposites are shown schematically in Fig. 1. Of the seven methods shown in the diagram, we avoid milling due to the lack of process control. Generally, we seek to develop methods that will allow the controlled fabrication of hierarchical nanocomposites through chemical techniques, physical manipulations, or a combination of the two. Ultimately, the success of any proposed process method is the production of materials which exhibit the desired mechanical and/or optoelectronic properties. In all of the methods described below, we seek to produce samples for testing under realistic conditions. To achieve this, we first must focus on developing suitable methods for producing the desired materials.
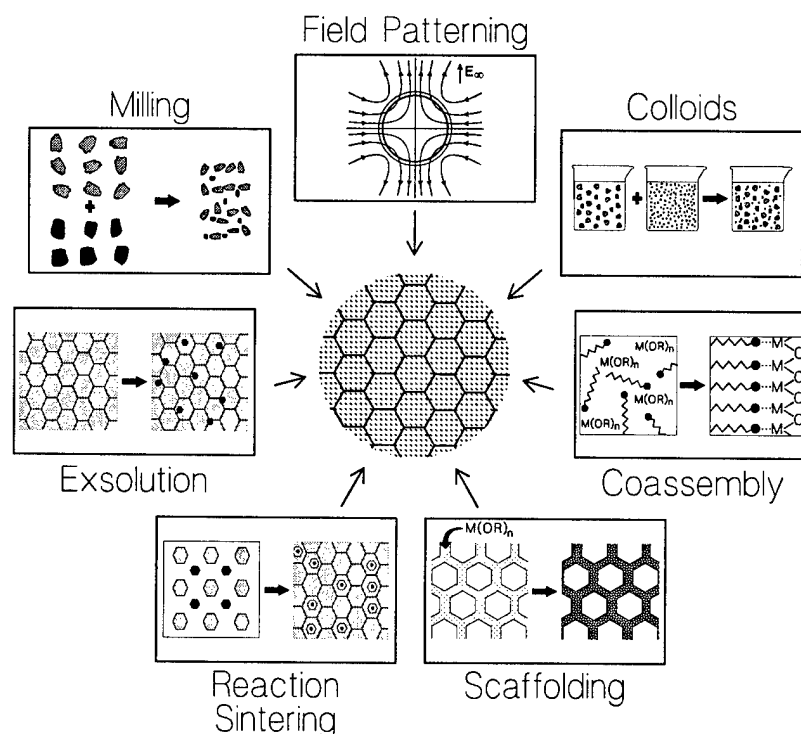
Fig. 1: Processing methods for the production of nanocomposites.

1.1.1. Pressure Filtration of Seeded Boehmite Gels for Monolithic α-Alumina

Previous research has shown that fully dense α-alumina of millimeter dimensions can be processed by sintering seeded boehmite gels in the temperature range of 1300 to 1400°C.[1-8] However, the processing of larger size samples has been hindered due to excessive cracking of the gels during drying. We have shown that this problem can be eliminated by densifying the gels by pressure filtration prior to drying. Acid stabilized suspensions of boehmite seeded with α-alumina have been gelled and pressure filtered to green densities of ~58%. Samples as large as 2.5 cm in diameter were sintered to densities higher than 99.4% TD at 1300°C without any cracking.

Seeded samples can be sintered crack-free and without deformation. The sintering densities of seeded samples were 99.4 and 99.7% of the theoretical density at 1300 and 1400°C, respectively; whereas, unseeded samples could be sintered to 98% of the TD only at temperatures above 1600°C (Fig. 2). A homogeneous microstructure with an average grain size of 2 μm was

Fig. 2: Sintered densities of seeded (●) and unseeded boehmite (□).

obtained with the seeded samples. This work demonstrates the importance of seeding as a processing tool in fabricating high density ceramics. These results are now being applied to functional ceramics such as PZT thin films (§2.3) and mesoporous silicates (§3.2.2).

1.1.2. The Osmotic Consolidation of Ceramic Suspensions

The fabrication of ceramic monoliths with consistent mechanical properties requires the production of highly dense and uniform green bodies. As the particle size decreases to the nanometer scale the effective packing density is found to decrease due to the increased attraction between the fine particles; aggregation is uncontrolled, highly porous ramified structures form, and the green density declines.[9] Model studies within this research project have used ultrafine gold particle suspensions to examine the sintering of nanoscale materials from colloidal suspensions (see §3.1.2). Other studies performed within our research group but not supported in the AFOSR program have studied the compaction behavior of powder suspensions with the goal of approaching slip-cast green densities. Miller and Zukoski have demonstrated a method by which extremely high pressures (~12MPa) can be exerted on suspensions and gels using osmotic pressure.[10] They report volume densities in excess of 60 vol% for alumina green bodies by this method. For the proposes of our project, osmotic consolidation offers a method by which consistently high green densities can be achieved in suspensions of ultrafine particles.

Miller and Zukoski obtained very dense alumina green bodies by placing dilute alumina suspensions (20 volume percent) inside dialysis bags immersed in a concentrated poly(ethylene oxide) (PEO) solution. Our modification of this procedure sought to maximize the amount of material that could be processed and to minimize the time necessary to achieve high densities. To meet these two goals, our procedure uses a constant flow of PEO through a ~2m long dialysis tube (2.1cm diameter) immersed in a ceramic suspension (initially 1 vol% AKP-30 alumina). The PEO solution could be recycled simply by removing the excess water by heating. Using this

4

method, the initial water extraction rate was measured to be ~350mL/h; the final water extraction rate was found to be 50mL/h. Green densities as high as 58% have been achieved.

Difficulties with the process include: (i) maintaining pH balance between the suspension and the PEO solution (differences significantly reduce the effective osmotic pressure); (ii) the increasing viscosity of the suspension as density increases; and (iii) the formation of nearly impermeable cake layer at the membrane. These issues are the current and future task areas for developing a useful application of osmotic pressure consolidation for use with ceramic suspensions.

1.1.3. Field-Induced Pattern Formation in Colloidal Dispersions

The formation of patterned colloidal structures has many applications in materials processing. Examples include catalytic support honeycombs produced by extrusion,[11,12] hierarchical electronic devices made with ceramic multilayers,[13] electro-rheological fluids,[13-16] and "smart materials" formed from patterned composites.[17] Moreover, nested levels of structural hierarchy in composite materials can impart vastly superior properties over a homogeneously structured material.[18-21] Due to the intrinsic dimensional limitations of mechanical forming, pattern formation in such materials has hitherto been restricted to length scales larger than a few tens of microns. We have been investigating the use of electrohydrodynamic forces which act directly on non-homogeneous regions in a colloidal dispersion so as to form patterned colloidal dispersions. Once the patterns are formed, the structures can be set by solidifying the fluid matrix via gelation or polymerization.

To illustrate the process, we used 100 nm barium titanate ($BaTiO_3$) particles prepared via a hydrothermal process (see §2.1) and dispersed in castor oil. Barium titanate was chosen because it has an extremely high dielectric constant (between 300 and 10,000, depending on its crystalline form), and is a technologically useful material in both the electronic and optical component industries. Castor oil was chosen as the fluid medium because: (i) it has a low conductivity ($\sigma = 1.8 \times 10^{-11}$ Sm^{-1}); (ii) fatty-acid based oils are good dispersing media for barium titanate particles; (iii) its conductivity may easily be varied over a wide range by doping with small amounts of soluble organic salts (e.g., tetrabutylammonium tetraphenylborate, TBATPB); and (iv) its viscosity is similar to those of polymerizable silicone oils used to prepare colloidal barium titanate structures within a solid silicone polymer matrix. To form the system depicted in Fig. 3, a dilute dispersion of barium titanate particles (0.025 vol%) in castor oil was injected into clear castor oil fluid via a pin hole in a metal electrode. Slow injection of the dispersion into the clear fluid results in a spherical bolus of the dispersion nested within clear castor oil [cf. Figs. 4(a) and (e)]. The 4 × 4 cm metal electrodes were 1.5 cm apart; the diameter of the colloidal bolus was approximately 5 mm.

Fig. 4 illustrates the results for two experiments, the first in which the conductivity of the dispersion is higher than that of the surrounding fluid and the second in which this
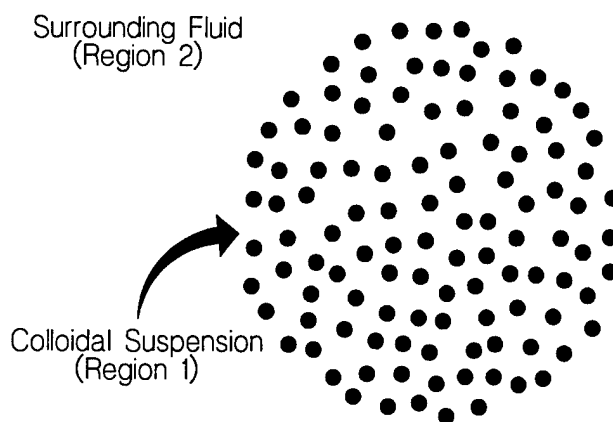
Fig. 3: A schematic diagram of our model system: a spherical, particle-containing bolus (region 1) nested inside clear ambient fluid (region 2).

5

was reversed. The series of images show the effect of applying a 2000 Vcm^{-1} electric field over a time interval of approximately 0.2 seconds. In sequence (a)-(d) (higher conductivity in the dispersion), the spherical droplet deforms immediately in the direction of the applied field and continues to stretch until it collides with the top electrode to form a near-perfect column. The column remains intact for several seconds. In the (e) to (h) sequence (higher conductivity in the surrounding fluid), a different flow pattern is caused by application of the field. The spherical bolus deforms orthogonal to the applied field, forming a disk shape which continues to expand laterally. After some time, a film forms across the bottom electrode. Steady (DC) fields were used to generate all of the patterns shown in Fig. 4 but the direction and speed of the motion was found to be insensitive to the field's polarity. Similar flow patterns are induced by applying low frequency AC fields (approximately 100 Hz) which shows that the particle motions are not the result of electrokinetic phenomena but can be explained in terms of an electrohydrodynamic flow.

A qualitative picture of the flow patterns can be obtained from a simple model where the dielectric constant and conductivity distributions are prescribed. This was done for situations where a transverse electric field acts on a circular region with dielectric constant ε_1 and conductivity σ_1, surrounded by a region with properties σ_2 and ε_2 and each property varies smoothly in the (thin) transition zone. Fig. 5 depicts the situation and shows the streamlines of the velocity field calculated when the dielectric constant and conductivity of the interior exceed those in the exterior. In this case the dispersion would be drawn out into a ribbon-like shape oriented parallel to the field (in three dimensions the shape would be a cylinder). The flow direction reverses when the conductivity of the interior is less than that of the exterior and the sample takes up a flat configuration orthogonal to the field. These qualitative features are in complete agreement with our experimental observations.

Although the experiments presented here have been performed solely on BaTiO$_3$/castor oil dispersions, this technique is in no way restricted to this system. Indeed, provided that there
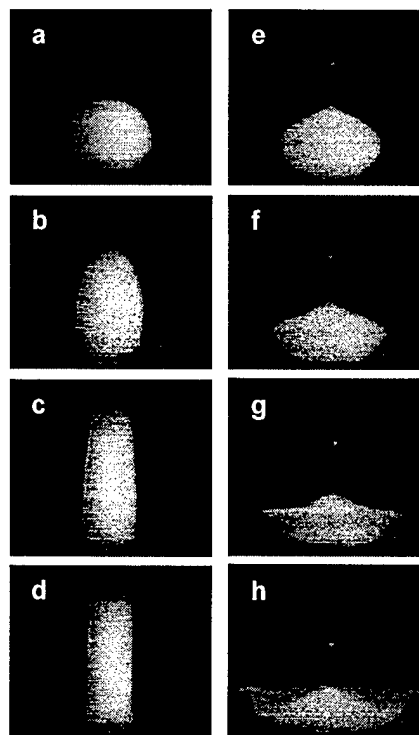
Fig. 4: Two examples of the deformation of a colloidal dispersion via an applied electric field. Panels (a)-(d) and (e)-(h) are video sequences taken after a steady DC field was applied to a spherical cloud of a BaTiO$_3$ dispersion nested inside clear castor oil. The dispersion consisted of 100 nm BaTiO$_3$ particles in castor oil (0.025% by volume). The resulting images have been enhanced to better the contrast between particle containing regions and clear fluid. In the two experiments the conductivity mismatch between the inner and outer bolus region was reversed by dissolving a trace amount of tetrabutyl-ammonium tetraphenylborate (0.2 x 10^{-3} mol·dm^{-3}) either in the inner region, sequence (a)-(d), or in the surrounding clear fluid, sequence (e)-(f). In both cases the magnitude of the applied field was 2000 Vcm^{-1}, applied in the vertical direction.

6

exists a sufficient mismatch in conductivity and/or dielectric constant, any colloidal dispersion nested within any ambient fluid may be manipulated in a similar manner (§1.1.4).

1.1.4. Field-Induced 2-Dimensional Nanolaminates

We have been conducting experiments to determine whether colloidal nanolaminates of controlled morphology can be produced by the technique of electrophoretic deposition (EPD).[22,23] EPD of colloidal particles is a long established technique for the production of macroscopic particulate films, however, hitherto has not been successfully applied to the formation of mono- or multilayered colloidal films with precise morphological control.[23] To observe the deposition mechanism in microscopic detail, we have constructed an apparatus consisting of an optically transparent indium tin oxide (ITO)

Fig. 5: Streamline pattern for flow engendered by a circular shaped cloud of a dispersion immersed in a clear fluid with a lower conductivity and dielectric constant.

electrode coupled to an optical microscope. A video camera is used to record the dynamics of the particles depositing on the electrode under the influence of an applied electric field.

Initial experiments have been performed on silica (900nm diameter) and polystyrene (2-4µm diameter) particles. These experiments have revealed very surprising results: Provided the colloidal stability of the particles is maintained with respect to each other and with respect to the electrode and in the presence of a sufficiently strong applied electric field, colloidal particles are attracted to each other on the surface of the electrode. This (lateral) attraction force acts in a direction normal to the applied field and is strong enough to bring the particles together to form ordered structures, such as 2-dimensional colloidal crystals (Fig. 6). This observed attraction is surprising given that a strong repulsion would be expected from electrostatic considerations: all of these particles are similarly charged and contain a diffuse ionic cloud (double layer) which will be polarized in the presence of the field; as these particles approach each other on the surface of the electrode, electrostatic repulsion should be experienced both from monopole and dipole interactions. Currently, we believe that the observed attraction is a result of a combination of the electrochemical reaction at the electrode interface (which allows for current to pass through the system) and fluid flow which is set in motion as a result of this reaction.

It has been observed that the magnitude of the lateral attraction between the particles can be modulated by either the amplitude or frequency of the applied external field. The ability to modulate the strength of the lateral attraction allows the formation of different colloidal phases on the
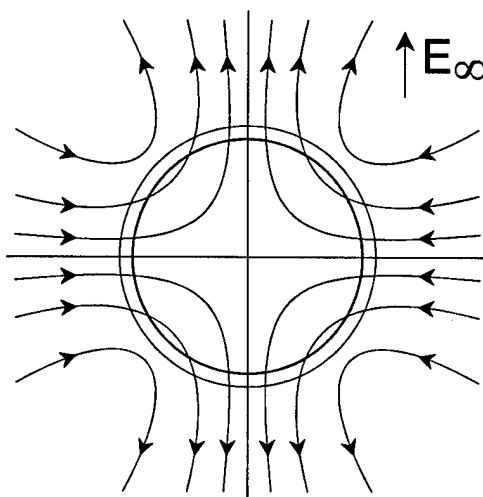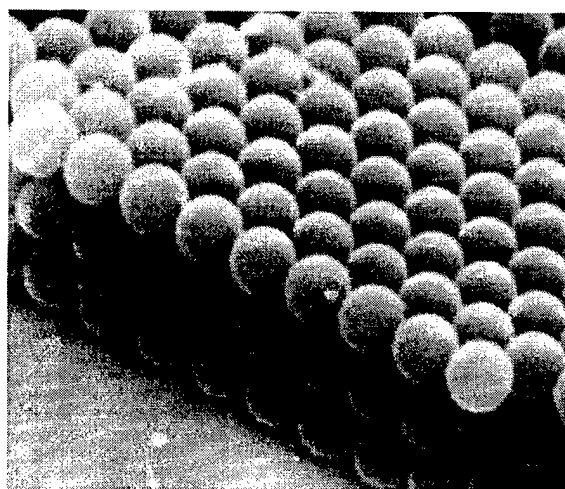
Fig. 6: Three layers of 2µm diameter polystyrene beads layered on a conductive substrate under an applied field of 2V.

7

surface of the electrode (e.g., crystalline, liquid and gaseous); phase transitions can be conveniently induced by varying the amplitude of the applied field. By cycling between liquid and solid phases (cyclic annealing), particles in the electrophoretically deposited layer can be continually redistributed until a perfect colloidal monolayer is formed (i.e., all EPD particles are located in the first layer, with no particles populating the second or third layers). Once the monolayer is formed, it can be "frozen" into place by inducing coagulation via the applied field. Using this approach, submicron monolayers of silica and polystyrene particles have been assembled and "frozen". We expect that this technique can be generally applied to any type of colloidal particles (§1.1.3). Research on the formation of controlled multilayered structures is continuing.

1.2. Mullite Matrix Composites (Ceramic/Ceramic Composites)

Investigators: David L. Milius, Fatih Dogan, Yoshihiro Sakka, Dilshad Shahid, Daniel M. Dabbs, and Ilhan A. Aksay

1.2.1. Effect of Cr_2O_3 and MnO_2 Additives on the Mechanical Properties of Colloidally Processed Alumina

MnO_2 and Cr_2O_3 are known to increase the hardness of alumina ceramics.[24] The effect of these additives on the microstructural evolution and mechanical properties of α-alumina is part of our continuing work on the processing of ceramic matrix composites. In order to achieve a uniform distribution of the additives, we coated submicron size alumina particles with soluble chromium- and manganese acetates. Suspensions were freeze dried to process granules which were then used in the preparation of compacts by dry pressing and slip casting. Chromia, as a solid solution additive, inhibited the grain growth. Excessive grain growth was observed with MnO_2 additions. In both cases, an increase in hardness was observed. Tensile strength increased with Cr_2O_3 and decreased with MnO_2 doping. The results were correlated with the microstructural features.

The hardness of alumina increased with both additives. Slip cast samples with Cr_2O_3 and MnO_2 additives yielded microhardnesses up to ~2600 and 2700, respectively. These values are higher than the hardnesses reported in previous studies.[24] We attribute these higher values to the homogeneity of the slip cast samples. Although we have not yet confirmed the respective mechanisms, additive, precipitation hardening is expected in the case of MnO_2 whereas in the case of Cr_2O_3 solid solution hardening is thought to be the dominant mechanism.

In the case of tensile strength, however, MnO_2 containing samples were lower in strength whereas the strength of Cr_2O_3 containing samples increased from 500 to 700 MPa. We attributed the decrease in the first case to significantly larger size (100 μm) grains since these grains can act as critical flaws. However, since in the case of chromia addition the grain size does not change noticeably in comparison that of the undoped samples, we attributed the increase in this case to the solid solution effect of the chromia. Studies are underway to confirm these suspected mechanisms.

1.2.2. Processing of Nanocomposites Silicon Nitride-Mullite-Alumina By Reaction Sintering

In the first phase of this work we developed a new method for processing SiC-mullite-Al_2O_3 nanocomposites by the reaction sintering of green compacts prepared by colloidal consolidation of a mixture of SiC and Al_2O_3 powders.[25] The surface of the SiC particles was first oxidized to

produce silicon oxide and to reduce the core of the SiC particles to nanometer size. Next, the surface of silicon oxide was reacted with alumina to produce mullite. This process results in particles with two kinds of morphologies: nanometer-sized SiC particles that are distributed in the mullite phase and mullite whiskers in the SiC phase. Both particle types are immersed in an Al_2O_3 matrix.

Densities greater than 95% of theoretical were obtained by sintering fine SiC and alumina at 1600°C for two hours in argon atmosphere. This process offers several advantages and thereby warrants further research: (i) it eliminates the need to reduce the particle size of the inclusion phase to the nanometer range by milling and thus provides better control in minimizing impurities; (ii) due to a volume increase during reaction sintering, sintering shrinkages are lower; and (iii) the presence of amorphous silica as a transient phase results in enhanced densification by viscous deformation and thus provides an opportunity to process these composites without pressure.

We are continuing studies on the high resolution imaging of the phase boundaries observed in these composites with the goal of determining the reaction parameters important to the formation of a stable nanocomposite. High temperature mechanical testing has not been done on these materials so the overall stability of these systems is not known. Future studies will principally concern the optimization of the mechanical properties and stability of the composite systems. Other nanocomposite systems involving silicon nitride have been added to this work as well as preliminary studies on the applicability of this procedure to other potential nanocomposite systems (§1.3.1).[26]

1.2.3. Processing of a Mullite Matrix, Molybdenum Disilicide Reinforced Composite

A mullite matrix reinforced with $MoSi_2$ particles was investigated as a potential high temperature composite material.[27,28] Samples containing 2.5 to 20 vol% $MoSi_2$ were processed using both hot pressing and pressureless sintering techniques.[29] Room temperature mechanical testing was performed both in the as-sintered state and after oxidation. Densities of greater than 97% of theoretical were attained for composites containing less then 7 vol% $MoSi_2$ via pressureless sintering. K_{Ic} and strength values of the as-sintered composite were found to be up to two times that of monolithic mullite. After oxidation at 1400°C for 96 hours, the strength improved by 1.5 times over the as-sintered strength, and fracture toughness improved by a factor of 2.5 over the as sintered fracture toughness, indicating that the composite was self-healing during oxidation.

Work in this project focuses on the pressureless sintering process for the production of fully dense composites, using the viscous phase that exists at the particle-matrix interface. High temperature mechanical tests are also planned to determine the suitability of this composite at high temperatures.

1.2.4. Processing of Nanocomposite Powders

The effect of nanoscale inclusions in ceramic monoliths has been reported by Niihara to greatly enhance the strength and toughness of dense ceramics.[30,31] More recently, Wu and Clausen has described enhanced physical properties in SiC/mullite matrix composites, although the intergranular inclusions are hundreds, rather than tens, of nanometers in size.[32] These claims are considered somewhat controversial principally due to the difficulty in synthesizing dense monoliths with uniform distributions of nanoscale inclusions. The results of our own investigations on materials strengthened by the addition of (microscale) inclusions (§§1.2.2,

9

1.2.3, and 1.3.1) plus our study on chromia and manganese oxide additives in colloidally processed alumina monoliths (§1.2.1) are positive indicators that the processing of powders containing nanoscale inclusions is a viable method for producing such monoliths.

Two processing routes are concurrently under study. One route uses sol-gel processing since powders made from sol-gels sinter to full density at low temperature, as shown in our past work.[33] In the case of mullite, densification is favored by the presence of a viscous phase up to the mullitization temperature (~1250° to 1300°C in TEOS/boehmite sol-gels). Furthermore, we have also shown that mullitization of sol-gels prepared from well-classified boehmite suspensions resulted in the formation of nanoscale silica-rich nanoscale inclusions within the mullite grains. The very fine grains that result from this process yields visibly translucent monoliths that are transparent in the mid-infrared (3-5µm) region of the electromagnetic spectrum.[34]

However, maintaining two phases at high temperature can lead to the concentration of the additive into one phase, encouraging phase segregation and/or the formation of large inclusions in the final powder. These artifacts can be avoided by maintaining chemical homogeneity in the powder. Flash pyrolysis results in dry homogeneous amorphous powders which, in the case of mullite, reduces the temperature of mullitization to ~1000°C.[35,36] Extremely fine grained, highly dense powders result. We believe that the proper processing conditions can result in the precipitation of nanoscale inclusions in these powders and that the precipitation can be controlled using simple thermal treatments. Mullite is very difficult to sinter due to its high creep resistance and this presents a possible limiting factor to the use of powders made using pyrolysis.

Three systems are currently under study: alumina/mullite, chromia/mullite, and titania/mullite. Powders containing varying levels of excess alumina have been made by both the sol-gel and pyrolysis methods. At higher processing temperatures (>1350°C), the resulting powders are similar, consisting of fine grained particles containing small inclusions ~10-20nm in diameter. At lower temperatures (>1000°C) mullitization in the pyrolyzed powders appears complete but the number of inclusions is reduced. XRD results suggest the presence of the second phase at lower processing temperatures in the pyrolyzed powders; high resolution TEM work is required to determine if smaller inclusions can be found within the grains of the powder particles.

Chromia/mullite and titania/mullite powders have been made using the pyrolysis method. Sol-gel procedures have not yet been used with these systems due to the rapid hydrolysis rate of the titania and chromia precursors. As in the alumina/mullite powders XRD characterization indicates the presence of a second phase after mullitization (~1100°C) but microscopic characterization to confirm the morphology of this phase has yet to be performed.

Following the completion of the characterization studies, future work will involve two goals: (i) determining and improving conditions required for the production of mullite powders containing nanoscale inclusions and (ii) using these methods to produce sufficient quantities of powder for densification and sintering studies. Ultimately, we plan to produce test bars from the nanocomposite powders for mechanical testing.

1.3. Ceramic/Metal Composites (<1000°C)
Investigators: Yong Li Zhang, David L. Milius, Jun Liu, and Ilhan A. Aksay

1.3.1. Processing of SiC/Al-Si Alloy Laminated and Monolithic Composites

Green compacts of mixtures of alumina and SiC powders have been prepared in our laboratory by colloidal processing.[37] In the next phase of the study, the following two steps were performed: (i) the surface of the SiC particles was oxidized to produce silicon dioxide and to reduce the size of the remaining SiC down to the nanometer scale; and (ii) this was followed by reaction sintering in which a matrix of mullite was produced by reacting the silicon dioxide with alumina, leaving the SiC particles suspended in the matrix material.[38-42]

Alumina and SiC powders were dispersed using PMAA in aqueous solution at high pH in order to obtain high-density green compacts. These suspensions were consolidated by filtration. The densities of the green bodies were 62 to 64% of theoretical density. Reaction sintering was carried out at temperatures ranging from 1550° to 1750°C for 2 or 5h in an argon atmosphere. During sintering the cristobalite phase disappeared and mullite was produced. The quantity of mullite produced depended on the extent of oxidation in the SiC. Moreover, the oxidation treatment was effective in forming high-density sintered bodies. SEM and TEM experiments are now planned to determine the degree of SiC dispersion and the structures of the interfaces.

Liquid metal infiltration in vacuum was successfully used for manufacturing SiC/Al-Si laminated and ceramic matrix monolithic composites . The chemical reactions between SiC and molten Al were studied by TEM.[37] It was confirmed that the formation of Al_4C_3 was through the dissolution of SiC into the liquid Al and then the reaction of SiC with liquid Al. Systematic X-ray diffraction investigations revealed that the amount of silicon in the metal phase and the free carbon content in the SiC powder were two of the main factors that affected the nucleation of Al_4C_3. The formation of Al_4C_3 was effectively eliminated with 8vol% Si addition. The infiltration was improved to some extent by coating SiC particles with K_2ZrF_6.[43] Strong chemical bonding at the interface provided an excellent combination of strength and fracture resistance. Composites with flexural strength higher than that of fully dense SiC and fracture toughness three times that of SiC were produced. Higher mechanical properties were obtained with SiC/Al-Si laminates, especially the laminate with metal foils between ceramic layers, due to the specific multi-layered structure and shorter infiltration distance resulting in better infiltration.[44] Toughening was apparently due to the ductile phase reinforcement.

From our past work, the following conclusions can be made: (i) In the system of SiC-Al, the formation of Al_4C_3 is through a two- step approach: dissolution of SiC into liquid Al and reaction of SiC with liquid Al. The Si level in the metal phase obviously affects the equilibrium of Al(Si)-SiC-Al_4C_3. The formation of Al_4C_3 is effectively eliminated by alloying Al with Si. (ii) Liquid Al-Si alloy infiltration of SiC in vacuum gives good bonding by mechanical trapping. The strong interface contributes to the good combination of strength and fracture resistance. (iii) Besides ductile phase reinforcement toughening, the specific structural features, the shorter infiltration distance and thus shorter infiltration period, and the versatile possibilities of designing materials are advantages provided by the laminated structure. SiC/Al-Si laminates with continuous metal phase are preferable for higher reliability requirements and higher toughness can be achieved with this structure.

11

1.3.2. The Wetting Behavior of SiC with Al(Si) Alloys

The effect of silicon addition on the wetting behavior of SiC with Al was evaluated by the sessile drop technique in vacuum. The measurement of the contact angle between SiC substrates and molten Al(Si) showed that at low temperatures there was no apparent difference in the contact angle with or without silicon additions; however, at high temperatures the rate of decrease in the contact angle increased with increasing Si content in the Al(Si) alloy.[45,46] It was also shown that the addition of Si to Al lowered the transition temperature from non-wetting to wetting for the SiC-Al system. EDS analysis indicated spreading and penetration of the Si(Al) alloy on the surface of and into the SiC substrate. A sharper drop in the contact angle was observed in the wetting of Zr containing compound coated SiC with Al(Si) alloy. X-ray diffraction identified the reaction products as ZrSi and AlZrSi.

This study demonstrates the feasibility of making SiC-Al(Si) cermets by liquid metal infiltration in vacuum. Future studies will characterize the SiC-Al(Si) interface through the use of high resolution electron microscopy.

1.4. Methods for Obtaining High Temperature (>1000°C) Ceramic/Metal Composites
Investigators: Fatih Dogan, John S. Lettow, David L. Milius, and I. A. Aksay

To be useful in structural applications it is necessary to engineer metal/ceramic composites to achieve high strength, oxidative resistance, creep resistance, coupled with the low density of the ceramic and the metal's toughness.[30,47-49] The mechanical properties of metal/ceramic composites depend on the properties of the constituents, phase compatibility, and microstructure. For a ceramic matrix containing metallic inclusions, the size, location, and connectivity of the included phase may significantly affect the mechanical properties (i.e., fracture strength) of the composite material.[50,51] The nickel/aluminum oxide system is particularly attractive as a potential high temperature structural material, possibly exhibiting significant improvements over nickel-based superalloys currently employed in high stress applications (e.g., jet engine turbine components).[52] While the maximum operating temperature of most superalloys is around 1000°C, nickel/alumina composites could potentially operate at temperatures hundreds of degrees higher, with greater creep and oxidation resistances.

Several methods for processing nickel/alumina composites have been developed. Ni/Al_2O_3 composites have been prepared by suspending Al_2O_3 particles in an aqueous solution of $Ni(NO_3)_2$ and adsorbing Ni^{2+} cations onto the surfaces of the particles.[53] Gels fabricated from aluminum alkoxides were used to improve sinterability in powders.[51] NiO powder and α-Al_2O_3 have been mixed in a ball mill and reacted at 1600°C in air for four days to obtain $NiAl_2O_4$. The $NiAl_2O_4$ was subsequently reduced to produce a nickel/alumina composite.[52] These samples were severely cracked due to the large volume difference between $NiAl_2O_4$ and the Ni/Al_2O_3 composite, calculated to be ~19% when going from $NiAl_2O_4$ to Ni/Al_2O_3.[50] However, it has been shown that keeping the size of the nickel inclusions in the reduced samples below ~2μm eliminated cracking in the composite.[50]

Our goal was to develop a viable processing method for producing highly dense Ni/Al_2O_3 composites for testing as high temperature structural materials. Two different means of accomplishing this were studied: (i) reduction of $NiAl_2O_4$ powder and (ii) electrophoretically depositing colloidally dispersed ceramic particles onto a substrate, then coating these with nickel metal through electrodeposition (§1.1.4).

12

For the thermal method, our first efforts focused on the production of suitable $NiAl_2O_4$ powders for subsequent reduction. A pH of approximately 9.5 was found to be optimum for the precipitation of nickel nitrate from solution. Coprecipitation of NiOH and AlOH (possibly containing AlOOH as well) from a 1:2 ratio of nickel nitrate and aluminum nitrate in aqueous solution at a pH of 9.5 produced an amorphous powder with the appropriate stoichiometry for conversion to $NiAl_2O_4$. With coprecipitation, processing temperatures and times for the formation of $NiAl_2O_4$ were reduced from 1600°C for four days to 900°C for four hours. Additionally, X-ray experiments have revealed that the average crystallite size in the $NiAl_2O_4$ powders converted at 900°C was 13nm. The small size of the nickel aluminate crystallites should facilitate the reduction of the $NiAl_2O_4$ to form nickel/alumina composite powders, the next phase of the study.

The electrical processing route for making metal/ceramic composites involves the electrophoretic deposition of a well packed monolayer of ceramic particles on to an electrode. After deposition the monolayer of ceramic particles is coated with a thin metal layer by electrodepositing metal cations from an aqueous solution. Experiments with high resistivity coated glass electrodes revealed that a thin (~1-2µm thick) layer of nickel metal could be electrodeposited on a ceramic monolayer which was previously formed through electrophoretic deposition of submicron ceramic particles on the electrode (§1.1.4). In regions of the ceramic monolayer well coated with nickel, the nickel deposits completely filled the gaps between ceramic particles and then spread laterally to form a smooth layer over the ceramic particles. On lower resistivity coated glass electrodes, an applied potential of -1.2V with a constant flow of nickel sulfate solution at 0.1µm/min produced regions of smooth but discontinuous nickel deposits. We propose that the electrical process for making nickel/alumina composites could be used to make highly patterned metal/ceramic laminates built up from submicron structures.

2. Functional Ceramics

Barium titanate, $BaTiO_3$, is a ferroelectric material with enormous potential for applications in photonic processing (e.g., optical information storage and optical computation). Because of the current difficulties associated with growing large, inexpensive, optical quality crystals, practical electro-optic or optical-optical switching devices have not yet been produced from $BaTiO_3$ based materials. In order to remedy this situation, the formation of polycrystalline thin films investigated via the synthesis of nanosized $BaTiO_3$ colloid particles, followed by sol/gel processing to produce polycrystalline films and monoliths (§2.1). Grains in these polycrystalline ceramics have to be significantly smaller than the wavelength of light, to minimize internal scattering, so that optically transparency is achieved.

Preliminary work in this area has suggested that the dielectric properties of the resultant film are sensitive to the grain size of the $BaTiO_3$ (§2.2). It is postulated that this effect could either be due to a different crystal domain structure within the particles (as opposed to the crystal domain structure within bulk crystalline material) or, for particles smaller than 10 nm, to quantum confinement (Stark) effects. Although these effects have extremely profound consequences for the performance characteristics of ferroelectric films and monoliths, to date no fundamental study has been performed to measure the dielectric properties of individual $BaTiO_3$ colloidal particles as a function of colloid size. A fundamental understanding of these effects should enable the dielectric properties of the final $BaTiO_3$ films and monoliths to be specifically tailored for required applications (§§2.5 and 2.6).

13

2.1. Formation of BaTiO₃ Particles by Low Temperature (<100°C) Hydrothermal Processing
Investigators: Chang-Min Chun, Fatih Dogan, and Ilhan A. Aksay

We have synthesized nanocrystalline dielectric $BaTiO_3$ particles at 80°C using hydrothermal methods. Since we seek to more fully understand the parameters that control particle size and morphology, our research in this area has been focused on a detailed study of the nucleation and growth of $BaTiO_3$ particles (a general discussion may be found in Nielsen[54]). In part, this has been motivated by the growing commercial demand for uniform particles to be used in applications but, in addition, our previous work has highlighted the conflicts between different mechanisms advanced to explain uniform particle formation. Therefore, our principal goals remain (i) to describe the parameters that control particle size and morphology in hydrothermal processing, and (ii) to determine the mechanism by which particles are formed and aggregate.

$BaTiO_3$ particles were formed from the reaction between nanometer-sized TiO_2 colloids (30nm diameter) $Ba(OH)_2$ (aq) at 80°C. Increasing the $Ba(OH)_2$ concentration was found to decrease the average particle diameter, from 200 nm in 0.46 M solution to 50 nm in 2.23 M solution. No significant difference in particle size (around 40~50 nm) was observed for particles produced at higher concentrations (>2.23 M). The particles were nanosized, spherical, finely divided, monodispersed, and very pure. On the other hand, particles formed at low $Ba(OH)_2$ concentrations (<0.23 M) produced quite different morphologies: the particles were observed to consist of aggregated structures composed of smaller subunits, each ~50nm on edge. Decreasing the $Ba(OH)_2$ concentration increased the aggregate size, from 0.25-0.5 μm in 0.23 M $Ba(OH)_2$ solution to 1.0-2.5 μm in 0.12 M solution.

We determined that the hydrothermal formation of $BaTiO_3$ is controlled by three distinct, but interrelated, processes: (i) Titania first dissolves in the $Ba(OH)_2$ solution, quickly followed by precipitation. (ii) The primary particles aggregate to form the $BaTiO_3$ nuclei. (iii) The $BaTiO_3$ clusters spherodize through the lowering of the total surface free energy via dissolution and recrystallization.

Hertl has proposed that the diffusion of barium ions to the TiO_2 particles is the rate-limiting step in the formation of $BaTiO_3$ particles.[55] This implies that nucleation of the $BaTiO_3$ should be observed at the TiO_2/solution interface. However, we have observed that $BaTiO_3$ nucleates directly from solution, implying that the dissolution of titanium oxide is the determinant in forming barium titanate in the colloidal suspension. This agrees both with the general feature of hydrothermal reactions (solution-based reactions) and with the effect of increasing $Ba(OH)_2$ concentrations and temperature, both of which enhance the solubility of TiO_2. Therefore, the particle size and morphology variation can be explained by considering two competing parameters, the nuclei generation rate and the diffusion rate for aggregation, both of which are limited by the dissolution rate of TiO_2.

The initial primary nuclei are unstable due to their small size (<10 nm), and aggregate although negatively charged (Fig. 7). Because the crystal structure of $BaTiO_3$ is cubic, cubical first generation aggregates with rough surfaces form. The evolution of $BaTiO_3$ illustrates that small $BaTiO_3$ nuclei emerge very early and implies that these particles are present throughout the growth stage. According to Zukoski's nucleation and aggregation model,[56] the critical supersaturation value was exceeded during the complete course of the process and that nucleation proceeded for a substantial fraction of the reaction period. Further studies should demonstrate that nucleation is continuing throughout most of the growth period.

14

Growth by aggregation results in faceted aggregates. The solubility of the small (<10nm diameter) primary particles, particularly at higher pH, encourages spherodization via dissolution and reprecipitation within the $BaTiO_3$ aggregates to form uniform, spherical particles.

We have not yet proven the existence of separate primary nuclei during the formation of $BaTiO_3$ from colloidal TiO_2 particles, nor have we quantified the clustering that leads to the forming of the ultimate particle. Our current research seeks to answer the remaining questions using titanium alkoxides as the titanium source, dynamic light scattering to chart the growth and aggregation of the primary particles, and TEM for adjunct studies on the structure of the particle clusters and the evolution to the final spherical particles found in suspension. These experiments will be used to construct a mechanism to explain particle aggregation with respect to particle formation and the energy of interaction between small particles.

Fig. 7: HREM image of $BaTiO_3$ particles formed within one minute of mixing the precursors. The nuclei precipitate to form an aggregate of crystallites with matching crystal lattices.

2.2. Theory of the Size Effect of Small BaTiO₃ Particles

Investigators: Wan Y. Shih, Wei-Heng Shih,* and I. A. Aksay
* Department of Materials Engineering, Drexel University, Philadelphia, PA 10104.

Bulk $BaTiO_3$ has a ferroelectric transition at $T_c = 122°C$. Above T_c, the crystals are nonpolar and the crystal structure is cubic. Below T_c, the crystals become ferroelectric and the crystal structure changes to tetragonal. However, unlike bulk materials, the $BaTiO_3$ particles made in our laboratory using a hydrothermal approach have diameters ranging from 0.03 to 0.3μm and are *cubic* at room temperature (§2.1). In addition, composites made of these particles in organic polymer displayed enhanced dielectric properties below room temperature.

Ishikawa et al.[57] and Uchino et al.,[58] using Raman spectroscopy and X-ray diffraction respectively, have shown that the cubic-to-tetragonal transition temperature of small $PbTiO_3$ and $BaTiO_3$ particles is size dependent. Arlt et al.[59] and others have shown that the dielectric constant ε of $BaTiO_3$ ceramics is also grain size dependent. The dielectric constant ε was observed to peak at a grain size near 1μm and the peak value is higher than the dielectric constant in either the **a** or the **c** directions. Arlt et al. also showed that in the ferroelectric phase the grains are highly twinned and the twin size decreases with decreasing grain size. They attributed the increase in ε with decreasing grain size to the increasing presence of twin boundaries resulting from a balance between the stress energy within the domains and the twin boundary energy. However, they could not account for the decrease of the dielectric constant at smaller grain sizes.[59]

Our goal is to develop a theory that can explain all of the above phenomena, including: (i) the size dependence of T_c in small particles, (ii) the dielectric anomaly in $BaTiO_3$ ceramics, and (iii) the unusual enhancement observed in the dielectric constant of $BaTiO_3$ particles/polymer composites at low temperatures.

For small particles, surface effects become important. For ferroelectric particles, the important surface effect is the depolarization effect due to the bound surface charge arising from polarization. Therefore, we will consider the effect of depolarization on ferroelectricity. $BaTiO_3$

is not perfectly insulating as a space charge layer will arise to shield the bound surface charge. To accurately account for the depolarization effect in BaTiO$_3$ particles, we must also include the space charge layer effect.

The depolarization energy is reduced through a process by which the small particles form internal domains. The domain size is determined by the balance between the depolarization energy of the domains and the domain-wall energy. The depolarization energy and the domain wall energy will be incorporated into the Landau-Ginsburg expression for free energy which is known to be a good description of the ferroelectric transitions in large single crystals. The domain-wall energy can also be put within the framework of the Landau-Ginsburg free energy by assuming a hyperbolic tangent polarization profile at the domain wall. The domain-wall energy and the domain-wall width for a given domain polarization can be obtained by minimizing the domain-wall energy with respect to the domain width. So, for a given particle size and a given temperature, the free energy (a function of the polarization P and the domain size D) will be minimized with respect to P and D to obtain the equilibrium values of both P and D.

Our results to date have shown that both the domain-wall energy and the domain-wall width are in good agreement with the literature values. We have also shown that the ferroelectric transition temperature T_c decreases with a decreasing particle size, in agreement with the XRD and Raman experiments of Ishikawa et al. and Uchino et al. The domain size decreases with decreasing particle size (Fig. 8), in agreement with the TEM observation of Arlt et al.[59] Finally, due to the size dependence of T_c at a given temperature, the dielectric constant peaks at a certain size (Fig. 9), again in agreement with past and current observations.[60]
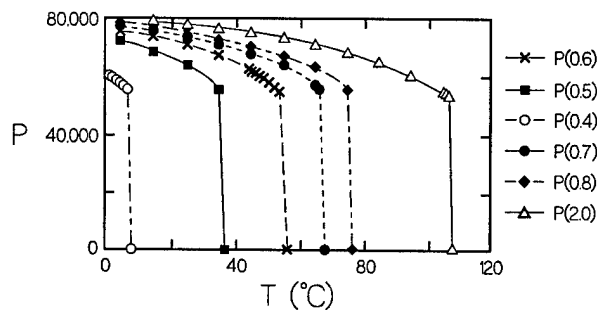
Fig. 8: The change in the ferroelectric transition temperature Tc as a function of particle size.
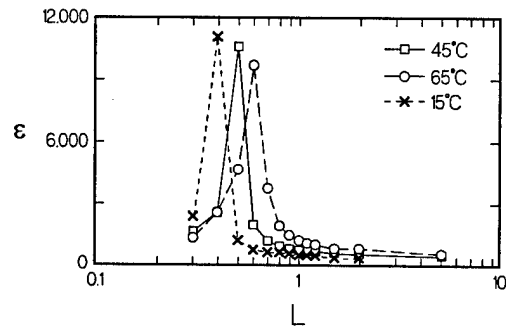
Fig. 9: Because of the size dependence of Tc at a given temperature, the dielectric constant ε peaks at a certain size L of the particles.

2.3. Low Temperature (<500°C) Processing of PZT Thin Films Through Seeding
Investigators: W. David Clifton, Fatih Dogan, and Ilhan A. Aksay

This study involves forming thin films of the ferroelectric material lead-zirconate-titanate (PbZr$_{0.52}$Ti$_{0.48}$O$_3$, PZT) onto the direct gap III-V semiconducting material GaAs. Direct gap semiconductors have been envisioned for use in a high speed optical computer which can operate at speeds several orders of magnitude greater than current silicon based electronic computers.[61] Development of these computers is hindered by the production of a material which can switch light at the high operating speeds desired of this new computer. Thin films of PZT have the potential of achieving the necessary high switching speeds for both light and electronic signals. This switching is only possible in the ferroelectric tetragonal perovskite crystal assemblage of

16

PZT. Unfortunately, to develop the perovskite phase within the film normally requires processing at 650°C, a temperature which destroys GaAs.[62-64] If a thin film of perovskite PZT can be produced below 400°C, the coupling of PZT and GaAs would be possible. This temperature reduction is the goal of this study.

To date, our work has isolated several problems which hinder the crystallization of the perovskite PZT phase at temperatures around 400°C and we have partially solved the crystallization temperature problem based on our observations. All current wet chemical techniques used for the deposition of PZT films require processing at 650-700°C to fully crystallize the perovskite phase. These films are initially amorphous after deposition and upon heating they first crystallize into an undesirable pyrochlore phase above 475°C followed by very slow crystallization of the perovskite phase. Lower temperature perovskite formation is hindered by the high perovskite nucleation temperature (>525°C) and the low density of perovskite nucleation sites (1-5 sites/100 mm^2), requiring long growing times for complete perovskite phase transformation.

We have prevented pyrochlore formation by depositing a monolayer of 100-200nm perovskite PZT 52/48 particles onto the substrate surface onto which we then spin coat a film of PZT 52/48 precursor solution. The perovskite particles act as nucleation sites for the perovskite phase and thus seed the growth of the perovskite.[65] Upon heat-treatment, the seeded films crystallize directly from the amorphous state to the perovskite phase at 460°C, completely circumventing the formation of the pyrochlore phase. Electrical property measurements of the low temperature seeded films indicated that they have a dielectric constant of over 700 and a remnant polarization of 11 mC/cm^2, while unseeded films have to be heated to 700°C to have similar properties. With these encouraging results, our future research will emphasize greater reductions in the perovskite crystallization temperature along with attempts to place PZT films onto GaAs substrates.

2.4. Piezoelectrical Properties of Pb(Zr$_{0.52}$Ti$_{0.48}$)O$_3$ Sintered at Low Temperature
Investigators: Fatih Dogan and Ilhan A. Aksay

Nb-doped PZT powders containing excess PbO have been prepared by coprecipitation from metal-nitrate solutions followed by freeze-drying. We have found that if, prior to freeze-drying, the precipitate is washed free of nitrates and then dispersed in a suitable solvent the formation of agglomerates could be controlled. Powders can be compacted without milling to a narrow nanometer-sized pore distribution and then sintered at 750°C to 98.5% of theoretic density. Evaporation of PbO during sintering is significantly reduced. For low temperature sintering, a diffusion-controlled mechanism has been proposed based on the high vapor pressure of PbO at lower temperatures.

Samples are thickness mode resonant from 1.5 to 1.75 MHz. The capacitance of the sample measured at 1 kHz gives a good estimate of the free dielectric constant and its associated loss tangent. Electrical impedance magnitude and phase were used to identify the thickness resonance frequencies f_s and f_p in order to calculate the electromechanical coupling coefficient k_t. Dielectric and piezoelectric properties are summarized in Table 1.

The improvement of piezoelectrical properties has been usually attributed to the increased grain size.[61,62] In this study, no significant difference in grain size was observed between the samples sintered at 800°C and the samples sintered at 1000°C. Detailed microstructural characterization is necessary to determine the influence of grain boundary composition,

17

development of tetragonal perovskite structure, and domain formation on the piezoelectrical properties. The calcination temperature has been shown to affect the sintering behavior and dielectrical properties of the samples. Powder (from a different batch as described above), calcined at 400°C resulted in 80.6 % of theoretic density after sintering at 800°C. Sintering density of >95 % theoretic density was obtained when the powder was calcined at 600°C. This may be attributed to the pyrochlore phase which forms at low calcination temperatures. The phase transformation during heat treatment can alter the pore structure of the compacts due to the density differences between the pyrochlore and perovskite phases.

Sintering Temperature	800°C	1000°C
Dielectric Const. (@ 1 kHz)	501	622
Loss Tangent	0.032	0.044
Coupling Coef. k_t	<<	0.55

Table 1. The sample sintered at 800°C shows no resonance peaks, thus exhibiting no measurable piezoelectrical activity. In contrast, a sample sintered at 1000°C exhibits normal resonance characteristics and piezoelectrical activity comparable to commercial PZT. The loss tangents are within normal bounds.

The dielectric constants (@ 25°C) of the samples calcined at 400°C and 600°C were ~500 and ~700, respectively. At the curie temperature the dielectric constants were 2100 and 4400 for low and high temperature calcined samples respectively. This behavior is attributed to the significant difference in the respective porosities of the samples as it is known that increasing porosity results in decreasing dielectric constant.[61]

2.5. Pressure Filtration of Hydrothermal BaTiO₃ Powder
Investigators: Fatih Dogan and Ilhan A. Aksay

Lowering the sintering temperatures of BaTiO₃ is necessary for reasons of economic processing in addition to maintaining material properties.[66] Lower sintering temperatures permit the use of low cost electrode materials having low melting temperatures in the manufacture of multilayer capacitors. Further, novel material properties are expected through better microstructural control, such as in making transparent materials for optoelectronic applications. Our long term goal is the processing of polycrystalline transparent BaTiO₃; our approach uses low sintering temperatures by reducing the grain size. To achieve highly dense green compacts with narrow pore size distribution colloidal processing and pressure filtration techniques are required.

The use of fine BaTiO₃ powders with particle size <0.1 μm should succeed in preparing fine-grained (<0.3 μm) BaTiO₃ monoliths under the correct conditions. We can control the average particle size of powders between 0.01 μm and 1 μm by adjusting the process parameters during hydrothermal processing. Sintering densities of up to ~99% of theoretical density have been achieved at 1225°C using dry pressed compacts. In these samples, the grain size was reduced to 0.4 μm using 0.9 wt% Nb addition.

Preliminary dispersion studies on BaTiO₃ in aqueous and nonaqueous solvents have revealed that the particles can be dispersed and sterically stabilized in water using PAA as the

18

dispersant and at a suspension pH of 9. Pressure filtration of sterically stabilized suspensions formed crack-free compacts (25 mm diameter by 5 mm thick). A highly concentrated acetate-based precursor of $BaTiO_3$ was used as dispersant to achieve *in situ* infiltration of the compacts during pressure filtration. This approach enables infiltration of bulk samples without forming concentration gradients.

Continuing studies on the pressure filtration of $BaTiO_3$ suspensions will be done with and without the addition of niobium as sintering aid. The role of niobium in controlling the grain size will be investigated using high resolution electron microscopy. The green and sintered densities of pressure-filtered samples will be compared with those of dry-pressed samples. To achieve yet higher packing densities, nanometer-sized particles (§1.1.2) will be pressure filtered. This will eliminate the drying step and thus the concomitant agglomeration of nanometer-sized particles.

2.6. Low Temperature Processing of BaTiO₃ Thin Films
Investigators: Fatih Dogan and Ilhan A. Aksay

The fabrication of $BaTiO_3$ thin films by conventional techniques, such as the use of sol-gels, requires high temperature heat treatments (>1000°C) mainly due to formation of $BaCO_3$ as an intermediate reaction product which decomposes above 900°C. Because of the high processing temperatures, controlling of the grain size is difficult, especially when small grain sizes are required. For the same reason, the selection of substrate materials is limited. Crystalline $BaTiO_3$ has been prepared at low processing temperatures (<200°C) through the reaction of a titania precursor and barium hydroxide solution (§2.1). Thermodynamically, the synthesis of $BaTiO_3$ at room temperature is possible.[67,68] The reaction is, however, kinetically favored above 50°C. Our goal is to prepare dense and crack-free $BaTiO_3$ thin films at low processing temperatures so that a variety of substrate materials can be used in the fabrication of optoelectronic devices and composites.

Sputtering titanium onto a substrate is a common technique used to form a continuous metal precursor layer prior hydrothermal treatment in $Ba(OH)_2$ solution.[66,69] Our titanium precursor films were prepared by sol gel process and spin coating of metalloorganic compounds having very slow hydrolysis rates (such as titanium diisopropoxide bis(2,4-pentanedionate)). The slow hydrolysis permits the formation of crack-free and transparent coatings after drying. Polystyrene and glass substrates were chosen due to their respective stability when exposed to strong bases at high temperature. The substrates were hydrothermally treated at 80°C to form crack-free, continuous transparent films composed of densely packed particles less than 0.1 µm in size. XRD analysis could not distinguished between cubic and hexagonal phases in the film.

The formation of the film is thought be via a mechanism of dissolution and precipitation as described for the formation of nano-sized particles. Experiments to confirm this model and the role of processing parameters in the production of fine grained thin films are continuing.

3. Model Systems

3.1. Formation and Sintering in Nanometer Size Particles
Investigators: Wan Y. Shih, Wei-Heng Shih,* Daniel M. Dabbs, Nan Yao, and Ilhan A. Aksay

*Department of Materials Engineering, Drexel University, Philadelphia, PA 10104.

Past studies within earlier AFOSR-sponsored projects have use gold particles for model studies on the formation, agglomeration, packing, and sintering of nanometer-sized particle

suspensions. As determined by our group in earlier and on-going studies (§3.2),[70,71] the growth of necks between touching particles falls into two kinetic regimes, the first in which the neck diameter scales with the cube root of the sintering time, the second in which the neck diameter scales with the square root of the sintering time . Our preliminary model relates this observation to the relative sizes of the domains within the particles in contact and the neck diameter (based on pore elimination models). We have further proposed that sintering between nanometer-sized particles is due to a form of viscous phase sintering since discrete boundaries were not observed between the particles.

3.1.1. Surfactant Mediated Deformation of Gold Agglomerates

In addition to the sintering of gold particles, we have observed the apparent surfactant driven "desintering" of ramified gold agglomerates. Using the method of Turkevich et al.,[72] we have made suspensions of nanometer size gold particles from mixtures of sodium citrate (aq) and gold chloride (aq). The formation process can be divided into three distinct stages: (i) In the first stage, nuclei of about 2nm in diameter form and aggregate to form large clusters. ζ-potential measurements showed that adsorption of the negatively charged citric ions onto the gold surface continued during this stage. The duration of the first stage was short, less than one minute at 90°C. The surface was soon saturated with citric ions and the size of the clusters stabilized. (ii) In the second stage, the clusters undergo extensive restructuring, leading to the breakup of the clusters into smaller gold particles. (iii) In the third stage, the gold particles reach a uniform size and remain stable in the suspension.
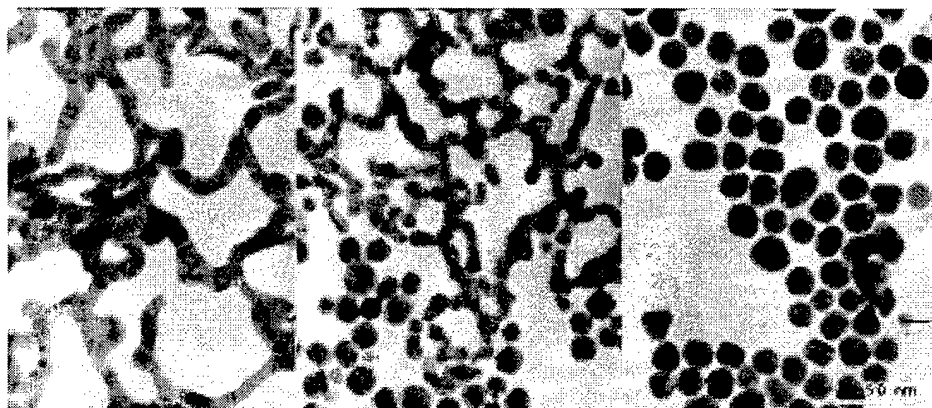
Fig. 10: (a) Ramified gold agglomerate with twin domains (domain size<10nm). (b) Intermediate desintering. (c) Final gold particles (~24nm average diameter).

We established that the negatively charged citric ions adsorbed on the gold surface were the principal components in the reaction mixture which determined the size of the final spherical particles seen at the end of stage (iii). The adsorption of the ions set the total electrostatic surface energy on the gold and the magnitude of the gold-water interfacial tension. The minimization of the total surface energy then set the final size of the gold particles. We have shown both theoretically and experimentally that the gold particle size is proportional to $(C_c/C_{Au})^{2/3}$, where C_c is the citric acid concentration and C_{Au} is the concentration of gold ions in solution.[70]

However, during the second stage of particle formation, we have recently observed that ramified clusters formed from the sintering of nanometer size nuclei formed in stage (i) (Fig. 10).[73] These structures were multiply twinned into domains smaller than 10 nm and eventually

20

broke up to form the final spherical particles. This breakup involves desintering or "dewelding"[74] from the continuous agglomerate to form the distinct particles.

The goals of this research topic are to (i) establish the mechanism of desintering and (ii) determine the effect of surface modifications on desintering and sintering.

Spectroscopic studies of citrate-stabilized gold suspensions have been done using attenuated total reflectance (ATR) infrared spectroscopy. As shown in Fig. 11, significant changes in the spectrum of the citrate result from its interaction with the gold particles. First, the strong presence of the two anti-symmetric and symmetric stretching modes at ~1550 and ~1400 cm^{-1} and the absence of significant absorption between 2500-3000 cm^{-1} in the citrate solution spectrum indicates that sodium citrate is completely dissociated in solution. Once gold particles have been formed, the spectrum shifts markedly. The presence of bands near 2860 cm^{-1} and 1700 cm^{-1} indicate the presence of saturated carboxylate ions, supported by the pronounced decrease in the ~1550 and ~1400 cm^{-1} bands. Absorbance bands now appear at 1150 and 1200 cm^{-1}; their location corresponds to the presence of hydroxides unencumbered by hydrogen bonding.

In terms of ultimate stability, the rod-like structures in the intermediate stage is unstable against the formation of spherical particles. It is known that the negatively charged citric ions have already adsorbed on the gold surface. With surface charges, the rod-like structures observed in the intermediate stage have a high electrostatic energy than spherical particles.

Fig. 11: ATR spectra for (i) sodium citrate in aqueous solution and (ii) gold particles stabilized by citrate ions in aqueous suspension.
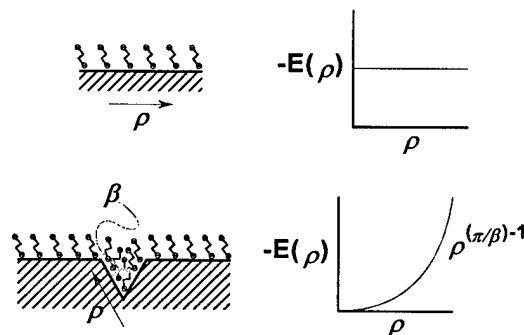
Fig. 12: Model of a smooth metal surface with constant potential (top) and surface containing cusp of low potential (bottom). The high density of adsorbates within the cusp forces migration of metal atoms from the apex, sharpening the cusp and eventually leading to separation.

Due to the adsorbed citric ions, the electrostatic energy not only influences the final particle size and shape but also governs the dewelding process. For example, let us consider a flat metal surface with a constant potential as illustrated in Fig. 12. On such flat surface, the formation of a corner is favored because the electric field is diminishing at the corner. The narrower the corner the more stable the corner. As driven by this electrostatic stability, the corner will become sharper and sharper until the rod breaks up, which is observed in our TEM micrographs. The dewelding phenomenon is the sharpening of the corners.

To facilitate the sharpening of the corners, gold atoms must be able to move around. It is well known surface atoms can have much higher (often several orders of magnitude higher) mobility than bulk atoms. The enhanced mobility of the gold atoms in these nanometer-size rods
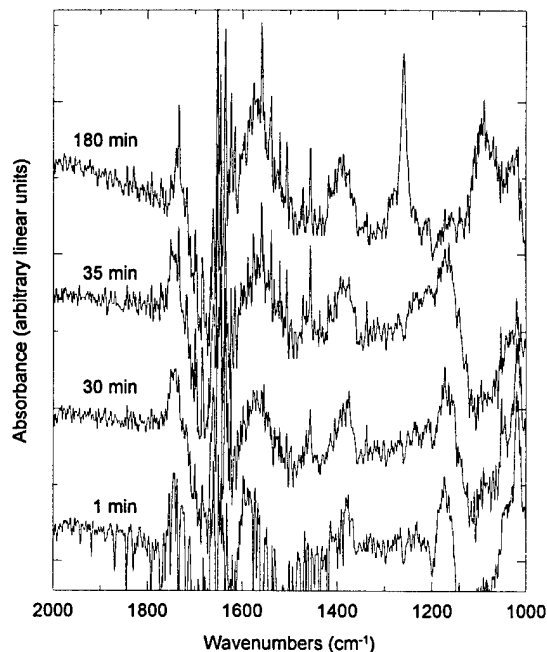
21

to facilitate dewelding is conceivable: (i) the diameter of the rods is on the order of 10 nm, therefore, a high percentage of atoms are on the surface. (ii) These rods are highly twinned. Each crystalline domain (likely separated by twin boundaries) is smaller then 10 nm. The high population of the domain boundaries also contributed to the high mobility of gold atoms in these rods. The other evidence is that each corner is connected to a domain boundary.

To conclude, the dewelding phenomenon observed in these gold rods is a process (a) driven by the minimization of the electrostatic energy and (b) facilitated by the high mobility of the gold atoms in these structures. The high mobility is attributed to the extensive presence of crystalline domain boundaries and the high surface area of these rods.

3.1.2. Neck Formation of Nanometer Sized Particles

Preliminary experimental observations of the necking between two nanometer size gold particles showed that the neck size L increases with time t as $L \propto t^{1/3}$ at small t and as $L \propto t^{1/2}$ at large t. Our previous simulations on single-pore elimination in a polycrystalline matrix also showed two scaling regimes:[75] for small pores, the pore elimination time t_p scales with the initial pore radius r as $r \propto t_p^{1/3}$ and for large pores, $r \propto t_p^{1/2}$. The crossover from $r \propto t_p^{1/3}$ to $r \propto t_p^{1/2}$ corresponds to a pore radius r that is approximately equal to the grain radius G.

We have observed that small gold particles are usually multiply twinned into about five or six domains as seen in TEM micrographs (Fig. 13). Therefore, we think that the observation of two scaling regimes in the neck formation between two nanometer-sized gold particles is a result of crossover from one regime where the neck is smaller than the domain size to another where the neck is larger than the domain size, analogous to the presence of two scaling regimes in single pore elimination. Thus, our objective in this portion of the project is to explain the observed crossover from one scaling regimes to another in the neck formation in nanometer sized gold particles.
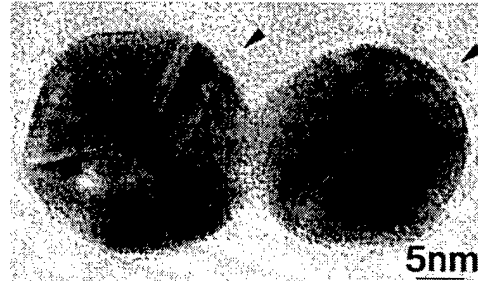
Fig. 13: Necking between nanometer sized particles.

Our approach consists of two parts: computer simulations of the necking process and scaling analysis. In the first, simulations are performed using a model we previously developed capable of modeling both orientational flipping and diffusion. Orientational flipping gives rise to grain growth and diffusion gives rise to sintering. The model is capable of displaying various sintering phenomena such as densification, the growth of large pores, pore coalescence, pore shrinkage, evaporation and condensation, thermal etching, rounding of a sharp corner, and necking. In this study, we are looking at the neck formation between two spherical particles each containing five to six domains of different crystalline orientations.

The results of our scaling analysis to date have shown that the neck size indeed goes as $L \propto t^{1/3}$ for L smaller than the domain size G and as $L \propto t^{1/2}$ for L larger than G. The difference in the scaling behavior between the region where L is smaller than G and the region where L is larger than G is a function of the total area of the intersecting domain boundaries. In the region where $L > G$, the total area of the domain boundaries intersecting the neck region is given by L^{d-1}/G, where d is the Euclidean dimension. Where $L < G$, the total area of the domain boundaries intersecting the neck region is L^{d-2}. The scaling laws have been shown to be independent of the dimensionality.

22

3.2. Mesoporous Silicate and Aluminosilicate Materials
Investigators: Michael D. McGehee, Sol M. Gruner, Nan Yao, Chang-Min Chun, Alexandra Navrotsky, Itaru Honma, Uthara Srinivasan, and Ilhan A. Aksay

The synthesis of materials with nanoscale (1-100 nm) pores and pore structure is important to a host of applications including catalysts, ultrafiltration, protein stabilization and characterization, and separation technology. Microporous materials are usually crystalline framework solids (such as zeolites) whose pore dimensions formed are in a range of 10-15Å. Recent work by Mobil scientists have revealed a surfactant-based procedure which yields mesoporous silicate/aluminosilicate materials with pores up to 10nm in size arranged in either lamellar, hexagonal, or bicontinuous cubic structures.[76,77] Two different models have been proposed to explain the formation of these materials: either (i) the mineral precipitates onto the exposed surface of a water-surfactant liquid crystal phase or (ii) the condensation of the mineral acts in concert with the crystallization of the surfactants to form the ordered structure (co-assembly). Our work using time-resolved X-ray diffraction show that transitions between the structures occur during synthesis, supporting the co-assembly model. We have also demonstrated that the morphology of the co-assembled phase can be controlled and have begun to apply these materials to coating and nanocomposite processing.

3.2.1. Self Assembling Mesoscopic Materials
Cubic surfactant-silicates were synthesized by mixing tetraethoxysilane (TEOS)with Arquad (a proprietary surfactant), NaOH, and water. The TEOS dispersed into the surfactant solution and hydrolyzed. Heating resulted in the formation of solid particles. The surfactants were removed from the particles by calcination at low temperature to preserve the pore structure.

X-ray diffraction (XRD) and TEM analyses showed that the particles had an Ia3d cubic symmetry before and after calcination, but that the lattice parameter shrank from 97 to 84Å as a result of the densification. Fig. 14 shows examples of the lamellar, cubic, and hexagonal surfactant-silicates made by similar methods, but with different chemical ratios of reactants.

The formation of cubic surfactant-silicates was studied with time-resolved XRD using a specialized X-ray beamline.[78,79] Three distinct phases were observed during reaction (Fig. 15). The first phase had an XRD pattern with only one broad peak and could not be identified (Fig. 15a). This phase persisted for weeks in synthesis solutions which were kept at 20°C, but was replaced by the second phase within 30min at 100°C. The second phase had a 2-peak XRD pattern (Fig. 15b) which was consistent with a lamellar morphology having a 35 Å repeat distance. The third phase had an XRD pattern (Fig. 15c) consistent with Ia3d symmetry. Transformation from the lamellar to cubic phase has been observed as the Ia3d cubic mesophase growing epitaxially from the lamellar phase. Controlled phase mor-
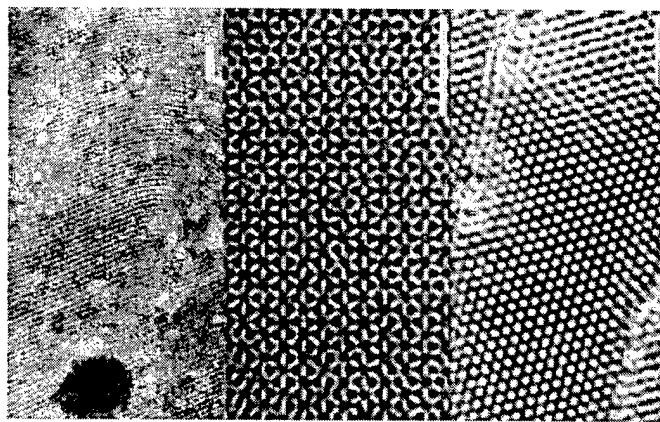

Fig. 14: TEM images of (a) the lamellar morphology, (b) the cubic phase with Ia3d symmetry viewed along its [111] zone axis, and (c) the hexagonal phase viewed along its [001] zone axis (bars = 30 nm).

23

phology is achieved by using slightly different surfactant groups and coassembling the surfactant and silicates into the desired structure. Although questions remain about the mechanism of coassembly, the knowledge that we can control the microstructure permits work on the applications of mesophase materials, described in the following sections (§§3.2.2 and 3.2.3).[80]

3.2.2. Thin Film Formation of Mesoporous Silicate

Mesoporous materials now include titanium silicate, antimony oxide, tungsten oxide, iron oxide, lead oxide, and zinc oxide.[81,82] The self-organized regular array structure of the mesoporous channels is formed through the replication of the liquid crystal templating (LCT) phase of the surfactant/water system. Depending on the LCT structure, lamellae, hexagonal, cubic crystalline phase particles can be precipitated homogeneously in the solution (§3.2.1). For applications involving chemically functionalized surfaces, a method for forming continuous and homogeneous films onto substrates would be a valuable tool. Ceramic thin-film formation on functionalized interfaces mimics biological processes responsible for forming natural composites such as teeth, bones and shells.[83] By manipulating the nucleation and growth on the functionalized interface, the films can be formed at ambient temperatures. The important parameters controlling formation appear to be the proper combination of solution chemistry and surface functionalization.

In general, we have observed that as the surfactant/TEOS ratio is decreased, the solution condition moves from the particle precipitation region to the film formation region. In the system used in this study, a four-

Fig. 15: XRD patterns from a time-resolved experiment. The numbers with the peak labels are the square of the peak indices. (a) 20min exposure taken during the first 20 min of heating. (b) 20min exposure taken after 160 min of heating. The two peaks are consistent with a lamellar structure, as shown by the peak labels. (c) The average of six 20min exposures taken after 20 h of heating. The 8 peaks are consistent with Ia3d symmetry, as shown by the peak labels. There were two faint rings at higher q which did not match the Ia3d pattern and are not explained.

fold dilution of the concentrated particle-precipitated solution can be used to form continuous films on substrates such as Mylar or glass. As water is removed the film forms as a white gel. Subsequent hydrothermal processing results in a rigid transparent glass. XRD and TEM studies showed that the obtained film structure consists of a disordered mesophase containing small inclusions of a crystalline phase. The mesophase has short range ordering of ~40-45Å, equivalent to the d-spacing of both the lamellae and hexagonal phase, but lacks long range ordering. This is probably related to the phase behavior in the biosurfactant/water system. Dilution can shift the equilibrium solution phase from hexagonal to disordered hexagonal/lamellae and, as a result, the film consists of the disordered mesostructure phase largely because the film structure replicates the LCT structure of the biosurfactant. Additionally, the seeding of crystalline particles onto the substrate did not enhanced the crystalline film growth indicating that modifying the substrate surface does not prevent the disordering of the film simply because the deposited film structure is primarily determined by the structure of the solution.
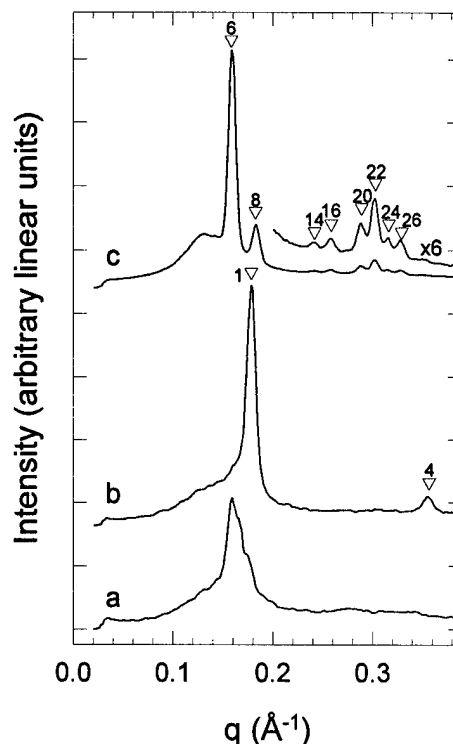
24

We have found that the film structure is closely related to the phase behavior of the surfactant/water system. The key goal in this work is to find the appropriate conditions under which the solution surfactant/silicate structure remains in crystalline hexagonal region and the film forms onto the substrate without particle precipitation. If transparent and continuous films can be successfully prepared on the substrate, new application are envisioned through the chemical and physical infiltration of functionalized molecules, clusters and small particles, dyes, and proteins into the mesoporous channels. Because of the potential advantage of uniformity of the pores, high doping ratio, and uniform orientation of the channels, such films can be used to form optical non-linear devices, high dielectric capacitors, separation membranes, and templated supports for nanocomposites.

3.2.3. Fabrication and Characterization of Mesosilicate Nanocomposites

Several synthesis routes are under investigation for fabricating nanocomposites using mesoporous materials. Second phase materials include: (i) metal alkoxide precursors (ceramic/ceramic composites), (ii) organic monomers, and (iii) metals. Once infiltrated, larger potentially more useful materials can be formed from the resultant nanocomposite powders. As described in the preceding section (§3.2.2), thin film formation is currently under investigation. Continuous mesoporous films offer a suitable substrate for the formation of nanocomposite layers that might be built up to form larger and/or graded materials. Further, chemical modification of the pore surfaces may be used to both stabilize the mesoporous structure and enhance the infiltration of the pores by the appropriate second phase precursor.

Attempts to infiltrate the mesoporous silicate with metal alkoxides has had mixed results. Using a technique developed for the infiltration of wood cell walls by alkoxides (§3.3), it was determined that slower hydrolyzing alkoxides achieved higher penetration depths. Infiltration by TEOS resulted in up to 40% of the pore volume being filled with silica gel. However, the more rapidly hydrolyzing aluminum and titanium alkoxides merely coated the outside of the mesoporous powder. In the coassembled materials, the surfactant is believed to act as a steric barrier to infiltration by organometallics; when the surfactant is removed, the high hydroxyl content on the pore surfaces favors hydrolysis and condensation and penetration is blocked by the plugging of the pores by the resulting ceramic or gel. Hydrolysis of the organometallic can be slowed by the use of larger functional groups on the metal cation but steric hindrance is enhanced and infiltration is not improved.

We have shown that suitable organics can infiltrate the mesostructure. A zwitterionic monomer can be inserted into the pores and then polymerized *in-situ* to form a ceramic/polymer composite. BET surface sorption and TGA measurements indicate that the polymer coats the pore surfaces although the uniformity of this coating has not been determined. Effective surface areas in the mesoporous material were reduced from $576m^2/g$ for the calcined material to $17.0m^2/g$ in the infiltrated material. Finally, metal infiltration has been attempted using a two step process: (i) solution infiltration by aqueous solutions of metal salts and (ii) reduction of the metal ions in the pores. The resulting materials are highly colored but we have not yet shown the formation of nanoscale metal particles within the mesostructure.

Current studies emphasize the role of the surface to the successful infiltration of the mesostructure by precursors or precursor solutions. Subsequent processing conditions, such as the method used to reduce the metal cations to metal, must be designed so as to optimize the retention of the second phase while preventing the collapse of the mesophase.

25

3.3. The Formation of Ceramic/Cellulose Cellular Composites
Investigators: Sara E. Keckler, Daniel M. Dabbs, Nan Yao, and Ilhan A. Aksay

Cellular structures such as wood can be used as scaffolds for the synthesis of complex structures of organic/ceramic nanocomposites. A wood cell is a fiber-reinforced resin composite of cellulose fibers in a lignin matrix; a single cell wall, containing several layers of different fiber orientations and lignin content, is separated from its neighboring wall by the middle lamella, a lignin-rich region.[84] In order to achieve total mineralization, deposition on and in the cell wall must be achieved.[85] Geological fossilization of wood occurs as permineralization (filling the void spaces with mineral) and petrifaction (mineralizing the cell wall as the organic component decays) through infiltration of wood with inorganics after growth.[85] Conversely, living plants can incorporate inorganics into their cells and in some cases into the cell walls during growth.[86] This project attempted to mimic geological fossilization by infiltrating inorganic precursors into wood cells; by doing so we hoped to enhance the physical properties of the wood.[87] Our most current work has used electron microscopy and vibrational spectroscopy to study the structure of silica formed in the cell walls after infiltration of the cell walls by tetraethoxy silane (TEOS).

Partially hydrolyzed TEOS in ethanol (25% by volume) was infiltrated into rehydrated kiln-dried samples of hemlock and pine. Impregnation was completed in a partially evacuated reaction chamber at room temperature. After curing at 105°C for two days, the impregnated samples were heat treated between 200° and 600°C to fully convert the precursor to silica and to remove part or all of the organic matrix. Electron micrographs reveal that the structure of the wood cell is unaffected by the presence of silica (as silica gel). Energy dispersive spectroscopy (EDS) measurements confirmed the presence of silica gel across the cell wall prior to heat treatment. Infrared spectroscopy revealed that gel formation is preferential within the cell wall. Binding between gel precursors and organic components of the cell wall was seen in the formation of C–O–Si bridges within the cell wall; these bridges decay with increasing temperature and the loss of organic phase.[88]

Two forms of silica are found within the cell wall: (i) particles on the wall bordering the middle lamella and (ii) dense uniform silica gel in the bulk of the cell wall. The pH of wood extractant is around 4.6 suggesting that the silica on exposed surfaces results from acid-catalyzed hydrolysis and condensation of TEOS. This is indicated by the particulate nature of silica observed at the boundary layer. The bulk silica is finer in texture than the boundary layer silica. We attribute the finer bulk texture to the geometrical constraint imposed on the polymerization of silica within the intercellulosic confinements of the cell wall. Before and after the removal of the organic phase by pyrolysis, the gross cellular structure of the wood is maintained, replicated on the micron scale by silica (Fig. 16).[88]
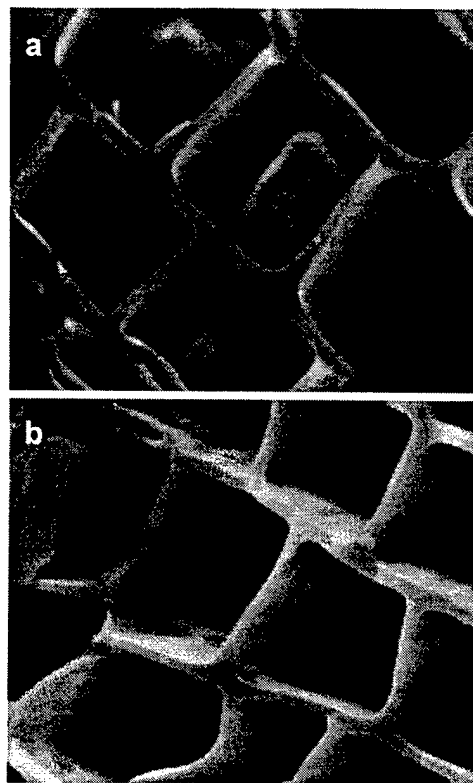

Fig. 16: SEM micrographs of infiltrated wood (a) before pyrolysis and (b) after pyrolysis at 600°C. The wood's cellular structure has been replaced by silica in (b).

26

References:

1. T. S. Yeh and M. D. Sacks, "Low-Temperature Sintering of Aluminum Oxide," *J. Am. Ceram. Soc.*, **71** [10] 841-44 (1988).
2. G. C. Bye and G. T. Sipkin, "Influence of Cr and Fe on Formation of α-Al_2O_3 from γ-Al_2O_3," *J. Am. Ceram. Soc.*, **57** [8] 367-71 (1974).
3. M. Kumagai and G. L. Messing, "Enhanced Densification of Boehmite Sol-Gels by α-Alumina Seeding," *J. Am. Ceram. Soc.*, **67** [11] C-230-31 (1984).
4. M. Kumagai and G. L. Messing, "Controlled Transformation and Sintering of a Boehmite Sol-Gel by α-Alumina Seeding," *J. Am. Ceram. Soc.*, **68** [9] 500-05 (1985).
5. D. S. Horn and G. L. Messing, "Alumina Monolith Formation by Flocculation of Boehmite Sols," *J. Am. Ceram. Soc.*, **72** [9] 1719-21 (1989).
6. I. A. Aksay and C. H. Schilling, "The Mechanics of Colloidal Filtration," in *Forming of Ceramics, Advances in Ceramics*, Vol. **9**, edited by J. A. Mangels and G. L. Messing (American Ceramic Society, Columbus, Ohio, 1984), pp. 85-93.
7. C. H. Schilling, W.-H. Shih, W. Y. Shih, and I. A. Aksay, "Advances in Drained Shaping of Ceramics," *Ceramic Powder Science IV, Ceram. Trans.*, Vol. **22**, edited by S. Hirano, G. C. Messing, and H. Hausner (American Ceramic Society, Westerville, Ohio, 1991), pp. 307-20.
8. R. A. Shelleman, G. L. Messing, and M. Kumagai, "Alpha Alumina Transformation in Seeded Boehmite Gels," *J. Non-Cryst. Sol.*, **82**, 277-85 (1986).
9. I. A. Aksay, "Molecular and Colloidal Engineering of Ceramics," *Ceramics International*, **17**, 267-74 (1991).
10. K. T. Miller and C. F. Zukoski, "The Osmotic Consolidation of Suspensions and Gels," *J. Am Ceram. Soc.* **77** [9] 2473-8 (1994).
11. R. D. Bagley, "Extrusion Method for Forming Thin-walled Honeycomb Structures," U.S. Patent #3,790,654.
12. I. M. Lachman, *et al.*, *Am. Ceram. Soc. Bull.*, **60** 202 (1981).
13. R. R. Tummala, *IBM J. Res. Develop.* **36** 817 (1992).
14. T. C. Halsey, *Science* **258** 761-766 (1992).
15. C. F. Zukoski, *Ann. Rev. Mater. Sci.* **23** 45-78 (1993).
16. A. P. Gast and C. F. Zukoski, *Adv. in Colloid and Interface Sci.* **30** 153-202 (1989).
17. R. Newnham and G. R. Ruschau, *J. Am. Ceram. Soc.* **74** 463 (1991).
18. I. A. Aksay, *et al.* (Eds.) *Hierarchically Structured Materials, MRS Proc.* **255** (1992).
19. R. Lakes, *Nature* **361** 511-515 (1993).
20. K. A. Lurie and A. V. Cherkaev, *Proc. Roy. Soc. Edinburgh* **99A** 71 (1984).
21. S. Torquato, *Appl. Mech. Rev.* **44** 37-76 (1991).
22. F. F. Reuss, "Notice sur un novel effet de l'eletricite galvanique," *Mem. Soc. Imp. Natur. Moscov*, **2** 327-37 (1809).
23. "Advanced Ceramic Processing and Technology" **Vol. 1**, J. G. P. Binner, ed.(Noyes Publications, Park Ridge, New Jersey, 1990).
24. R. C. Bradt, "Cr_2O_3 Solid Solution Hardening of Al_2O_3," *J. Am. Ceram. Soc.* **50** [1] 54-55 (1967).
25. Y. Sakka, D. D. Bidinger, and I. A. Aksay, "Processing of SiC-Mullite-Al_2O_3 Nano-composites," *J. Am. Ceram. Soc.*, **78** [2] 479-86 (1995).

26. Y. Sakka and I. Aksay, "Processing of Nanocooomposite Silicon Nitride-Mullite-Alumina By Reaction Sintering," *NanoStructured Materials*, **Vol. 44**, No. 2, pp. 169-182, (Elsevier Science Ltd. Pergamon, 1994).

27. M. P. Borom, M. K. Brun, L. E. Szala (GE corporate R&D), "Kinetics of Oxidation of Carbide and Silicide Dispersed Phases in Oxide Matrices," *Advanced Ceramic Materials* **3** [5] 491-97 (1988).

28. J. Schlichting, "Molybdenum Disilicide as Component of Modern High Temperature Composites," *High Temp.- High Pressures*, **10** 241-69 (1978).

29. R. Brynsvold, "Processing of a Mullite Matrix, Molybdenum Disilicide Reinforce Composite," M.Sc. thesis, University of Washington (1991).

30. K. Niihara, "New Design Concepts of Structural Ceramics - Ceramic Nanocomposite," *J. Ceram. Soc. Jpn.*, **99** [10] 974-82 (1991).

31. H. Takada, A Nakahira, H. Ohnishi, S. Ueda, and K. Niihara, "Improvement of Mechanical Properties of Natural Mullite/SiC Nanocomposite," *Jpn. J. Powder and Powder Met.*, **38** 348-51 (1991).

32. S. Wu and N. Clausen, "Reaction Bonding and Mechanical Properties of Mullite/Silicon Carbide Composites," *J. Am. Ceram. Soc.* **77** [11] 2898-904 (1994).

33. N. Shinohara, unpublished research, University of Washington (1986).

34. N. Shinohara, D. M. Dabbs, and I. A. Aksay, "Infrared Transparent Mullite through Densification of Monolithic Gels at 1250°C," *Infrared and Optical Transmitting Materials*, R. W. Schwartz, ed., Proc. SPIE **683**, 12-18 (1986).

35. C. Han, G. D. Maupin, I. A. Aksay, G. C. Stangle, C. B. Martin, and R. P. Kurosky, "Ceramic Precursor Mixture and Technique for Converting the Same to Ceramic," U.S. Patent #5,061,682 (October 29, 1991).

36. G. L. Messing, S.-C. Zhang, and G. V. Jayanthi, "Ceramic Powder Synthesis by Spray Pyrolysis," *J. Am. Ceram. Soc.*, **76** [11] 2707-26 (1993).

37. Y. L. Zhang, D. L. Milius, I. A. Aksay, "Effect of Structural Morphology on the Mechanical Properties of SiC/A1 Ceramic-Metal Composites," *Proc. 5th International Symp. on Ceramic Materials and Components for Engines*, 1994.

38. T. Iseki, T. Kameda, and T. Maruyama, "Interfacial Reactions Between SiC and Al During Joining," *J. Mat. Sci.*, **19** 1692-1698 (1984).

39. T. Yano, S. Kato, and T. Iseki, "High Resolution Electron Microscopy of SiC/Al_4C_3 Interface,"

40. J. C. Viala, F. Bosselet, P. Fortier, and J. Bouix, "Chemical Aluminum or Aluminum-Silicon Alloys", *ICCM&ECCM,* **2** 2.147-2.155, F. L. Matthews, ed.

41. D. L. Milius, "The Sintering of Silicon Carbide with Liquid Aluminum," M.S. Thesis, University of Washington, 1986.

42. D. J. Lloyd and E. Dewing, "Stability of SiC in Molten Aluminum," D. S. Wilkinson, ed., 71-77 (Pergamon Press).

43. S. Schamm, J. P. Rocher, and R. Naslain, "Physicochemical Aspects of the K_2ZrF_6 Process Allowing the Spontaneous Infiltration of SiC (or C) Preforms by Liquid Aluminum," *Developments in the Science and Technology of Composite Materials, ECCM,* Vol. 3, 157-163 (1989).

44. M. Yasrebi, G. H. Kim, K. E. Gunnison, D. L. Milius, M. Sarikaya, and I. A. Aksay, "Biomimetic Processing of Ceramics and Ceramic- Metal Composites," *Mat. Res. Soc. Symp. Proc.*, **180** 625-635 (1990).

45. F. Delannay, L. Froyen, and A. Deruyttere, "Review: The Wetting of Solids by Molten Metals and it's Relation to the Preparation of Metal-Matrix Composites," *J. Matl. Sci.*, **22** 1-16 (1987).

46. S. Y. Oh, J. A. Cornie, and K. C. Russell, "Wetting of Ceramic Particles with Liquid Aluminum Alloys," *Met. Trans. A*, **20A** 527-41 (1989).

47. N. D. Corbin, G. A. Rossi, and P. M. Stephan, "Making Ceramics Tougher," *Machine Design*, 84-89 (July 23, 1987).

48. R. P. Andres, R. S. Averback, W. L. Brown, W. A. Goddard III, A. Kaldor, S. G. Louie, M. Moscovits, P. S. Peercy, S. J. Riley, R. W. Siegel, F. Spaepen, and Y. Wang, "Research Opportunities on Cluster And Cluster-Assembled Materials," *J. Mater. Res.*, **4** [3] 705-36 (1989).

49. R. W. Siegel, R. Ramasamy, H. Hahn, L. Tiang, and R. Gronsky, "Synthesis, Characterization, and Properties of Nanophase TiO_2," *J. Mater. Res.*, **3** 1367-72 (1988).

50. E. Ustundag, R. Subramanian, R. Dieckmann, and S. L. Sass, *In-Situ Composites: Science and Technology*, M. Singh and D. Lewis eds., p97 (The Minerals, Metals, and Materials Society, 1994).

51. E. Breval, Z. Deng, S. Chiou, and C. G. Pantano, *J. Mat. Sci.* **27** 1464 (1992).

52. R. Subramanian, E. Ustundag, R. Dieckmann, and S. L. Sass, in *Advances in Ceramic-Matrix Composites*, Edited by 127.

53. R. Roy, S. Komarneni, and D. M. Roy, in *Better Ceramics Through Chemistry*, Edited by C. J. Brinker, D. E. Clark, and D. R. Ulrich, *Mater. Soc. Symp. Proc.* **32** 347 (1984).

54. A. E. Nielsen, "Precipitates: Formation, Coprecipitation and Aging," in *Treatise of Analytical Chemistry, Part I, Theory and Practice*; 2nd ed., Vol. 5, I. M. Kolthoff and P. J. Elving, eds., 269-347 (Wiley, New York, 1983).

55. W. Hertl, "Kinetics of Barium Titanate Synthesis," *J. Am. Ceram. Soc.*, **71** [10] 879-83 (1988).

56. G. H. Bogush and C. F. Zukoski, "Studies on the Formation of Monodisperse Silica Powders", in *Ultrastructure Processing of Advanced Ceramics*, J. D. Mackenzie and D. R. Ulrich, eds., 477-486 (Wiley, New York, 1988).

57. Ishikawa et al., *Phys. Rev. B*, **37** 5852 (1988).

58. Uchino et al., *J. Am. Ceram. Soc.*, **72** 1555 (1989).

59. G. Arlt, D. Hennings, and G. de With, *J. Appl. Phys.* **58** 1619 (1985).

60. W. Y. Shih, W.-H. Shih, and I. A. Aksay, "Size Dependence of the Ferroelectric Transition of Small $BaTiO_3$ Particles: Effect of Depolarization," *Phys. Rev. B*, **50** [21] 15,575-85 (1994).

61. J. F. Scott and C. A. P. DeAraujo, "Ferroelectric Memories," *Science*, **246** 1400-05 (1989).

62. B. A. Tuttle, T. J. Headley, B. C. Bunker, R. W. Schwartz, T. J. Zender, C. L. Hernandez, D. C. Goodnow, R. J. Tissot, and J. Michael, "Microstructural Evolution of $Pb(Zr,Ti)O_3$ Thin Films Prepared by Hybrid Metallo-Organic Decomposition," *J. Mater. Res.*, **7** [7] 1876-82 (1992).

63. R. W. Schwartz, Z. Xu, D. A. Payne, T. A. DeTemple, and M. A. Bradley, "Preparation and Characterization of Sol-Gel Derived PbTiO$_3$ Thin Layers on GaAs," *Mat. Res. Soc. Symp.*, **200** 167-72 (1990).

64. K. D. Budd, "Structure Evolution in Sol-Gel Derived Lead Titanate-Based Materials, and Applications to the Processing of Thin Dielectric Layers," Ph.D. Thesis, University of Illinois (1986).

65. G. L. Messing, M. Kumagai, R. A. Shelleman, and J. L. McArdle, "Seeded Transformations for Microstructural Control in Ceramics," *Science of Ceramic Chemical Processing*, L. L. Hench and D. R. Ulrich eds., pp. 259-271 (John Wiley & Sons, New York 1986).

66. P. Bendale, S. Venigalla, J. R. Ambrose, E. D. Verink, and J. H. Adair, "Preparation of Barium Titanate Films at 55°C by an Electrochemical Method," *J. Am. Ceram. Soc.* **76** 2619-27 (1993).

67. K. Oseeo-Asare, F. J. Arriagade, and J. H. Adair, "Solubility Relationship in the Coprecipitation Synthesis of Barium Titanate: Heterogeneous Equilibria in the Ba-Ti-C$_2$O$_4$-H$_2$O-System," *Ceramic Powder Science II*, edited by: G. L. Messing, E. R. Fuller Jr., and H. Hausner, The American Ceramic Society Inc., Westerville, OH (1988).

68. M. M. Lencka and R. E. Riman, "Thermodynamic Modeling of Hydrothermal Synthesis of Ceramic Powders," *Chem. Mater.* **5** 61-70 (1993).

69. M. Yoshimura, S. E. Yoo, M. Hayashi, and N. Ishizawa, "Preparation of BaTiO$_3$ Thin Film by Hydrothermal Electrochemical Method," *Jap. J. Appl. Phys.* **28** 2007-2009 (1989).

70. J. Liu, W. Y. Shih, W.-H. Shih, M. Sarikaya, I. A. Aksay, "On the Growth and Monodispersity of Colloidal Gold Particles," to be submitted to *Langmuir* (1995).

71. J. Liu, "Structures and Properties of Colloidal Systems of Nanometer-Sized Particles," Ph.D. Dissertation, University of Washington (1990).

72. J. Turkevich, P. C. Stevenson, and J. Hillier, "A Study of the Nucleation and Growth Processes in the Synthesis of Colloidal Gold," *Trans. Faraday Soc., Disc.* **11** 55-75 (1961).

73. D. M. Dabbs, N. Yao, and I. A. Aksay, "Surfactant Mediated Deformation of Gold Particles," *Proc. Ann. MSA*, **52** 446-7 (1994).

74. G. S. Ferguson, M. K. Chaudhury, G. B. Sigal, and G. M. Whitesides, "Contact Adhesion of Thin Gold Films on Elastomeric Supports: Cold Welding Under Ambient Conditions," *Science*, **253** 776-8 (1991).

75. W. Y. Shih, W.-H. Shih, and I. A. Aksay, "Elimination of an Isolated Pore: Effect of Grain Size," *J. Mat. Res.* **8** [4] 1 (1995).

76. C. T. Kresge, M. E. Leonowicz, W. J. Roth, J. C. Vartuli, and J. S. Beck, "Ordered mesoporous molecular sieves synthesized by a liquid-crystal template mechanism," *Nature* **359** 710 (1992).

77. J. S. Beck, J. C. Vartuli, W. J. Roth, M. E. Leonowicz, C. T. Kresge, K. D. Schmitt, C. T.-W. Chu, D. H. Olson, E. W. Sheppard, S. B. McCullen, J. B. Higgins, and J. L. Schlenker, "A new family of mesoporous molecular sieves prepared with liquid crystal templates," *J. Am. Chem. Soc.* **114** 10834 (1992).

78. J. R. Milch, *J. Appl. Cryst.* **16** 198 (1983).

79. S. M. Gruner, J. R. Milch, and G. T. Reynolds, *Rev. Sci. Instrum.* **53** 1770 (1982).

80. M. D. McGehee, "Self-Assembling Mesoscopic Surfactant/Silicate Materials" Senior Thesis, Princeton University (1994).

81. Q. Huo, D. I. Margolese, U. Ciesla, P. Feng, T. E. Gier, P. Sieger, R. Leon, P. M. Petroff, F. Schuth, and G. D. Stucky, "Generalized synthesis of periodic surfactant/inorganic composite materials," *Nature* **368** 317 (1994).

82. P. T. Tanev, M. Chibwe, and T. J. Pinnavala, "Titanium-containing mesoporous molecular sieves for catalytic oxidation of aromatic compounds," *Nature* **368** 321 (1994).

83. B. C. Bunker, P. C. Rieke, B. J. Tarasevich, A. A. Campbell, G. E. Fryxell, G. L. Graff, L. Song, J. Liu, J. W. Virden, and G. L. McVay, "Ceramic thin-film formation on functionalized interfaces through biomimetic processing," *Science* **264** 48 (1994).

84. A. J. Panshin and C. de Zeeuw, *Textbook of Wood Technology*, (New York, McGraw-Hill 1980) p. 85.

85. P. Buurman, "Mineralization of Fossil Wood," *Scripta Geol.* **12** 1-42 (1972).

86. P. B. Kaufman, J. D. LaCroix, P. Dayanandan, L. F. Allard, J. J. Rosen, and W. C. Bigelow, "Silicification of Developing Internodes in the Perennial Scouring Rush (*Equisetum* hyemale var. affine) *Dev. Biol.* **31** 124-35 (1973).

87. D. M. Dabbs, D. R. Treadwell, W. C. Hicks, I. A. Aksay, and F. Kayihan, "Ceramic/Wood Composites," unpublished research (1992).

88. S. E. Keckler, "Incorporation of Silica into Wood Cell Walls," Senior Thesis, Princeton University (1994).

4. Personnel

Senior Research Personnel:

Ilhan A. Aksay	David L. Milius
Helen Chan	Mao-Xu Qian
Daniel M. Dabbs	Wan Y. Shih
Fatih Dogan	Matt Trau
Itaru Honma	Nan Yao

Graduate Research Personnel:

Donald B. Bidinger	Kirk M. Slenes
Chang-Min Chun	James Vartuli
W. David Clifton	

Undergraduate Research Personnel:

Sara E. Keckler	Dilshad Shahid
John S. Lettow	Uthara Srinivasan
Michael D. McGehee	Joe Teltser
John Mellowes	

Collaborators:

Shyamsunder Erramilli (Physics, Princeton University)

Sol M. Gruner (Physics, Princeton University)

Bernard Keimer (Physics, Princeton University)

Alexandra Navrotsky (Geophysics, Princeton Univ.)

Dudley A. Saville (Chemical Engr., Princeton Univ.)

Wei-Heng Shih (Materials Engineering, Drexel University)

5. Manuscripts

5.1. Published Articles

RJ = Refereed Journal; IRP = Invited/Refereed Proceedings; IP= Invited Proceedings; and RP = Refereed Proceedings
★ = Copy of manuscript is available in the Appendices

1992

1. (RP42) F. Dogan, J. Liu, M. Sarikaya, and I. A. Aksay, "A Study on the Formation of Hydrothermally Prepared BaTiO₃ Particles," in *Proc. 50th Ann. Meeting EMSA*, edited by G. W. Bailey (San Francisco Press, San Francisco, 1992), pp. 304-05.

2. RP44) G. H. Kim, M. Sarikaya, and I. A. Aksay, "Measurement of Residual Stresses in B₄C-Al Cermets by CBED," in *Proc. 50th Ann. Meeting EMSA*, edited by G. W. Bailey (San Francisco Press, San Francisco, 1992) pp. 154-55.

1993

3. (CP19) H. Erkalfa, Z. Misirli, T. Baykara, F. Dogan, and I. A. Aksay, "Mechanical Properties of Colloidally Processed Alumina with Cr₂O₃ and MnO₂ Additives," in *Proc. of the Third Euro-Ceramics, Vol. 3*, edited by P. Duran and J. F. Fernandez (Faenza Editrice Ibérica, San Vicente, Spain, 1993) pp. 549-53.

4. (RP49) Y. Sakka, D. D. Bidinger, J. Liu, M. Sarikaya, and I. A. Aksay, "Processing of SiC-Mullite-Al₂O₃ Nanocomposite," in *Proc. 16th Annual Conf. Metal Matrix, Carbon, and Ceramic Matrix Composites*, edited by J. D. Buckley, NASA CP-3175 Part 1, (NASA Langley, February 1993) pp. 15-26.

5. (RP51) C. H. Schilling, L. Bergstrom, H.-L. Ker, and I. A. Aksay, "Particle Attraction Effects on the Centrifugal Casting and Extrusion of Alumina," in *Handbook on Characterization Techniques for the Solid-Solution Interface*, edited by J. H. Adair, J. A. Casey, and S. Venigalla (the Am. Ceram. Soc., Westerville, OH., 1993) pp. 35-51.

6. (CP20) S. Sevinçtav, T. Baykara, F. Dogan, and I. A. Aksay, "Monolithic α-Alumina Through Pressure Filtration of Seeded Boehmite Gels," in *Proc. of the Third Euro-Ceramics, Vol. 1*, edited by P. Duran and J. F. Fernandez (Faenza Editrice Ibérica, San Vicente, Spain, 1993) pp. 687-90.

7. (RP52) W.-H. Shih, W. Y. Shih, S.-I. Kim, and I. A. Aksay, "Equilibrium-State Density Profiles of Centrifuged Cakes of Flocculated Suspensions," *MRS Symp. Proc.*, **289**, 251-56 (1993).

1994

8. (RJ47) J. S. Abel, G. J. Stangle, C. H. Schilling, and I. A. Aksay, "Sedimentation in Flocculating Colloidal Suspensions," *J. Mater. Res.*, **9** [2] 451-61 (1994).

★ 9. (RP53) D. M. Dabbs, N. Yao, and I. A. Aksay, "Surfactant Mediated Deformation of Gold Particles," in *Proc. 52nd Ann. Mtg. MSA*, eds.: G. W. Bailey and A. J. Garratt-Reed, (Microscopy Society of America, 1994) pp. 446-7.

★ 10. (RJ48) Y.-N. Jun, D. M. Dabbs, I. A. Aksay, and S. Erramilli, "Processing of Monolithic Magnetic Gels for Magnetophoresis," *Langmuir,* **10** [10] 3377-79 (1994).

11. (RP55) S. E. Keckler, D. M. Dabbs, N. Yao, and I. A. Aksay, "Silicification of Wood-cell Walls," in *Proc. 52nd Ann. Mtg. MSA*, eds.: G. W. Bailey and A. J. Garratt-Reed, (Microscopy Society of America, 1994) pp. 428-9.

★ 12. (RP56) M. D. McGehee, S. M. Gruner, N. Yao, C. M. Chun, A. Navrotsky, and I. A. Aksay, "Synthesis of Mesoscopic Structures by Co-assembly," in *Proc. 52nd Ann. Mtg. MSA,* eds.: G. W. Bailey and A. J. Garratt-Reed, (Microscopy Society of America, 1994) pp. 448-49.

★ 13. (RJ51) Y. Sakka and I. A. Aksay, "Processing of Nanocomposites of Silicon Nitride-Mullite-Alumina by Reaction Sintering," *Nanostructured Materials*, **4** [2] 169-82 (1994).

★ 14. (RJ52) W.-H. Shih, W. Y. Shih, S.-I. Kim, and I. A. Aksay, "Equilibrium-State Density Profiles of Centrifuged Cakes," *J. Am Ceram. Soc.*, **77** [2] 540-46 (1994).

★ 15. (RJ53) W. Y. Shih, W. -H. Shih, and I. A. Aksay, "Size Dependence of the Ferroelectric Transition of Small $BaTiO_3$ Particles: Effect of Depolarization," *Phys. Rev. B*, **50** [21] 15,575-85 (1994).

16. (RJ54) Y.-B. Son, C.-H. Kim, S.-D. Jang, J. Liu, M. Sarikaya, and I. A. Aksay, "Crystallization Behavior of Cordierite-Based Glass with Excess SiO_2 and Al_2O_3 at Initial Stage," *Jpn. J. Appl. Phys.*, **32** [2] 1101-08 (1994).

★ 17. (RJ55) T. Yogo and I. A. Aksay, "Synthesis of Mullite Fibre form an Aluminosiloxane Precursor," *J. Mater. Chem.*, **4** [2] 353-59 (1994).

18. (RJ56) Y. L. Zhang, D. L. Milius, I. A. Aksay, "The Effect of Si on the Wetting Behavior of SiC-Al System," *Materials Science and Engineering* (Chinese), **12** [2] 16-23 (1994).

19. (RP59) Y. L. Zhang, D. L. Milius, I. A. Aksay, "Effect of Structural Morphology on the Mechanical Properties of SiC/Al Ceramic-Metal Composites," *Proc. 5th International Symp. on Ceramic Materials and Components for Engines*, 1994.

1995

20. (IP22) I. A. Aksay and D. M. Dabbs, "Bioinspired Processing of Nanostructured Materials," in *Proc. 8th International Metallurgy and Materials Congress, Istanbul* (Chamber of Metallurgical Engrs, Turkey, Publ. 32, 1995) pp. 775-94.

★ 21. (IP23) I. A. Aksay, D. M. Dabbs, I. Honma, S. Manne, D. L. Milius, N. Nakagawa, M. Trau, and N. Yao, "Synthesis and Processing of Nanostructured Ceramics," in *Neptis-IV: Nano-sized Powders and Related Composite Materials* (Nisshin Engineering Co., Ltd., Japan, 1995) pp. 49-57.

★ 22. (RP60) C. M. Chun, A. Navrotsky, and I. A. Aksay, "Aggregation Growth of Nanometer-Sized $BaTiO_3$ Particles," in *Proc. Microscopy and Microanalysis,* eds.: G. W. Bailey, M. H. Ellisman, R. A. Hennigar, and N. J. Zaluzec, (Jones and Begell Pub., New York, 1995) pp. 188-89.

★ 23. (RP61) J. W. Mellowes, C. M. Chun, and I. A. Aksay, "Amorphous Silica Coating on α-Alumina Particles," in *Proc. Microscopy and Microanalysis,* eds.: G. W. Bailey, M. H. Ellisman, R. A. Hennigar, and N. J. Zaluzec, (Jones and Begell Pub., New York, 1995) pp. 212-13.

★ 24. (RJ60) Y. Sakka, D. D. Bidinger, and I. A. Aksay, "Processing of SiC-Mullite-Al_2O_3 Nanocomposites," *J. Am. Ceram. Soc.* **78** [2] 479-86 (1995).

★ 25. (RJ61) W. Y. Shih, W.-H. Shih, and I. A. Aksay, "Elimination of an Isolated Pore: Effect of Grain Size," *J. Mater. Res.* **10** [4] 1000-15 (1995).

★ 26. (RP62) U. Srinivasan, I. Homma, C. M. Chun, D. M. Dabbs, D. A. Hajduk, S. M. Gruner, and I. A. Aksay, "Nanocomposite Processing via Infiltration of Mesoporous Silica," in *Proc. Microscopy and Microanalysis,* eds.: G. W. Bailey, M. H. Ellisman, R. A. Hennigar, and N. J. Zaluzec, (Jones and Begell Pub., New York, 1995) pp. 210-11.

★ 27. (RJ62) M. Trau, S. Sankaran, D. A. Saville, and I. A. Aksay, "Electric-Field-Induced Pattern Formation in Colloidal Dispersions," *Nature* **374** 437-39 (1995).

★ 28. (RJ63) M. Trau, S. Sankaran, D. A. Saville, and I. A. Aksay, "Pattern Formation in Non-Aqueous Colloidal Dispersions via Electrohydrodynamic Flow," *Langmuir* **11** 4665-72 (1995).

★ 29. (RP65) N. Yao, W. Y. Shih, D. M. Dabbs, and I. A. Aksay, "The Breakup of the Intermediate Gold Aggregates," in *Proc. Microscopy and Microanalysis,* eds.: G. W. Bailey, M. H. Ellisman, R. A. Hennigar, and N. J. Zaluzec, (Jones and Begell Pub., New York, 1995) pp. 196-97.

1996

30. (IP24) I. A. Aksay, J. T. Staley, and R. K. Prud'homme, "Ceramics Processing with Biogenic Additives," in *Biomimetic Materials Chemistry*, ed. S. Mann (VCH Publishers, New York, NY, 1996) pp. 361-78.

31. (RP66) C. M. Chun, A. Navrotsky, and I. A. Aksay, "Nucleation and Growth of $SrTiO_3$ on Nanometer-Sized $BaTiO_3$ Particles," in *Proc. Microscopy and Microanalysis,* eds.: G. W. Bailey (Jones and Begell Pub., New York, 1996) pp.

32. (RP67) C. M. Chun, A. Navrotsky, and I. A. Aksay, "Morphological Evolution of Nanometer-Sized $BaTiO_3$ Particles," in *Proc. Microscopy and Microanalysis,* eds.: G. W. Bailey (Jones and Begell Pub., New York, 1996) pp.

33. (RP68) N. Durlu, N. Yao, D. L. Milius, and I. A. Aksay, "Liquid Phase Sintering of BN Doped Fe-Cu/TiC Composites," in *Proc. Microscopy and Microanalysis,* eds.: G. W. Bailey (Jones and Begell Pub., New York, 1996) pp.

34. (RJ70) M. D. Rintoul, S. Torquato, C. Yeong, S. Erramilli, D. Keane, D. M. Dabbs, I. A. Aksay, "Structure and Transport Properties of a Porous Magnetic Gel via X-ray Tomography," *Phys. Rev. E* (1996) (in press).

35. (RJ72) W. Y. Shih, W.-H. Shih, and I. A. Aksay, "Heteroflocculation in Binary Colloidal Suspensions: Monte Carlo Simulations," *J. Am. Ceram. Soc.* (1996) (in press).

★ 36. (RJ74) M Trau, D. A. Saville, and I. A. Aksay, "Field Induced Layering of Colloidal Crystals," *Science* **272** [5262] 706-09 (1996).

★ 37. (RJ75) D. R. Treadwell, D. M. Dabbs, and I. A. Aksay, "Mullite ($3Al_2O_3 \cdot 2SiO_2$) Synthesis with Aluminosiloxanes," *Chem. Mater.* **8** [8] XX-XX (1996).

38. (RP69) N. Yao, D. M. Dabbs, and I. A. Aksay, "Mullite Phase Separation in Nanocomposite Powders," in *Proc. Microscopy and Microanalysis,* eds.: G. W. Bailey (Jones and Begell Pub., New York, 1996) pp.

5.2. Patents and Invention Disclosures

1. M. Hama, D. M. Dabbs, and I. A. Aksay, "Low Temperature Sintering of Ceramic Materials," U.S. Patent #5,135,692, August 4, 1992.

2. I. A. Aksay, M. Yasrebi, D.L. Milius, G.-H. Kim, and M. Sarikaya, "Laminated B_4C/Al Composites through Melt Infiltration," U.S. Patent #5,308,422, 1994.

3. M. Yasrebi, H. Nakagawa, and I. A. Aksay, "Method for Stabilizing Ceramic Suspensions," U.S. Patent Application Serial No.08/239,706; Filed May 9, 1994.

6. Biographical Sketches

6.1. Ilhan A. Aksay

Dr. Aksay is a Professor in the Chemical Engineering Department and the Princeton Materials Institute at Princeton University. Prior to joining Princeton University, Dr. Aksay was a professor in the Department of Materials Science and Engineering at the University of Washington from 1983 through August 1992. He earned his B.Sc. degree (with honors) in Ceramic Engineering at the University of Washington in 1967. He received his M.Sc. degree in 1969 and Ph.D. in 1973, both in Materials Science and Engineering at the University of California, Berkeley. Upon completing a one-year postdoctoral appointment at the University of California, Berkeley, he worked at Xerox, Webster Research Center (1973-75) and the Middle East Technical University in Ankara (1975-81). In 1981, Dr. Aksay joined UCLA's Materials Science and Engineering Department as a visiting Associate Professor. In September 1983, he joined the faculty of the University of Washington as an Associate Professor in the Department of Materials Science and Engineering and was promoted to Professor in 1985. His most recent research activities have been on the utilization of colloidal and biomimetic techniques in ceramic processing. In recognition of his contributions in this area, he received the Richard M. Fulrath Award of the American Ceramic Society in 1987. In 1987, he was also named as the first Pacific Northwest Laboratory Professor by the U.S. Department of Energy. More recently, he received the Puget Sound Engineering Council's 1988 Academic Engineer of the Year award for his "contributions to advances in ceramic processing technology and the transfer of this technology to industry and students." Dr. Aksay is a Fellow of the American Ceramic Society.

Research Interests
- processing science of ceramics
- thermodynamics and phase equilibria
- diffusion and structural studies in ionic systems
- interfacial reactions and capillary phenomena
- utilization of colloidal and biomimetic techniques in ceramic processing

6.2. Daniel M. Dabbs

Daniel M. Dabbs received his B.Sc. degree in Chemistry at Texas Tech University in 1977. Both his M.Sc. degree (Physical Chemistry, 1979) and Ph.D. (Materials Science and Engineering, 1984) were awarded by the University of Washington. Upon completion of his doctoral work, he went to work for Wacker Siltronic (Portland, Oregon) as a Materials Characterization Engineer. In March of 1986, Dr. Dabbs joined the research group of Dr. Ilhan A. Aksay at the University of Washington as a Postdoctoral Research Associate. A year later, he accepted the position of Acting Program Manager, Advanced Ceramics Materials Laboratory, within the Washington Technology Center and College of Engineering, University of Washington; he was promoted to Program Manager in August 1987. In September 1992 Dr. Dabbs joined Princeton University as a Research Staff Member in the Ceramic Materials Laboratory. His research interests include vibrational spectroscopic characterization of ceramics and precursors, phase transitions in ceramic precursors, fiber-matrix interaction studies, and electron transfer mechanisms. He has also performed several studies in the physical chemistry of trace elements in crystalline material. As a graduate Research Assistant, his studies on the behavior of arsenic in fayalitic slags earned him a Fellowship in the Washington Minerals Resource and Research Institute.

Research Interests
- vibrational spectroscopic characterization of ceramics and precursors
- phase transitions in ceramic precursors
- fiber-matrix interaction studies
- electron transfer mechanisms
- physical chemistry of trace elements in crystalline material

6.3. David L. Milius

David L. Milius received his B.Sc. degree in Ceramic Engineering from Iowa State University in 1984. In 1986 he received his M.Sc. in Ceramic Engineering from the University of Washington, Seattle; his thesis was entitled "The Sintering of SiC with Liquid Aluminum." Following graduation he went to work for the Advanced Ceramic Materials Laboratory in the Washington Technology Center at the University of Washington. From 1986 to 1992 he participated in a joint project on the processing of ceramic-metal composites with both the Lawrence Livermore National Laboratory and the Los Alamos National Laboratory. These materials were tested as potential lightweight armor materials for the Air Force Office of Scientific Research. In 1992 he joined the Princeton University as a Research Technical Staff Member in the Ceramic Materials Laboratory, Princeton Materials Institute. His interests include ceramic-metal composites, superconducting single crystals, and ceramic-ceramic nanocomposites. He has also worked on the processing of ceramics for engine component applications.

Research Interests
- processing and fabrication of ceramic-metal composites
- high temperature ceramic superconductors
- nanocomposites

6.4. Wan Y. Shih

Wan Y. Shih received her B.S. in Physics from Tsing-Hua University, Hsin-Chu, Taiwan, ROC, in 1976 and her Ph.D. in Physics from the Ohio State University, Columbus in 1984. She worked as a Postdoctoral Research Associate in the Materials Research Laboratory at the Ohio State University from 1984-1985. She worked as a Research Scientist in the Department of Materials Science and Engineering and the Washington Technology Center at the University of Washington, Seattle, from 1985 to 1992. Since 1993, she has held two simultaneous appointments: as a Research Staff Member in the Chemical Engineering Department and the Princeton Materials Institute, Princeton University, Princeton, New Jersey, and as a Research Associate Professor in the Department of Materials Engineering, Drexel University, Philadelphia.

Research Interests
- materials theory
- superconductivity
- dielectrics and ferroelectrics
- smart materials,
- numerical simulations
- structure and rheological properties of colloidal suspensions
- sintering of nanometer-size particles

7. Appendices: Selected Papers

SURFACTANT MEDIATED DEFORMATION OF GOLD PARTICLES

D. M. Dabbs,[§‡] N. Yao,[‡] and I. A. Aksay[§‡]

[§]Department of Chemical Engineering and
[‡]Princeton Materials Institute, Princeton University, Princeton, NJ 08544-5263

Ultrafine (~ 20 nm diameter) gold particles produced by the reduction of an aqueous $AuCl_3$ solution with citric acid have been used as model systems for the study of structural control in systems of nanometer-sized colloids and for the study of sintering between such particles.[1] Liu[2] has observed that the final, monosized particles evolve from sintered (welded) aggregates (Fig. 1). This process is visible as the color of the gold suspension changes over time. Liu[2] also noted that the ultimate particle size was a function of the gold/citrate ion ratio in the original solution. Similarly, Ferguson et al.[3] have observed the low temperature welding of gold surfaces when organic adsorbates move laterally to increase metal-metal contact. Although Liu[2] has shown that aggregation and deaggregation processes are important in the evolution of colloidal particles, no explanation has been given for the dewelding mechanism of larger aggregates to form discrete particles. In this work, we combine the techniques of electron microscopy and infrared spectroscopy to propose a chemical influence for the dewelding process.

Colloidal gold suspensions were made using the technique described by Turkevich et al.[4] with modifications described by Liu.[2] Aqueous $AuCl_3$ (50 mg Au/l) was heated to 95°C and mixed with aqueous sodium citrate (1 wt%) with continued heating. After 30 minutes, a stable suspension of nearly monosized particles (~ 200 nm diameter) was formed. Samples of the heated mixture were taken at different time intervals and cooled rapidly to room temperature. Cylindrical internal reflectance infrared (CIR) spectroscopy and photon correlation spectroscopy (PCS) were used to chart the progress of the process. Samples for TEM studies (on a Philips CM-20 TEM) were made by taking small amounts of the suspensions and transferring them to carbon grids.

In Fig. 2 the evolution of particle diameter as a function of time is shown. The initial suspension consists of structures of large apparent diameter which break down to form smaller particles. The particle size does not change once it reaches the stable size after 3 hours at 95°C. The dispersion of the particles is maintained by the presence of a surfactant layer, seen in Fig. 3. The formation of the surfactant layer appears to play an important role in the evolution from welded aggregates to single particles.

The addition of citrate ion to a solution of $AuCl_3$ results in rapid (< 1 minute) oxidation of citrate ion, apparently producing a ketone diacid, 3-oxo-1,5 pentanedioic acid. Between 1 and 35 minutes, features at 1465 and 1525 cm^{-1} indicate the adsorption of bidentate carboxylates onto the metal (Fig. 4); this process appears to be completed after 35 minutes as shown by the stability of these bands from 35 to 180 minutes. Coincident with the appearance of the adsorbed carboxylate is the disappearance of a feature at 1025 cm^{-1}; the significance of this (if any) is not yet known. After 180 minutes at 95°C a strong new feature is apparent at 1262 cm^{-1}; again, the significance of this feature is not known. We propose that the presence of the adsorbed carboxylate and its evolution to the bidentate form is responsible for the deformation of the aggregates to form single particles, through a mechanism that we do not yet fully understand.[5]

References

1. J. Liu, M. Sarikaya, and I. A. Aksay, *Proc. Ann. MSA*, **46**(1988)716.
2. J. Liu, Ph.D. Dissertation, University of Washington (1990).
3. G. S. Ferguson *et al.*, *Science*, **253**(1991)776.
4. J. Turkevich, P. C. Stevenson, and J. Hillier, *Trans. Faraday Soc., Discussions*, **11**(1951)55.
5. This work was supported by a grant from the U.S. Air Force Office of Scientific Research (AFOSR-F49620-93-1-0259).
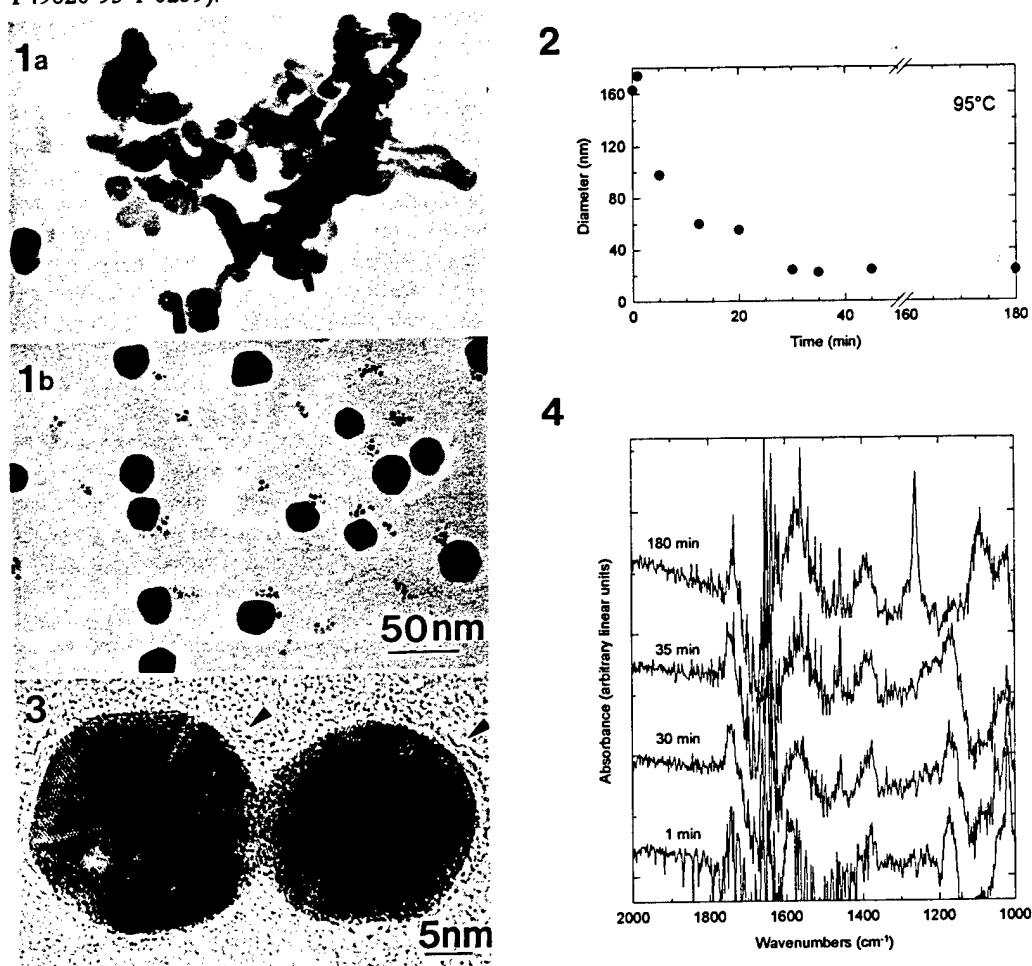
Fig. 1.—TEM images of gold cluster (a) before and (b) after dewelding.

Fig. 2.—PCS measurements of effective particle diameter with time.

Fig. 3.—High resolution TEM image showing the surfactant layer (10-20Å) attached on gold particle surface. Note the necking between the two particles.

Fig. 4.—CIR measurements on selected gold/citrate suspensions as a function of time.

447

Processing of Monolithic Magnetic Gels for Magnetophoresis

Yong-Nam Jun,[†] Daniel M. Dabbs,[‡] Ilhan A. Aksay,[‡] and
Shyamsunder Erramilli[*,†]

*Departments of Physics and Chemical Engineering and Princeton Materials Institute,
Princeton University, Princeton, New Jersey 08544*

Received May 26, 1994

Magnetite particles and monosized polystyrene beads were trapped in a silica sol–gel, which was then dried by using supercritical fluid extraction. When the monolithic dried gel is sintered, the polystyrene beads are pyrolyzed, leaving a porous magnetized piece of ceramic with controlled pore sizes. These "magnetic gel" ceramics provide a novel class of materials for use in gel magnetophoresis and other biophysical applications.

We report the synthesis of a "magnetic gel" oxide glass with controlled pore sizes intended for magnetophoresis applications in biology. Magnetophoresis, where magnetically labeled cells or DNA are trapped by high magnetic field gradients, is a rapidly evolving technique that is complementary to the more widely used electrophoresis method. Existing implementations of high magnetic field gradients use either steel wool[1] or metal spheres.[2] However, there exists a need for finer control of the pore sizes and a way to tailor the magnetic and structural properties of the filter material for specific applications, while at the same time ensuring that metal filters do not react with salt solutions that comprise most biological samples.

The goal of the present research is to separate magnetically labeled biological particles, which are either targeted cells or DNA molecules bound to magnetic beads. This application immediately specifies the engineering properties that must be displayed by the processed materials: (i) The magnetic "gel" has to generate large field gradients ($\sim 10^4 - 10^5$ T/m) in order to generate sufficient forces to effectively trap small magnetic particles. (ii) The material must have a low remnant magnetization in order to allow trapped particles to be eluted after switching off an external magnetic field. (iii) The pore sizes should be controllable, to suit the specific application—whether it is to filter magnetically labeled nucleic acids or target biological cells. This report describes a procedure for the rational synthesis of materials that satisfy these criteria.

There has been considerable interest in adapting sol–gel processing to the rational synthesis of composite materials engineered for specific applications by including inorganic and organic molecules into the sol–gel.[3] The chief advantage of this approach is that is allows for processing at much lower temperatures than direct fusion of mixed solids, thus making it possible to introduce guest molecules into the glass without destroying them during the high temperature treatment. By use of this approach, oxide glasses have been engineered with specific optical properties with applications in nonlinear optics and optical information storage.[4–5] Recently, Chaput et al.[6] have reported synthesizing a novel magneto-optic oxide gel with permanent optical birefringence. The possibility of incorporating composite nanoparticles with desired optical, electrical, or magnetic properties (see, for example, Lukehart et al.[7]) makes sol–gel processing ideal for applications in biotechnology, where control of materials properties often have to be tailored for specific applications.

I. Materials and Methods

A sol was made from tetraethoxysilane (TEOS), ethanol, and water with the volume ratio 1.5:1:1 and was left stirring for 24 h. Aliquots of this solution were placed in Pyrex tubes (~ 2 mL each) and then mixed with 1 mL of ferrofluid (EMG 705 from Ferrofluidics), which is an aqueous suspension of highly monodisperse colloidal particles of magnetite (Fe_3O_4) of ~ 100 Å diameter, stabilized by a surfactant.[8] Commercial polystyrene bead suspensions of varied amounts (Duke Scientific) were added to these mixtures to obtain a final material with controlled porosity, according to the method originally developed by Sonuparlak and Aksay.[9] A gel formed within a few minutes of the addition of the ferrofluid, suggesting that constituents of the ferrofluid enhance the gelation of the TEOS. In order to retain uniformity, the samples were shaken during gelation. Larger fractions of ethanol resulted in flocculation of the ferrofluid particles, whereas too little ethanol prevented complete hydrolysis of TEOS. Solvent extraction was performed above the critical point of the ethanol–water solution using a supercritical fluid extraction method.[10] The supercritical fluid extraction method has been described extensively in the literature and provides the most reliable and convenient method for drying gels while retaining monolithicity without cracking.[11,12]

To determine an appropriate temperature profile for the sintering, a piece of the aerogel was placed in a thermogravimetric analyzer (TGA, Perkin-Elmer). A steep drop in the mass of the sample was observed at around 300 °C, indicating the pyrolysis

---

(1) Roath, S.; Smith, A.; Watson, J. H. P. *J. Mag. Mag. Mater.* **1990**, *85*, 285.
(2) Miltenyi, S.; Muller, W.; Weichel, W.; Radbruch, A. *Cytometry* **1990**, *11*, 231.
(3) Brinker, C. J.; Scherer, G. W. *Sol-Gel Science: The Physics and Chemistry of Sol-Gel Processing*; Academic Press, Inc.: Boston, MA, 1990.
(4) Canva, M.; Le Saux, G.; Georges, P.; Brun, A.; Chaput, F.; Boilot, J.-P. *Opt. Lett.* **1992**, *17*, 218.
(5) Prasad, P. N. *SPIE* **1990**, *1328*, 168.
(6) Chaput, F.; Boilot, J.-P.; Canva, M.; Brun, A.; Perzynski, R.; Zins, D. *J. Non-Cryst. Solids* **1993**, *160*, 177.
(7) Lukehart, C. M.; Carpenter, J. B.; Milne, S. B. *CHEMTECH* **1993**, *23*, 29.
(8) Rosensweig, R. E. *Ferrohydrodynamics*; Cambridge University Press: Cambridge, 1985.
(9) Sonuparlak, B.; Aksay, I. A. Process for the Production of Porous Ceramics Using Decomposable Polymeric Microspheres and the Resultant Product; U.S. Pat. 4,777,153, 1988.
(10) Reece, G. Senior Thesis, Princeton University, 1993.
(11) Zarzycki, J.; Prassas, M.; Phalippou, J. *J. Mater. Sci.* **1982**, *17*, 3371.
(12) Because the solvent has been removed from these materials, they might be more appropriately called "magnetic xerogels". We prefer to use the short form "magnetic gels".
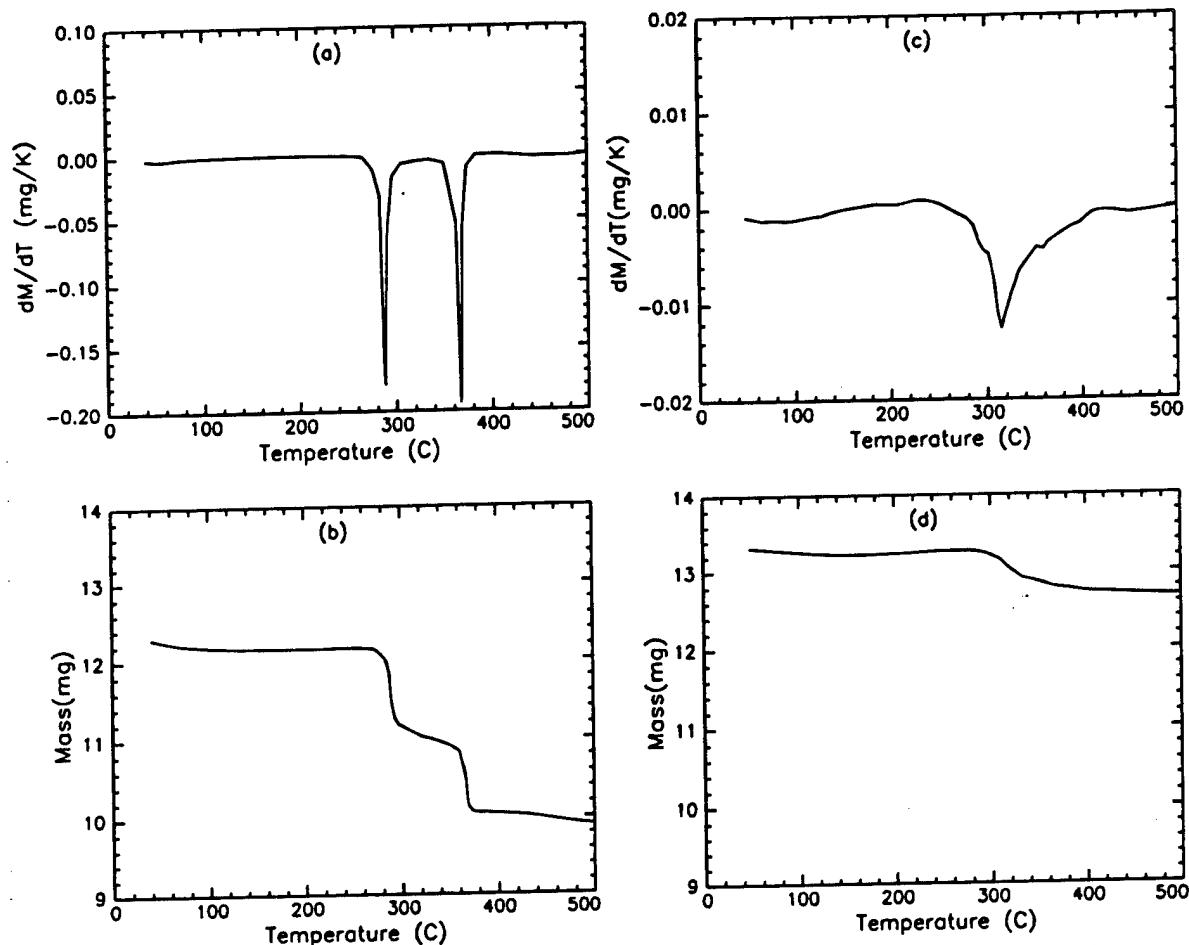
Figure 1. TGA profile for porous magnetic gels. (a) Derivative of the multistep mass loss profile shown in (b) is for a sample with a polystyrene beads with 3.4 μm diameter beads at a starting concentration of 0.02 (v/v). (c) Derivative of the mass loss profile shown in (d), for a sample with 10.2 μm diameter polystyrene beads also at 0.02 (v/v).

Figure 2. SEM of sintered porous magnetic gel. The circular holes are the locations of the polystyrene beads (21.7 ± 3.2 μm diameter), at a starting volume fraction of 0.015. The voids are the remnants of the polystyrene beads that were thermally removed, while the structure of the gel is maintained.

of polystyrene beads (Figure 1). Samples with large polystyrene beads (~10 μm diameter) showed only one step in the TGA loss-of-mass profile, similar to the in vacuo decomposition of polystyrene. Samples with smaller beads (~3 μm) showed a more complex multistep profile. Differently sized polystyrene beads may have different decomposition profiles, even in open air.

Sintering was done as follows. The sample was initially placed in an open air oven at 300 °C for a period of 45 min to ensure full oxidation of the polymer. The sample was then slowly heated in a nitrogen atmosphere to 700 °C and soaked for 3 h to give it greater structural integrity. The slightly reducing atmosphere had the advantage of reversing the partial oxidation of magnetite, which is inevitable during polymer oxidation at 300 °C. The

sample was then allowed to cool to room temperature. The result of this processing was a black porous ceramic. In samples that were sintered in ambient air at 700 °C, the magnetite in the ceramic appeared to oxidize and formed an extremely friable reddish brown ceramic resembling hematite with poor magnetic properties.

II. Analysis

Since the morphology of the gel is one of the most interesting parameters, the microscopic structure was characterized by scanning electron microscopy (SEM, Phillips 515). An SEM image of a gel with controlled

porosity is shown in Figure 2. The porosity was further characterized by measuring the BET isotherm, using helium gas as the adsorbate (Micromeritics). The surface area per gram was measured to be 22.76 ± 0.46 cm^2 g^{-1}. A careful study of a number of such SEM micrographs suggests that the voids left by the polystyrene spheres may not be randomly distributed; some clustering, perhaps as a result of van der Waals attraction between the spheres, is observed. While the microscopic origin of this phenomenon is not understood, clustering lowers the percolation threshold required to form a continuous channel across the sample. Nonrandom clustering may also be enhanced by preparing the gel in the presence of an external magnetic field, which can orient the magnetic particles to form field induced structures.[13,14]

Magnetic susceptibility measurements were performed using a SQUID magnetometer (Quantum Design) (see Figure 3). The magnetic property of particular interest is the saturation magnetization M_s and the remnant magnetization. The measured value of M_s is 39.8 ± 0.1 erg/(G g) and the remnant magnetization is 0.9 ± 0.02 erg/(G g) with saturation setting in at an applied field strength of ~2000 G. The large M_s is needed to obtain large field gradients to trap magnetically labeled particles, and the small remnant magnetization, which results from the small size of the superparamagnetic particles, ensures that particles can be eluted after switching off an externally imposed magnetic field.

The pore size and shape can be tailored for the specific filtration application by simply changing the diameter, shape, and volume fraction of the included polystyrene beads. A systematic investigation of the filtration characteristics of these new materials has begun. We believe

(13) Dickstein, A. J.; Erramilli, S.; Goldstein, R. E.; Jackson, D. P.; Langer, S. A. *Science* **1993**, *261*, 1012.

(14) Wang, Hao; Zhu, Yun; Biyd, C.; Luo, Weili; Cebers, A.; Rosensweig, R. E. *Phys. Rev. Lett.* **1994**, *72*, 1929.
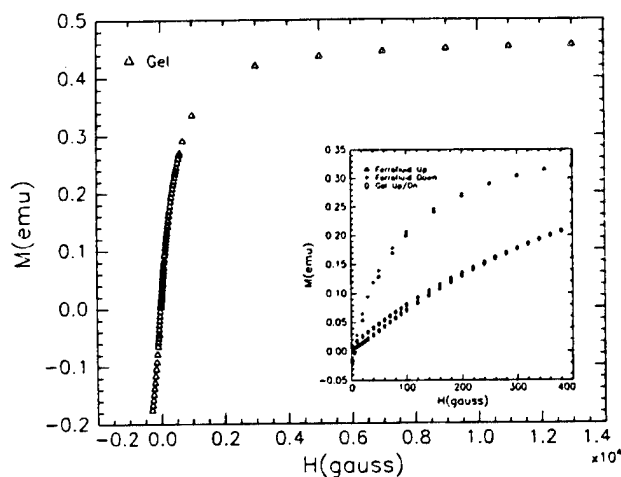
Figure 3. Magnetization of the porous magnetic gel. Inset shows the same data showing the extent of the hysteresis at lower values of the magnetic field. Also shown for comparison is the magnetization profile of the ferrofluid used.

that sol−gel technology can be used to synthesize new classes of materials that can be designed specifically to satisfy needs in biotechnology.

SYNTHESIS OF MESOSCOPIC STRUCTURES BY CO-ASSEMBLY

M. D. McGehee,* S. M. Gruner,*‡ N. Yao,‡ C. M. Chun,†† A. Navrotsky,†† and I. A. Aksay‡†

*Physics, †Geological and Geophysical Sciences, ‡Chemical Engineering
‡Princeton Materials Institute, Princeton University, Princeton, NJ 08544-5263

Synthesis of materials with nanoscale (1-100 nm) organization is of utmost importance in various applications. Recently, scientists at Mobil described a surfactant-based procedure which yields mesoporous silicate/aluminosilicate materials with pores up to 10 nm in size and lamellar, hexagonal, and bicontinuous cubic structures.[1] Two models were proposed to explain the formation of these materials. The first model assumes that silica polymerizes around a water-surfactant liquid crystal phase while the second model contends that the polymerization of the silica determines the ordering of the surfactants in a co-assembly fashion.[1,2] Our time-resolved x-ray diffraction studies show that transitions between structures occur during synthesis, supporting the co-assembly model.

The procedure for synthesizing cubic surfactant-silicates was as follows: 10.41 g of TEOS (tetraethoxy silane, Alpha Chemicals) was added to 35.86 g of Arquad (29% by weight $C_{16}TMACl$ in water, Akzo Chemicals), 25 ml of 1M NaOH, and 5.34 mL of deionized water. This mixture was stirred for 30 min with a magnetic stir bar, causing the TEOS to disperse with the surfactant solution and hydrolyze. Next, the mixture was heated at 100°C for 3 days in a closed Teflon bottle. The resulting solid particles were recovered by centrifugation, rinsing with deionized water, and drying in ambient air. The surfactants were removed from the particles by calcining them at 400°C for 4 h (heated from room temperature at a rate of 2°C/min).

X-ray diffraction (XRD) and TEM showed that the particles had an Ia3d cubic symmetry before and after calcination, but that the lattice parameter shrunk from 97 to 84 Å as a result of the densification of the silica matrix during calcination. Electron microscopy studies were performed on a Philips CM-20 TEM operated at 200 keV. Specimens of ~ 60 nm thick were prepared by microtomy. Figures 1a to 1c show examples of lamellar, cubic, and hexagonal surfactant-silicates made by similar methods, but with different chemical ratios.

The formation of cubic surfactant-silicates was studied with time-resolved XRD using a specialized x-ray beamline.[3,4] After the synthesis solution had been stirred, it was pipetted into an x-ray capillary, which was then sealed with epoxy and placed in a thermostatted sample chamber at 100°C. The reaction was monitored by periodic 20min x-ray exposures. Three distinct phases were observed (Fig. 2). The first phase had an XRD pattern with only one broad peak and therefore could not be identified (Fig. 2a). This phase persisted for weeks in synthesis solutions which were kept at 20°C, but was replaced by the second phase within the first 30 min at 100°C. The second phase had a 2-peak XRD pattern (Fig. 2b) which was consistent with a lamellar morphology having a 35 Å repeat distance; this is characteristic of the lamellar surfactant-silicates made with $C_{16}TMACl$. The third phase had an XRD pattern (Fig. 2c) which was consistent with Ia3d symmetry. The conversion of the phase which we suspect was lamellar to the cubic phase started after 6 h of heating and was complete after 16 h. In the future we will study this transition more closely so that we can determine the co-assembly mechanisms in detail.[5]

References

1. J. S. Beck *et al., J. Am. Chem. Soc.* **114**(1992)10834.
2. A. Monnier *et al., Science* **261**(1993)1299.
3. J. R. Milch, *J. Appl. Cryst.* **16**(1983)198.
4. S. M. Gruner, J. R. Milch, and G. T. Reynolds, *Rev. Sci. Instrum.* **53**(1982)1770.
5. This work was supported by grants from the U.S. Department of Energy (DE-FG02-87ER60522) (MDMc and SMG) and the U.S. Air Force Office of Scientific Research (AFOSR-F49620-93-1-0259) (CMC and IAA).
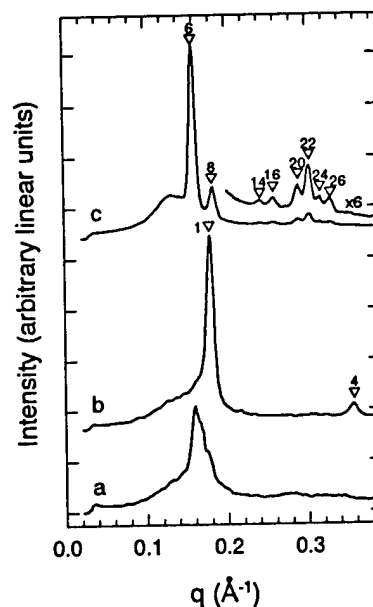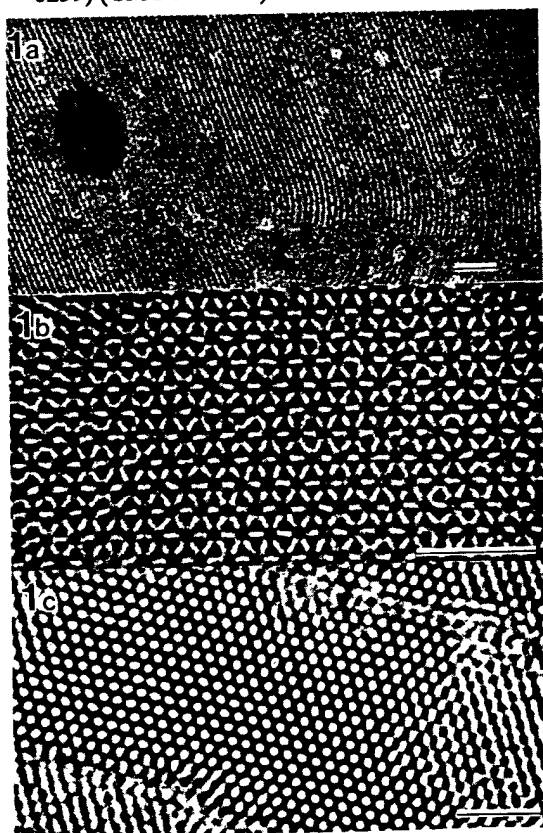
FIG. 1.—TEM images of (a) the lamellar morphology, (b) the cubic phase with Ia3d symmetry viewed along its [111] zone axis, and (c) the hexagonal phase viewed along its [001] zone axis (bars = 30 nm).

FIG. 2.—Selected XRD patterns from a time-resolved experiment. The numbers which accompany the peak labels are the square of the peak indexes. (a) A 20min exposure taken during the first 20 min of heating. (b) A 20min exposure taken after 160 min of heating. The two peaks are consistent with a lamellar structure, as shown by the peak labels. (c) The average of six 20min exposures taken after 20 h of heating. The 8 peaks are consistent with Ia3d symmetry, as shown by the peak labels. There were two faint rings at higher q which did not index with the Ia3d pattern and could not be explained.

449

Pergamon

PROCESSING OF NANOCOMPOSITE SILICON NITRIDE-MULLITE-ALUMINA BY REACTION SINTERING

Y. Sakka* and I.A. Aksay**

*Chemical Processing Division, National Research Institute for Metals
2-1, Sengen-1, Tsukuba, Ibaraki 305, Japan
**Department of Chemical Engineering and Princeton Materials Institute
Princeton University, Princeton, NJ 08544-5263

Abstract—We describe a new method for processing Si_3N_4-mullite-Al_2O_3 nanocomposites by reaction sintering of the green compacts after partial oxidation treatment. Bimodal powder compacts used in this process were prepared by a colloidal filtration method. Si_3N_4 and Al_2O_3 powders were dispersed in aqueous suspensions at pH=10 with the aid of an electrosteric stabilizer, polymethacrylic acid. A binary mixture of Al_2O_3 powder was used to attain high green densities. This process results in the following morphology: nanometer-sized Si_3N_4 particles that are distributed in the mullite phase which is embedded in an Al_2O_3 matrix.

I. INTRODUCTION

Advanced ceramic matrix composites are used in many fields, such as electronic, structural, or biomaterial applications. Recently, ceramic matrix nanocomposites have been receiving increasing attention largely due to their significantly enhanced mechanical properties, low-temperature densification, machinability, and superplastic behavior (1-3). Nanocomposites can be classified into two general categories (3). One category consists of composites of only nanometer-sized grains. The other consists of composites where nanosized particles are distributed within the intra-and/or intergrain regions of micron-sized grains. The main advantage of using nanocomposites of the first category is that they can be shaped by superplastic deformation, whereas the main advantage of the nanocomposites of the second category is their enhanced high temperature stability against grain coarsening and mechanical properties. In this paper, we deal with the processing of the second type of nanocomposite with a novel reaction sintering method.

In a recent study, we illustrated the use of reaction sintering as an economical and reliable method for the processing of SiC-mullite-Al_2O_3 nanocomposites (4,5). In this study, we extend this technique to the processing of Si_3N_4-mullite-Al_2O_3 nanocomposites. Our procedure consists of three steps shown in Figure 1 (4,5). First, we consolidate submicron-sized Si_3N_4 and Al_2O_3 powders homogeneously through colloidal consolidation. For the composite material processing of submicron size powder, colloidal dispersion and consolidation techniques have high potential

in controlling pore volume and pore size distribution of compacts and achieving a desired microstructure (6,7).

Here, the effect of using bimodal Al_2O_3 powders (8-10) on the microstructure of the green compacts is also examined. Second, partial oxidation treatment is conducted to oxidize the surface of the Si_3N_4 particles to SiO_2. This reduces the size of the Si_3N_4 particles to nanometer size. Finally, we react the surface oxide and Al_2O_3 to produce mullite. As we illustrate in the following sections, the advantages of this method are that (1) the reduction of the inclusion phase to nanoscale can be achieved without milling, (2) due to a volume increase during reaction sintering, the sintering shrinkage is low, and (3) since the oxidation product silica is in amorphous form, the viscous deformation of silica allows the densification process to occur at lower temperatures (11,12), and aids in the formation of dense sintered bodies without pressure.

II. EXPERIMENTAL PROCEDURE

Two types of α-Al_2O_3 powders were used in this study, Sumitomo Chemical's high-purity alumina ($\geq$ 99.995%): the fine powder (AKP-50, indicated as Al_2O_3(F)) with a mean particle diameter of 0.21 μm and specific surface area of 9.5 m^2/g, and the coarse powder (AKP-15, indicated as Al_2O_3(C)) with a mean particle diameter of 0.78 μm and specific surface area of 2.4 m^2/g. Bimodal powder where the ratio of Al_2O_3(C) to Al_2O_3(F) was 7/3 is designated as Al_2O_3(B). The Si_3N_4 powder used was Ube Industries' α-Si_3N_4 (SN-E10; α content above 95%) with a mean particle diameter of 0.2 μm and specific surface area of 10.0 m^2/g. The data presented here for the alumina and silicon nitride are the manufacturer's reported data except the specific surface area. The specific surface areas were measured by standard BET N_2 adsorptions.

Stable colloidal suspensions with a solids content of 45 vol% were prepared electrosterically in distilled water with an NH_4 salt of polymethacrylic acid (PMAA, Darvan C) at pH = 10 as described in the next section. NH_4OH was used to adjust the pH. After ultrasonic vibration (Sonic Materials Vibracell 600W Unit, Danbury, CT) was applied for 10 min to facilitate the dispersion of the powders agglomerates, the suspension was stirred for over 12 h at room temperature. Degassing of the suspension was performed in a bell jar connected to a vacuum pump for about 30 min. A colloidal consolidation technique (slip cast) employing a gypsum mold was used to consolidate the colloidal particles. The compacts were then dried overnight at 100°C.
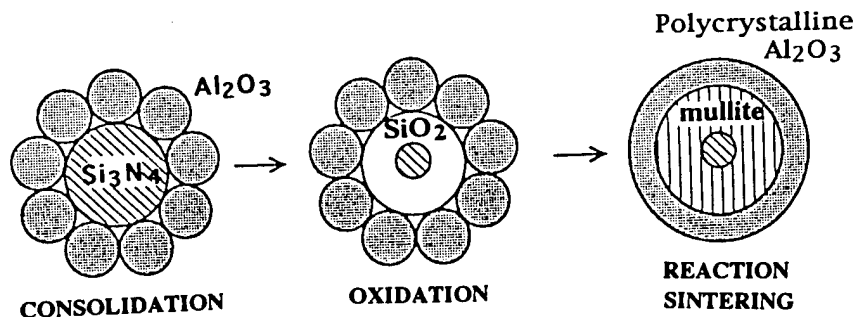

Figure 1. Schematic illustration of the process steps used to produce nanocomposites by reaction sintering.

Rheological properties of the suspensions were measured by a cone and plate viscometer (Visconic EMD type, Tokyo Keiki Co., Tokyo, Japan) at 20°C as a function of shear rate over a range of shear rates of 1.92 to 383 s^{-1}.

Thermogravimetric analysis (TGA; TGA7 Thermogravimetric analyzer, Perkin Elmer, Norwalk, CT) was conducted to determine the oxidation level of the Si_3N_4 by weight increase. The dried compacts were put in a platinum pan and heated to soaking temperatures between 1000 and 1300°C at a heating rate of 10°C/min in a stream of dry air. Reaction between the Pt and the Si_3N_4 powder was not observed.

The reaction sintering for the samples after partial oxidation treatment in air was conducted in an alumina crucible in a stream of Ar (above 99.9 % purity) using a graphite furnace at a heating rate of 25°C/min and a cooling rate of 5°C/min. The densities of the green compacts and the sintered bodies were measured by the Archimedes' method using kerosene or distilled water, respectively. Pore channel size distribution of the compacts was investigated by mercury porosimetry (9,10). The pore channel size distribution was obtained using standard values for the mercury surface energy (0.48 N/m) and the contact angle (140°). Phase analysis was conducted by X-ray diffraction (XRD; X-ray Diffractometer, Rigaku RU-300, Tokyo, Japan) using Ni-filtered CuKα radiation.

Sintered samples were polished down to 1 μm surface finish with diamond paste and then thermally etched at 1450°C for 20 min in an Ar atmosphere. The resulting microstructures were evaluated by scanning electron microscopy (SEM; Philips 515 Scanning Electron Microscope) and transmission electron microscopy (TEM; Philips 300 Transmission Electron Microscope). A coating of gold and palladium was sputtered on the surface of the samples for SEM.

III. RESULTS AND DISCUSSION

Dispersion and Consolidation

In the preparation of the colloidal suspensions, controlling the interactions between particles has a significant influence on the stability of a suspension. In our system, an electrosteric stabilization approach was preferred over an electrostatic one since it was not possible to disperse both Si_3N_4 and Al_2O_3 equally well at the same pH level. When only electrostatic dispersion was used, Si_3N_4 dispersed best under basic conditions, whereas Al_2O_3 dispersed best under acidic conditions (13-16). Consequently, an NH_4 salt of PMAA was used as an electrosteric stabilizer (0.4 g/m^2) (13,14) to improve the stability of Al_2O_3 under basic conditions so that a low viscosity composite suspension could be prepared at pH = 10. Figure 2 shows the rheological behavior of the Al_2O_3(F)-15Si_3N_4 suspensions with and without the PMAA. A significant decrease in viscosity of the 45 vol% solids suspension with PMAA is seen in comparison with 30 vol% solids suspension without PMAA. Adding PMAA decreased the viscosity significantly, which indicates the suspension dispersion is significantly improved. Figure 3 shows the rheological behavior of 45 vol% solids suspensions using the three types of Al_2O_3 powders. All the suspensions were fluid enough for slip casting and the suspension with bimodal Al_2O_3 had the lowest viscosity due to space filling of smaller particles into a matrix of larger particles. At a fixed solids content, nearly an order of magnitude decrease in viscosity can be realized simply with addition of smaller particles into a nearly monosized matrix (29).
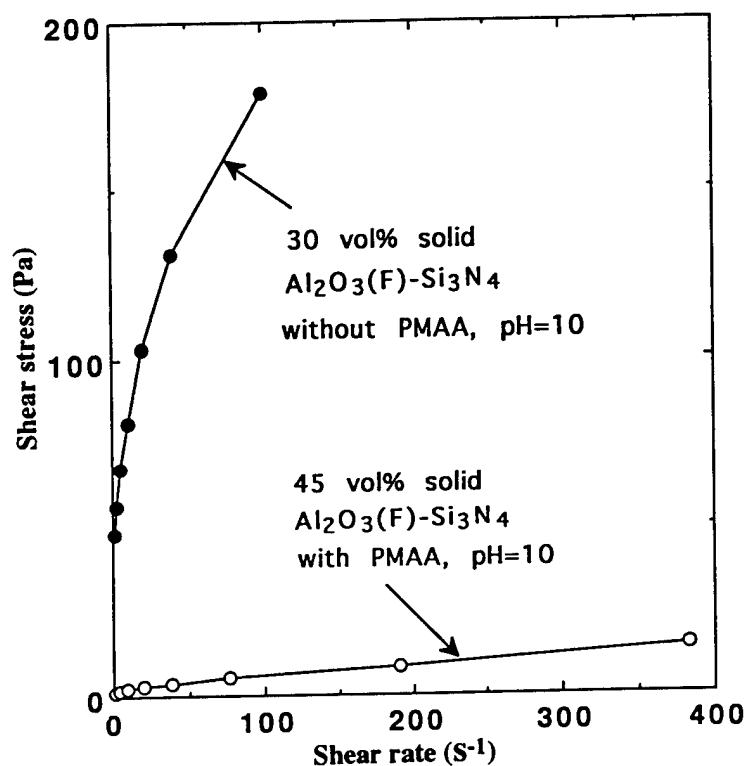
Figure 2. The shear stress-shear rate relation for the 45 vol% solids $Al_2O_3(F)$-$15Si_3N_4$ with PMAA and the 30 vol% solids $Al_2O_3(F)$-$15Si_3N_4$ without PMAA.

During colloidal consolidation of multi-component suspensions, a key problem is the segregation of particles either due to gravitational (9,10,17) or thermodynamic phase separation (18,19) effects. The best solution for minimizing particle segregation is to prepare the suspensions as highly concentrated as possible (9,10,17-19). Since significant segregation and/or phase separation did not occur while using a 45 vol% solid suspension of Al_2O_3-SiC systems (5), we also prepared 45 vol% solid suspensions in this system. Homogeneous microstructure (Figure 4) and narrow pore channel size distributions (Figure 5) were obtained with all these compacts. The relative green densities of $Al_2O_3(F)$-$15Si_3N_4$, $Al_2O_3(B)$-$15Si_3N_4$ and $Al_2O_3(C)$-$15Si_3N_4$ were 61.5, 65.7 and 65.1%, respectively. Increase of density in $Al_2O_3(B)$-$15Si_3N_4$ system is not significant in comparison with that in $Al_2O_3(C)$-$15Si_3N_4$ system. This may be due to the fact that the mixtures of $Al_2O_3(C)$ and Si_3N_4 are a binary combination of the coarse Al_2O_3 and the fine Si_3N_4 powders and thus they also display the advantages of binary mixtures.

Oxidation Process

A typical weight loss during heating $Al_2O_3(F)$-15Si3N4 at a heating rate of 10°C/min is shown in Figure 6. Upon heating to 700°C weight loss was observed in two regions; in the first
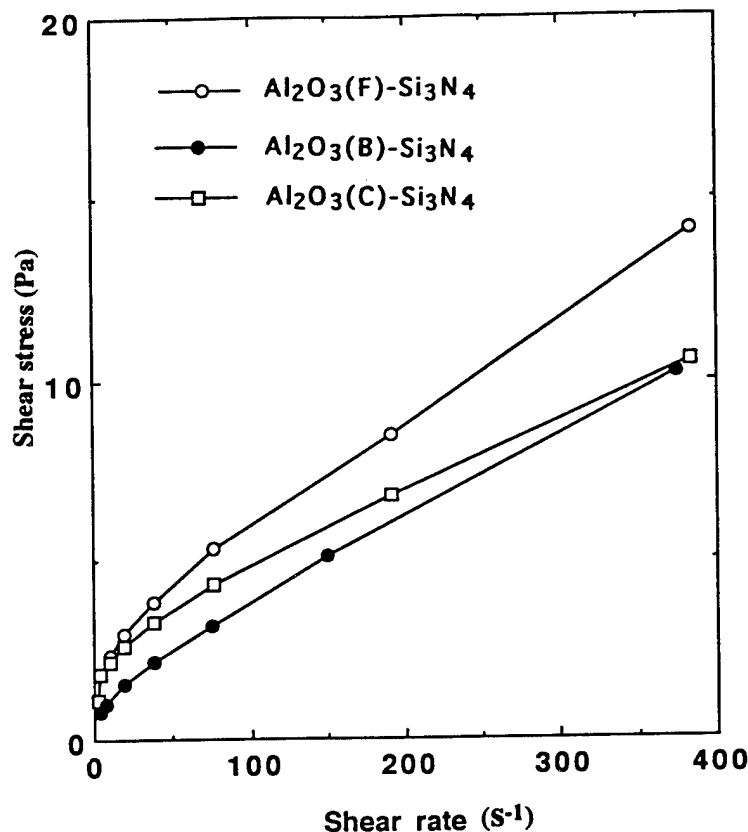
Figure 3. The shear stress-shear rate relation for the 45 vol% solids Al_2O_3-$15Si_3N_4$ systems.

region (up to 300°C) the weight decrease is due to the desorption of water and the second region (around 350°C) is mainly due to decomposition of the surfactant. Above 500°C, the weight loss reaches a maximum value, and due to the onset of Si_3N_4 oxidation, a weight gain is observed at higher temperatures. The plateau value at the maximum weight loss was used as the reference point to determine the fraction of silica that forms as the oxidation product on the surface of the Si_3N_4 particles.

The size of the Si_3N_4 core particles was controlled by determining the fraction of Si_3N_4 oxidized during heat treatment. Figure 7 shows the oxidation fraction in weight. The oxidation behavior of the Si_3N_4 powder in this temperature range is believed to follow a passive oxidation reaction (20):

$$Si_3N_4 + 3O_2 \rightarrow 3SiO_2 + 2N_2 \qquad\qquad [1]$$

Many authors have reported that oxidation of Si_3N_4 powders in various oxidizing atmospheres follows parabolic kinetics (21-24). The oxidation fraction is represented by the following Jander's equation (25).
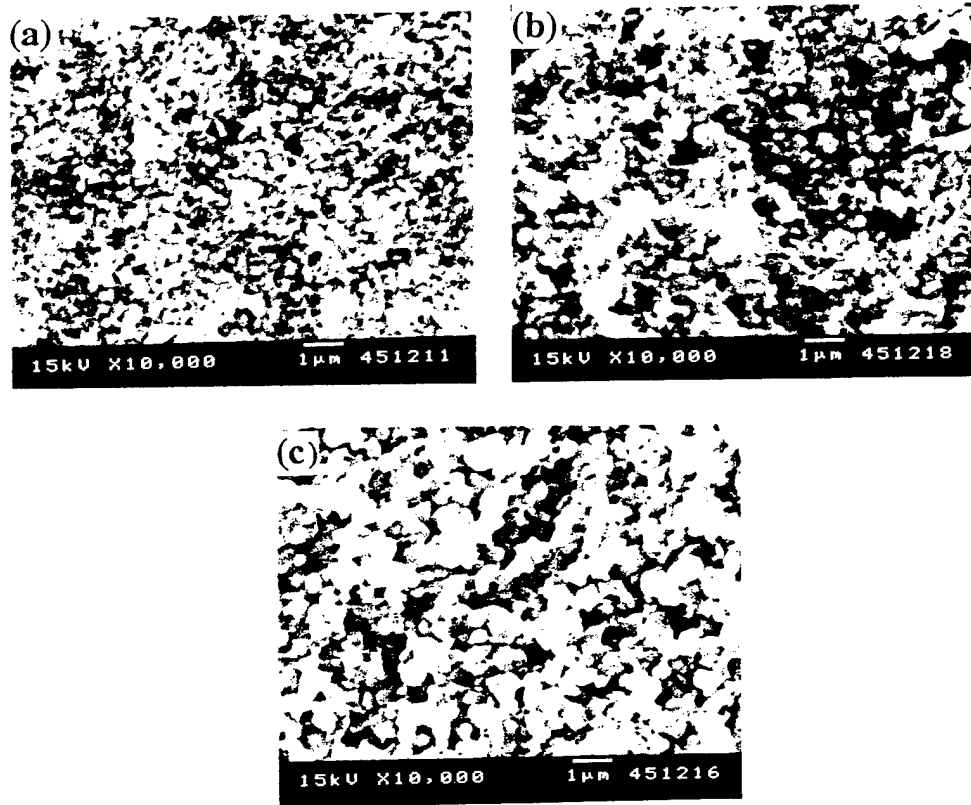
Figure 4. SEM images of the fractured surfaces of (a) $Al_2O_3(F)15Si_3N_4$, (b) $Al_2O_3(B)$-$15Si_3N_4$,and (c) $Al_2O_3(C)$-$15Si_3N_4$ after consolidation.

$$1 - (1- f)^{1/3} = (kt)^{1/2} \qquad\qquad [2]$$

where f is the oxidation fraction, t is the reaction time, and k is the rate constant. As shown in Figure 8, when the $[1 - f)^{1/3}]$ is plotted versus the square root of time, a linear variation is observed, suggesting that oxidation is rate limited by a diffusion process. Using eq. [2] we can calculate the rate constants at every temperature. An Arrhenius plot of the rate constants in the temperature range of 1000-1300°C is shown in Figure 9. The activation energy for $Al_2O_3(F)$-Si_3N_4 system is 340 kJ/mol. Activation energies reported in the literature vary from 250 to 480 kJ/mol (21-24). This large amount of scatter has been attributed to the different types of materials (powder, poly-crystal and single-crystal), with varying concentrations of impurities, which can alter the oxidation kinetics significantly. The activation energies obtained in our study are close to the activation energy of the oxygen diffusion in vitreous silica (298 kJ/mol) (26) but not to that of the molecular oxygen diffusion (113 kJ/mol)(27), or not to the formation of an intermediate phase Si_2N_2O (480 kJ/mol) (24). The present oxidation reaction seems to proceed via oxygen diffusion through the silica film.
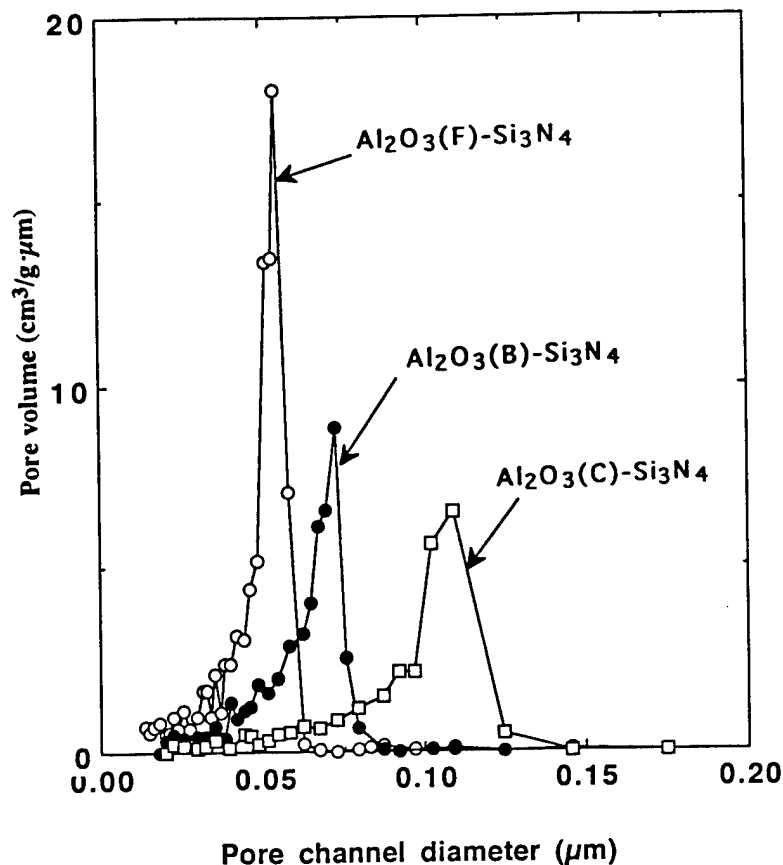
Figure 5. Hg porosimetry pore channel size distributions of the $Al_2O_3.15Si_3N_4$
compacts consolidated by the colloidal consolidation.

Figure 10 shows the X-ray diffraction patterns of Al_2O_3-$15Si_3N_4$ oxidized at 1300°C for 2
h in air. The decrease in the amount of Si_3N_4 can be seen from the figure, where amorphous SiO_2
might be produced as is the case of Al_2O_3-SiC system using fine powders (5).

Reaction Sintering and Microstructure

The comparison of the X-ray diffraction patterns in Figure 10 confirms the premise of this
study, that SiO_2 phase is formed as the oxidation product and is then consumed to form mullite
during the final stage heat treatment in Ar. Transformation of α-Si_3N_4 to β-Si_3N_4 was observed
for the samples sintered at 1700°C but not at 1600°C. The existence of Si_2N_2O phase is not
observed.

In calculating the theoretical densities of the compacts, two types of volume expansion had
to be considered (28). Volume expansion of Si_3N_4 upon oxidation is 76% and formation of
stoichiometric mullite from the reaction of $3Al_2O_3$ and $2SiO_2$ results in a volume increase of 5%
(5). The theoretical densities were determined by the following equation:
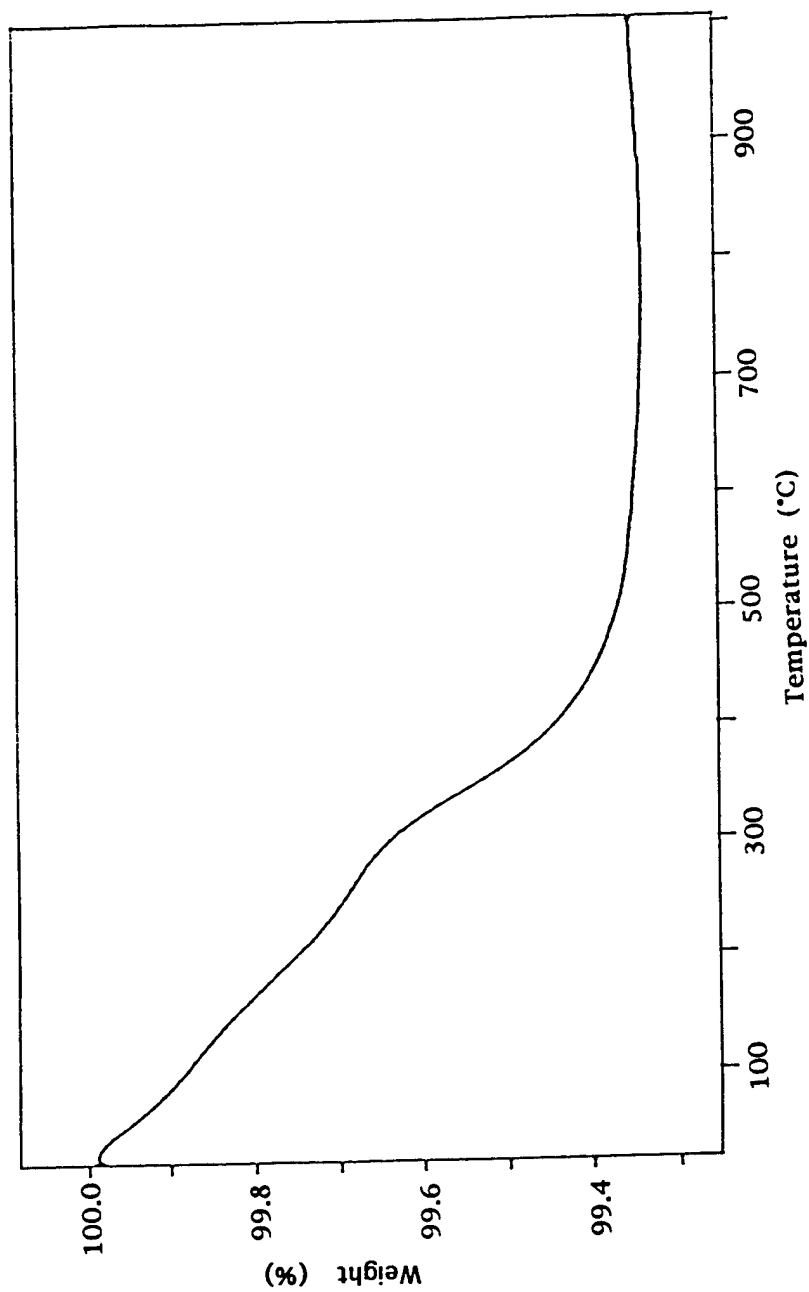
Figure 6. TGA curves of colloidal consolidated compacts of $Al_2O_3(F)$-$15Si_3N_4$ at a heating rate of $10°C$/min in a stream of dry air.
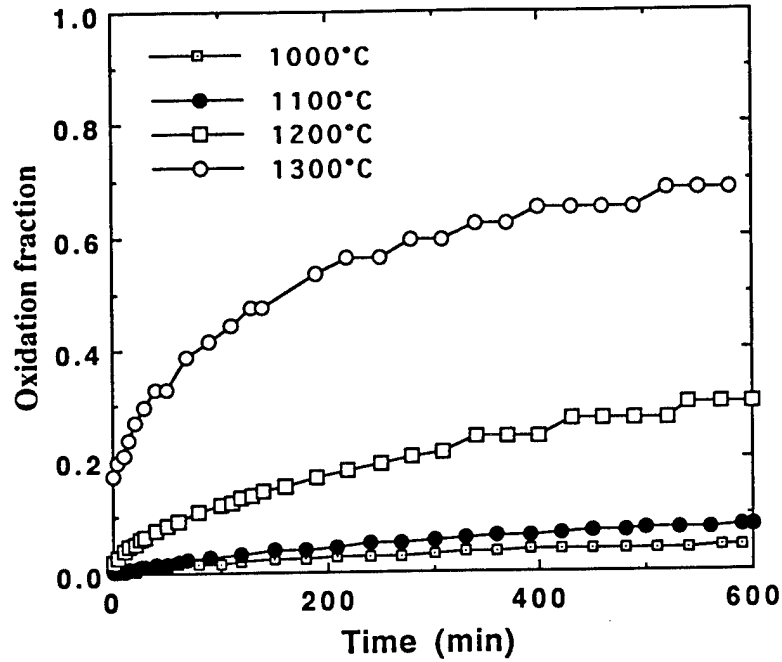
Figure 7. Oxidation fraction in weight of $Al_2O_3(F)$-15Si_3N_4 system during
isothermal holding in a stream of dry air.

$$\rho = [V_s\rho_s + (1-V_s)\rho_A]W/K \qquad [3]$$

where ρ_s and ρ_A are the theoretical densities of Si_3N_4 and Al_2O_3, respectively, V_s the volume fraction of Si_3N_4, and W is the oxidation weight increase ratio. K is a factor controlled by the composition and the respective volume expansions, as

$$K = \frac{fv_s(1.76 \times 1.05 - 1)}{[1+(1-f)V_s]} + 1 \qquad [4]$$

where f is the oxidation fraction of Si_3N_4. The linear shrinkage L is calculated by the following equation:

$$L = (K \rho_o / \rho)^{1/3} - 1 \qquad [5]$$

where ρ_o is the green density. It is easily calculated using above equation that sinter shrinkage is lower due to the two types of volume increase.

Figure 11 shows the relative sintered densities of the samples which partially oxidized at 1300°C for 2 h and reaction-sintered at 1600°C for 2 h. Higher sintered densities were obtained by sintering at 1600°C for 2h in an Ar atmosphere without pressure. As is the case in transient

Y Sakka and IA Aksay
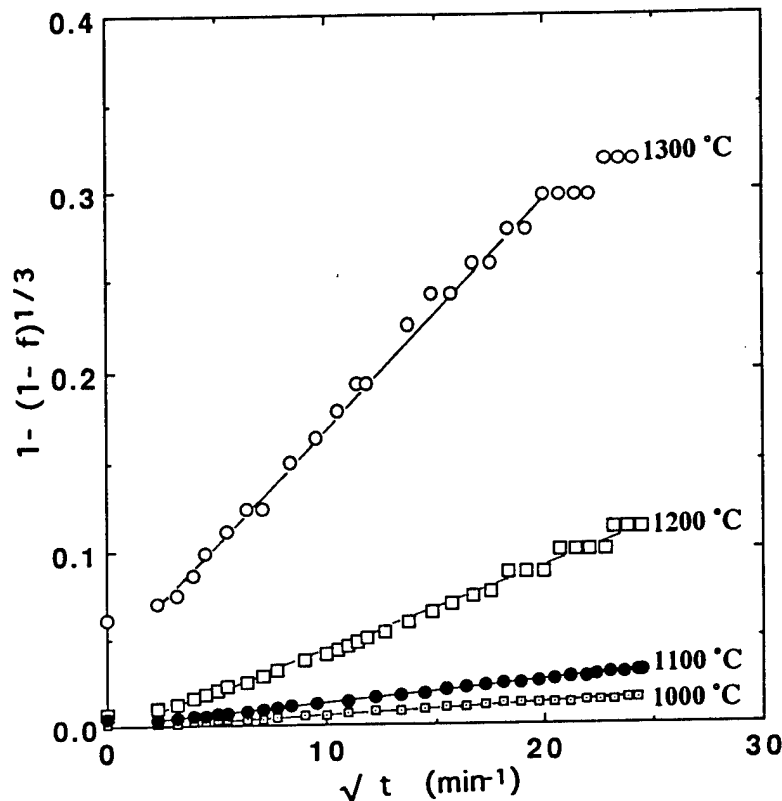
Figure 8. Relationship between square root of time and $[1-(1 - f)^{1/3}]$
for $Al_2O_3(F)-15Si_3N_4$ composites during isothermal holding in a stream of dry air.

viscous phase processing of mullite in homogeneously mixed compacts of amorphous SiO_2 and Al_2O_3 powders (11,12), viscous deformation of silica is the most likely mechanism contributing to the enhanced densification of the compacts in this study.

Figure 12 shows a SEM image of a polished and etched $Al_2O_3(F)-15Si_3N_4$-mullite sample that was oxidized at 1300°C and sintered at 1600°C for 2h. At this resolution, although small second phase inclusions are observed, it is not obvious whether these inclusions extend to the nanoscale range. Figure 13 shows a TEM image of the same samples of Figure 12. Nanometer-sized spherical Si_3N_4 particles are observed as inclusions within a mullite matrix as confirmed by energy dispersive X-ray spectroscopy (EDS). This morphology shows that the surface of the Si_3N_4 is oxidized uniformly and nanometer-sized Si_3N_4 particles remain in the mullite matrix as illustrated in Figure 1.

IV. CONCLUSIONS

Si_3N_4-mullite-Al_2O_3 nanocomposites were processed through a novel colloidal consolidation and reaction sintering process. First, micron-sized Si_3N_4 and Al_2O_3 particles were colloidally
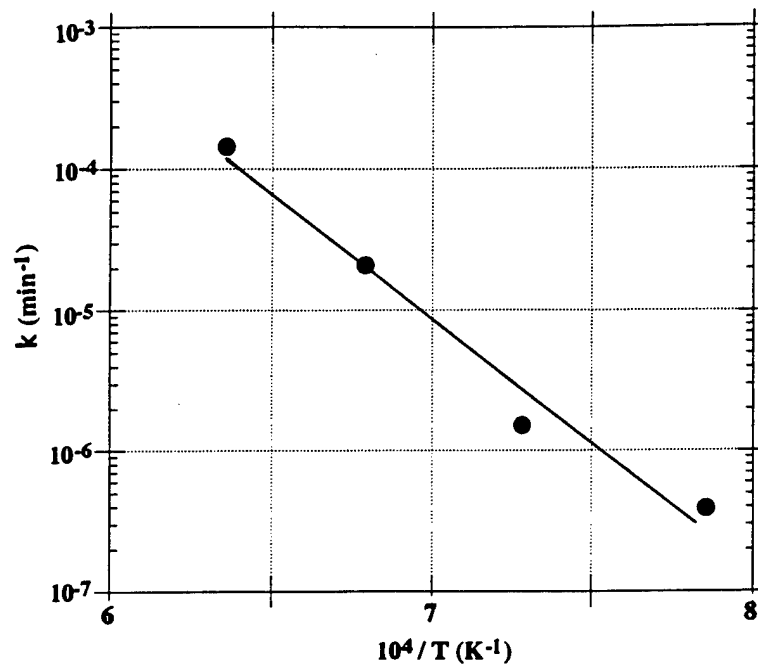
Figure 9. Arrhenius plot of the passive oxidation rate constants.
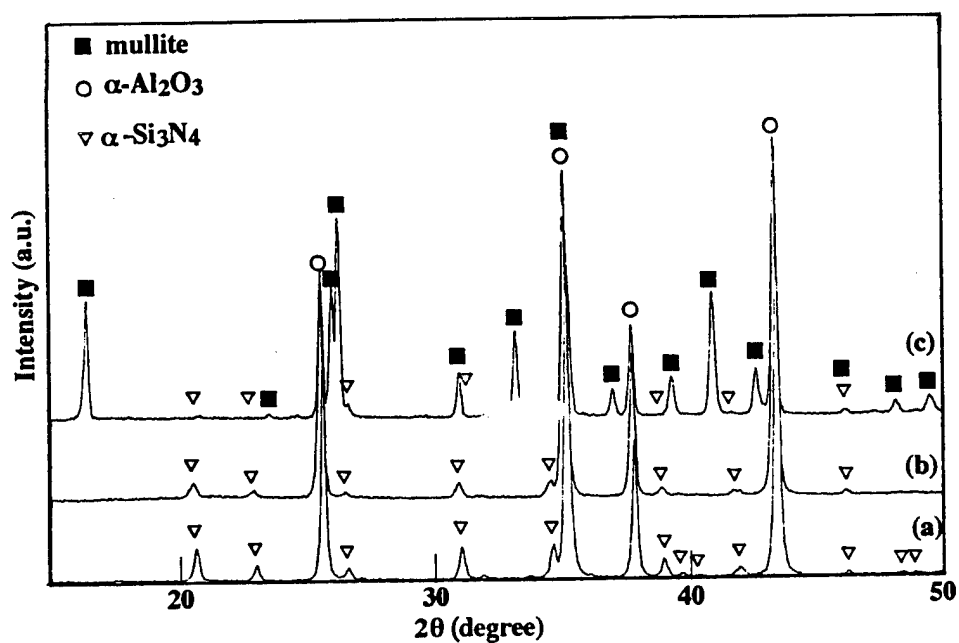
Figure 10. X-ray diffraction patterns of $Al_2O_3(F)$-$15Si_3N_4$ (a) as colloidal consolidation, (b) after oxidation, and (c) after reaction sintering at 1600°C for 2 h in Ar.
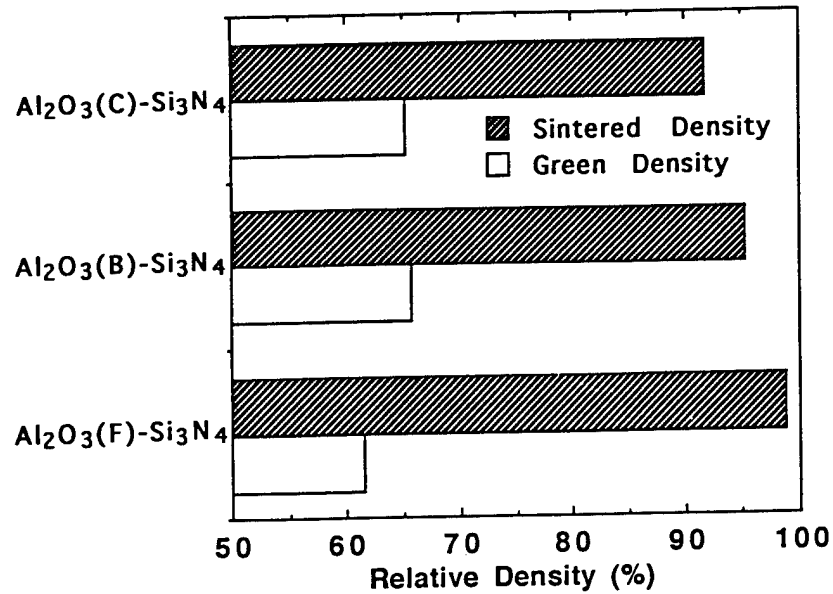
Figure 11. Density after an initial oxidation at 1300°C in air and then a final sintering at 1600°C for 2 h in Ar.
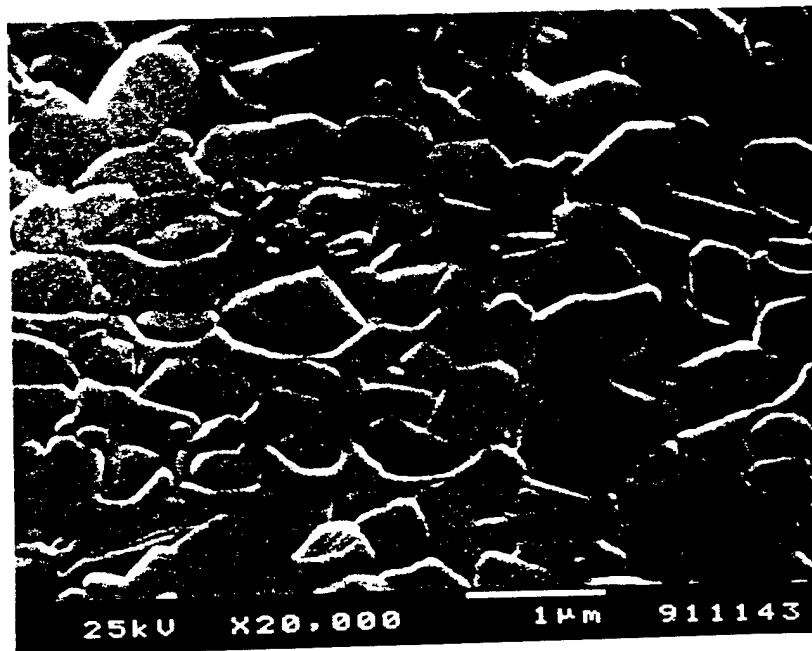
Figure 12. SEM image of polished and a thermally etched $Al_2O_3(F)$-15Si_3N_4-mullite nanocomposite first oxidized at 1300°C for 2 h and followed by a 1600°C sintering for 2 h in Ar.

100 nm

Figure 13. TEM image of $Al_2O_3(F)$-Si_3N_4-mullite nanocomposites first oxidized at 1300°C for 5 h in air and followed by final sintering treatment at 1600°C for 2h in Ar. (Spherical particles are Si_3N_4.)

dispersed and consolidated to form uniformly mixed compacts. Second, Si_3N_4 particles were partially oxidized until the Si_3N_4 particles was reduced to a nanometer-sized core. Third, these nanometer-sized core particles were trapped within a mullite matrix as the silica oxidation product reacted with the alumina to form the mullite matrix.

This process offers several advantages and thereby warrants further research: (1) it eliminates the need to reduce the particle size of the inclusion phase to the nanometer range by milling and thus provides better control in minimizing impurities; (2) due to volume increase during reaction sintering, sintering shrinkage are lower, and (3) the presence of amorphous silica as a transient phase results in enhanced densification by viscous deformation and thus provides an opportunity to process these composites without pressure.

ACKNOWLEDGEMENTS

REFERENCES

1.   R.P. Andres, R.S. Averback, W.L. Brown, W.A. Goddard III, A. Kaldor, S.G. Louie, M. Moscovits, P.S. Peercy, S.J. Riley, R.W. Siegel, F. Spaepen, and Y. Wang, J. Mater. Res. 4, 705 (1989).
2.   R.W. Siegel, R. Ramasamy, H. Hahn, L. Tiang, and R. Gronsky, J. Mater. Res. 3, 1367 (1988).
3.   K. Niihara, J. Ceram. Soc. Jpn. 99, 974 (1991).
4.   Y. Sakka, D.D. Bidinger, J. Liu, M. Sarikaya, and I.A. Aksay, in The 16th Conference of Metal Matrix, Carbon, and Ceramic Matrix Composites, J. D. Buckley, editor, NASA Conference Publ. #3175, (1992) pp. 15-26.
5.   Y. Sakka, D.D. Bidinger and I.A. Aksay, J. Am. Ceram. Soc., in press.
6.   I.A. Aksay, F.F. Lange, and B.I. Davis, J. Am. Ceram. Soc. 60, C190 (1983).
7.   F.F. Lange, J. Am. Ceram. Soc. 72, 3 (1989).
8.   J.P. Smith and G.L. Messing, J. Am. Ceram. Soc. 67, 238 (1984).
9.   C. Han, M.S. Thesis, University of California, Los Angeles, CA (1985).
10. C. Han, I.A. Aksay, and O.J. Whittemore, in Advances in Materials Characterization II, R.L. Snyder, R.A. Condrate, Sr., and P.F. Johnson, Eds. (Plenum, New York, 1985) pp. 339-47.
11. M.D. Sacks, N. Bozkurt, and G.W. Scheiffele, J. Am. Ceram. Soc. 74, 2428 (1991).
12. J.E. Webb, M.S. Thesis, University of Washington, Seattle, WA (1991) .
13. J. Cesarano III, I.A. Aksay, and A. Bleier, J. Am. Ceram. Soc. 71, 250 (1988).
14. J. Cesarano III and I.A. Aksay, J. Am. Ceram. Soc. 71, 1062 (1988).
15. E. Liden, L. Bergström, M. Persson, and R. Carlsson, J. Europ. Ceram. Soc. 7, 361 (1990).
16. Y. Hirata, S. Nakagame and Y. Ishihara, J. Mater. Res. 5, 640 (1990) .
17. Y. Hirata and I.A. Aksay, in Advances in Materials, Processing and Manufacturing, Proceedings of the Advanced Materials Technology Ceramic Workshop, Number 4 (International Committee for Advanced Materials Technology, Nagoya, Japan, 1988) pp. 3-15.
18. J. Liu, W.Y. Shih, R. Kikuchi, and I.A. Aksay, J. Colloid Interface Sci. 142, 369 (1991).
19. M. Yasrebi, W.Y. Shih, and I.A. Aksay, J. Colloid Interface Sci. 142, 357 (1991).
20. W.L. Vaughn and H.G. Maahs, J. Am. Ceram. Soc. 73, 1540 (1990).
21. R.M. Horton, J. Am. Ceram. Soc. 52, 121 (1969).
22. M. Mitomo and J.H. Sharp, Yogyo-Kyokai-Shi 84, 33 (1976).
23. T. Sato and K. Fujii, Yogyo-Kyokai-Shi 90, 110 (1982).
24. H. Du, R.E. Tressler, K.E. Spear and C.G. Pantano, J. Electrochem. Soc. 136, 1527 (1989).
25. W. Jander, Z. Anorg. Allgem. Chem. 163, 1 (1927).
26. E.W. Sucov, J. Am. Ceram. Soc. 46, 14 (1963).
27. F.J. Norton, Nature 191, 4789 (1961).
28. S. Wu and N. Claussen, J. Am. Ceram. Soc. 74, 2460 (1991).
29. I.A. Aksay, in Ceramic Powder Science II, Ceramic Transactions Volume 1, G.L. Messing, E.R. Fuller, Jr., and H. Hausner, Eds. (The American Ceramic Society, Ohio, 1988) pp.663-674.

journal

Equilibrium-State Density Profiles of Centrifuged Cakes

Wei-Heng Shih,*,† Wan Y. Shih,†,‡ Seong-Il Kim,§ and Ilhan A. Aksay*,‡

Department of Materials Engineering, Drexel University, Philadelphia, Pennsylvania 19104

Department of Chemical Engineering and Princeton Materials Institute, Princeton University,
Princeton, New Jersey 08544-5211

Ferro Corporation, Santa Barbara, California 93117-3092

We have examined the equilibrium-state density profiles of centrifuged cakes both theoretically and experimentally. The theoretical density profiles were obtained by implementing the experimental pressure–density relationship into the general differential equation for centrifugation with appropriate boundary conditions. With a power-law pressure–density relationship, $P = \beta\phi^n$, we show that

$$\frac{\phi(z)}{\phi_{max}} = \left(1 - \frac{z}{z_m}\right)^{1/(n-1)}$$

where ϕ_{max} is the density at the bottom of the cake, z the distance measured from the bottom of the cake, and z_m the distance at which the cake density vanishes. Experimentally, the density profiles were examined with γ-ray densitometry. The predicted density profiles are in good agreement with the experimental ones. We also show that the form $\frac{\phi(z)}{\phi_{max}} = \left(1 - \frac{z}{z_m}\right)^{1/(n-1)}$ applies to sedimentation cakes as well, provided the pressure–density relationship of sedimentation cakes is also a power-law one.

I. Introduction

PACKING-DENSITY variations in a powder compact often result in nonuniform shrinkages and/or cracking during subsequent drying and sintering. In case of dry-pressed compacts, the effect of consolidation conditions on density variations has been sufficiently detailed by theoretical models.[1] However, although recent trends have favored the use of colloidal consolidation methods in order to attain a higher degree of uniformity in packing densities, the effect of the forming methods on density variations in colloidally consolidated compacts is still poorly understood. A variety of colloidal processing methods are now utilized in shape forming. These methods can be grouped into two categories, depending on whether the starting suspension is in a dispersed or flocculated state.[2,3] A thorough discussion on the benefits of these two methods has been provided by Lange.[4] Since, in both methods, a central issue is the minimization of packing density variations, the goal of this paper is to provide a theoretical model for the variation of packing density in flocculated suspensions when the flocculated network is subjected to a nonuniform pressure field.

In prior studies, Schilling et al.[5] used γ-ray densitometry to study the density variation in a sedimentation cake and showed

that the sediment of a flocculated alumina suspension exhibited significant density variations within the cake, whereas the sediment of a dispersed alumina suspension showed a constant-density profile. Auzerais et al.[6] used medical X-ray computer tomography to study the settling of dispersed and flocculated silica suspensions and obtained similar results: The sediment of a dispersed silica suspension had a fairly uniform cake density, whereas those of flocculated silica suspensions showed significant density variations within the cake.[6] Shih et al.[7] examined the density variations in pressure-filtered cakes with γ-ray densitometry and showed that the density profiles of pressure-filtered cakes of flocculated alumina suspensions were uniform,[7] in contrast to their sedimentation counterparts, which showed significant density variations.[5] In order to control the density uniformity in the consolidated cakes, it is essential to know how the density variation in a cake is related to the consolidation parameters such as the pressure range, the suspension condition, the particle size, and the density range.

Previous studies on sedimentation, centrifugation, or pressure filtration focused on dynamic phenomena such as transient settling of stable and weakly flocculated suspensions in sedimentation[6] or the filtration process during centrifugal or pressure filtration.[8] The emphasis has been on the movement of the particles through a suspension[6] or the flow properties during filtration.[8] In this paper, we examine the equilibrium-state density variation of a centrifuged cake under various conditions both theoretically and experimentally. By equilibrium state we refer to the stage of the centrifugation process where the cake height no longer changes. Our goal is to provide a rigorous examination of the equilibrium-state density profiles of centrifuged cakes by relating the density variations to the experimentally obtained pressure–density relationships of the cakes. The result of the present study provides not only a practical way of estimating density variations in a cake without actual densitometry measurements but also the fundamental understanding about how local density variations occur in a centrifuged cake.

It has been shown that the pressure–density relationships exhibited by the consolidated cakes can be used to characterize the consolidation behavior of suspensions under various suspension and consolidation conditions.[7,9] For the centrifuged cake of a flocculated suspension, the mean pressure $P_{s,m}$ of the cake follows a power-law dependence on the average cake density ϕ_{ave} as[7,9] $P_{s,m} = \beta\phi_{ave}^n$ for the density range the authors have worked with, where the coefficient β and the exponent n depend on the suspension pH, the materials, the particle size, and also the initial suspension density. Generally, the exponent n in this relationship increases as the degree of flocculation decreases,[7,9] or as the density increases.[7] With the pressure–density relationships obtained in the centrifugation experiments, we develop a theory that relates the density profile of a centrifuged cake to the experimentally obtained pressure–density relationships. The approach is to implement the power-law density–pressure relationship[7,9] into the general differential equation for centrifugation with appropriate boundary conditions. We show that the equilibrium-state density profile of a centrifuged cake can be

described by a universal form as $\dfrac{\phi(z)}{\phi_{max}} = \left(1 - \dfrac{z}{z_m}\right)^{1/(n-1)}$ where

ϕ_{max} is the density at the bottom of the cake, z the distance from the bottom of the cake, z_m the distance at which the cake density vanishes, and n the exponent which appears in the pressure-density relationship.

Experimentally, we examine the density profiles with γ-ray densitometry. The predicted density profiles are in good agreement with the experimental ones. The exponent n that appears in the power-law pressure-density relationship is the most crucial variable that dictates how the local density varies in a cake. The higher the value of n, the less the local density variation in the main portion of the cake.

We organize the rest of the paper as follows. Section II contains a brief description of the experimental procedures. Section III describes the theory and the comparison with experiments. Concluding remarks are given in Section IV.

II. Experimental Procedures

The ceramic powders used in this study were α-alumina (AKP-30) powders supplied by Sumitomo Chemical Company in Osaka, Japan and boehmite powders by Vista Chemical Company in Houston, TX. The median diameter of AKP-30 was 0.4 μm. The boehmite powders were agglomerated platelike crystallites. The dry agglomerates were irregular in shape with an average size of about 65 μm as determined by optical microscopy. These agglomerates were dispersed in acidic solutions (pH 3) and partially broken up into single crystallites (50–100 Å in diameters and 10–20 Å in thickness) and largely small agglomerates (<1 μm) with application of ultrasonic energy. Powder suspensions were prepared by electrostatic stabilization. Both α-alumina and boehmite suspensions were prepared under flocculation conditions, i.e., boehmite at pH 5.5 and 7.0 and alumina at pH 7.0, respectively.

The centrifugation experiments were done on an IEC Model CL Centrifuge by DAMON/IEC Division at Needham Heights, MA. The distance from the center of rotation to the bottom of the tube was $R = 13.92$ cm. The centrifugation frequency ranged from $\omega = 48$ to $\omega = 241$, resulting in a corresponding gravitational force ranging from 32.8 to 824.3 g at the bottom of the tube, where g denotes the acceleration of gravity.

The experimental density profiles of centrifuged cakes were obtained by γ-ray transmission measurements performed with a 3.2-mm-diameter beam of collimated photons of 661 keV from cesium 137 immediately after the samples were removed from the centrifugation unit. The average density at each elevation was calculated using the Beer–Lambert law.[5]

A schematic of the centrifugation tube is shown in Figs. 1(A) and (B). Initially, the tube is filled with a suspension of density ϕ_0 and height h_0 as shown in Fig. 1(A). The suspension, after it is centrifuged for a sufficiently long time, separates into two regions; on the top is the supernatant, and at the bottom the centrifuged cake. Eventually, the system reaches an equilibrium state in which the cake height h no longer changes and the cake has an average density $\phi_{ave} = h_0\phi_0/h$. Below, we develop a theoretical model to predict the density and the pressure profiles of these cakes.

(1) Density Profiles

Let us first consider the general differential equation for centrifugation in cylindrical coordinates:[8]

$$\frac{dP_s}{dr} + (1 - k_0)\frac{P_s}{r} = \Delta\rho\phi\omega^2 r + \frac{\eta\phi_1}{2\pi\kappa r}\left(\frac{q_1}{\phi_1} - \frac{q_s}{\phi}\right) \tag{1}$$

where r denotes the distance from the center of rotation, P_s the compressive pressure on the network in the cake, ϕ_1 and $\phi = 1 - \phi_1$ the volume fraction of the fluid and that of the solid, respectively, $\Delta\rho$ the mass density difference between the solid
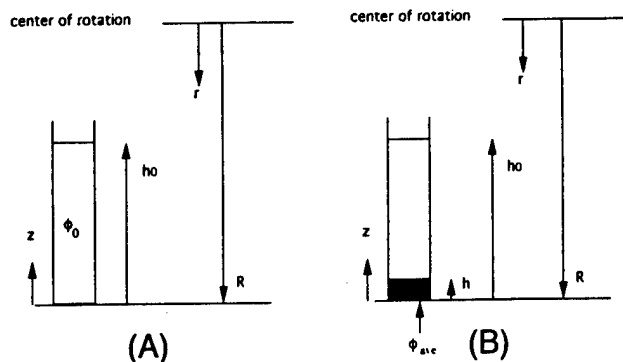
Fig. 1. Schematic of the centrifugation tube (A) with an initial suspension of density ϕ_0 and an initial suspension height h_0 and (B) at the final state, in which the suspension is separated into two regions with the supernatant on the top and the cake with an average density ϕ_{ave} and a height h that no longer changes. The density profile of a centrifuged cake in the final state is the focus of this study.

and the fluid, ω the angular centrifugation frequency, η the viscosity of the fluid, κ the permeability of the cake, q_1 the flux of the fluid, q_s the flux of the solid, and k_0 the coefficient of lateral pressure defined as the ratio of the horizontal pressure to the vertical pressure. Cakes are similar to soils. It is known in soil mechanics that the compressive pressure on the solid network is not uniform in all directions. The coefficient k_0 is an empirical way of taking into account the directional dependence of the compressive pressure acting on the particulate network. A typical value of k_0 for granular materials ranges from 0.4 to 0.7.

In the equilibrium state, the cake height no longer changes, indicating that there is neither material flow nor fluid flow, i.e., $q_s = q_1 = 0$. Therefore, the second term on the right-hand side of Eq. (1) can be neglected and Eq. (1) becomes

$$\frac{dP_s}{dr} + (1 - k_0)\frac{P_s}{r} = \Delta\rho\phi\omega^2 r \tag{2}$$

In order to proceed further, we need to know the relationship between the compressive pressure P_s and the solid volume fraction ϕ so that a differential equation between ϕ and r can be obtained. As mentioned earlier, the mean compressive pressure $P_{s,m}$ of a flocculated centrifuged cake is a power-law function of the average density ϕ_{ave},[7,9] namely

$$P_{s,m} = \beta\phi_{ave}^n \tag{3}$$

where $P_{s,m} = \frac{1}{2}(R - \frac{h}{2})\omega^2\Delta\rho h_0\phi_0$, with $R = 13.92$ cm being the distance from the bottom of the cake to the center of rotation as depicted in Figs. 1(A) and (B). The values of the coefficient β and the exponent n for alumina centrifuged cakes at pH 7.0 and for boehmite cakes at pH 7.0 and 5.5 are listed in Table I. Also listed in Table I is the initial suspension density ϕ_0. The power-law pressure-density relationships of flocculated centrifuged cakes are also evident in other suspension systems such as polystyrene and clay.[10] As shown in Table I, the values for β and n not only depend on the suspension pH, and the characteristics of the particles but are also sensitive to the initial suspension density as characteristic of the nonequilibrium nature of a flocculated system.[7,9] The value for n tends to increase as the cake density increases; the boehmite cake at pH 5.5 with $\phi_0 = 2.25$ vol% has a higher n than the one with $\phi_0 = 0.88$ vol%. Note that the cake density ranges that Eq. (3) describes are much higher than the percolation threshold densities of these systems. Therefore, the scaling behavior of pressure with respect to density in these density ranges is not due to the percolation effect near a percolation threshold. Rather, the power-law dependence of $P_{s,m}$ on ϕ_{ave} is a manifestation of the fractal nature of the flocs that pack to form the cake[11] and is indicative

Table I. Values of β, n, ϕ_0, and h_0, for Alumina at pH 7.0 and Boehmite Centrifuged Cakes at pH 7.0 and 5.5*

	β (MPa)[t]	n[t]	ϕ_0(vol%)[t]	h_0 (cm)[t]
Alumina, pH 7.0	1.73×10^2	8.9	14.82	7.88
Boehmite, pH 7.0	1.33×10^3	3.6	0.88	8.1
Boehmite, pH 7.0	1.364×10^3	4.0	2.25	7.6
Boehmite, pH 5.5	0.46	1.44	0.94	8.22

*The value of both β and n may differ as the initial suspension density changes.[13] [t]β is the coefficient in the pressure–density relationship. [t]n is the exponent in the pressure–density relationship. [t]ϕ_0 is the density of the initial suspensions. [t]h_0 is the height of the initial suspensions.

of the lack of network restructuring that occurs in pressure filtration.[7,9,12] Besides the influence from the initial suspension density, the exponent n is also closely related to the fractal dimension of the flocs that pack to form the cake. Generally, the value of n decreases as the degree of flocculation increases. Among the three suspension conditions represented here, the boehmite suspensions at pH 5.5 are the most strongly flocculated, as evidenced by their linear viscoelasticity and low gelation densities.[11] The boehmite suspensions at pH 7.0 are the second most strongly flocculated, and the alumina suspensions at pH 7.0 are the least strongly flocculated among the three. As we will show below, the density profiles of these cakes are closely related to the n value. Using Eq. (3) to approximate the relationship between P_s and ϕ, we obtain

$$\frac{dX}{dr} + \frac{n-1}{n}(1 - k_0)\frac{X}{r} = \frac{n-1}{n}\frac{\Delta\rho}{\beta}\omega^2 r \tag{4}$$

where $X = \phi^{n-1}$. The solution to Eq. (4) is $X = a_1 r^2 + a_2 r^{-b}$, and the density as a function of r is then

$$\phi(r) = [a_1 r^2 + a_2 r^{-b}]^{1/(n-1)} \tag{5}$$

where $a_1 = \dfrac{(n-1)\omega^2 (\Delta\rho/\beta)}{2n + (n-1)(1-k_0)}$, $b = \dfrac{n-1}{n}(1-k_0)$, and a_2 a constant to be determined by the boundary conditions. The values for a_1 and b for alumina and boehmite centrifuged cakes at various frequencies ω are listed in Table II. The quantity a_1 can be readily calculated using the input from the centrifugation experiment. The quantity b involves k_0, which ranges from 0.4 to 0.7. Even though the actual value of k_0 is uncertain, we find that the calculated density profiles are insensitive to the choice of k_0. The values for b listed in Table II are calculated with $k_0 = 0.5$.

If we let z denote the distance measured from the bottom of the cake as depicted in Figs. 1(A) and (B), the density as a function of z is then expressed as

$$\phi(z) = [a_1(R - z)^2 + a_2 (R - z)^{-b}]^{1/(n-1)} \tag{6}$$

Note that $r = R - z$ is an approximation. At a given elevation z, the distance of a point on the cross section of the tube to the center of rotation r depends not only on z but also on the lateral position of that point. However, it is a good approximation as long as both the diameter of the tube and the height of the cake are much smaller than R, which is true under the experimental conditions. In a centrifugation process, the supernatant will

always be present, as illustrated in Fig. 1(B). Since the solid content in the supernatant is negligible, let us assume that the supernatant has $\phi = 0$. Thus, the density of the top portion of a centrifuged cake must drop significantly to merge with that of the supernatant at some point. If we let z_m be the distance at which ϕ vanishes, the density profiles must obey the boundary conditions that

$$\phi(z_m) = 0 \tag{7}$$

and that

$$\int_0^{z_m} \phi(z)dz = \phi_0 h_0 \tag{8}$$

With the known values of a_1 and b and the boundary condition Eqs. (7) and (8), we solve for a_2 and z_m, and, thus, the entire density profile. The obtained values of a_2 and z_m for alumina centrifuged cakes at pH 7.0 and boehmite cakes at pH 5.5 and 7.0 are listed in Table II. Also listed in Table II for comparison are the visual cake heights, h. The density profiles for alumina and boehmite centrifuged cakes at different frequency settings calculated using the parameters listed in Tables I and II are shown in Figs. 2–4. Also plotted are the density profiles obtained by γ-ray densitometry at $\omega = 241$ as full circles. Within the experimental uncertainty of γ-ray densitometry measurements, the theoretical density profiles of alumina cake at pH 7.0 and those of boehmite at pH 7.0 and 5.5 with $\omega = 241$ agree well with the corresponding experimental ones. The positions of the visual cake tops, h, are also shown: open triangles represent those for $\omega = 241$, open squares for $\omega = 175$, and the open circle for $\omega = 48$. The calculated z_m may or may not coincide with the visual cake height h. For the alumina and the boehmite cakes at pH 7.0, both of which have a large n, z_m is close to h. For the boehmite cakes at pH 5.5, which have a smaller n, the difference between z_m and h becomes substantial. The reason for the large difference between z_m and h for the boehmite cake at pH 5.5 is as follows. From Fig. 4, we can see that for the boehmite cake at pH 5.5, from $z = h$ to $z = z_m$, the predicted profile shows a very low-density tail and the density range in the tail region, $h < z < z_m$, is below the sensitivity of the densitometer. It is conceivable that the tail region cannot be detected accurately. This is in agreement with the experimental observation that at pH 5.5, the boundaries between the boehmite cakes and the supernatant are diffuse and the supernatant cloudy. In contrast, the predicted profiles for the alumina cakes and the boehmite cakes at pH 7.0 do not have low-density tails. The absence of a low-density tail in the predicted profiles is again in agreement with the observation of sharp cake-supernatant boundaries for these two cases, which consequently gives rise to the close agreement of the calculated z_m with the position of the visual cake top h for these cases.

If we let ϕ_{max} be the density at the bottom of the cake, the relative density $\phi(z)/\phi_{max}$ may be expressed as a function of the relative distance z/z_m as follows. The constant a_2 is related to z_m through Eq. (7) as

$$a_2 = -a_1 (R - z_m)^{2+b} \tag{9}$$

Inserting Eq. (9) into Eq. (6), we express $\phi(z)$ and ϕ_{max} as

Table II. Values of b, a_1, z_m, h, α, and γ

	ω^*	b[t]	a_1[t]	a_2[t]	z_m (cm)[t]	h (cm)[t]	α[t]	γ[t]
Alumina, pH 7.0	48	0.444	1.41×10^{-6}	-3.84×10^{-4}	4.0	3.87	0.207	0.98
	175	0.444	1.87×10^{-5}	-6.48×10^{-3}	2.98	2.82	0.154	0.98
	241	0.444	3.53×10^{-5}	-1.32×10^{-2}	2.66	2.66	0.138	0.98
Boehmite, pH 7.0	175	0.37	1.41×10^{-6}	-2.69×10^{-4}	4.4	4.04	0.23	1.03
	241	0.37	2.66×10^{-6}	-6.20×10^{-4}	3.7	3.35	0.196	1.03
Boehmite, pH 5.5	175	0.153	189×10^{-3}	-0.156	6.15	3.91	0.254	1.25
	241	0.153	3.58×10^{-3}	-0.553	3.53	1.55	0.146	1.25

*ω is centrifugation frequency. [t]As defined in text. [t]h is visual cake height.
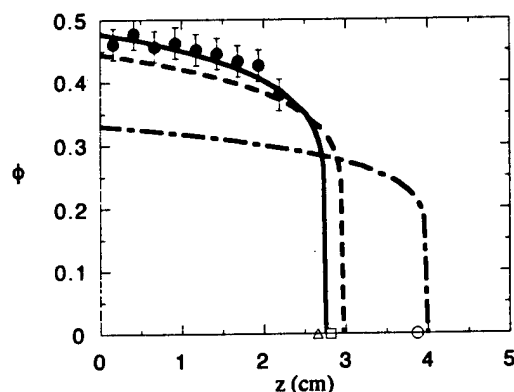
Fig. 2. Theoretical density profiles of flocculated alumina centrifuged cakes at pH 7.0. The solid line represents $\omega = 241$, the dashed line $\omega = 175$, and the broken line $\omega = 48$. Also shown are the experimental profile obtained by γ-ray densitometry at $\omega = 241$ (full circle) and the positions of the visual cake top indicated by the open triangle for $\omega = 241$, the open square for $\omega = 175$, and the open circle for $\omega = 48$. The theoretical density profile at $\omega = 241$ agrees very well with the experimental one.
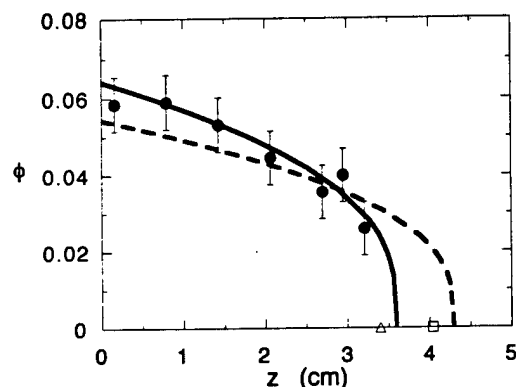

Fig. 3. Theoretical density profiles of flocculated boehmite centrifuged cakes at pH 7.0. The solid line represents $\omega = 241$, the dashed line $\omega = 175$. Also shown are the experimental profile obtained by γ-ray densitometry at $\omega = 241$ (full circles) and the positions of the visual cake top indicated by the open triangle for $\omega = 241$, the open square for $\omega = 175$. Within the experimental error bar, the theoretical density profile at $\omega = 241$ agrees very well with the experimental one.
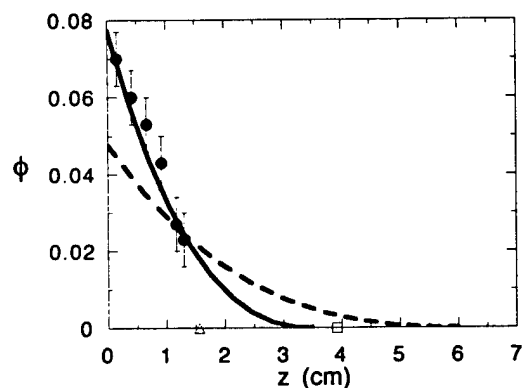

Fig. 4. Theoretical density profiles of flocculated boehmite centrifuged cakes at pH 5.5. The solid line represents $\omega = 241$, the dashed line $\omega = 175$. Also shown are the experimental profile obtained by γ-ray densitometry at $\omega = 241$ (full circles) and the positions of the visual cake top indicated by the open triangle for $\omega = 241$, the open square for $\omega = 175$. The long tail in the top portion of the cake that extends into the supernatant agrees very well with the observations of a cloudy supernatant and the diffusiveness of the cake–supernatant boundary.

$$\phi(z) = a_i[-(R - z_m)^{2+b}(R - z)^{-b} + (R - z)^2]^{1/(n-1)}$$

(10)

and

$$\phi_{max} \equiv \phi(z = 0) = a_i[-(R - z_m)^{2+b}R^{-b} + R^2]^{1/(n-1)}$$

(11)

respectively. The relative density $\dfrac{\phi(z)}{\phi_{max}}$ can then be related to $\dfrac{z}{R}$ and $\dfrac{z_m}{R}$ as

$$\left(\frac{\phi(z)}{\phi_{max}}\right)^{n-1} = \frac{\left(1 - \frac{z}{R}\right)^2 - \left(1 - \frac{z_m}{R}\right)^{2+b}\left(1 - \frac{z}{R}\right)^{-b}}{1 - \left(1 - \frac{z_m}{R}\right)^{2+b}}$$

(12)

Since both z and z_m are much smaller than R, the right-hand side of Eq. (12) can be expanded in terms of both z/R and z_m/R. To the first order in z/R and z_m/R, we arrive at a simple equation that relates the relative density $\phi(z)/\phi_{max}$ to the relative distance z/z_m as

$$\frac{\phi(z)}{\phi_{max}} \cong \left(1 - \frac{z}{z_m}\right)^{1/(n-1)}$$

(13)

The contribution of higher-order terms in z/R and z_m/R is negligible. For example, if we expand the right-hand side of Eq. (12) to the second order of z/R and z_m/R, we obtain

$$\left(\frac{\phi(z)}{\phi_{max}}\right)^{n-1} \cong 1 - (1 + \alpha)\frac{z}{z_m} + \alpha\gamma\left(\frac{z}{z_m}\right)^2$$

(14)

where $\alpha = \dfrac{(b + 1)z_m}{2R}$ and $\gamma = \dfrac{b + 3}{(b + 1)(b + 2)}$. The values of α and γ for alumina and boehmite centrifuged cakes are also listed in Table II. Here, γ is close to unity and α is much smaller than unity, the correction due to the terms $\alpha\dfrac{z}{z_m} + \alpha\gamma\left(\dfrac{z}{z_m}\right)^2$ is negligible even near z_m. Thus, practically, Eq. (13) represents a universal description for the density profiles of centrifuged cakes, provided the compressive stress is a power-law function of the cake density. The exponent n in the pressure–density relationship is the critical parameter which dictates how the relative density $\phi(z)/\phi_{max}$ changes with the relative distance z/z_m.

To compare both the calculated density profiles and the experimental ones with Eq. (13), we first replot all the density profiles in Figs. 2–4 as $\phi(z)/\phi_{max}$ versus z/z_m as in Fig. 5. There are three sets of curves in Fig. 5. Set (a) is for alumina cakes at pH 7.0. The solid line, the open triangles, and the open squares represent the calculated curves for $\omega = 241$, 175, and 48, respectively. The full diamonds represent the experimental data points. Set (b) is for the boehmite cakes at pH 7.0. The solid line and the open diamonds represent the calculated curves for $\omega = 241$ and 175, respectively. The full circles represent the experimental data points. Set (c) is for the boehmite cakes at pH 5.5. The solid line and the open circles represent $\omega = 241$ and 175. The full squares represent the experimental points. Clearly, all the curves for alumina cakes represented in Fig. 2 collapse onto one single curve, i.e., curve (a), all the curves for boehmite cakes at pH 7.0 represented in Fig. 3 collapse onto curve (b), and all the curves for boehmite cakes at pH 5.5 represented in Fig. 4 collapse onto curve (c). Figure 5 shows that for cakes that have the same exponent n, the relative density change $\phi(z)/\phi_{max}$ has a universal dependence on z/z_m.

To compare the universal $\phi(z)/\phi_{max}$ vs z/z_m as curves shown in Fig. 5 with Eq. (13), we replot the three curves of Fig. 5
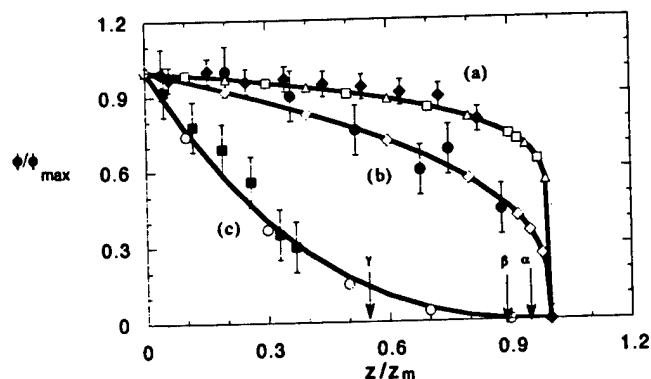
Fig. 5. $\phi(z)\phi_{max}$ vs z/z_m. Set (a) is for alumina at pH 7.0. The solid line, the open triangles, and the open squares are calculated values for $\omega = 241$, 175, and 48, respectively. The full diamonds are the experimental values at $\omega = 241$. Set (b) is for boehmite at pH 7.0. The solid line and the open diamonds are the calculated values for $\omega = 241$ and 175, respectively, and the full circles are the experimental values at $\omega = 241$. Set (c) is for boehmite at pH 5.5. The solid line and the open circles are for the calculated values at $\omega = 241$ and 175, respectively, and the full squares are the experimental values at $\omega = 241$. The arrows indicate the positions of the experimental visual cake tops at $\omega = 241$: α for alumina at pH 7.0, β for boehmite at pH 7.0, and γ for boehmite at pH 5.5

in Fig. 6(A) as solid line (a) for alumina cakes, solid line (b) for boehmite cakes at pH 7.0, and solid line (c) for boehmite cakes at pH 5.5. Also plotted are open circles representing $\left(1 - \dfrac{z}{z_m}\right)^{1/(n-1)}$ at selected values of $\dfrac{z}{z_m}$. To better see the universality of Eq. (13), we replot Fig. 6(A) as $\left(\dfrac{\phi(z)}{\phi_{max}}\right)^{n-1}$ vs $\dfrac{z}{z_m}$ in Fig. 6(B), where the open circles represent curve (a), the open squares curve (b), and the crosses curve (c) of Fig. 6(A).

For all cases, $\dfrac{\phi(z)}{\phi_{max}}$ is indeed well described by $\left(1 - \dfrac{z}{z_m}\right)^{1/(n-1)}$. Meanwhile, Fig. 6(A) shows that the relative

density drop within the main portion of the cake, e.g., $0 < z < 0.8z_m$, increases as the value of n decreases. Note that $n = 2$ is a boundary for the shapes of the density profiles. For $n > 2$, such as in the alumina cakes at pH 7.0 and boehmite cakes at pH 7.0, $1/(n-1)$ is smaller than unity, and thus the $\phi(z)/\phi_{max}$ vs z/z_m

curve is a convex one. For $n < 2$, such as in the boehmite cakes at pH 5.5, $1/(n-1)$ is greater than unity and therefore, the $\phi(z)/\phi_{max}$ vs z/z_m curve is a concave one. The result of a concave $\phi(z)/\phi_{max}$ vs z/z_m curve is that the cake–supernatant boundary tends to be diffuse and the supernatant cloudy as observed in the boehmite system at pH 5.5.

As for cakes that have the same n value but are centrifuged at different frequencies, the consequence of the universal dependence of $\phi(z)/\phi_{max}$ on z/z_m is that the density gradient will increase as the average cake density increases with the increasing centrifugation frequency, due to an increase in ϕ_{max} and a decrease in z_m with the increasing centrifugation frequency, both of which contribute to the increase in the density gradient. Indeed, this is clearly shown in Figs. 2–4.

(2) Pressure Profiles

Since the calculated density profiles are based on the use of Eq. (3) between the mean pressure $P_{s,m}$ and the average density ϕ_{ave} of the cakes rather than that between the actual local pressure and the actual local density, one may question whether Eq. (3) can represent the relationship between the local density and the local pressure. One way to check this is to compare the stress

$$P_s(z) = \Delta\rho\omega^2 \int_{z_m}^{z} (R - z_1)\,\phi(z_1)\,dz_1 \tag{15}$$

which is the compressive stress at position z due to the weight of the cake above z, with the stress

$$P(\phi(z)) = \beta(\phi(z))^n \tag{16}$$

which is the compressive stress at position z due to the local density $\phi(z)$ according to the pressure–density relationship Eq. (3). If Eq. (3) can indeed approximate the relationship between the local density and the local pressure, $P(z)$ must agree with $P(\phi(z))$. To see how well $P_s(z)$ compares with $P(\phi(z))$, we plot both $P_s(z)$ and $P(\phi(z))$ as a function of z for the alumina cakes at pH 7.0 with $\omega = 241$ in Fig. 7, those for the boehmite cakes at pH 7.0 with $\omega = 241$ in Fig. 8, and those for the boehmite cakes at pH 5.5 with $\omega = 241$ in Fig. 9. The solid lines represent $P_s(z)$ and the open circles $P(\phi(z))$ at selected values of z. $P(\phi(z))$ is computed according to Eq. (16) with the calculated density profiles $\phi(z)$ as the input. For all three cases, $P(\phi(z))$ agrees very well with $P_s(z)$, indicating that Eq. (3) can indeed approximate the relationship between the local pressure and the local density in the cake. One of the reasons that Eq. (3) can be used to represent the relationship between the actual pressure and the actual density is that the relative density profiles $\phi(z)/\phi_{max}$ have a universal dependence on the relative distance z/z_m as depicted by Eq. (13). Thus, as long as one defines ϕ_{ave} and $P_{s,m}$ systematically for all cakes as we have done, the relationship between
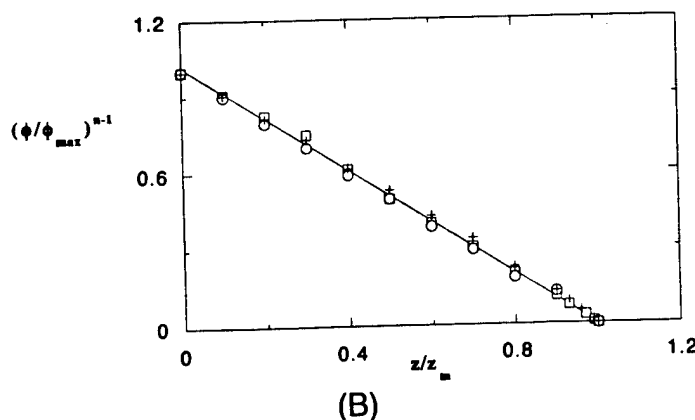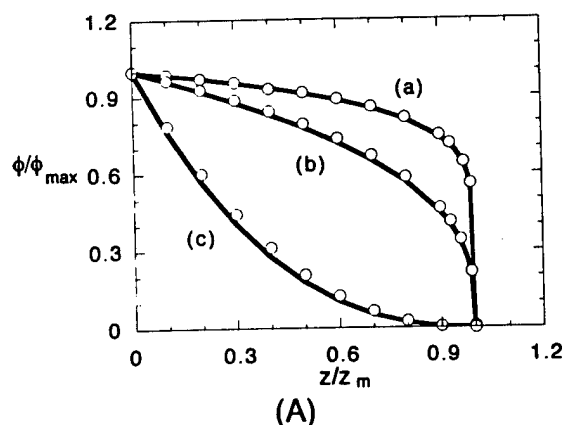

(A)

(B)

Fig. 6. (A) Comparison of $\phi(z)/\phi_{max}$ with $(1 - z/z_m)^{1/(n-1)}$. The solid lines are replotted from Fig. 5. The open circles represent $(1 - z/z_m)^{1/(n-1)}$ at selected values of z/z_m. (B) $(\phi(z)/\phi_{max})^{n-1}$ vs z/z_m. The open circles represent curve (a), the open square curve (b) and the crosses curve (c) of Fig. 6(A).

ϕ_{ave} and $P_{s,m}$ will be similar to that between the actual pressure and the actual density.

Since $P(\phi(z)) = \beta(\phi(z))^n$ can well represent the local pressure, we will then use $P(\phi(z))$ as $P(z)$ for the discussion below. Substituting Eq. (13) into Eq. (16), we obtain the relative pressure profiles as

$$\frac{P(z)}{P_{max}} = \left(1 - \frac{z}{z_m}\right)^{n/(n - 1)} \tag{17}$$

where P_{max} is the pressure at the bottom of the cake. Thus, for

Fig. 7. Pressure profile for the centrifuged cake of alumina at pH 7.0 with $\omega = 241$. The solid line represents $P_s(z)$ and the open circles $P(\phi(z))$, where $P_s(z)$ and $P(\phi(z))$ are as defined in the text.

Fig. 8. Pressure profile for the centrifuged cake of boehmite at pH 7.0 with $\omega = 241$. The solid line represents $P_s(z)$ and the open circles $P(\phi(z))$, where $P_s(z)$ and $P(\phi(z))$ are as defined in the text.
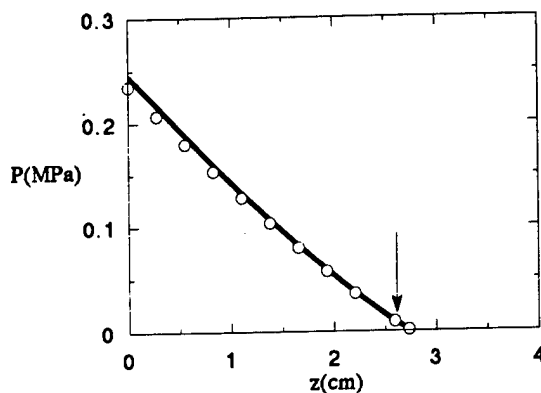

Fig. 9. Pressure profile for the centrifuged cake of alumina at pH 5.5 with $\omega = 241$. The solid line represents $P_s(z)$ and the open circles $P(\phi(z))$, where $P_s(z)$ and $P(\phi(z))$ are as defined in the text.
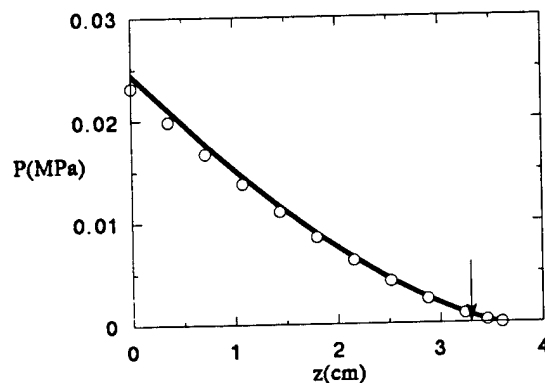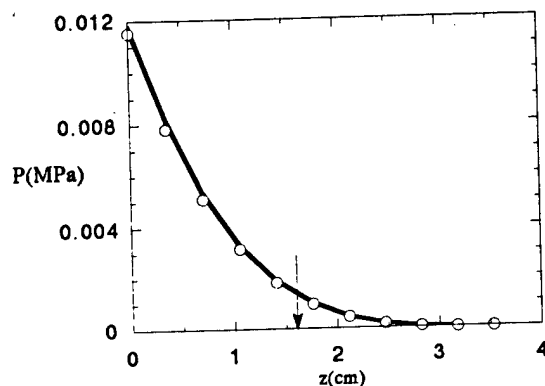
large n such as the case of less strongly flocculated suspensions, e.g., alumina at pH 7.0 where $n/(n - 1) = 1.12$ or boehmite at pH 7.0 where $n/(n - 1) = 1.33$, $P(z)$ is close to a linear function of z except in the narrow region near the top of the cake. For a small n such as in the case of boehmite at pH 5.5 where $n/(n - 1) = 3$, $P(z)$ can no longer be approximated as a linear function of z.

IV. Concluding Remarks

We have examined the equilibrium-state density profiles of flocculated centrifuged cakes both theoretically and experimentally. Experimentally the density profiles were examined with γ-ray densitometry. Theoretically, the density profiles were obtained by implementing the experimentally obtained power-law pressure–density relationships $P = \beta\phi^n$ into the general differential equations for centrifugation with appropriate boundary conditions. The exponent n in the pressure–density relationship depends on the suspension pH, the characteristics of the particles, and the initial suspension density. The value of n may increase as the cake density increases[8] or as the suspension changes from strongly flocculated, e.g., boehmite suspensions at pH 5.5 where $n = 1.44$ to less strongly flocculated, e.g., boehmite suspensions at pH 7.0 where $n = 4.0$ and alumina suspensions at pH 7.0 where $n = 8.9$.[7,9] We show that the density profiles $\phi(z)$ vs z can be described in a simple form as

$$\frac{\phi(z)}{\phi_{max}} = \left(1 - \frac{z}{z_m}\right)^{1/(n - 1)}.$$ Thus, the relative density variation

within the cake increases as n decreases. The calculated density profiles were shown to be in good agreement with the experimental ones. The relative pressure can be expressed as

$$\frac{P(z)}{P_{max}} = \left(1 - \frac{z}{z_m}\right)^{n/(n - 1)}$$

For the same suspension conditions, i.e., with the same n, ϕ_{max} increases and, therefore, z_m decreases with an increasing ω. As a result of the universal dependence of $\phi(z)/\phi_{max}$ on z/z_m, the density gradient actually increases with an increasing ω despite increase in the average cake density.

It should be noted that for the boehmite cakes both at pH 5.5 and at pH 7.0, the P_s–ϕ relationship is best described by the power law depicted in Eq. (3). However, for the alumina cakes, the exponent n in the power-law P_s–ϕ relationship is rather large, i.e., $n = 8.9$. A power-law function with a large exponent is numerically indistinguishable from an exponential one. Indeed, the density ϕ of the alumina cakes can be alternatively fitted as a logarithmic function of P_s or P_s as an exponential function of ϕ.[12] Thus, one may question the validity of using Eq. (13) to describe the density profiles for the alumina cakes, since Eq. (13) is derived using a power-law P_s–ϕ relationship. However, since P_s as an exponential function of ϕ is numerically indistinguishable from that as a power-law one with a large n, the density profiles for the alumina cakes obtained by using an exponential form for P_s would be numerically indistinguishable from those predicted by Eq. (13). The advantage of using Eq. (13) to describe the density profiles of centrifuged cakes is that it provides a simple analytic form for the density profiles through the exponent n that other forms of P_s–ϕ relationship cannot provide.

The form $\dfrac{\phi(z)}{\phi_{max}} = \left(1 - \dfrac{z}{z_m}\right)^{1/(n - 1)}$ can also be used to

describe the density profiles of a sedimentation cake, provided the pressure–density relationship of a sedimentation cake is also a power-law function $P = \beta\phi^n$ (see Appendix A). While the $\left(1 - \dfrac{z}{z_m}\right)^{1/(n - 1)}$ dependence of the relative density $\phi(z)/\phi_{max}$ is an approximation for centrifuged cakes, it is exact for sedimentation cakes.

The uniform density profiles observed in the sedimentation cakes of disperse suspensions[5,6] can also fit this

$$\frac{\phi(z)}{\phi_{max}} = \left(1 - \frac{z}{z_m}\right)^{1/(n-1)}$$ form as explained below. The cake

density of dispersed suspensions has been shown to be independent of the applied pressure.[7,9] The independence of the cake density with respect to the pressure means that n is very large if $P = \beta\phi^n$ is used to describe the pressure–density relationship.

The large n value gives negligible $\frac{1}{n-1}$ value, therefore, negligible density variations in the main portion of the cake as observed in the density-profile measurements.[5,6]

Finally, in the case of strongly flocculated cakes, especially the ones formed by nanometer-sized particles such as boehmite at pH 5.5, the viscoelasticity of such cakes will allow the cakes to spring back significantly. The springback of the cake may give rise to nonmonotonic density profiles. The density profiles after significant springback are not within the scope of the present paper. The monotonic density profiles predicted by the form

$$\frac{\phi(z)}{\phi_{max}} = \left(1 - \frac{z}{z_m}\right)^{1/(n-1)}$$ are good for cakes that are immediately

removed from the centrifugation unit as we have done in the experiment or cakes that do not have significant springback such as alumina at pH 7.0 or boehmite at pH 7.0.

APPENDIX A

The differential equation for sedimentation in the final state is written as

$$\frac{dP_s}{dz} = -\Delta\rho g \phi \qquad (A-1)$$

where z is the distance measured from the bottom of the cake. Eq. (A–1) can be rewritten as

$$\frac{dP_s}{\phi} = -\Delta\rho g \, dz \qquad (A-2)$$

If the pressure–density relationship of a sedimentation cake is also a power-law function as $P_s = \beta\phi^n$, Eq. (A–2) can be rewritten as

$$\frac{d\phi^n}{\phi} = -\frac{\Delta\rho g}{\beta} dz \qquad (A-3)$$

The solution to Eq. (A–3) is

$$\phi(z) = (-c_1 z + c_2)^{1/(n-1)} \qquad (A-4)$$

where $c_1 = \frac{n\Delta\rho g}{(n-1)\beta}$ and c_2 is a constant to be determined by

the boundary conditions, i.e., Eqs. (7) and (8). By definition,

$\phi_{max} = c_2^{1/(n-1)}$ and $z_m = \frac{c_2}{c_1}$. Eq. (A–4) can then be written as

$$\frac{\phi(z)}{\phi_{max}} = \left(1 - \frac{z}{z_m}\right)^{1/(n-1)} \qquad (A-5)$$

For sedimentation cakes, the relative density $\frac{\phi(z)}{\phi_{max}}$ also follows

the $\left(1 - \frac{z}{z_m}\right)^{1/(n-1)}$ dependence. However, note that this

$\left(1 - \frac{z}{z_m}\right)^{1/(n-1)}$ dependence is an approximation for centrifuged

cakes but is exact for sedimentation cakes.

APPENDIX B
Nomenclature Table

R	Distance from the center of rotation to the bottom of the cake
r	Position variable measured from the center of rotation
z	Position variable measured from the bottom of the cake
h_0	Initial suspension height
h	Visible cake height
ϕ_0	Initial suspension solid volume fraction
ϕ	Volume fraction of the solid
$\phi(z)$	Local solid volume fraction at position z
ϕ_{max}	Solid volume fraction at the bottom of the cake
ϕ_{ave}	Average solid volume fraction of the cake
P_s	Compressive pressure on the particulate network in the cake
$P_{s,m}$	Mean compressive pressure of the cake
P_{max}	Compressive pressure at the bottom of the cake
n	Exponent for P_s as a power-law function of ϕ
β	Coefficient for P_s as a power-law function of ϕ
ϕ_1	Volume fraction of the fluid
k_0	Ratio of the horizontal compressive pressure to the vertical compressive pressure
$\Delta\rho$	Mass density difference between the solid and the fluid
ω	Angular centrifugation frequency
η	Viscosity of the fluid
κ	Permeability of the cake
q_l	Flux of the fluid
q_s	Flux of the solid
z_m	Distance at which ϕ vanishes
$P(\phi(z))$	Local solid pressure at z calculated as a power-law function of $\phi(z)$
$P(z)$	Local solid pressure at z due to the weight of the cake above z

References

[1]R. A. Thompson, "The Mechanics of Powder Pressing: I–III," *Am. Ceram. Soc., Bull.*, **60** [2] 237–45 (1981).

[2]I. A. Aksay and R. Kikuchi, "Structure of Colloidal Solids"; p. 513 in *Science of Ceramic Chemical Processing*. Edited by L. L. Hench and D. R. Ulrich. Wiley, New York, 1986.

[3](a) W. Y. Shih, I. A. Aksay, and R. Kikuchi, "Phase Diagram of Charged Colloidal Particles," *J. Chem. Phys.*, **86** [9] 5127–32 (1987). (b) W. Y. Shih, I. A. Aksay, and R. Kikuchi, "Reversible-Growth Model: Cluster–Cluster Aggregation with Finite Binding Energies," *Phys. Rev. A: Gen. Phys.*, **36** [10] 5015–19 (1987).

[4]F. F. Lange, "Powder Processing Science and Technology for Increased Reliability," *J. Am. Ceram. Soc.*, **72** [1] 3–15 (1989).

[5]C. H. Schilling, G. L. Graff, W. D. Samuels, and I. A. Aksay, "Gamma-ray Densitometry: Nondestructive Analysis of Density Evolution during Ceramic Powder Processing"; pp. 239–51 in MRS Conference Proceedings, *Atomic and Molecular Processing of Electronic and Ceramic Materials: Preparation, Characterization, and Properties*. Edited by I. A. Aksay, G. L. McVay, T. G. Stoebe, and J. F. Wager. Materials Research Society, Pittsburgh, PA, 1988.

[6]F. M. Auzerais, R. Jackson, W. B. Russel, and W. F. Murphy, "The Transient Settling of Stable and Flocculated Dispersions," *J. Fluid Mech.*, **221**, 613–39 (1990).

[7]W.-H. Shih, S. I. Kim, W. Y. Shih, C. H. Schilling, and I. A. Aksay, "Consolidation of Colloidal Suspensions," *Mater. Res. Soc. Symp. Proc.*, **180**, 167–72 (1990).

[8]F. M. Tiller, C. S. Yeh, C. D. Tsai, and W. Chen, "Generalized Approach to Thickening, Filtration, and Centrifugation," *Filtr. Sep.*, **24**, 121 (1987).

[9]W.-H. Shih, J. Liu, W. Y. Shih, S. I. Kim, M. Sarikaya, and I. A. Aksay, "Mechanical Properties of Colloidal Gels," *Mater. Res. Soc. Symp. Proc.*, **155**, 82–92 (1989).

[10]R. Buscall, I. J. McGowen, P. D. A. Mills, R. F. Stewart, D. Sutton, L. R. White, and G. E. Yates, "The Rheology of Strongly-Flocculated Suspensions," *J. Non-Newtonian Fluid Mech.*, **24**, 183 (1987).

[11]W.-H. Shih, W. Y. Shih, S. I. Kim, J. Liu, and I. A. Aksay, "Scaling Behavior of the Elastic Properties of Colloidal Gels," *Phys. Rev. A: Gen. Phys.*, **42**, 4772–79 (1990).

[12]W. Y. Shih, W.-H. Shih, and I. A. Aksay, "Mechanical Properties of Colloidal Gels Subject to Particle Rearrangement," *Mater. Res. Symp. Proc.*, **195**, 477–84 (1990).

[13]S. I. Kim, W.-H. Shih, W. Y. Shih, and I. A. Aksay, unpublished work.   □

Size dependence of the ferroelectric transition of small BaTiO$_3$ particles: Effect of depolarization

Wan Y. Shih

Department of Chemical Engineering and Princeton Materials Institute, Princeton University, Princeton, New Jersey 08544
and Department of Materials Engineering, Drexel University, Philadelphia, Pennsylvania 19104

Wei-Heng Shih

Department of Materials Engineering, Drexel University, Philadelphia, Pennsylvania 19104

Ilhan A. Aksay

Department of Chemical Engineering and Princeton Materials Institute, Princeton University, Princeton, New Jersey 08544
(Received 18 May 1994; revised manuscript received 5 August 1994)

A theory has been developed to examine the depolarization effect on the ferroelectric transition of small BaTiO$_3$ particles. To reduce the depolarization energy, a crystal would break up into domains of different polarization. In this study, we consider cubic particles with alternating domains separated by 180° domain walls. The depolarization energy and the domain-wall energy were incorporated into the Landau-Ginzburg free-energy density. Assuming a hyperbolic tangent polarization profile across the domain wall, the domain-wall energy γ and the domain-wall half thickness ξ can be obtained by minimizing γ with respect to ξ. To account for BaTiO$_3$ not being a perfect insulator, a Schottky space charge layer beneath the particle surface that shields the interior of the crystal from the depolarization field was considered. The equilibrium polarization P and domain width D can be obtained by minimizing the total free-energy density with respect to both P and D. The results of the calculations show that the ferroelectric transition temperature of small particles can be substantially lower than that of the bulk transition temperature as a result of the depolarization effect. Consequently, at a temperature below the bulk transition temperature, the dielectric constant ϵ can peak at a certain cube size L. These results agree with the existing experimental observations. Finally, the theory can also be applied to other ferroelectric materials such as KH$_2$PO$_4$ or PbTiO$_3$.

I. INTRODUCTION

The effect of particle size on the ferroelectric phase transition and the dielectric properties of small BaTiO$_3$ particles has long been an interest of research. Experiments with submicrometer size BaTiO$_3$ and PbTiO$_3$ particles have revealed that particle size plays an important role on the paraelectric-to-ferroelectric transition and on the dielectric properties of small particles.[1-7] For example, early x-ray-diffraction (XRD) experiments on BaTiO$_3$ powders at room temperature showed a reduced c/a ratio of the tetragonal ferroelectric phase as the particle size was decreased below 1 μm.[1,2] More recent experiments on powder samples clearly showed that the paraelectric-to-ferroelectric transition temperature T_c decreases with a decreasing particle size. Ishikawa, Yoshikawa, and Okada[3] showed that the transition temperature T_c of PbTiO$_3$ particles decreases with a decreasing particle size as the particle size reaches about 500 Å by probing the softening of the transverse optical mode with Raman spectroscopy. Later, Uchino, Sadanaga, and Hirose[4] used x-ray diffractometry to show that the transition temperature T_c of BaTiO$_3$ particles also decreases with a decreasing particle size when the particle size is below 0.2 μm. Other researchers[5-7] have also reported similar observations that small BaTiO$_3$ particles are cubic at room temperature. However, the critical size below which BaTiO$_3$ particles become cubic seems to vary with the preparation methods.[6,7]

Meanwhile, the size dependence of the dielectric constant has also been observed in both PbTiO$_3$ composites[8] and in BaTiO$_3$ ceramics[9,10] and composites.[11] The dielectric constant of a composite of small PbTiO$_3$ particles in a conductive matrix (polymer with carbon) was shown to decrease with a decreasing particle size.[8] The authors suggested that the decrease in the dielectric constant with smaller PbTiO$_3$ particles is due to the lack of domain formation in the small particles.[8] The size dependence of the dielectric constant of BaTiO$_3$ ceramics is an intriguing one. It was shown that the dielectric constant exhibited a peak with respect to the grain size and the peak value of the dielectric constant was higher than the dielectric constant of a BaTiO$_3$ single crystal in either the c or a direction.[9,10] Moreover, with transmission electron microscopy (TEM), Arlt, Hennings, and de With[9] showed that the 90° domain width of the BaTiO$_3$ ceramics decreases with a decreasing grain size. When a BaTiO$_3$ crystal transforms from the cubic nonpolar phase to the tetragonal ferroelectric phase, it undergoes expansion in the c direction and contraction in the a direction. Overall, the crystal undergoes a volume expansion as it transforms to the ferroelectric phase. Therefore, a grain within a BaTiO$_3$ ceramic would experience a pressure exerted by the surrounding grains as the ceramic transforms from the nonpolar phase to the polar phase. Arlt, Hennings, and de With[9] suggested that the decrease in

the 90° domain width with a decreasing grain size is a result of minimizing the stress energy associated with the cubic-to-tetragonal phase transformation. They further attributed the increased dielectric constant with a decreasing grain size as a result of the increased volume fraction of the domain walls as the grain size becomes smaller. However, the theory of Arlt, Hennings, and de With[9] cannot explain why the dielectric constant of a ceramic sample decreased again as the grain size was further decreased; nor can they explain the decrease of T_c in the powder samples.

It is conceivable that stresses can develop in a ceramic sample since grains cannot expand freely as the ceramic transforms from the nonpolar phase to the polar phase and stresses may affect the dielectric behavior. However, unlike ceramic samples, powder samples in the polar phase should be stress free since particles can undergo a free expansion at the transition. It is unclear what causes the change in the transition temperature of powders as the particle size decreases. One possible explanation for the decrease in the transition temperature is the pressure effect. It is well known that the ferroelectric transition temperature of $BaTiO_3$ decreases with an increasing pressure.[12] Uchino, Sadanaga, and Hirose[4] suggested that the decrease of the transition temperature of small $BaTiO_3$ particles is a result of the higher pressure due to the decreased radius of curvature of the small particles. However, to produce the observed change in T_c, it would require the polar crystals to have a surface tension two orders of magnitude higher than that of a typical ceramic crystal.

A plausible explanation for $BaTiO_3$ and $PbTiO_3$ particles to have the observed decrease in T_c with a decreasing particle size is the depolarization effect. Batra, Wurfel, and Silverman[13] have shown that the ferroelectric transition of thin films can be strongly affected by the depolarization field. Depolarization has also been demonstrated to affect the transition temperature of small KH_2PO_4 (KDP) particles.[14] Experiments on KDP particles embedded in an insulating medium showed that particles smaller than 150 nm exhibited no ferroelectric transition at 123 K, in contrast to particles larger than 400 nm. By replacing the insulating medium with a conductive one, the transition of small KDP particles at 123 K was restored, demonstrating that the absence of the transition of small KDP particles in an insulating medium was due to the depolarization effect. Even though $BaTiO_3$ and $PbTiO_3$ are not perfect insulators, it is possible that the reduction of T_c in the small $BaTiO_3$ and $PbTiO_3$ particles is also due to the depolarization effect.

The reason that the depolarization effect suppresses the ferroelectric transition of small KDP particles is that it increases the energy of the polar phase. The depolarization energy can be reduced by domain formation or conduction. While the experiment on KDP particles qualitatively demonstrated the depolarization effect on the ferroelectric transition temperature of small particles, detailed knowledge about how the depolarization effect influences the ferroelectric transition of small particles is lacking. For example, how is the formation of domains within a particle affected by the size and conductivity of the particle? How does this in turn affect the transition temperature of the particle?

The purpose of this paper is to theoretically examine the depolarization effect on the paraelectric-to-ferroelectric transition of small particles. The approach is to include the terms associated with depolarization in the Ginzburg-Landau free-energy density[2,14,15] of a particle. The calculations will be carried out for $BaTiO_3$, since the coefficients of the Ginzburg-Landau free energy for $BaTiO_3$ are well known.[2,14,15] To reduce the electrostatic energy due to the depolarization field, the crystal would break up into domains of different polarizations. Therefore, the energy associated with depolarization should include (1) the energy due to the depolarization field and (2) the energy of the domain walls. For simplicity, we only consider cubic particles with planar domains separated by 180° domain walls in this paper. It should be noted that for $BaTiO_3$ both 90° and 180° domain walls can occur in the tetragonal phase; the shape of the particles is not exactly cubic, and the domains may not be planar. Nonetheless, the present approach is an attempt to qualitatively give an estimate of the depolarization effect on the ferroelectric transition of small particles. Considerations of other particle geometries (e.g., spheres) or other types of domain walls would only modify the quantitative results slightly.

For a given cubic particle size at a given temperature, the equilibrium polarization and the equilibrium domain width can be obtained by minimizing the total free-energy density with respect to both the polarization and domain width. Since the theory involves the energy of the 180° domain walls, to be self-consistent, we also calculate the domain-wall energy within Ginzburg-Landau theory. For a given polarization, assuming a hyperbolic tangent polarization profile with the domain-wall thickness as a variable, the domain-wall energy can be obtained by minimizing the domain-wall energy with respect to the domain-wall thickness. To take into account the fact that particles are not perfect insulators, a Schottky-type space-charge layer near the surface[14-17] that shields the interior of the particles from the depolarization field is also considered. The results of the calculations are compared to the existing experiments. It should be noted that the depolarization effect has no counterpart in ferromagnetic crystals, as the magnetostatic self-energy is about 10^3 times smaller than the transition energy and thus cannot suppress the spontaneous magnetization.[14]

The rest of the paper is organized as follows. Section II contains the theory. The results of the calculations and a discussion are given in Sec. III. Concluding remarks are given in Sec. IV.

II. THEORY

For a crystal that undergoes a paraelectric-ferroelectric transition, the total free-energy density (free energy per unit volume) F may be separated into two parts:

$$F = F(P) + F_0 , \qquad (1)$$

where P denotes the polarization, $F(P)$ the part of the free-energy density that arises from a nonzero polarization, and F_0 the part of the free-energy density that is not related to the polarization. According to the theory of Ginzburg and Landau,[2,14,15] $F(P)$ can be expanded in terms of P. Many ferroelectric materials such as perovskite ferroelectrics undergo a first-order transition as temperature is lowered below the transition temperature T_c. Therefore, it is necessary to expand the polar part of the free-energy density $F(P)$ at least to the sixth order in P as[2,14,15]

$$F(P) = \frac{\alpha}{2}P^2 + \frac{\beta}{4}P^4 + \frac{\sigma}{6}P^6 , \tag{2}$$

where the coefficient $\alpha = a(T - T_{0\infty})$, with a being the inverse of the Curie constant and $T_{0\infty}$ the Curie-Weiss temperature, and the coefficients β and σ for the fourth- and sixth-order terms are more or less constant. The equilibrium P is determined by minimizing Eq. (2) with respect to P. For BaTiO$_3$ crystals, the numerical values for the coefficients α, β, and σ are well known. However, Eq. (2) only describes the polar part of the bulk free-energy density of large single-domain crystals and it does not include the energy contribution associated with depolarization. It is the purpose of this paper to incorporate the depolarization contribution into Eq. (2).

A. Depolarization energy

For simplicity, let us consider a cubic crystal. If the crystal is a perfect insulator and has only one single domain with polarization P, the polarization would lead to surface charges on the top and bottom surfaces as illustrated in Fig. 1(a), resulting in a depolarization field $E_1 = -4\pi P$ whose direction is opposite to that of P. Therefore, the depolarization energy per unit volume is

$$E_d = - \int_0^P E_1 dP' = 2\pi P^2 , \tag{3}$$

and for a single-domain crystal, the total polar part of the free-energy density should then be

$$F_{\text{tot}}(P) = F(P) + 2\pi P^2 . \tag{4}$$

The depolarization energy E_d is negligible when P is small. However, ferroelectrics generally have high polarization. The polarization of perovskite ferroelectric crys-

tals is on the order of 10^5 esu/cm^2. To reduce the depolarization energy in the ferroelectric state, the crystals tend to break up into domains of different polarization. It was shown that when a cube of side L breaks up into domains of alternating slices of up polarization and down polarization with a domain width D as illustrated in Fig. 1(b), the depolarization energy per unit volume is reduced to[18]

$$E_d = 1.7P^2 \frac{D}{L} . \tag{5}$$

By breaking up into domains, the depolarization energy of a crystal is reduced by a factor of D/L in addition to a constant numerical factor. Meanwhile, the breakup creates domain walls. Let γ denote the domain-wall energy. Including the domain-wall contribution, the total depolarization-energy density of a multiple-domain cube is then

$$E_d = 1.7P^2 \frac{D}{L} + \gamma \left[\frac{L}{D} - 1 \right] \frac{1}{L} . \tag{6}$$

Equations (5) and (6) are valid if the domain-wall thickness is negligible compared to the domain width D.[18]

B. Space-charge layer

Note that Eqs. (3)–(6) are good for perfect insulators. If the crystal is not a perfect insulator, a space-charge layer at the surface can affect the ferroelectric properties of the crystal. The existence of a space-charge layer near the surface of BaTiO$_3$ has been studied by many investigators using various techniques. These experiments can be found in many reviews.[14-17] Space-charge layers can be due to surface ionic vacancies as suggested by Känzig[2,19] or to Schottky exhaustion barriers[20] as suggested by Triebwasser.[21] In this paper, we will consider the Schottky space-charge layer that effectively shields the interior of the crystal from the depolarization field. The width of the Schottky barrier depends on the charge-carrier concentration. Generally, it was estimated that for BaTiO$_3$ the thickness of the space-charge layer ranges from 10^2 to 10^4 Å, depending on the mobile charge-carrier concentration.[14-17] In general, the charge distribution within the layer is nonuniform.[13,22] In the present paper, for simplicity, we will assume a Schottky type of space-charge layer. The charge density within the layer is uniform as illustrated in Fig. 2. Let t denote the thickness of the space-charge layer, and let us first consider a single-domain crystal for the convenience of dis-
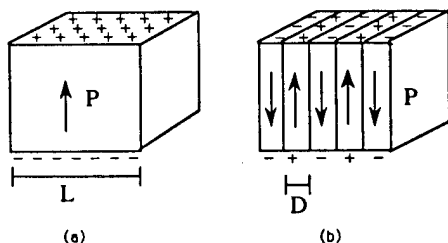

FIG. 1. (a) A cubic crystal of size L with one single domain of polarization P. (b) A crystal of size L with domains of alternating polarization separated by 180° domain walls. The domain width is D.
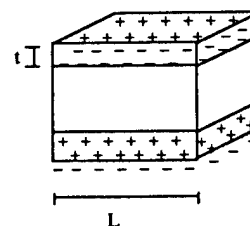

FIG. 2. Space-charge layers of thickness t with uniform charge distribution.

cussion. Assuming that the surface-charge density due to the polarization is totally balanced by the opposite charges within the layer, the charge density ρ in the space-charge layer would then be

$$\rho = \frac{-P}{t} \; . \qquad (7)$$

The electric field E in the layer is then

$$E = \frac{-4\pi P}{t}(t-z) \quad \text{for } 0 < z < t \; , \qquad (8)$$

and $E = 0$ outside of the layer. Therefore, for a single-domain crystal, the depolarization-energy density is modified as

$$E_d = -2 \int_0^P \int_0^t \frac{-4\pi P'}{t}(t-z)dz\,dP'/L = 2\pi P^2 \frac{t}{L} \; , \qquad (9)$$

where the factor 2 takes into account that there are two space-charge layers, one at the top and the other at the bottom. The consideration of a Schottky space-charge layer of thickness t modifies the depolarization-energy density by a factor t/L. Applying the same analysis for multiple-domain crystals, the total depolarization energy depicted in Eq. (6) becomes

$$E_d = 1.7P^2 \frac{D}{L} \frac{t}{L} + \gamma \left[\frac{L}{D} - 1 \right] \frac{1}{L} \; . \qquad (10)$$

C. 180° domain walls

There have been quite a number of theoretical calculations for both 90° and 180° domain-wall energies of BaTiO$_3$.[23-28] In the present paper, we are only concerned with the 180° domain walls. To be consistent with the Ginzburg-Landau theory we used for this study, we will calculate the energies of the 180° domain walls within Ginzburg-Landau theory. If the polarization is nonuniform, the polar part of the free-energy density at position $\mathbf{r}$ becomes a functional of $\mathbf{P}(\mathbf{r})$ as

$$F(\mathbf{P}(\mathbf{r})) = \frac{\alpha}{2}\mathbf{P}(\mathbf{r})^2 + \frac{\beta}{4}\mathbf{P}(\mathbf{r})^4 + \frac{\sigma}{6}\mathbf{P}(\mathbf{r})^6 + c|\nabla\mathbf{P}(\mathbf{r})|^2 \; . \qquad (11)$$

If a domain wall is located at $x = 0$, assuming that $\mathbf{P}$ is a function of x only and is independent of y and z, one can define the domain-wall energy γ as

$$\gamma = \int_{-\infty}^{\infty} \Delta F(\mathbf{P}(x))dx \; , \qquad (12)$$

where $\Delta F(\mathbf{P}(x)) = F(\mathbf{P}(x)) - F(P)$, where P and $F(P)$ denote the bulk polarization and the bulk free-energy density, respectively. The equilibrium polarization profile $\mathbf{P}(x)$ across the wall can be obtained by requiring

$$\int_{-\infty}^{\infty} \frac{\partial \Delta F(\mathbf{P}(x))}{\partial \mathbf{P}(x)} dx = 0 \; . \qquad (13)$$

We will assume that the polarization profile $\mathbf{P}(x)$ is a hyperbolic tangent function of x, i.e.,

$$\mathbf{P}(x) = P\tanh(x/\xi) \; , \qquad (14)$$

where P denotes the bulk polarization and ξ the half width of the wall. A schematic of a 180° domain wall is shown in Fig. 3. With Eq. (14), the domain-wall energy minimization requirement shown in Eq. (13) becomes

$$\frac{\partial \gamma}{\partial \xi} = 0 \; . \qquad (15)$$

Therefore, given a bulk polarization P, the equilibrium domain-wall polarization profile $\mathbf{P}(x)$ and the domain-wall energy can be obtained by minimizing γ with respect to ξ. Note that the hyperbolic tangent domain-wall polarization profile of Eq. (14) is a reasonable approximation considering that (i) the equilibrium domain-wall polarization profile is hyperbolic tangent if the free-energy density is a fourth-order function of the polarization, i.e.,

$$F(\mathbf{P}(x)) = \frac{\alpha}{2}\mathbf{P}(x)^2 + \frac{\beta}{4}\mathbf{P}(x)^4 + c|\nabla\mathbf{P}(x)|^2 \; ,$$

and (ii) experimental domain-wall profiles obtained by electron holograms[29] agreed fairly well with a hyperbolic tangent one. With $\mathbf{P}(x) = P\tanh(x/\xi)$, the domain-wall energy γ between two semi-infinite domains can be written as

$$\gamma = -\alpha\xi P^2 - \frac{2}{3}\xi\beta P^4 - \frac{23}{45}\xi\sigma P^6 + \frac{4}{3}\frac{c}{\xi}P^2 \; . \qquad (16)$$

The half thickness of a wall between two semi-infinite domains can be obtained analytically by minimizing γ with respect to ξ:

$$\xi = [\tfrac{4}{3}c(-\alpha - \tfrac{2}{3}\beta P^2 - \tfrac{23}{45}\sigma P^4)^{-1}]^{1/2} \; . \qquad (17)$$

Once the domain-wall half thickness is known, the domain-wall energy may simply be rewritten as

$$\gamma = \frac{8}{3}\frac{c}{\xi}P^2 \; . \qquad (18)$$

For multiple-domain crystals with a domain width D and the polarization at the center of a domain P, the domain-wall energy becomes

$$\gamma = \int_{-D/2}^{D/2} [F(\mathbf{P}(x)) - F(P)]dx \qquad (19)$$
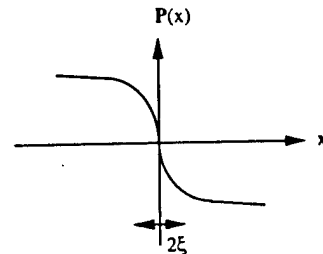
and can be written analytically as

FIG. 3. Schematic of a hyperbolic tangent polarization profile across a 180° domain wall. The domain-wall thickness is 2ξ, where ξ is as defined in the text.

$$\gamma = -a_1\xi(\alpha P^2) - a_2\xi\left[\frac{1}{2}\beta P^4\right] - a_3\xi\left[\frac{1}{3}\sigma P^6\right]$$

$$+ a_4\left[2\frac{c}{\xi}P^2\right], \tag{20}$$

where

$$a_1 = \tanh^{-1}(D/2\xi),$$

$$a_2 = \tanh^{-3}(D/2\xi)[1 + \tfrac{1}{3}\tanh^2(D/2\xi)],$$

$$a_3 = \tanh^{-5}(D/2\xi)[1 + \tfrac{1}{3}\tanh^2(D/2\xi) \tag{21}$$

$$\qquad + \tfrac{1}{5}\tanh^4(D/2\xi)],$$

$$a_4 = \tanh^{-1}(D/2\xi)[1 - \tfrac{1}{3}\tanh^2(D/2\xi)].$$

In the limit $D \gg 2\xi$,

$$a_1 = 1 + 2e^{-D/4\xi},$$

$$a_2 = \tfrac{4}{3} + \tfrac{20}{3}e^{-D/4\xi},$$

$$a_3 = \tfrac{23}{15} + \tfrac{186}{15}e^{-D/4\xi}, \tag{22}$$

$$a_4 = \tfrac{2}{3} + \tfrac{4}{3}e^{-D/4\xi}.$$

Therefore, for a finite domain width D, the domain-wall energy not only depends on the domain-wall half thickness ξ, but also the domain width D. However, as we will show below, it turns out that ξ is much smaller than D. Therefore, the modification of γ and ξ due to a finite D is rather limited as can be seen from Eqs. (20)–(22).

D. Free-energy density of a multiple-domain crystal

Combining Eqs. (2) and (10), the polar part of the free-energy density of a multiple-domain crystal of size L can be written as

$$F(P,D,L) = \frac{\alpha}{2}P^2 + \frac{\beta}{4}P^4 + \frac{\sigma}{6}P^6$$

$$+ 1.7P^2\frac{D}{L}\frac{t}{L} + \gamma\left[\frac{L}{D} - 1\right]\frac{1}{L}, \tag{23}$$

with γ being depicted in Eqs. (20)–(22). Thus, for a given crystal size L, the equilibrium polarization P and the domain width D can be determined by minimizing the free-energy density $F(P,D,L)$ with respect to P and D, i.e.,

$$\frac{\partial F(P,D,L)}{\partial P} = 0 \tag{24}$$

and

$$\frac{\partial F(P,D,L)}{\partial D} = 0. \tag{25}$$

Once the equilibrium polarization P is obtained, the dielectric constant can be obtained by

$$\epsilon = 4\pi\chi + 1, \tag{26}$$

where χ is the dielectric susceptibility defined as

$$\chi^{-1} = \frac{\partial^2 F(P,D,L)}{\partial P^2}. \tag{27}$$

The minimization of F with respect to D, i.e., Eq. (25), gives

$$D = \left[\frac{\gamma}{1.7P^2}\right]^{1/2} L^{1/2}\left[\frac{L}{t}\right]^{1/2}. \tag{28}$$

From Eq. (28), one can see that for a given polarization the domain width D is roughly proportional to the particle size L. Note that if there is no consideration for the space-charge layer, D would be proportional to $L^{1/2}$. The consideration of a Schottky-type space-charge layer that totally balances the surface charge changes the dependence of D from $L^{1/2}$ to L. If we consider a more realistic charge distribution, D may not be exactly linear in L. However, it is fair to say that if we assume $D \sim L^\nu$, the exponent ν must be larger than $\frac{1}{2}$. In the TEM experiment of Arlt, Hennings, and de With,[9] the domain width as a function of the grain size in a double-logarithmic plot indeed appeared to have a slope larger than $\frac{1}{2}$.

Finally, the effect of the depolarization energy and the domain-wall energy on the transition temperature of small cubic crystals of size L can be qualitatively understood as follows. With the depolarization energy $1.7P^2(D/L)(t/L)$ and the domain-wall energy $\gamma(L/D-1)/L$, the coefficient of the P^2 term in the free-energy density is no longer $\alpha = a(T - T_{0\infty})$ but α'. For simplicity, let us assume $\xi \ll D$, so that $\tanh(D/2\xi) \approx 1$, which is indeed the case as we will show in the following section. Using Eq. (16) for γ, one finds

$$\alpha' = \alpha + 3.4\frac{Dt}{L^2} + \left[-\frac{2\xi}{D}\alpha + \frac{8}{3}\frac{c}{\xi}\right]. \tag{29}$$

Rewriting $\alpha' = a'(T - T_0)$, one obtains

$$a' = a\left[1 - \frac{2\xi}{D}\right] \tag{30}$$

and

$$T_0 = T_{0\infty} - \frac{1}{a'}\left[1.7\frac{Dt}{L^2} + \frac{8}{3}\frac{c}{\xi}\right]. \tag{31}$$

Equation (31) shows that as the crystal size L is reduced, the Curie-Weiss temperature and hence the transition temperature T_c are lowered.

III. RESULTS AND DISCUSSION

The coefficients α, β, and σ in the Landau-Ginzburg free energy can be obtained from the literature. The coefficient α for the P^2 term is related to the Curie constant and the Curie-Weiss temperature as $\alpha = a(T - T_{0\infty})$, where $T_{0\infty}$ is the bulk Curie-Weiss temperature and a the inverse of the bulk Curie constant. For $BaTiO_3$, above and near the bulk transition temperature $T_{c\infty}$, the coefficient β of the P^4 term has a mild tem-

WAN Y. SHIH, WEI-HENG SHIH, AND ILHAN A. AKSAY

TABLE I. Coefficients of the Landau-Ginzburg free energy of BaTiO$_3$.

$T_{c\infty}$	122 °C
$T_{0\infty}$	112 °C
a	7.4×10^{-5}
β	1.13×10^{-12}
σ	3.34×10^{-22}
c	0.3×10^{-16}

FIG. 4. P vs T for various L (in μm) with $t = 500$ Å. Note that the drop of P at T_c is roughly the same for all L.

perature dependence and can be written as $\beta = 18 \times 10^{-15}(T_{0\infty} - T_2)$ with $T_2 = 175$ °C. However, it is not clear what value β should be at lower temperatures. In this paper, we use $\beta = 18 \times 10^{-15}$ $(T_{0\infty} - T_2)$ for all temperatures. This β value gives very good quantitative agreement between the calculated polarization-temperature curve and the experimental one for bulk BaTiO$_3$. The quantitative values for a, $T_{c\infty}$, $T_{0\infty}$, β, and σ are listed in Table I.

A. 180° domain walls

To calculate the domain-wall polarization profile and the domain-wall energy, one needs to know the coefficient c for the gradient term in Eq. (11). However, the coefficient c is not known. Recent electron holographic experiments[29] on BaTiO$_3$ showed that at room temperature a 90° domain wall has a thickness of about 20 Å. If one assumes that the thickness of a 180° domain wall is roughly the same as that of a 90° one, then Eq. (17) can be used to estimate the coefficient, i.e.,

$$c = \tfrac{3}{4}\xi^2(-\alpha - \tfrac{2}{3}\beta P^2 - \tfrac{23}{45}\sigma P^4) . \qquad (32)$$

Using a polarization $P = 78\,000$ esu/cm^2 and $2\xi = 18$ Å at $T = 25$ °C and the coefficients α, β, and σ listed in Table I, $c = 0.3 \times 10^{-16}$. Plugging this c value back into Eq. (16), we obtain a domain-wall energy $\gamma = 5.3$ ergs/cm^2 for $P = 78\,000$ esu/cm^2 and $2\xi = 18$ Å at $T = 25$ °C, which is in line with the existing theoretical calculations,[23-26] which ranges 1–10 ergs/cm^2 for the 180° domain walls in BaTiO$_3$. Therefore, we feel that $c = 0.3 \times 10^{-16}$ is a fairly good representation for the coefficient of the gradient term.

B. Multiple-domain crystals

For multiple-domain crystals, the results shown below were for the space-charge layer thickness $t = 75, 100, 167$, and 500 Å. The layer thickness is related to the charge-carrier concentration. A smaller t represents a higher charge-carrier concentration (i.e., higher electrical conductivity). We will discuss more about the space-charge layer thickness in Sec. IV. To show the effect of particle size on the transition temperature T_c, Fig. 4 shows the polarization P as a function of temperature T for $L = 0.4$, 0.5, 0.6, 0.7, 0.8, 2.0, and 1000 μm with $t = 500$ Å. As L becomes smaller, the transition temperature T_c is decreased. Note that although the transition temperature is lowered, the first-order nature of the transition is un-

changed. Furthermore, the polarization P at T_c is about 55 000 esu/cm^2 for all L. The reason for the more or less constant P at T_c for all L will be discussed in the next section. For ferroelectric crystals such as BaTiO$_3$, it is known that the spontaneous strain $(c/a - 1)$ is proportional to the square of the spontaneous polarization.[14] The constant P at T_c for all L shown in Fig. 4 suggests that $(c/a - 1)$ should also be constant at T_c regardless of the particle size. Indeed, the experiment of Uchino, Sadanaga, and Hirose[4] showed a constant $(c/a - 1)$ at T_c for all the particle sizes studied.
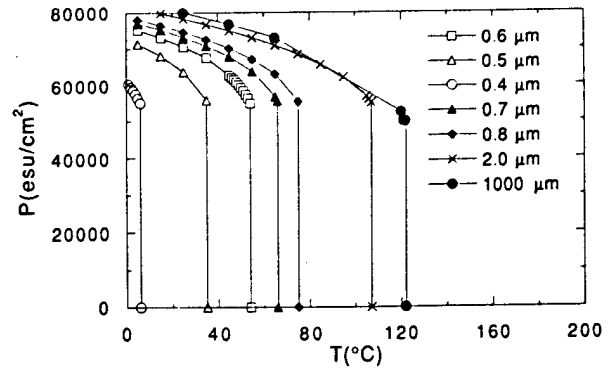
Meanwhile, from Fig. 4, one can see that at a given temperature, e.g., 25 °C, the polarization decreases with a decreasing L. Since the spontaneous strain $(c/a - 1)$ is proportional to the square of the spontaneous polarization, the decreased P with a decreasing L shown in Fig. 4 should also indicate a decrease of $(c/a - 1)$ with a decreasing particle size. In Fig. 5, we plot the room-temperature $(P/P_\infty)^2$ as a function of L for $t = 75, 100, 167$, and 500 Å where P_∞ is the bulk polarization. P does not change significantly with L at large L until L is reduced to a certain size below which P decreases sharply. Moreover, below a critical size L_c, the crystal becomes nonferroelectric at room temperature. The critical

FIG. 5. $(P/P_\infty)^2$ vs L for $t = 75, 100, 167$, and 500 Å. Also plotted are the experimental $(c/a - 1)/(c/a - 1)_\infty$ from Uchino, Sadanaga, and Hirose (Ref. 4) and Känzig and co-workers (Refs. 1 and 2), where $(c/a - 1)_\infty$ denotes the bulk $(c/a - 1)$ value.

size L_c depends on the value of t: $L_c = 0.45$, 0.26, 0.2, and 0.175 μm for $t = 500$, 167, 100, and 75 Å, respec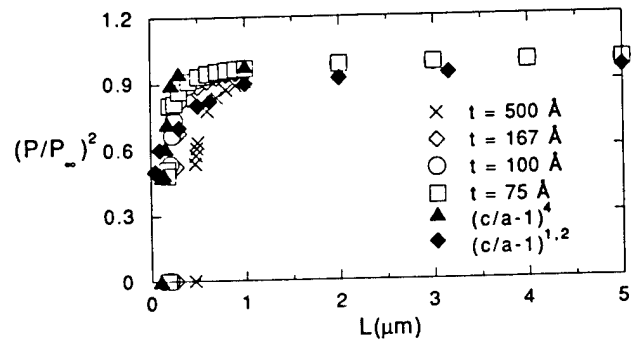tively. As t becomes smaller, the ferroelectric phase can remain stable to a smaller particle size. This qualitatively explains why different authors seem to observe different size dependence. Also plotted in Fig. 5 are the experimental $(c/a - 1)/(c/a - 1)_\infty$ for comparison: solid triangles from Uchino, Sadanaga, and Hirose[4] and solid diamonds from Anliker, Brugger, and Känzig, where $(c/a - 1)_\infty$ denotes the bulk $(c/a - 1)$ value. One can see the different size dependence of $(c/a - 1)$ among the two experiments.

In Fig. 6, we plot T_c as a function of L for $t = 500$, 167, 100, and 75 Å. Again, T_c does not change much at large L, but decreases sharply below a certain L, similar to the behavior of P versus L shown in Fig. 5. Also plotted in Fig. 6 are the data points from the experiment of Uchino, Sadanaga, and Hirose.[4] Note that even though the $(c/a - 1)/(c/a - 1)_\infty$ curve of Uchino, Sadanaga, and Hirose appears to coincide with the calculated curve of $(P/P_\infty)^2$ for $t = 75$ Å as shown in Fig. 5, the change in T_c in the experimental system of Uchino, Sadanaga, and Hirose is much more abrupt than the calculated curve of T_c versus L for $t = 75$ Å when the particle size is around 0.1–0.2 μm. One possible explanation for the more abrupt change of T_c in the experiment is that the particle size in the experimental system has a distribution. Since larger particles have a higher T_c, the observed transition temperature T_c of particles that have a size distribution would be determined by that of the largest particles in the distribution rather than that of the average-size particles. Therefore, experimentally, T_c would be very sensitive to the particle-size distribution. On the other hand, the quantity $(c/a - 1)$ at a certain temperature is an averaged quantity over all particles and is, therefore, not as sensitive to the presence of the larger particles. As a result, experimentally, one may not see the same size dependence between $(c/a - 1)$ and T_c.

Meanwhile, the shape of the particles also has an effect on the size dependence. It is known that the depolarization factor of a single-domain spherical particle is one-third of that of a single-domain cubic particle. It is not known what the depolarization factor of a multiple-

domain spherical particle would be. However, it can be expected that for multiple-domain crystals, spheres would also have a lower depolarization factor than cubes. Therefore, the ferroelectric phase can be stable to a smaller particle size with a sphere than with a cube. If one assumes that the depolarization of a multiple-domain sphere is also one-third of that of a multiple-domain cube, then the effect of $t = 167$ Å for a cube would be equivalent to that of $t = 500$ Å for a sphere of the same size. That is, at room temperature, a cube with $t = 500$ Å would become nonpolar for $L \leq 0.45$ μm, whereas a sphere with $t = 500$ Å would not become nonpolar until $L \leq 0.26$ μm (Fig. 5). Similar to an infinitely large system, the dielectric constant ϵ of a small crystal also reaches a very high value at T_c. As an example, we plot the polarization P and the dielectric constant ϵ as a function of T for $L = 0.6$ μm and $t = 500$ Å in Fig. 7. As we have discussed above, the value of α' is insensitive to L. Therefore, the dielectric constant ϵ of the $L = 0.6$ μm crystal reaches about the same high value at T_c as the infinitely large system.[2,14,15] The dielectric constant ϵ as a function of T for various L with $t = 500$ Å is shown in Fig. 8. Since the dielectric constant peaks at T_c and T_c decreases with a decreasing L, the dielectric constant at a given temperature would also peak at a certain L for which the transition temperature T_c is close to the given temperature. As an example, the dielectric constant ϵ as a function of L for $t = 500$ Å at $T = 15, 25, 45$, and 65 °C is plotted in Fig. 9. One can see that ϵ indeed peaks at a certain L value, similar to the experimental observations in BaTiO$_3$ ceramics.[9,10] In Fig. 10, we plot room-temperature ϵ versus L for $t = 75$, 100, 167, and 500 Å. Again, the value of L at which ϵ peaks is also affected by the value for t. As t is decreased, ϵ peaks at a smaller L as similar to the change in L_c (Fig. 5).

Since most of the domain-wall studies were carried out at room temperature, the values for the domain-wall energy γ and the domain-wall thickness 2ξ in the existing literature are only suitable for room temperature. It is worth noting that both γ and ξ change substantially with temperature, especially near the bulk transition temperature $T_{c\infty}$. In Fig. 11, we plot ξ and γ versus T for a 180° domain wall that separates two semi-infinite domains. One can see that ξ tends to increase and γ tends to de-
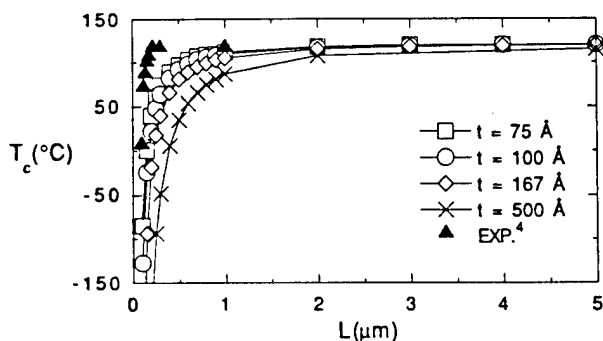

FIG. 6. T_c vs L for $t = 75$, 100, 167, and 500 Å. Also plotted are the experimental values from Uchino, Sadanaga, and Hirose (Ref. 4).
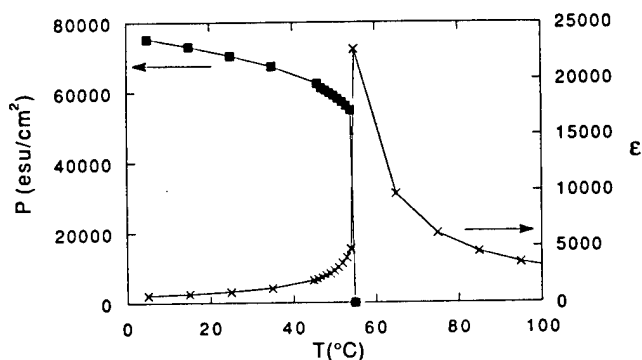

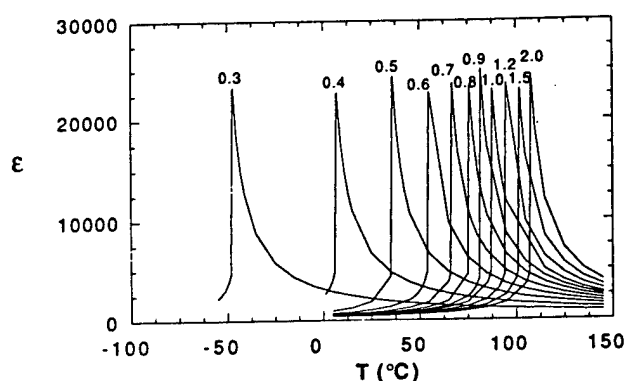FIG. 7. P and ϵ vs T for $L = 0.6$ μm and $t = 500$ Å.

FIG. 8. ϵ vs T for various L (in μm) with $T=500$ Å.

FIG. 10. ϵ vs L at $T=25$ °C for $t=75$, 100, 167, and 500 Å. Note that at a given T the peak position also changes with t.

crease with an increasing temperature, especially near $T_{c\infty}$.

The value of the polarization at the transition temperature T_c depends on the values of a', T_c-T_0, β, and σ. Both β and σ are constant, and a' and T_0 are given in Eqs. (30) and (31). A constant P at T_c, for all L, requires that $a'(T_c-T_0)$ be a constant. We found that for all L, T_c-T_0 is about 8 °C, roughly a constant. Meanwhile, even though the ratio ξ/D tends to increase with an increasing T, it generally remains small at T_c as can be seen in Fig. 12, where we plot ξ/D ($T=T_c$) versus L for $t=75$, 100, 167, and 500 Å. Therefore, a' remains more or less constant at T_c. The constant a' at T_c together with the constant T_c-T_0 gives the constant drop of P at T_c as shown in Fig. 4.

Note that even though for larger particles ξ/D at T_c is small and tends to increase with a decreasing L, for smaller particles, i.e., $L \leq 1$ μm, ξ/D at T_c saturates at a constant value of about 0.145. It is interesting to note that the range $L \leq 1$ μm where ξ/D at T_c is constant is also the range where T_c is substantially lower than the bulk transition temperature $T_{c\infty}$. Therefore, one may think of this constant ξ/D ratio at T_c as a ferroelectric analog of the Lindemann criterion for melting, which states that at the melting temperature the ratio $\sqrt{\overline{\Delta x^2}}/\bar{x}$ in a solid reaches a constant value where $\sqrt{\overline{\Delta x^2}}$ is the

root-mean-square displacement and $\bar{x}$ the mean nearest-neighbor distance. In other words, when the ratio ξ/D at T_c reaches a critical value, the ferroelectric phase is no longer stable.

The saturation of the ratio ξ/D at T_c in small particles sets the limit as to how small the domain width D can get and helps explain why smaller particles have a lower T_c or why at a given temperature there is a critical size L_c below which the ferroelectric phase is absent. For example, the explanation for the latter may be given as follows. At a given T, the domain width D decreases with a decreasing L as shown in Fig. 13, where D at room temperature is plotted versus L for $t=75$, 100, 167, and 500 Å. Meanwhile, at a given T, ξ does not change very much with a decreasing L as shown in Fig. 14, where ξ as a function of L for $t=75$, 100, 167, and 500 Å is plotted. As a result, at a given T, the ratio ξ/D increases with a decreasing L as shown in Fig. 15, where the room-temperature ξ/D for $t=75$, 100, 167, and 500 Å is plotted as a function of L. On the other hand, the saturation of ξ/D at around 0.145 at T_c shown in Fig. 12 indicates that there is a limit on how small D can be. The intercepts of the extrapolated curves of ξ/D with the dashed

FIG. 9. ϵ vs L (in μm) at $T=15, 25, 45$, and 65 °C with $t=500$ Å. Note that ϵ peaks at a certain L whose T_c is close to the given temperature.

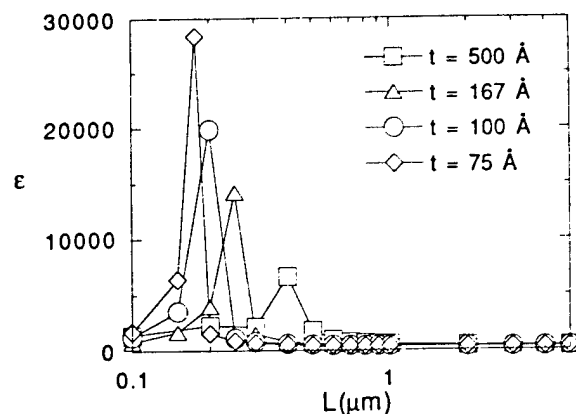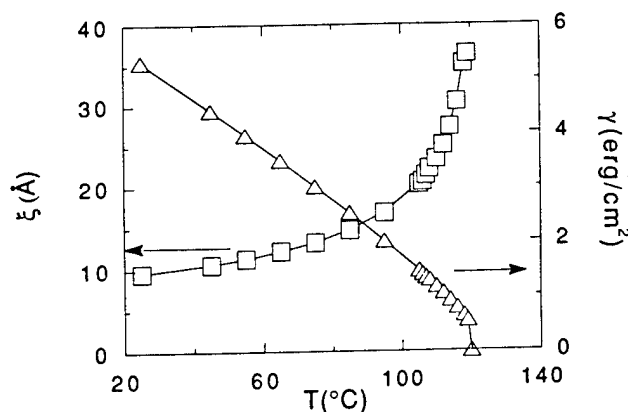FIG. 11. Half domain-wall thickness ξ and domain-wall energy γ as a function of temperature. Note that both ξ and γ change substantially near $T_{c\infty}$, where $T_{c\infty}$ is the bulk transition temperature.
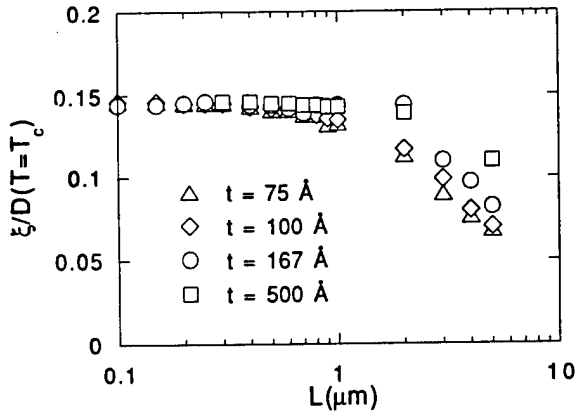
FIG. 12. ξ/D $(T=T_c)$ vs L. Note that for small L, ξ/D at T_c reaches a constant value of about 0.145, which may be thought of as an analog of the Lindemann rule.

line at $\xi/D=0.145$ gives the critical sizes L_c at room temperature, which are 0.45, 0.26, 0.2, and 0.175 μm for $t=500$, 167, 100, and 75 Å. Below L_c, the extrapolated D would give a ξ/D ratio larger than 0.145. Therefore, the ferroelectric phase becomes unstable for $L \le L_c$ at room temperature. Similarly, the ξ/D ratio of the smaller particles reaches the constant value 0.145 at a lower temperature, giving rise to the lower T_c of the smaller particles.

Finally, for the present calculations, in the bracket on the right-hand side of Eq. (31) can be neglected and Eq. (31) can be reduced as

$$T_0 = T_{0\infty} - \frac{1}{a'} \left[1.7 \frac{Dt}{L^2} \right] . \tag{33}$$

Equation (33) describes how the Curie-Weiss temperature of small particles changes with the particle size L. Since a' is independent of L as we have discussed above, for a constant t, it follows from Eq. (33) that $\Delta T_0 = T_0 - T_{0\infty}$ is proportional to D/L^2. Meanwhile, since $T_c - T_0 \cong 8°$ for all L, it follows that $\Delta T_c \propto D/L^2$. In Figs. 16 and 17, we plot ΔT_c and D $(T=T_c)$ as a function of L, respectively, where $\Delta T_c = T_c - T_{c\infty}$, with
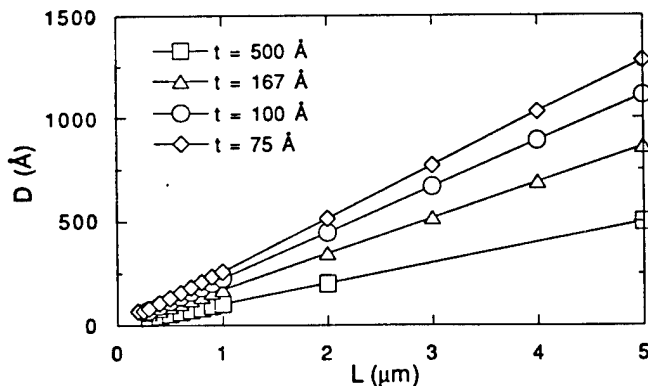
FIG. 14. ξ $(T=25°C)$ vs L for $t=500$, 167, 100, and 75 Å.
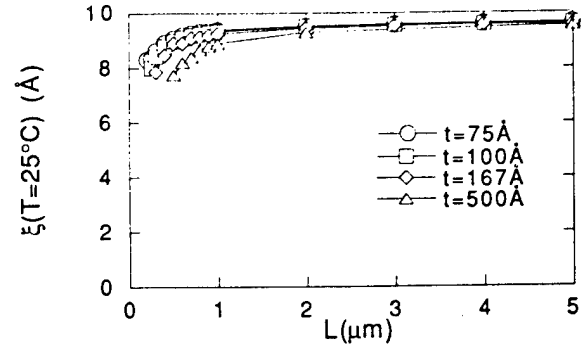
$T_{c\infty}$ denoting the transition temperature of an infinitely large crystal. D $(T=T_c)$ as a function of L can be fitted as D $(T=T_c) \propto L^{0.7}$, and ΔT_c is indeed proportional to D $(T=T_c)/L^2$ as $L^{-1.3}$. Note that at room temperature D increases linearly with L as shown in Fig. 13 instead of D $(T=T_c) \propto L^{0.7}$ as shown in Fig. 17. The difference is that D $(T=T_c)$ is taken at the transition temperature of each L, whereas the room-temperature D shown in Fig. 13 is taken at a fixed temperature for all L. The linear dependence of the room-temperature D with respect to L is a result of using the Schottky type of space-charge layer as discussed above.

IV. CONCLUDING REMARKS

We have examined the effect of depolarization on the ferroelectric transition of small BaTiO$_3$ particles. To reduce the depolarization energy, particles break up into domains of different polarization. The depolarization energy, which includes both the energy due to the depolarization field and the domain-wall energy, was incorporated into the Landau-Ginzburg free energy. Furthermore, to take into account that BaTiO$_3$ is not perfectly insulating, a Schottky-type space-charge layer about a few hundred Å thick as estimated by many researchers was considered. The domain-wall energy is calculated within Landau-Ginzburg theory by assuming a hyperbolic

FIG. 13. D $(T=25°C)$ vs L for $t=500$, 167, 100, and 75 Å.
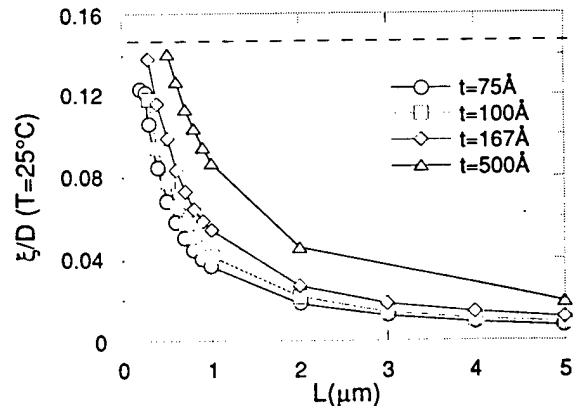
FIG. 15. ξ/D $(T=25°C)$ vs L for $t=500$, 167, 100, and 75 Å.
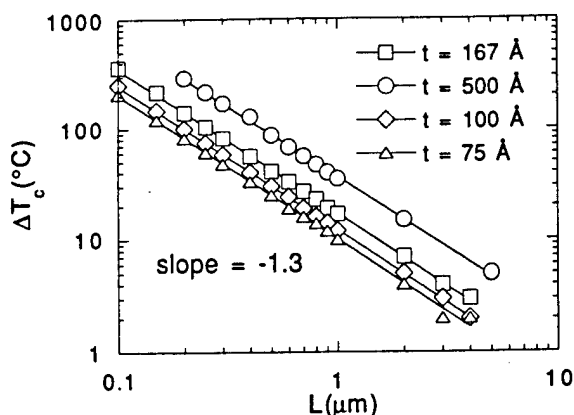
FIG. 16. ΔT_c vs L for $t=500$, 167, 100, and 75 Å.

tangent polarization profile and by minimizing the domain-wall energy with the domain-wall thickness.

We showed that with a Schottky space-charge layer 75–500 Å thick the polar phase becomes unstable for cubic particles smaller than 0.2–0.5 μm at room temperature, depending on the space-charge layer thickness, in line with many experimental observations.[4,6,7] In addition, the polarization of small particles at a constant temperature decreases with a decreasing particle size, in agreement with the experimental result that the tetragonality $(c/a-1)$ of small particles decreases with a decreasing particle size.[1,4] Meanwhile, we also showed that the polarization at T_c is constant regardless of the cubic particle size, which is in line with the experimental observation of a constant value of c/a at T_c for various particle sizes.[4] It was also shown that the domain width D decreases with the cubic particle size, which agrees with the TEM observation of the 90° domain walls in BaTiO$_3$ ceramics,[9] although 180° domain walls were considered in this study. Because of the size dependence of T_c, at a given temperature, the dielectric constant peaks at a certain cubic particle size at which the transition temperature T_c is closest to that temperature. This result agrees with the observation in BaTiO$_3$ ceramic samples.[9]

FIG. 17. $D(T=T_c)$ vs L for $t=500$, 167, 100, and 75 Å.

In principle, for a given bulk charge-carrier concentration, one can calculate the Schottky-layer thickness by solving the Poisson (or Poisson-Boltzmann) equation for the actual charge-carrier distribution in the particle,[13,22] which was not done in the present paper. However, we can estimate the charge-carrier concentration 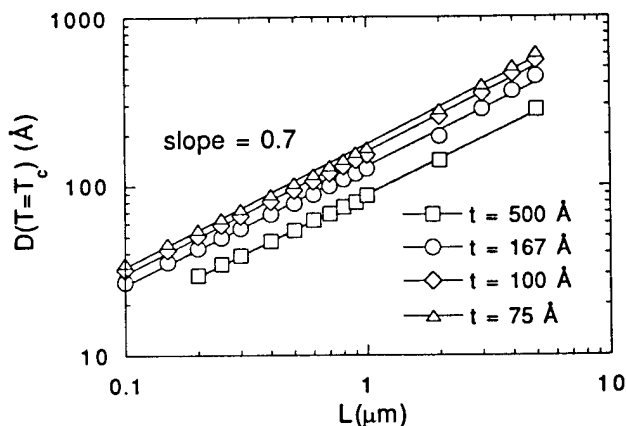within the layer, which is related to the charge-carrier concentration within the particle. Assuming a Schottky-type layer, the carrier concentration within the layer can be estimated by $n=p/e$, where p is the charge density in the layer as depicted in Eq. (7) and e the electronic charge. With $P=78\,000$ esu/cm^2 at room temperature, $n\cong3\times10^{19}$ and 2×10^{20} cm^{-3} for $t=500$ and 75 Å, respectively. The space-charge layer thickness t decreases with an increasing charge-carrier concentration in the layer. The charge-carrier concentration within the layer should increase with an increasing charge-carrier concentration in the particle. Therefore, a smaller t represents a higher charge-carrier concentration (i.e., higher conductivity) in the particle.

Generally, the theory works for semiconductors down to insulators. As the conductivity of the material is parametrized by the Schottky-layer thickness t, a smaller t represents a higher bulk charge-carrier concentration in the particle. For particles with a Schottky-layer thickness $t<L$, the depolarization energy is reduced by a factor of t/L as discussed in the text. In the case of insulators, one may think that t is so large that $t>L$ for all L. Therefore, the depolarization field exists in the entire particle and there is no reduction in the depolarization energy; i.e., the t/L factor is replaced by L/L.

In addition, the present theory should be applicable to all small ferroelectric particles regardless of the mechanism of the ferroelectric transition. The reason is that the depolarization effect which is the focus of the present theory is independent of the transition mechanism. As long as there is polarization, there is a depolarization field regardless of how the polarization comes about. Meanwhile, Landau-Ginzburg theory, which is the foundation of the present theory, does not address the transition mechanism either. It only describes the ferroelectric transitions by expanding the free energy in terms of the polarization. With different values for the coefficients in the free-energy expansion, Landau-Ginzburg theory is applicable not only to perovskite ferroelectrics, but also to KDP whose transition mechanism is different from that of the perovskite ferroelectrics. Thus the present theory can be readily applied to other ferroelectric materials such as KDP or PbTiO$_3$ provided that the coefficients in the Landau-Ginzburg free energy for these materials are known.

It should be noted that some ferroelectric materials may have more than one ferroelectric phase. For example, BaTiO$_3$ can transform from the tetragonal phase to another ferroelectric phase (i.e., the orthorhombic phase) at a lower temperature. The present theory only deals with the effect of particle size on the paraelectric-to-ferroelectric transition. We did not consider the transition among different ferroelectric phases at the moment, although the effect of particle size on the transition among different ferroelectric phases is also an interesting

problem.

Experimentally, the depolarization effect on small $BaTiO_3$ particles can be examined by embedding the small $BaTiO_3$ particles in both an insulating medium and a conducting medium as has been done for small KDP particles.[14] The difference in the XRD and dielectric constant measurements on the two types of composites would be the result of the depolarization effect.

Besides the depolarization effect examined in this paper, the contribution of the stress development is also important in ceramic samples and thin films.[30] The present theory is more applicable to powders since stress development is less likely in powders than in ceramic samples or thin films. To take into account the stress effect or the presence of 90° domain walls, a Devonshire type of theory[27] will be needed.

Finally, it is worth mentioning again that the depolarization effect on the ferroelectric transition of small ferroelectric particles has no counterpart in ferromagnetic crystals, as the magnetostatic self-energy is about 10^3 times smaller than the transition energy and thus cannot suppress the spontaneous magnetization.[14]

ACKNOWLEDGMENTS

[1] M. Anliker, H. R. Brugger, and W. Känzig, Helv. Phys. Acta 27, 99 (1954).

[2] W. Känzig, Ferroelectrics and Antiferroelectrics (Academic, New York, 1957), p. 58.

[3] K. Ishikawa, K. Yoshikawa, and N. Okada, Phys. Rev. B 37, 5852 (1988).

[4] K. Uchino, E. Sadanaga, and T. Hirose, J. Am. Ceram. Soc. 72, 1555 (1989).

[5] K. Saegusa, W. E. Rhine, and H. K. Bowen, J. Am. Ceram. Soc. 76, 1505 (1993).

[6] F. Dogan, C. M. Chun, and I. A. Aksay (unpublished).

[7] W.-H. Shih and Q. Lu, Ferroelectrics 154, 241 (1994).

[8] M.-H. Lee, A. Halliyal, and R. E. Newnham, Ferroelectrics 87, 71 (1988).

[9] G. Arlt, D. Hennings, and G. de With, J. Appl. Phys. 58, 1619 (1985).

[10] See the references cited in Ref. 9.

[11] For example, see J. Paletto, G. Grange, R. Goutte, and L. Eyraud, J. Phys. D 7, 78 (1974).

[12] G. A. Samara, Phys. Rev. 151, 378 (1966).

[13] I. P. Batra, P. Wurfel, and B. D. Silverman, Phys. Rev. B 8, 3257 (1973).

[14] F. Jona and G. Shirane, Ferroelectric Crystals (Dover, New York, 1962).

[15] E. Fatuzzo and W. Merz, Ferroelectricity (North-Holland, Amsterdam, 1967).

[16] W. Merz, Progress in Dielectrics (Academic, New York, 1962), Vol. 4.

[17] F. S. Galasso, Structure, Properties and Preparation of Perovskite Compounds (Pergamon, New York, 1969).

[18] S. Chikazumi, Physics of Magnetism (Wiley, New York, 1964), p. 554.

[19] W. Känzig, Phys. Rev. 98, 549 (1955).

[20] For example, see Metal-Semiconductor Schottky Barrier Junctions and Their Applications, edited by B. L. Sharma (Plenum, New York, 1984).

[21] S. Triebwasser, Phys. Rev. 118, 100 (1960).

[22] P. E. Bloomfield, I. Lefkowitz, and A. D. Aronoff, Phys. Rev. B 4, 974 (1971).

[23] W. J. Merz, Phys. Rev. 95, 690 (1954).

[24] W. Kinase and H. Takahashi, J. Phys. Soc. Jpn. 12, 464 (1957).

[25] W. Kinase, Prog. Theor. Phys. (Kyoto) 13, 529 (1955).

[26] V. A. Zhirnov, Z. Eksp. Theor. Fiz. 35, 1175 (1959) [Sov. Phys. JETP 8, 822 (1959)].

[27] A. F. Devonshire, Philos. Mag. 42, 1065 (1951); 40, 1040 (1949).

[28] W. Cao and E. Cross, Phys. Rev. B 44, 5 (1991).

[29] X. Zhang and D. C. Joy, Appl. Phys. Lett. 60, 787 (1992).

[30] B. S. Kwak, A. Erbil, B. J. Wilkens, J. D. Budai, M. F. Chisholm, and L. A. Boatner, Phys. Rev. Lett. 68, 3733 (1992).

Synthesis of Mullite Fibre from an Aluminosiloxane Precursor

Toshinobu Yogo*[a] and Ilhan A. Aksay[b]
[a] *Department of Applied Chemistry, School of Engineering, Nagoya University, Furo-cho, Chikusa-ku, Nagoya 464-01, Japan*
[b] *Princeton Materials Institute, Princeton University, Princeton, New Jersey 08544-5263, USA*

Mullite fibre was successfully synthesized by pyrolysis of aluminosiloxane formed from ethyl 3-oxobutanoatodiisopropoxyaluminium and di-(sec-butoxy)aluminoxytriethoxysilane. Aluminosiloxane increased in viscosity with increasing coordination number of aluminium, which was analysed by ^{27}Al NMR spectroscopy. The viscosity of aluminosiloxane was controlled by the amount of added glacial acetic acid as well as the working temperature for the spinning of precursor fibre. Aluminosiloxane gave amorphous SiO_2–Al_2O_3 at 500 °C, which began to crystallize to mullite at 930 °C. Single-phase mullite was produced on heating to 1000 °C for 1 h. The polymer fibre spun from aluminosiloxane was pyrolysed yielding crack-free mullite fibre at 1000 °C for 1 h.

Mullite ($3Al_2O_3\cdot2SiO_2$) has various attractive properties such as high-temperature strength, creep resistance and a low thermal expansion coefficient. Fibre-reinforced materials have been receiving great attention because of their applications in the field of composites materials.[1,2] Alumina, alumina–silica, and alumina–zirconia fibres are mainly used as temperature-resistant fibres.[3] Refractory oxides have extremely high melting points and low viscosity of melts making melt spinning impractical, which leads to the development of chemical techniques including the sol–gel process for the synthesis of ceramic fibres.

The synthesis of silica-stabilized alumina fibres by the sol process using aluminium oxychloride was demonstrated by Morton et al.[4] Aluminosilicate and aluminium borosilicate fibres were made via similar processes employing aqueous aluminium acetate and colloidal silica.[5] Horikiri et al. reported the fabrication of alumina and silica–alumina fibres from the partially hydrolysed diethylaluminium isopropoxide and polysilicic acid esters.[6]

Usually, the spinning conditions are critical in the sol–gel process, since the viscosity of the sol changes with time, and increases very rapidly once gelation starts. The control of viscosity during rapid gelation, therefore, is a key processing factor, since the viscosity of the sol is not sufficiently high for spinning. Soluble organic polymers, such as polyvinyl alcohol and polyethylene oxide, were added not only to raise the viscosity of the sols but also to improve their spinning characteristics.[4] On the other hand, the time-independent viscosity of the starting polymer in the polymer route is one of the most distinct differences from the sol–gel process. Various spinning methods, such as melt-spinning and dry-spinning result from the suitable solubility and viscoelastic properties of polymers.

Andrianov synthesized various metalloxane polymers including aluminosiloxanes, which comprise Al−O−Si backbones.[7] Organoaluminosiloxane polymer obtained from diacetoxydimethylsilane and ethyl acetoacetatealuminium diisopropoxide was used for the fabrication of aluminosilicate films on metal substrates.[8,9] Oxyalkoxide polymer synthesized from aluminium butoxide and tetrachlorosilane was reported to form mullite when the initial Al:Si ratio was appropriate.[10]

The formation process of mullite in the solution–precipitation processes in aqueous systems depends upon the mixing level of aluminium and silicon in the precipitated powders.[11] The difference of the hydrolysis rates between aluminium alkoxide and silicon alkoxide results in the segregation of aluminium- and silicon-containing species in the precipitated powders.[11] The degree of formation of silica and Al–Si spinel

during mullitization is explained by the segregation level of starting materials.[12] The slow hydrolysis/condensation of alkoxides under controlled conditions[12-14] and the spray pyrolysis of aluminium nitrate–silicon ethoxide system[15] are reported to be effective for chemical homogeneity in the powders. When the formation of mullite is accompanied by Al–Si spinel and silicious phase, the mechanical properties of the mullite degrade at high temperatures due to the formation of a grain-boundary liquid phase.[15] The synthesis of single-phase mullite is required to achieve the optimal high-temperature properties.

This paper describes the synthesis of mullite fibre from an aluminosiloxane precursor synthesized by the reaction of ethyl 3-oxobutanoatodiisopropoxyaluminium and di-(sec-butoxy) aluminoxytriethoxysilane in the presence of glacial acetic acid. The synthesis conditions using glacial acetic acid were found to be useful for avoiding the segregation of aluminium- and silicon-containing species as well as avoiding gelation of the precursor. Aluminosiloxane with controlled viscosity was spun into precursor fibres, which were successfully crystallized in crack-free, single-phase mullite fibres.

Experimental

Starting Materials

Ethyl 3-oxobutanoatodiisopropoxyaluminium, (iso-$C_3H_7O)_2Al(CH_3COCHCO_2C_2H_5)$, (EOPA) was prepared according to Patterson et al.[16] Di-(sec-butoxy)aluminoxytriethoxysilane, (sec-$C_4H_9O)_2Al−O−Si(OC_2H_5)_3$, (BAES) was commercially available (Hüls America Inc., Piscataway, NJ, USA). Glacial acetic acid was refluxed over diphosphorus pentaoxide, and distilled before use.

Synthesis of Mullite Precursor

The synthesis of an aluminosiloxane precursor with a mullite composition ($3Al_2O_3\cdot2SiO_2$, Al:Si = 3) was carried out under an argon atmosphere without any solvent.

A mixture of EOPA (18.37 g, 66.61 mmol) and BAES (11.74 g, 33.30 mmol) with an Al:Si ratio of 3 was refluxed at 220 °C for 2 h. After cooling to room temperature, glacial acetic acid (3.20 g, 53.29 mmol, 80 mol% of EOPA) was added dropwise to the reaction mixture to give an exothermic reaction. The resulting viscous liquid was refluxed at 200 °C for 4 h. After the reaction mixture was cooled to room temperature, the low boiling components (<85 °C/10^5 Pa) were distilled out from the reaction mixture affording a viscous liquid as a residue. The volatile components were removed

thoroughly from the residue at 50 °C and 10^2 Pa for 5 h providing a transparent pale-yellow liquid with an extremely high viscosity.

Synthesis of Powder

The viscous metallo-organic product was heated from room temperature to 500 °C at 1 °C min⁻¹ in air using a muffle furnace with a 6000 cm³ chamber. The powder thus formed was heat-treated at temperatures between 900 and 1200 °C.

Synthesis of Mullite Fibre

The precursor was charged in a brass extruder (Fig. 1), which was then set in a hand press (Riken Seiki, P-16B). The precursor was melted in the extruder using a flexible heater above 80 °C, and then extruded through the spinneret with a diameter of 300 μm below 60 °C. The temperature was measured using a calibrated thermocouple set inside the heater. The extruded fibre was collected with a glass rod. The fibre diameter ranged from 100 to 200 μm. Alternatively, precursor fibres were spun from a bulk polymer with hand-drawing using a glass rod of diameter of 8 mm at room temperature. The length of fibre was 50–80 cm. The polymer fibres were dried in air at room temperature for 2 or 3 days prior to heat treatment. The diameter of fibre by hand-drawing was 5–100 μm. The polymer fibres were cut into lengths of 3–6 cm, and then fired in air from room temperature to 900 °C at 0.2 °C min⁻¹. The ceramic fibres were subsequently heat-treated between 1000 and 1200 °C for 1 h at 1 °C min⁻¹ above 900 °C.

Characterization of Aluminosiloxane and Aluminosilicate

Aluminosiloxane and organic products were characterized by IR (Hitachi, 260–30), NMR spectroscopy and gas chromatography (GC, Hitachi, 263–50). IR spectra of organic and metallo-organic products were measured by the liquid-film method using a pair of KBr plates (4 mm thick and 30 mm diameter). The powder samples were mixed with KBr powders and pressed to disks (0.3 mm thick and 10 mm diameter), and then measured. ^{13}C NMR spectra were recorded by a Gemini 200 spectrometer (Varian) in $CDCl_3$ solution using tetramethylsilane as an internal standard. Solution ^{27}Al NMR spectra were measured using a Bruker AC 250 spectrometer at 65.18 MHz in $CDCl_3$ solution with $Al(H_2O)_6^{3+}$ as an external standard. The volatile components as reaction

Fig. 1 Extrusion apparatus of aluminosiloxane precursors

by-products were collected by a chilled trap immersed in a dry-ice–acetone bath, and analysed by ^{13}C NMR and GC. The viscosity of precursor was measured by a rotational viscometer using a cone-and-plate (Tokyo Keiki, EHD) from 45 to 75 °C. Molecular weights were determined cryoscopically using benzene as a solvent.[17]

The crystallization behaviour of the amorphous product was measured with DTA and TG (Perkin-Elmer, 7) at a heating rate of 10 °C min⁻¹. The pyrolysis product was analysed by X-ray diffraction analysis (XRD) with Cu-Kα radiation (Rigaku, RAD-II) after heat treatment at temperatures between 900 and 1200 °C from 1 to 10 h. Ceramic fibres were observed by scanning electron microscopy (SEM) using a JEOL JSM-T20. The ratio of aluminium to silicon in the mullite fibres was analysed by ICP (inductively coupled plasma) emission spectroscopy (Shimadzu ICPQ-1000). The solution for ICP analysis was prepared according to the literature.[18] The density of fibres was determined by a sink-float method using a mixture solution of thallium formate and thallium malonate.

Results and Discussion

Synthesis of Aluminosiloxane for Mullite

A mixture of EOPA and BAES with a molar ratio of 2 (the Al:Si atomic ratio of 3) was reacted with various amounts of glacial acetic acid yielding viscous liquids. The product was transparent, and soluble in usual organic solvents, such as benzene and chloroform. No water was used for the reaction in order to avoid the gelation of products.

BAES has an advantage for molecular mixing of aluminium and silicon, since it has an Al—O—Si bond in monomer itself. In addition, the silicon site of BAES is at least trifunctional to condensation reaction because three ethoxy groups are bonded to the silicon atom. The multifunctional silicon compound has higher possibility for the formation of cross-linkage and branching via M—O bonds than that of di- and mono-functional compounds. Since silicon-organics consisting of Si—OR (R = methyl, ethyl) bonds are generally less volatile than those including Si—R bonds, the loss of silicon moieties can be minimized during calcination. Also, EOPA is a difunctional compound, since the isopropyl group is more susceptible than the chelate ligand for the elimination and substitution reaction. The M—O—M′ (M,M′ = Al and Si) bond in a starting aluminosiloxane is introduced to minimize the loss of silicon and aluminium moiety during the initial stage of pyrolysis below 300 °C.

Characterization of Aluminosiloxane for Mullite

IR spectra of starting EOPA–BAES mixture of mullite composition ($3Al_2O_3·2SiO_2$, Al:Si = 3, a molar ratio of EOPA:BAES = 2) and its reaction product with 8.0 mol% acetic acid are shown in Fig. 2. The spectrum of starting mixture shows the absorption bands ascribed to Al—O bond at 570, 630 and 700 cm⁻¹ [Fig. 2(a)].[19] The bands changed from sharp peaks to a broad coalesced band after the treatment of acetic acid as shown in Fig. 2(b). This change suggests the formation of a product with various kinds of Al—O bond including ligand-exchange reactions. The Si—O absorption bands of Al—O—Si bond are reported to appear at 1064 and 810 cm⁻¹.[19] BAES itself shows the absorption at 1060 cm⁻¹ as well as those of Si—O at 770 and 670 cm⁻¹. However, these bands are covered with those of EOPA in Fig. 2. The reaction product between BAES and 8 mol% AcOH shows the decrease in intensity and broadening of these absorptions at 1060, 770 and 670 cm⁻¹. The Al—O—Si bond in the
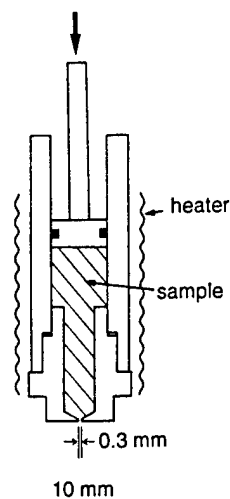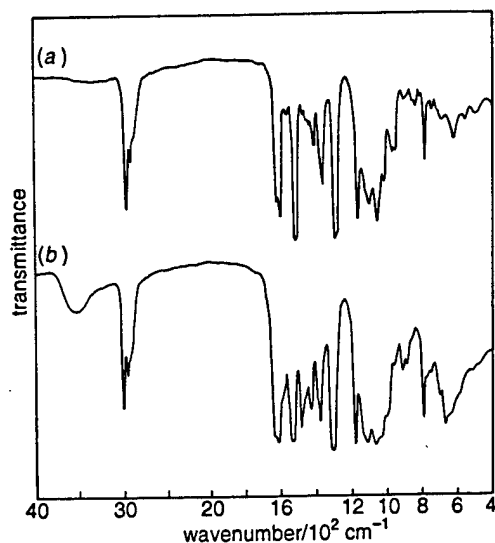
Fig. 2 Infrared spectra of starting EOPA-BAES(2:1) and polymeric product: (a) starting EOPA-BAES (2:1); (b) polymeric product formed from EOPA-BAES-8 mol% acetic acid

EOPA-BAES mixture may, therefore, undergo the ligand redistribution including the cleavage of the Al—O—Si bond. Both 2(a) and 2(b) contained the absorption bands due to ethyl 3-oxobutanoato ($CH_3COCHCO_2C_2H_5$, EOB) ligand at 1640, 1620, 1535 and 1300 cm^{-1}. The OH absorption at 3500 cm^{-1} in Fig. 2(b) shows the formation of a small amount of water or alcohols in the reaction product.

Fig. 3 shows the change of ^{13}C NMR spectra of EOPA-BAES (molar ratio, 2) with the amount of acetic acid. The signals of the starting mixture of EOPA and BAES in
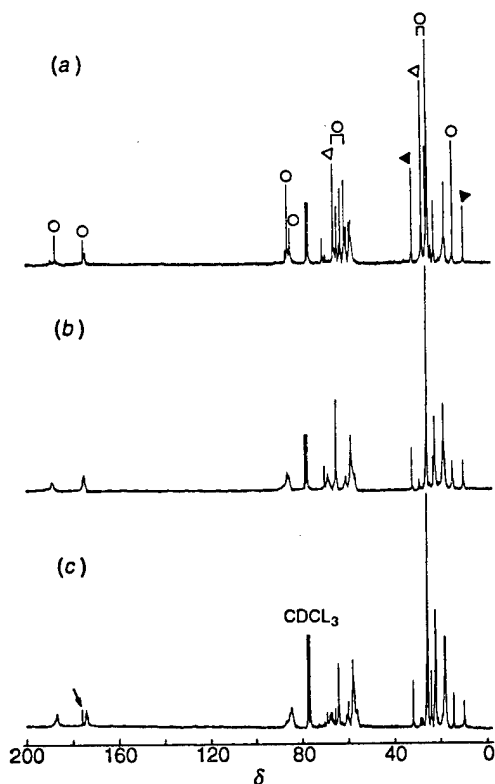
Fig. 3 ^{13}C NMR spectra of starting EOPA-BAES(2:1) and polymeric products synthesized from EOPA-BAES and various amounts of acetic acid: (a) starting EOPA-BAES; (b) product formed from EOPA-BAES and 8 mol% AcOH; (c) product formed from EOPA-BAES and 30 mol% AcOH

Fig. 3(a)† were assigned according to the literature.[20] The main signals of free ethyl 3-oxobutanoate (EOB) appear at 50.3, 167.6 and 201.3 ppm. These signals shifted to 86.0, 174.9 and 187.2 ppm, respectively, due to coordination to aluminium [Fig. 3(a)]. The signals of EOPA are marked with ○ in Fig. 3(a). The others are assigned to BAES. The sharp signals of EOB in the starting EOPA-BAES changed to broad multiplet on treatment with acetic acid as shown in Fig. 3(b). The multiplet results from carbons having slightly different chemical environment from each other. The signals assigned to isopropoxy (27.9 and 66.0 ppm, marked with ▽) and sec-butoxy groups (10.0 and 32.0 ppm, marked with ▼) decreased in intensity with increasing amount of acetic acid as shown in Fig. 3(b) and 3(c). The alkoxy groups on aluminium atoms in both EOPA and BAES are eliminated on treating with acetic acid. However, the alkoxy groups still remain in the product treated with 30 mol% of acetic acid, since the signals of alkoxy groups are observed in Fig. 3(c).

The elimination of both the isopropoxy from EOPA and the sec-butoxy group from BAES shows the possibility of the cross-condensation reaction between EOPA and BAES. The new signal at 176.2 ppm with an arrow in Fig. 3(c) appeared with increasing amount of acetic acid from 8 to 30 mol%. The signal is assigned to the carboxy carbon of CH_3CO_2 group substituted on metals, since free acetic acid shows a signal at 178.7 ppm. The signal at 176.2 ppm was not observed for the reaction product from EOPA itself and 30 mol% acetic acid. Therefore, the substitution of alkoxy groups on silicon for the carboxy group of acetic acid proceeds yielding the signal at 176.2 ppm. Glacial acetic acid not only eliminates the alkoxy groups from EOPA-BAES but also substitutes alkoxy groups for CH_3CO_2 at the concentration of 30 mol% acetic acid.

Fig. 4 shows solution ^{27}Al NMR spectra of starting EOPA-BAES and its reaction products with acetic acid. The starting EOPA-BAES has a signal at 4.2 ppm, and broad signals centred at 40 and 62 ppm. The broad signal centred at 62 ppm derives from four-coordinated aluminium.[21,22] The signal at 40 ppm is assigned to five-coordinated aluminium.[22,23] A monomeric EOPA is four-coordinated, since EOB is a bidentate ligand including two carbonyl oxygens coordinating aluminium. The strong resonance at 4.2 ppm is due to the six-fold coordination of aluminium-oxygen octahedra.[21] On the basis of these results, EOPA or BAES associates affording dimers in $CDCl_3$ solution as reported on aluminium alkoxides, such as $Al(OC_2H_5)_3$, $Al(O^iC_3H_7)_3$ and $Al(O^iC_4H_9)_3$.[22]

The signal at 4.2 ppm in the starting EOPA-BAES increased in half-value width by the reaction with acetic acid from Fig. 4(a) to 4(b). The half-value width of the signals at 4.2 ppm in Fig. 4(a), 4(b) and 4(c) are 391, 769 and 965 Hz, respectively. ^{27}Al ($I = 5/2$) is one of the quadrupole nuclei. The linewidth of a quadrupole nucleus is strongly related to its quadrupole moment and the value of the electric-field gradient along the

†EOPA, isopropoxy $^1CH_3 {}^2CHCH_3$, ^{1}C 27.7, 27.9, ^{2}C 66.0, 66.8 ppm.
 |
 O

EOB $^3CH_3 {}^4C^5CH^6CO^7CH_2 {}^8CH_3$, ^{3}C 25.2, 26.0, ^{4}C 187.2, ^{5}C 86.0,
 ‖ ‖
 O O

84.7, ^{6}C 174.9, ^{7}C 61.3, 62.8,
^{8}C 14.5, 14.3 ppm.

BAES, sec-butoxy $^1CH_3 {}^2CH_2 {}^3CH^4CH_3$, ^{1}C 10.0, 9.6, ^{2}C 32.0, 32.2,
 |
 O

^{3}C 71.4, 64.6, ^{4}C 22.7,
25.0 ppm.

ethoxy $O^5CH_2 {}^6CH_3$, ^{5}C 58.3, ^{6}C 18.1 ppm.

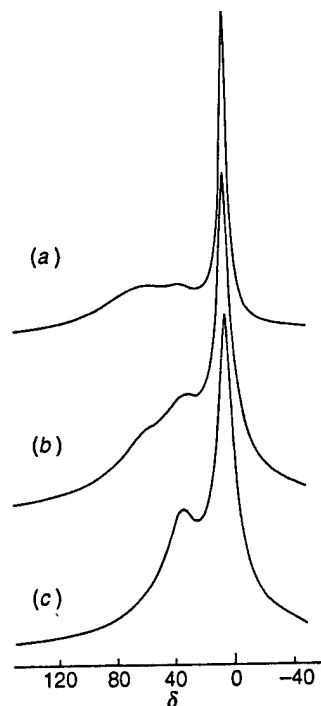Fig. 4 Change of ^{27}Al NMR spectra of starting EOPA–BAES(2:1) and polymeric precursor with the amount of acetic acid: (a) starting EOPA–BAES; (b) product formed from EOPA–BAES and 8 mol% AcOH; (c) product formed from EOPA–BAES and 80 mol% AcOH

bond. A more perfect cubic symmetry (O_h or T_d) arrangement of substituent about ^{27}Al decreases the electric-field gradient yielding sharper lines.[21] Thus, the broadening of the signal is attributable to the increase both in distortion and imbalance around octahedrally coordinated aluminium.[21] This change shows the redistribution of ligands around aluminium through the reaction of aluminium compounds to each other as well as with acetic acid. The signal at 35 ppm increased in intensity after treatment with 8 mol% acetic acid as shown in Fig. 4(b). When EOPA–BAES was allowed to react with 80 mol% acetic acid, the signal at 35 ppm continued to increase, and the four-coordinated aluminium at 62 ppm almost disappeared in the broad signal centred at 35 ppm as shown in Fig. 4(c). EOPA–BAES reacts with acetic acid as a chelating ligand increasing the amount of higher coordinated aluminium atom, which is sterically more crowded aluminium than that of starting EOPA–BAES.

The molecular weight of the EOPA–BAES mixture was 550 ± 30 [calcd. for EOPA–BAES(2:1), 282.4] with cryoscopic measurements in benzene. This indicates that the starting EOPA or BAES associates affording an equilibrium mixture. The molecular weight of polymeric product increased from 590 ± 30 to 1050 ± 50 when the molar percent of acetic acid was raised from 2.5 to 30 mol%. Therefore, the product consists mainly of dimers and trimers.

The reaction between EOPA–BAES and acetic acid gave a mixture of aluminosiloxane and low boiling point components. The low boiling point products comprise alkyl alcohol and its acetate. The formation of ethyl, isopropyl and sec-butyl alcohol and corresponding ethyl, isopropyl and sec-butyl acetate was confirmed by ^{13}C NMR and GC. The amount of alkoxy groups obtained as these alcohols and acetates ranged from 25 to 35% of the total amounts of alkoxy groups in the starting EOPA–BAES. Glacial acetic acid eliminates alkoxy groups from EOPA–BAES by a substitution reaction:

$$M(OR)_n + CH_3CO_2H \rightarrow \qquad (1)$$

$$M(OR)_{n-1}(OCOCH_3) + ROH$$
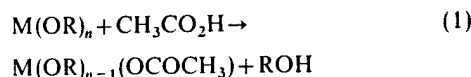
Also the eliminated alkoxy groups reacted with acetic acid yielding water and acetates:

$$ROH + CH_3CO_2H \rightarrow CH_3CO_2R + H_2O \qquad (2)$$
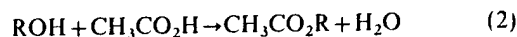
Acetate species may again undergo transesterification with metal alkoxides in the reaction mixture.[24]

$$M(OR)_n + xCH_3CO_2M' \rightarrow \qquad (3)$$

$$M(OR)_{n-x}(OM')_x + xCH_3CO_2R$$
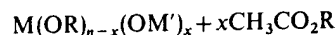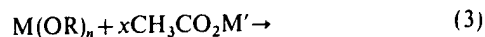
M—O—M' bonds could be formed according to the transesterification as well as according to the usual condensation between M—OH and M'—OR, since a small amount of water was formed in the reaction system. The limited amount of water generated by the reaction between acetic acid and eliminated alcohol suppresses the further condensation, resulting in the formation of the oligomeric precursors. The reaction between EOPA–BAES and acetic acid is summarized as follows, although the formation process of the mullite precursor is composed of several reactions:

$$(Pr^iO)_2Al(EOB) + (Bu^sO)_2Al-O-Si(OEt)_3$$

$$\xrightarrow[\quad CH_3CO_2H \quad]{} RO(-\overset{\overset{\displaystyle L^1}{|}}{Al}-O-\overset{\overset{\displaystyle L^2}{|}}{\underset{\underset{\displaystyle L^3}{|}}{Si}}-)_n \qquad (4)$$

$$+ ROH + CH_3CO_2R + H_2O$$

$$L^1 = EOB, \quad L^2, L^3 = OEt, OR, OAc, OM$$
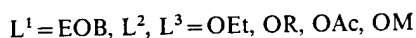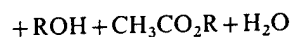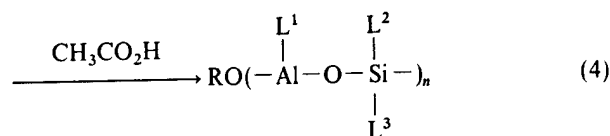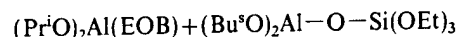
The polymeric product has ethyl 3-oxobutanoato (EOB) ligands on the basis of IR and ^{13}C NMR spectroscopy (Fig. 2 and 3). The oligomers in the polymeric product consist of a structure unit of [-Al(EOB)-O-], which undergoes the intermolecular association affording an octahedrally coordinated aluminium. Since alkoxy groups remain bonded to aluminosiloxane as shown in Fig. 3(c), a structure of -Al(EOB)(OR)-O-might constitute a part of five-coordinated aluminiums.

Viscosity and Spinnability of Polymeric Precursor

The change of viscosity at 75 °C with the amount of added acetic acid is shown in Fig. 5. Both EOPA and BAES are
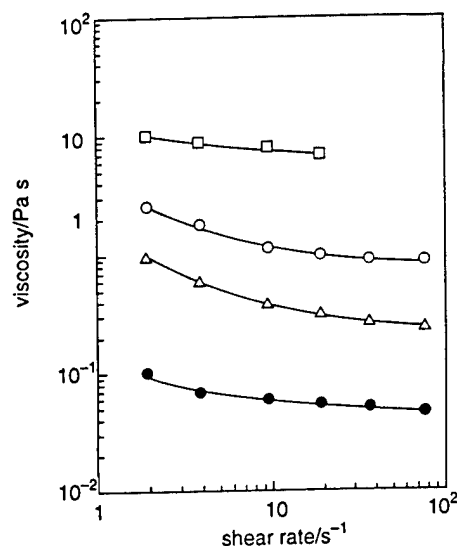
Fig. 5 Change of viscosity for polymeric precursor with the amount of acetic acid and shear rate at 75 °C: ●, starting EOPA–BAES; △, EOPA–BAES-2.5 mol% AcOH; ○, EOPA–BAES-30 mol% AcOH; □, EOPA–BAES-50 mol% AcOH

liquids at room temperature. However, the magnitude of viscosity below 0.1 Pa s for the starting EOPA–BAES was not high enough for spinning. The viscosity increased by one order of magnitude on treatment with only 2.5 mol% acetic acid, and then continued to increase with increasing amounts of acetic acid from 30 to 50 mol%. The increase in molecular weight is responsible for the increase in viscosity. Also, the viscosity of product increases by the intra- and inter-molecular coordination of aluminium, which increases the coordination number of oxygen to aluminium atom as shown in Fig. 4.

Fig. 6 shows the relation between viscosity and $1/T$ for the starting EOPA–BAES and EOPA–BAES–AcOH at a constant shear rate of 1.9 s^{-1}. The logarithm of viscosity has a linear relationship to the temperature, and follows the Andrade (Arrhenius) equation. The activation energies calculated from the log η–$1/T$ slopes are 10.5 (no AcOH), 91.0 (30 mol% AcOH) and 132.0 kJ mol^{-1} (50 mol% AcOH), and increase with increasing amount of acetic acid. The increased activation energy for flow reflects the increase in the chain length and in the interchain interactions of the polymer.[25]

The product formed from EOPA–BAES and glacial acetic acid had a time-independent and stable viscosity. The precursor viscosity can be controlled by the amount of AcOH and the working temperature. The viscosity for EOPA–BAES–30 mol% AcOH decreased in magnitude from 50.2 Pa s (502 poise) to 2.76 Pa s (27.6 poise) on increasing the measurement temperature from 45 to 75 °C. The precursor formed from EOPA–BAES–30 mol% AcOH was extruded through a spinneret into a fibrous shape. The viscosity of the present precursor suitable for extrusion was found to be from several Pa s to 10^2 Pa s in Fig. 6. The working temperature for extrusion was from 30 to 50 °C. The shear thinning behaviour of the precursor enables spinning. Cooling after the extrusion results in the increased viscosity, which also favours spinning.

On the other hand, the viscosity for hand-drawing was ca. 10^2 Pa s^{-1}. The viscosity range for hand-drawing was smaller than that for extrusion.

The dry-spinning of the precursor also results from the complete solubility of the aluminosiloxane in organic solvents. The precursor fibre was drawn from the benzene solution of precursor with the concentration above 80 wt.% at room temperature using a glass rod. The fibre diameter ranged from 10 to 200 μm.

Synthesis of Mullite from Aluminosiloxane Precursor

The aluminosiloxane formed from EOPA–BAES–50 mol% AcOH was heated from room temperature to 500 °C at 1 °C min^{-1} to afford white powders. The weight loss on heating was ca. 73 wt.%.

A halo pattern was observed for the X-ray diffraction of the product formed at 500 °C. The IR spectrum of the product had a broad absorption centred at 1027 cm^{-1}, which is lower than that of ν(Si–O) for amorphous silica at 1100 cm^{-1}. The shift of the absorption band is attributable to the substitution of Si–O–Si bond for Si–O–Al bond as reported.[26] This fact reflects the formation of Si(Al)O$_4$-tetrahedra in the amorphous silica–alumina.

The DTA and TG curves of the amorphous silica–alumina formed by pyrolysis of EOPA–BAES–50 mol% AcOH at 500 °C are shown in Fig. 7. On heating at 10 °C min^{-1}, the amorphous powder lost the physically absorbed water to give the endothermic peak at 162 °C. The second endothermic peak at 462 °C is due to the loss of water by dehydroxylation reaction. Finally, the amorphous powder crystallized exothermically at 980 °C without weight loss.

Fig. 8 shows the change of XRD patterns of the amorphous silica–alumina powder with heat treatment temperature for 1 h. The amorphous silica–alumina began to crystallize to mullite after heat treatment at 950 °C for 1 h, and then increased its crystallinity on increasing heat-treatment temperature.

The crystallinity of amorphous silica–alumina increased at 930 °C as the duration time increased from 1 to 10 h as shown in Fig. 9. The crystallinity of mullite heat-treated at 930 °C for 10 h [Fig. 9(c)] was comparable with that formed at 950 °C for 1 h [Fig. 8(c)]. The mullitization of the amorphous powder was found to proceed at 930 °C.

Several papers have reported the crystallization of mullite directly from the amorphous phase.[12–15] Similarly, Al and Si were mixed at the molecular level in the aluminosiloxane of sufficient degree of condensation yielding mullite directly from amorphous silica–alumina.

Synthesis of Mullite Fibre

The viscosity of aluminosiloxane was controlled by the amount of glacial acetic acid for condensation as shown in a previous section. The polymer fibre spun from the aluminosiloxane formed from EOPA–BAES–50 mol% AcOH was burned out to produce ceramic fibres.

The amorphous silica–alumina fibres with mullite composition were formed at 900 °C for 1 h. The amorphous fibres
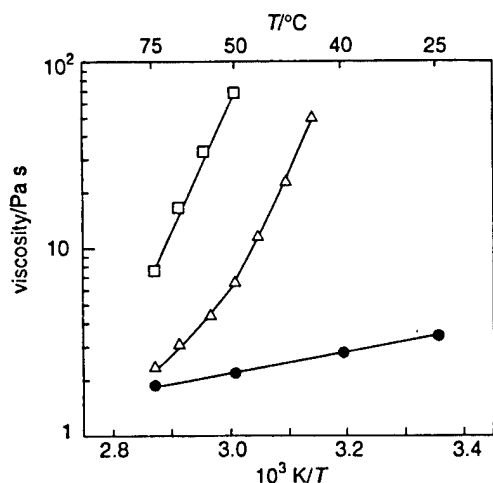
Fig. 6 Variation of viscosity for precursor formed from EOPA–BAES–AcOH with measurement temperatures at a shear rate of 1.9 s^{-1}: ●, starting EOPA–BAES; △, EOPA–BAES–30 mol% AcOH; □, EOPA–BAES–50 mol% AcOH
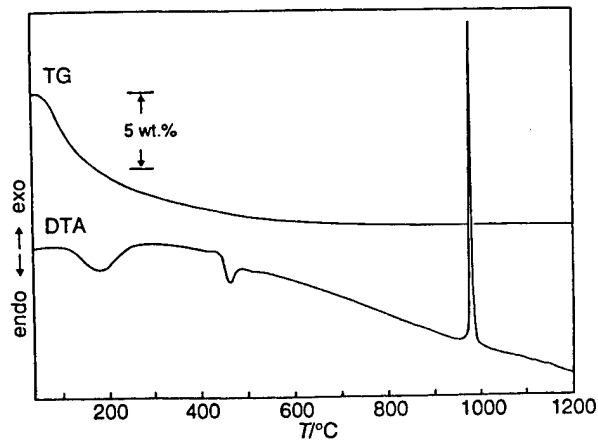
Fig. 7 DTA–TG curves for amorphous silica–alumina formed by pyrolysis of aluminosiloxane at 500 °C
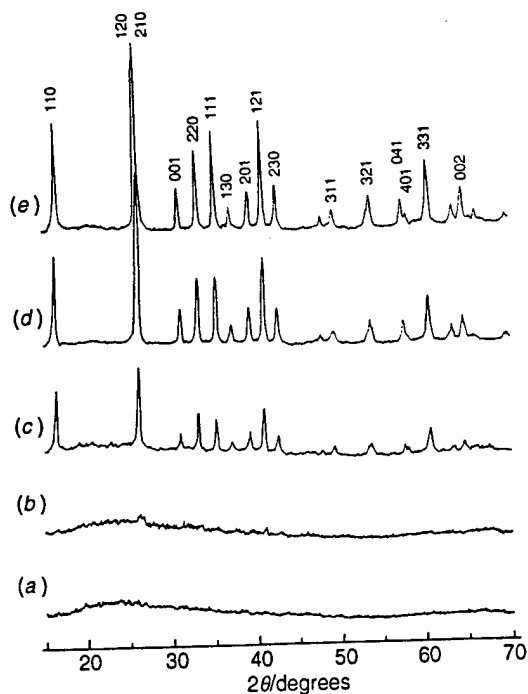
Fig. 8 XRD profiles of pyrolysed products at temperatures from 900 to 1200 °C for 1 h: (a) 900 °C; (b) 930 °C; (c) 950 °C; (d) 1000 °C; (e) 1200 °C
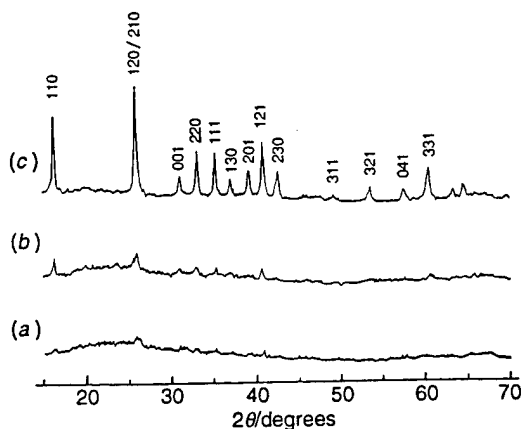
Fig. 9 Change of crystallinity of silica–alumina with duration time at 930 °C: (a) 1 h; (b) 3 h; (c) 10 h

were then heated from 900 to 1200 °C at 1 °C min^{-1} in order to avoid the rapid crystallization shown in Fig. 7. The mullite fibres heat-treated at 1000 °C had smooth surfaces, and diameters from 20 to 100 μm [Fig. 10(a)]. The cross-section of fibre was circular, and was composed of quite smooth surfaces as shown in Fig. 10(b). The fibres were confirmed to be mullite by XRD analysis. The density of mullite fibres thus formed at 1200 °C was from 3.05 to 3.08 (the reported value of the density for mullite is 3.17 g cm^{-3}).[27] The weight percentage of Al_2O_3 in mullite fibres was found to be 71.2 wt.% (theoretical, 71.80 wt.%) by chemical analysis.

Conclusions

Mullite fibre was synthesized successfully from aluminosiloxane precursor without any additives of polymer for the adjustment of viscosity. The results are summarized as follows. (i) A mixture of ethyl 3-oxobutanoatodiisopropoxyaluminium and di-(sec-butoxy)aluminoxytriethoxysilane was reacted with
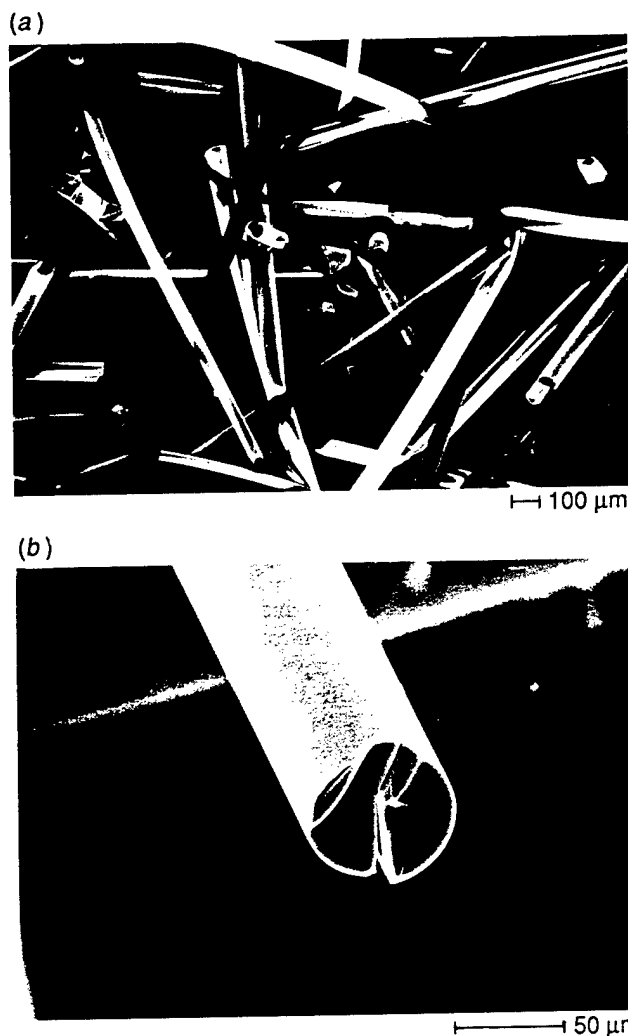
Fig. 10 SEM photographs of mullite fibre synthesized from EOPA–BAES–50 mol% AcOH: (a) 1000 °C, 1 h; (b) fracture surface of mullite fibre crystallized at 1200 °C for 1 h

glacial acetic acid yielding the viscous precursor for mullite fibre. (ii) The polymeric product had a molecular weight below 1000, and contained the increased amount of five-coordinated aluminium, which is responsible for an appropriate viscosity for spinning. The viscoelastic properties required for the spinning resulted from the oligomeric aluminosiloxane with suitable intra- and inter-molecular coordination. (iii) The viscosity of bulk polymer was independent of time, and was controlled by the selection of temperature in order to obtain the appropriate viscosity for spinning. (iv) The preceramic fibre spun from the polymeric precursor was converted to a single-phase mullite fibre after heat treatment at 1200 °C.

References

1 G. Winter, Angew. Chem. Intl. Ed. Engl., 1972, 11, 751.
2 G. Geiger, Am. Ceram. Soc. Bull., 1991, 70, 212.
3 H. G. Sowman, Am. Ceram. Soc. Bull., 1988, 67, 1911.
4 M. J. Morton, J. D. Birchall and J. D. Cassidy, Br. Pat., 1974, 1 360 199.
5 A. Borer and G. P. Krogseng, Ger. Offen., 1972, 2 210 288.
6 S. Horikiri, K. Tsuji, Y. Abe, A. Fukui and E. Ichiki, Ger. Offen., 1974, 2 408 122.
7 K. A. Andrianov, in Metalorganic Polymers, Interscience, New York, 1965, ch. IV.
8 L. V. Interrante and A. G. Williams, Polym. Prep., 1984, 25, 13.
9 A. G. Williams and L. V. Interrante, in Better Ceramics through

Chemistry, ed. C. J. Brinker, D. E. Clark and D. R. Ulrich, Elsevier, Amsterdam, 1984, p. 151.

10 P. D. E. Morgan, in *Better Ceramics through Chemistry II*, ed. C. J. Brinker, D. E. Clark and D. R. Ulrich, Materials Research Society, Pittsburgh, 1986, p. 751.

11 M. D. Sacks, H-W. Lee and J. A. Pask, in *Ceramic Transactions 6*, ed. S. Somiya, R. S. Davis and J. A. Pask, Amer. Ceram. Soc. Inc., Westerville, 1990, p. 167.

12 K. Okada and N. Otsuka, *J. Am. Ceram. Soc.*, 1986, **69**, 652.

13 D. W. Hoffman, R. Roy and S. Komarneni, *J. Am. Ceram. Soc.*, 1984, **67**, 468.

14 J. A. Pask, X. W. Zhang, A. P. Tomsia and B. E. Yoldas, *J. Am. Ceram. Soc.*, 1987, **70**, 704.

15 S. Kanzaki, H. Tabata, T. Kumazawa and S. Ohta, *J. Am. Ceram. Soc.*, 1985, **68**, C6.

16 T. R. Patterson, F. J. Pavlik, A. A. Baldoni and R. J. Frank, *J. Am. Chem. Soc.*, 1959, **81**, 4213.

17 W. L. Jolly, in *The Synthesis and Characterization of Inorganic Compounds*, Prentice-Hall, Englewood Cliffs, N.J., 1970, p. 283.

18 H. Uchida, T. Uchida and C. Iida, *Anal. Chim. Acta*, 1979, **108**, 87.

19 C. G. Barraclough, D. C. Bradley, J. Lewis and I. M. Thomas, *J. Chem. Soc.*, 1961, 2601.

20 E. Breitmaier and W. Voelter, in *Carbon-13 NMR Spectroscopy*, VCH, New York, 1987, pp. 208 and 218.

21 J. W. Akitt, in *Multinuclear NMR*, ed. J. Mason, Plenum Press, New York, 1987, p. 259.

22 O. Kriz, B. Casensky, A. Lycka, J. Fusek and S. Hartmanek, *J. Magn. Reson.*, 1984, **60**, 375.

23 R. Benn, A. Rufinska, H. Lehmkuhl, E. Janssen and C. Kruger, *Angew. Chem. Intl. Ed. Eng.*, 1983, **22**, 779.

24 D. C. Bradley, R. C. Mehrotra and D. P. Gaur, in *Metal Alkoxides*, Academic Press, London, 1978, pp. 33 and 180.

25 L. E. Nielsen, in *Polymer Rheology*, Marcel Dekker, New York, 1977, ch. 3.

26 H. H. W. Moenke, in *The Infrared Spectra of Minerals*, ed. V. C. Farmer, Mineralogical Society, London, 1974, p. 365.

27 JCPDS card, 15-776.

SYNTHESIS AND PROCESSING OF NANOSTRUCTURED CERAMICS

Ilhan A. Aksay, Daniel M. Dabbs, Itaru Homma, Srinivas Manne, David L. Milius, Nobuyoshi Nakagawa, Matt Trau, and Nan Yao

Department of Chemical Engineering and Princeton Materials Institute
Princeton University, Princeton, New Jersey 08544-5263 USA

Over the last two decades, a significant research emphasis has been on the use of colloids to improve the quality of ceramic objects produced with powders. Although major advances have been made, one of the biggest challenges facing us today is developing processing methods to reduce the cost of manufacturing. In most applications, machining and surface finishing costs exceed 50% of the total final cost. Thus, one of the major goals of our research is to improve on the colloidal processing methods to meet this challenge. Similarly, nanostructured composites have been reported to display uniquely different and enhanced properties. But their wide use is hindered due to the lack of reproducible data on their advantages and the difficulty of fabrication. A second major goal of our work is to use tailored colloids to produce ceramic-matrix nanocomposites.

In both activities, we use biological composites as a source of information since many biological materials systems exhibit a combination of properties that is not found in synthetic systems.[1,2] *Biomimetics* is the study of these biological materials, their designs, their functions, and their synthesis methods in order to stimulate new ideas and to develop these ideas into materials systems similar to those found in biological systems. Three lessons from biogenic composites are central to our efforts: (i) Biogenic composites themselves are the building blocks for larger scale composite structures and nested levels of structural hierarchy appears to yield improved properties for particular functions. (ii) In biogenic composites, hierarchical organization always starts on the length scales of 1-100 nm, i.e., nanostructural design is the building block. (iii) Nanostructural design is accomplished through the self-assembly of organics. Inorganic structures are formed as these structurally organized organic surfaces catalytically or epitaxially induce growth of the inorganics. In recent years, various efforts have been made to develop different aspects of this larger goal with emphasis on (i) nanoscale structures through self-assembly; (ii) nanocomposites through molecular recognition and scaffolding; and (iii) pattern development through chemical reactions and with the aid of applied fields. In all, the processes used are akin to those found in biogenic systems. An example of these biogenic materials is the sedimentary diatoms which contain a siliceous skeleton. In the first part of the presentation, we will use this example to illustrate synthesis and processing methods to mimic the hierarchical structural designs observed in biogenic composites through coassembly of organics with inorganics. In addition to these biomimetic methods, we rely on several other methods that offer promise for the development of nanocomposites with the use of tailored powders: (i) exsolution, (ii) reaction sintering, (iii) scaffolding, and (iv) field assisted patterning. In the second part of the presentation, we will focus on exsolution and reaction sintering as two powerful means of producing ceramic/ceramic nanocomposites.

The concept of hierarchy is based upon the observation that macroscopic properties are influenced by phenomena associated across many length scales, and are determined by the

accumulation of "substructural" properties at ever-increasing length scales, starting at the atomic level. For example, the structure of an abalone shell consists of the layering of plates of ceramic (~ 200 nm) oriented in a specific crystallographic direction held together by a much thinner (< 1 nm) "mortar" of organic polymer (Figure 1).[3] Applying a simplified version of this layering to B$_4$C/aluminum composites (Figure 2)[4] resulted in significant increases in the mechanical properties of these composites (Figure 3).[5] We have shown that these composites are strengthened as a result of residual stresses with nanoscale modulations in the interpenetrating network of the ceramic and the metal phases.[6]
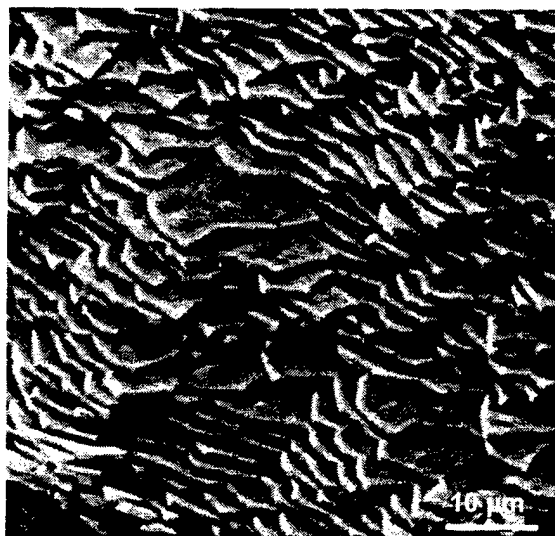
Figure 1. Scanning electron microscope (SEM) image of the fracture surface of red abalone shell (*Haliotis rufescens*) showing multiple tiling of ~200 to 500 nm thick aragonite (CaCO$_3$) crystals. The organic layer between the tiles is < 10 nm thick and is not visible at this magnification.
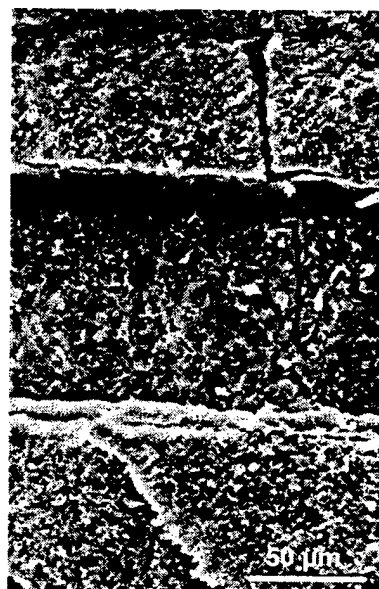
Figure 2. SEM image of a cross-section in a laminated B$_4$C/aluminum composite showing crack arresting at the aluminum layers. The layers of B$_4$C/Al composites are separated by aluminum, resembling the structure of nacre but on a larger scale.

In addition to the ceramic/metal composites, in most recent years our research program has mainly focused on the fundamentals of nanostructural design in a wide spectrum of materials.[7] The primary goal has been to establish unifying guidelines for the manufacture of materials with deliberately introduced nanoscale features and also to understand how such nanoscale modulations affect macroscopic properties. Several methods of controlling nanostructure have been demonstrated (Figure 4): (i) Work on the hydrothermal synthesis of nanosized BaTiO$_3$ below 100°C has resulted in a fundamental understanding of size control in the range from 10 to 200 nm by controlling the population density of the nuclei and their hierarchical clustering characteristics;[8] (ii) The seeding of gels with nanosized colloids resulted in the fabrication of PZT thin films at temperatures as low as 460°C;[9] (iii) Exsolution (or phase partitioning) has been applied to the development of nanocomposite powders of mullite/alumina through low temperature heat treatment of sol/gel precursors;[7] (iv) Reaction sintering has been applied to

alumina/mullite/SiC nanocomposites;[10] and, (v) Coassembly of surfactants with inorganic precursors has been applied to the formation of nanostructured thin films and monoliths.[11]

We first illustrate the potential of self-assembly in the development of ceramic/organic nanocomposites. We will then discuss our work using two unique methods to develop nanostructured ceramic/ceramic composites: (i) exsolution, as applied to the development of mullite/alumina nanocomposites and (ii) reaction sintering which has been applied to formation of SiC/mullite/alumina nanocomposites.
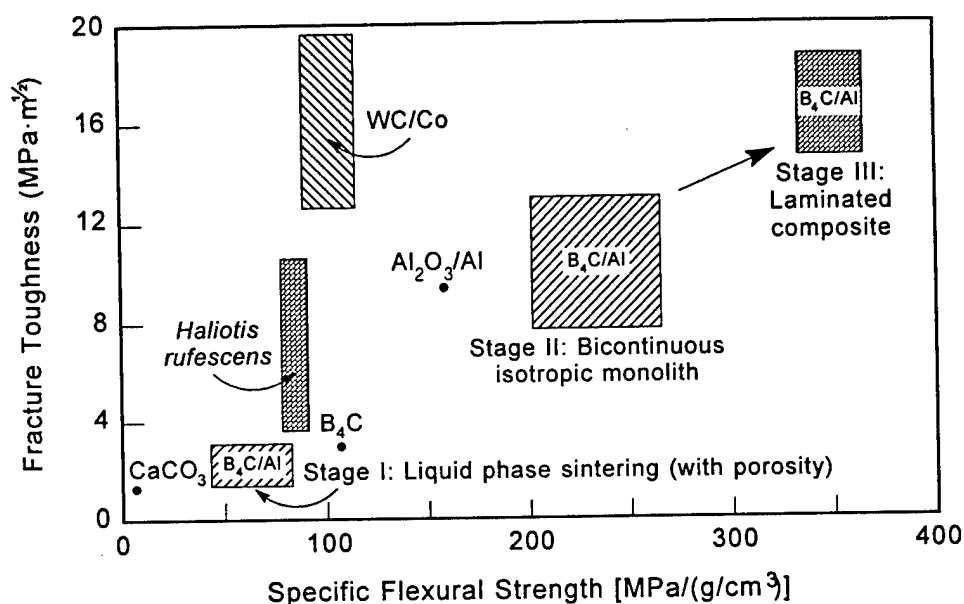
Figure 3. Chart comparing the mechanical properties of different composite systems. Seashell (represented by abalone, *Haliotis rufescens*) is many times stronger than $CaCO_3$. Stage I B_4C/Al composites were formed by liquid phase sintering and retained high porosity. Stage II composites were made by melt infiltrating continuous B_4C matrices to form a bicontinuous ceramic/metal composite. Stage 3 B_4C/Al composites were made by laminating alternating layers of B_4C and aluminum, then heat treating to form the laminate (Figure 2).

Exsolution

Mullite/alumina composites are suitable high temperature (>1000°C) composites due to high thermal resistance under oxidizing atmospheres, high creep resistance, and thermal shock resistance.[12] Although mullite has relatively low fracture toughness and strength at low temperature (2.2 $MPa \cdot m^{1/2}$ and 200-500 MPa, respectively), it retains the greater part of its physical strength up to 1500°C.[12] Our goal is to improve the mechanical properties of mullite through the fabrication of mullite matrix nanocomposites, in which the nanosized inclusions act to strengthen the matrix in a manner akin to precipitation hardening in metals.[13] Our approach is to make nanocomposite powders and monoliths with controlled chemical composition and phase distribution on the nanometer length scale (1-10 nm). We emphasize chemical synthesis because this sets the scale of homogeneity in the precursor and thereby controls the temperature of mullitization and phase evolution in the matrix.[12,14] After forming the precursor powder, two different methods can be used to produce the final nanocomposite monolith: (i) synthesize nanocomposite powders (in which each particle consists of nanometer sized inclusions contained in the matrix phase), then densify and sinter these to form the monolith, or (ii) while maintaining

homogeneity, compact and densify the precursor and either simultaneously or subsequently precipitate the included phase. In the first path, exsolution occurs within the homogeneous precursor prior to sintering; in the second, exsolution is induced after compaction and during heat treatment.
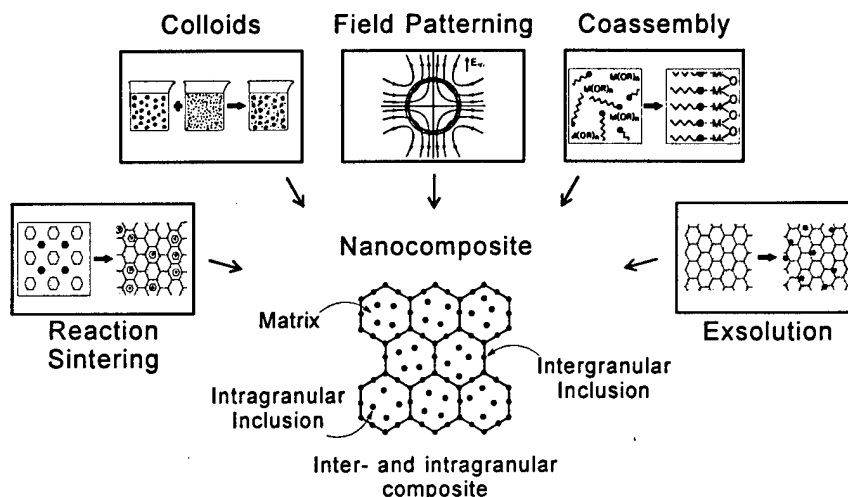
Figure 4. Methods of nanocomposite processing. Reaction sintering, coassembly, colloids, field patterning, and exsolution have been used within our work on the forming of nanocomposites.

The low temperature chemical synthesis approach provides an effective means for maintaining chemical homogeneity and purity in precursor materials through solution chemistry. Using powders containing the matrix and included phases (although the original composition may be chemically homogeneous) avoids conventional milling processes. This improves the overall composition by avoiding contamination. The shortcomings of these systems include sinterability and the inability to effectively control particle size. Due to its highly covalent character as reflected in its high creep resistance, mullite does not sinter well. This could be circumvented by one of two techniques, one using viscous phase formation, the other sintering nanosized powders. We have used viscous phase deformation to sinter mullite to high density in previous work[15] and have chosen to emphasize this method when forming high density monoliths. Sintering nanosized particles would depend less on the bulk properties of the matrix due to the high surface/volume ratio of nanometer diameter particles but the inability to effectively control particle size and size distribution limits in these precursors limits application to patterning techniques such as electrophoretic deposition. Chemical vapor deposition (CVD) has been used to fabricate spherical mullite particles of high purity[16] and could be used to fabricate spherical particles for building layered mullite nanostructures.

In our past work, three methods have been developed to control the scale of homogeneity within the precursors: (i) molecular mixing (scale of homogeneity < 1 nm) can be achieved through the simultaneous hydrolysis and condensation of monomers to form polymeric precursors;[17,18] (ii) sol-gels (scale of homogeneity 5 to 50 nm) are systems that are well understood and can be used to synthesize precursor powders with well-dispersed heterogeneities and good sinterability;[15,19] and (iii) spray pyrolysis (scale of homogeneity < 10 nm) which maintains chemical homogeneity in powders formed from solution.[15,20]

We have recently demonstrated the formation of a nanocomposite powder from spray pyrolyzed precursors (Figure 5).[21] The precursor is formed from a solution of TEOS and

aluminum nitrate nonahydrate in ethanol, mixed in proportions equivalent to the stoichiometry of a mullite/alumina composite containing 20 wt% alumina in a mullite matrix. The solution is sprayed onto a hot surface, resulting in immediate pyrolysis of the solvent and functional groups and forming puffy white agglomerates. The agglomerates are ground and heat treated to form an alumina/mullite composite powder. The high chemical homogeneity of the precursor powder is indicated by the low temperature of conversion to mullite (< 1000°C).[22,23] Powder heat treated at 1500°C for one hour is found to be composed of nanometer size inclusions of 3:2 mullite ($3Al_2O_3 \cdot 2SiO_2$) and alumina dispersed within a 2:1 mullite ($2Al_2O_3 \cdot SiO_2$) matrix. It is unlikely that this is a stable phase composition (as alumina precipitates from the matrix, the 2:1 mullite will convert to 3:2) but with these results, we have demonstrated the proof of concept that a low temperature reaction pathway can be used to achieve exsolution in a matrix, without using a high temperature melt.

Although we have shown that it is possible to produce a nanocomposite using low temperature exsolution, several important issues remain. First is the high temperature stability of these composites. As noted, we do not expect a 3:2/2:1 mullite/mullite matrix to remain stable. However, the decay of the 2:1 mullite to form 3:2 should result in the precipitation of the alumina. As seen in Figure 5, the alumina phase appears to be growing as fingers into the mullite matrix.
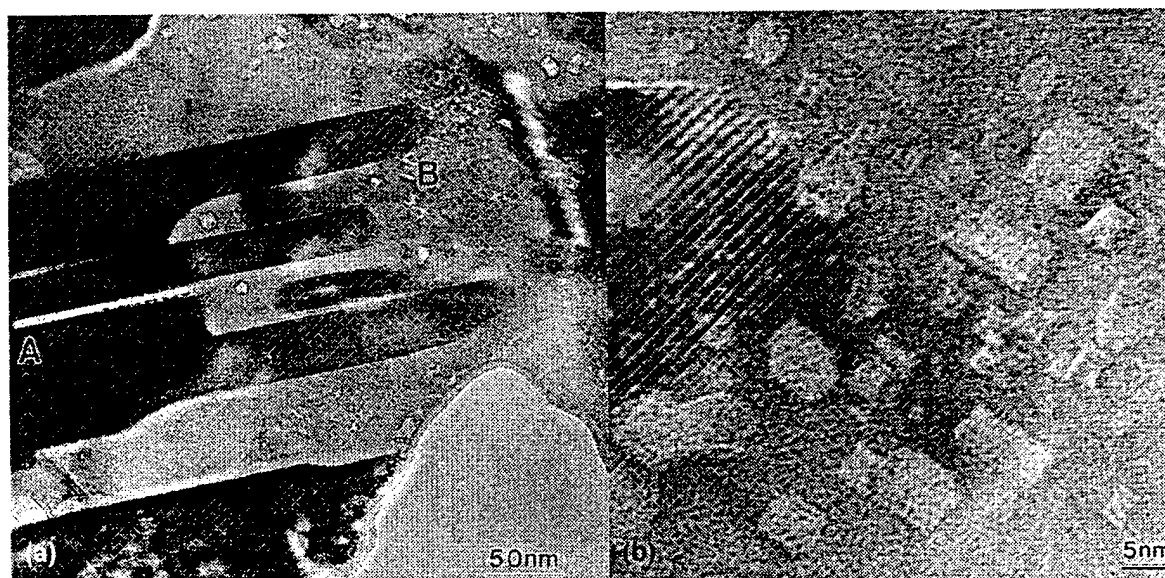
Figure 5. HRTEM micrographs of alumina/mullite nanocomposite powder formed by exsolution of alumina from a mullite matrix. (a) Region A consists of alumina (dark phase) containing mullite fingers (light phase). Region B consists of a 2:1 mullite matrix containing small dispersoids of 3:2 mullite. (b) A magnification of region B, more clearly showing the 3:2 inclusions in the 2:1 matrix. Alumina appears to be growing from the left edge of the micrograph.

Reaction Sintering

The goal of this study is to gain an understanding of how the enhanced mechanical properties of SiC/mullite/alumina nanocomposites are affected by the size of SiC dispersoids within mullite/alumina matrix. We have previously demonstrated that these nanocomposites can

be produced through a reaction sintering process (Figure 6).[10,24,25] First, a green compact of SiC and alumina is synthesized using colloidal dispersion and consolidation. To reduce the SiC particles to nanometer size the samples are then oxidized at 1300°C in air and reaction sintered at 1600°C in argon. Samples containing SiC, mullite, and alumina are synthesized using varying times of oxidation to produce different particle sizes in the composite. For an oxidation time of 5 hours and a sintering time of 2 hours, coherent interfaces have been observed using transmission electron microscopy (TEM) (Figure 7).[25]
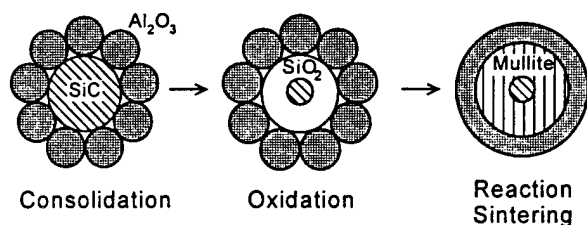
Figure 6. A schematic diagram of steps leading to the forming of SiC/mullite/alumina composites by reaction sintering.

Niihara and coworkers have reported fracture strengths of 1.6 GPa for nano sized SiC dispersed in a silicon nitride matrix.[26] This accomplishment has been brought into question by researchers at Lehigh University who explained the increase in mechanical properties as a result of sample preparation.[27] They concluded that the observed strengthening effect was induced by compressive stress cause by machining. But since the Lehigh samples contained inclusions measuring 0.15 µm in size, it is questionable that their composites can reasonably be defined as true nanocomposites. One of our tasks in this thrust area is to ascertain the true nature of the size effect for nanosized inclusions in a matrix phase. A possible mechanism for strengthening a matrix with nanosize inclusions is that the interface between the matrix and the inclusion is coherent as a result of the small size of the inclusions.

Enhanced hardness caused by small second-phase precipitates (precipitation hardening) has been well documented in metallurgy.[13] It is known that the hardness will be enhanced if the precipitates are small (<20-30 nm) and that the hardness decreases as the precipitates coarsen.[13]

Figure 7. (a) A bright field image of a SiC particle (A) surrounded by amorphous silica (B) within an alumina matrix (C).[25] (b) HRTEM micrograph of a nanosized SiC particle in a mullite. The interfaces between the mullite and the SiC particle are coherent (visible around the upper right edge of the particle).

The increase in the hardness by small precipitates is attributed to coherence at the interface.[13] A coherent interface is an energetic barrier for dislocation movement, enhancing the hardness of the material. But coherence has a size limit; beyond the critical radius the elastic energy arising from coherency dominates the reduction in the coherent interfacial energy and the interface becomes incoherent.[13] Incoherent interfaces at the surfaces of large inclusions facilitate slip plains thereby reducing the hardness of the material.

Dislocation movement can only account for the creep behavior at high temperatures for both metals and ceramics and the low-temperature yield behavior for metals. For ceramics at low temperatures, dislocation movement is largely prohibited due to the strong covalent or ionic bonding between atoms. Strengthening by coherent interfaces between small silicon carbide or silicon nitride inclusions and an oxide matrix at low temperatures can arise as follows: Carbides and nitrides often have smaller interatomic spacing than oxides. Therefore, a coherent interface between a carbide or nitride inclusion and the oxide matrix would impose compression in the oxide matrix and expansion in the carbide or nitride inclusion. It is well known that compression in ceramics increases the fracture strength of the ceramics. Thus, compression in the continuous oxide matrix imposed by the coherent interface may account for the increase in the fracture strength of ceramic composites containing small inclusions. The compressive stress is generally referred to as residual stress. Our current work indicates that mullite formation begins at 1350°C at the alumina/silica interface formed during the oxidation of the SiC particles (Figure 7).[25] We have found that both the SiC/mullite and the mullite alumina interface are coherent interfaces. Further, by examining the peak shifts in SiC using X-ray diffraction, we have measured ~1.75 GPa of residual stress in the SiC phase.

3. REFERENCES

1. *Hierarchical Structures in Biology as a Guide for New Materials Technology*, National Research Council, NMAB-464 (National Academy Press, Washington, D.C., 1994).

2. *Biomimetics: Design and Processing of Materials*, M. Sarikaya and I. A. Aksay (eds.) (AIP Press, Woodbury, NY, 1995).

3. M. Sarikaya and I. A. Aksay, "Nacre of Abalone Shell: A Natural Multifunctional Nanolaminated Ceramic-Polymer Composite Material," Chpt. 1 in *Structure, Cellular Synthesis and Assembly of Biopolymers*, S. T. Case, ed. pp. 1-25 (Springer-Verlag, New York, 1992).

4. D. C. Halverson, A. J. Pyzik, and I. A. Aksay, "Boron-Carbide-Aluminum and Boron-Carbide-Reactive Metal Cermets," U.S. Patent #4,605,440 (August 12, 1986); A. J. Pyzik and I. A. Aksay, "Multipurpose Boron Carbide-Aluminum Composite and Its Manufacture via the Control of the Microstructure," U.S. Patent #4,702,770 (October 27, 1987); I. A. Aksay, M. Yasrebi, D. L. Milius, G.-H. Kim, and M. Sarikaya, "Laminated B_4C/Al Composites through Melt Infiltration," U.S. Patent #5,308,422 (1994).

5. M. Yasrebi, G. H. Kim, K. E. Gunnison, D. L. Milius, M. Sarikaya, and I. A. Aksay, "Biomimetic Processing of Ceramics and Ceramic-Metal Composites," in *Better Ceramics through Chemistry IV*, MRS Symp. Proc., Vol. 180, edited by B. J. J. Zelinski, C. J.

Brinker, D. E. Clark, and D. R. Ulrich (Materials Research Society, Pittsburgh, Pennsylvania, 1990), pp. 625-35.

6. G. H. Kim, M. Sarikaya, D. L. Milius, and I. A. Aksay, "Microstructural and Fractographic Characterization of B_4C-Al Cermets Tested Under Dynamic and Static Loading," *Proc. 47th Ann. Meeting EMSA*, G. W. Bailey, ed., 562-63 (San Francisco Press, San Francisco, 1989).

7. I. A. Aksay, *Nanodesigning of Hierarchical Multifunctional Ceramics*, annual report, Air Force Office of Scientific Research, grant number AFOSR-F49620-93-1-0259 (Princeton University, September 15, 1995).

8. C. M. Chun, A. Navrotsky, and I. A. Aksay, "Aggregation Growth of Nanometer-Sized $BaTiO_3$ Particles," in *Proc. 53rd Ann. Mtg. MSA,* G. W. Bailey and A. J. Garratt-Reed, eds. (Microscopy Society of America, 1995).

9. W. D. Clifton and I. A. Aksay, "Modifying Sol-Gel Lead-Zirconate-Titanate Thin Films to Reduce the Crystallization Temperature," American Ceramic Society, 44th Pacific Coast Regional Meeting (San Diego, CA, October 31-November 2, 1991); W. D. Clifton, M.S. Thesis (1993).

10. Y. Sakka and I. A. Aksay, "Processing of Nanocomposite Silicon Nitride-Mullite-Alumina by Reaction Sintering," *NanoStructured Materials* **4** [2] 169-82 (1994).

11. U. Srinivasan, I. Homma, C. M. Chun, D. M. Dabbs, D. A. Hajduk, S. M. Gruner, and I. A. Aksay, "Nanocomposite Processing via Infiltration of Mesoporous Silica," in *Proc. 53rd Ann. Mtg. MSA,* eds.: G. W. Bailey and A. J. Garratt-Reed, (Microscopy Society of America, 1995).

12. I. A. Aksay, D. M. Dabbs, and M. Sarikaya, "Mullite for Structural, Electronic, and Optical Applications," *J. Am. Cer. Soc.*, **74** [10] 2343-58 (1991).

13. For example, see P. Haasen, *Physical Metallurgy*, Chpt. 14 and the references therein (Cambridge University Press, Cambridge, 1986).

14. S. Sundaresan and I. A. Aksay, "Mullitization of Diphasic Aluminosilicate Gels," *J. Am. Cer. Soc.*, **74** [10] 2388-92 (1991).

15. N. Shinohara, D. M. Dabbs, and I. A. Aksay, "Infrared Transparent Mullite through Densification of Monolithic Gels at 1250°C," *Infrared and Optical Transmitting Materials*, R. W. Schwartz, ed., Proc. SPIE **683**, 12-18 (1986).

16. S. Hori and R. Kurita, "Characterization and Sintering of Al_2O_3–SiO_2 Powders Formed by Chemical Vapor Deposition," *Mullite and Mullite Matrix Composites*, Ceramic Transactions **6** 311-22; S. Somiya, R. F. Davis, and J. A. Pask, eds. (American Ceramic Society, Westerville, OH 1990).

17. D. M. Dabbs, J. J. Lannutti, D. R. Treadwell, and I. A. Aksay, "Evolution of Mullite from Inorganic Polymers," in preparation (1995).

18. J. J. Lannutti, *Doctoral Dissertation* (University of Washington, Seattle WA, 1990).

19. C. J. Brinker and G. W. Scherer, *Sol-Gel Science: The Physics and Chemistry of Sol-Gel Processing* (Academic Press, Inc., New York 1990).

20. T. Kumazawa and S. Ohta, "Influence of Powder Characteristics on Microstructure and Mechanical Properties of Mullite Ceramics," *Mullite and Mullite Matrix Composites*, Ceramic Transactions **6** 401-11; S. Somiya, R. F. Davis, and J. A. Pask, eds. (American Ceramic Society, Westerville, OH 1990).

21. D. M. Dabbs, D. M. Shahid, and I. A. Aksay, "The Processing of Nanocomposite Powders Through Solution Chemistry," **97**th Annual Meeting, American Ceramic Society, (Cincinnati, Ohio, April 30-May 3, 1995).

22. K. Okada and N. Otsuka, "Changes in Chemical Composition of Mullite Formed from $2SiO_2 \cdot 3Al_2O_3$ Xerogel During the Formation Process," *J. Am. Cer. Soc.* **70** [10] (1987).

23. C. Gerardin, S. Sundaresan, J. Benziger, and A. Navrotsky, "Structural Investigation and Energetics of Mullite Formation from Sol-Gel Precursors," *Chem. Mater.* **6** [2] 160 (1994).

24. Y. Sakka, D. B. Bidinger, and I. A. Aksay, "Processing of Silicon Carbide-Mullite-Alumina Nanocomposites," *J. Ceram. Soc.* **78** [2] 479-86 1995.

25. C. Sousa, "Mechanism of Mullite Formation in SiC-Mullite-Al_2O_3 Nanocomposites," Senior Thesis (Princeton University, 1995).

26. K. Niihara, "New Design Concepts of Structural Ceramic-Ceramic Nanocomposites," *J. Ceram. Soc. Jpn.,* **99** [10] 974-82 (1991).

27. J. Zhao, L. C. Stearns, M. P. Harmer, H. M. Chan, G. A. Miller, and R. F. Cook, "Mechanical Behavior of Alumina-Silicon Carbide 'Nanocomposites'," *J. Am. Ceram. Soc.* **76** [2] 503-10 (1993).

AGGREGATION GROWTH OF NANOMETER-SIZED BaTiO₃ PARTICLES

C. M. Chun,[†*] A. Navrotsky[†*], and I. A. Aksay[#*]

†Department of Geological and Geophysical Sciences, #Department of Chemical Engineering, and
*Princeton Materials Institute, Princeton University, Princeton, New Jersey 08544-5211

Nanocrystalline BaTiO₃ particles are synthesized under hydrothermal conditions by the reaction of nano-sized TiO_2 colloids with aqueous solutions of $Ba(OH)_2$ at 80°C.[1] A dissolution-precipitation mechanism is proposed for the formation of BaTiO₃ by this route, because suspended TiO_2 nano-particles dissolve into $Ba(OH)_2$ solution, supersaturate the solution phase, and subsequently precipitate BaTiO₃ particles.[2] The origin of the rough "raspberry-like" BaTiO₃ particles during growth stages can be explained by one of two mechanisms: (i) the morphological instability at the growth front during continuous growth, or (ii) aggregation of colloidal particles by multiple clustering. Our TEM studies on samples prepared by controlled seeding experiments show that a multiplicity of low or high angle grain boundaries occur during growth, supporting the aggregation growth.

In order to separate the nucleation step from the growth step more efficiently, seed BaTiO₃ particles were prepared by adding TiO_2 colloids (Degussa, P-25) to 2.23 M $Ba(OH)_2$ solution and hydrothermally reacting at 80°C under atmospheric pressure for 48 hours in polyethylene bottles. The resulting seed particles were recovered by centrifugation, rinsed with CO_2-free deionized water and freeze-dried. Final particles were prepared by adding these seeds (50 nm) into a supernatant prepared after a 1 hour reaction of TiO_2 in 1 M $Ba(OH)_2$ solution at 80°C and aged for 30 min and 48 hours at 80°C.

At the early stages of growth of the seeds, primary BaTiO₃ nuclei of 5~10 nm in size were observed on the surface of seed particles (Fig. 1(a)). In contrast, at the final stage of growth of seeds, the size of BaTiO₃ seeds increased to 120 nm and the morphology was more or less spherical (Fig. 1(b)). HREM images corresponding to the early stages of growth show low angle tilt boundaries (Fig. 2), misfit orientation, and kink in lattice fringes (Fig. 3). Because randomly oriented primary nuclei are attached to the seeds, there is a misfit at the interface equivalent to the insertion of a row of dislocations. The angle of misfit is small and the boundary consists of regions of perfect fit and regions of misfit which result in the formation of dislocations. For a seed with relatively many primary nuclei, crystal lattices are completely matched (Fig. 4) suggesting that initially misaligned primary nuclei are rapidly restructured to form a single crystallite with the same crystallographic orientation. These observations then strongly support the growth mechanism where the primary particles first homogeneously nucleate within the solution and then aggregate with the seed particles. Homogeneous nucleation appears to be favored due to relatively high saturation levels used in our experiments. These observations also illustrate that unless the interfaces are examined at the early stages of clustering, "raspberry-like" morphologies do not provide sufficient information on the exact growth mechanism.

References:

1. W. Hertl, *J. Am. Ceram. Soc.*, 71(1988)879.
2. R. J. Pugh and L. Bergstrom, Eds., *Surface and colloid chemistry in advanced ceramic processing*, Marcel Dekker (1994)29-69.
3. This work made use of MRSEC Shared Facilities supported by the NSF under Award Number DMR-940032 and was supported by a grant from the U. S. Air Force Office of Scientific Research AFOSR-F49620-93-1-0259.
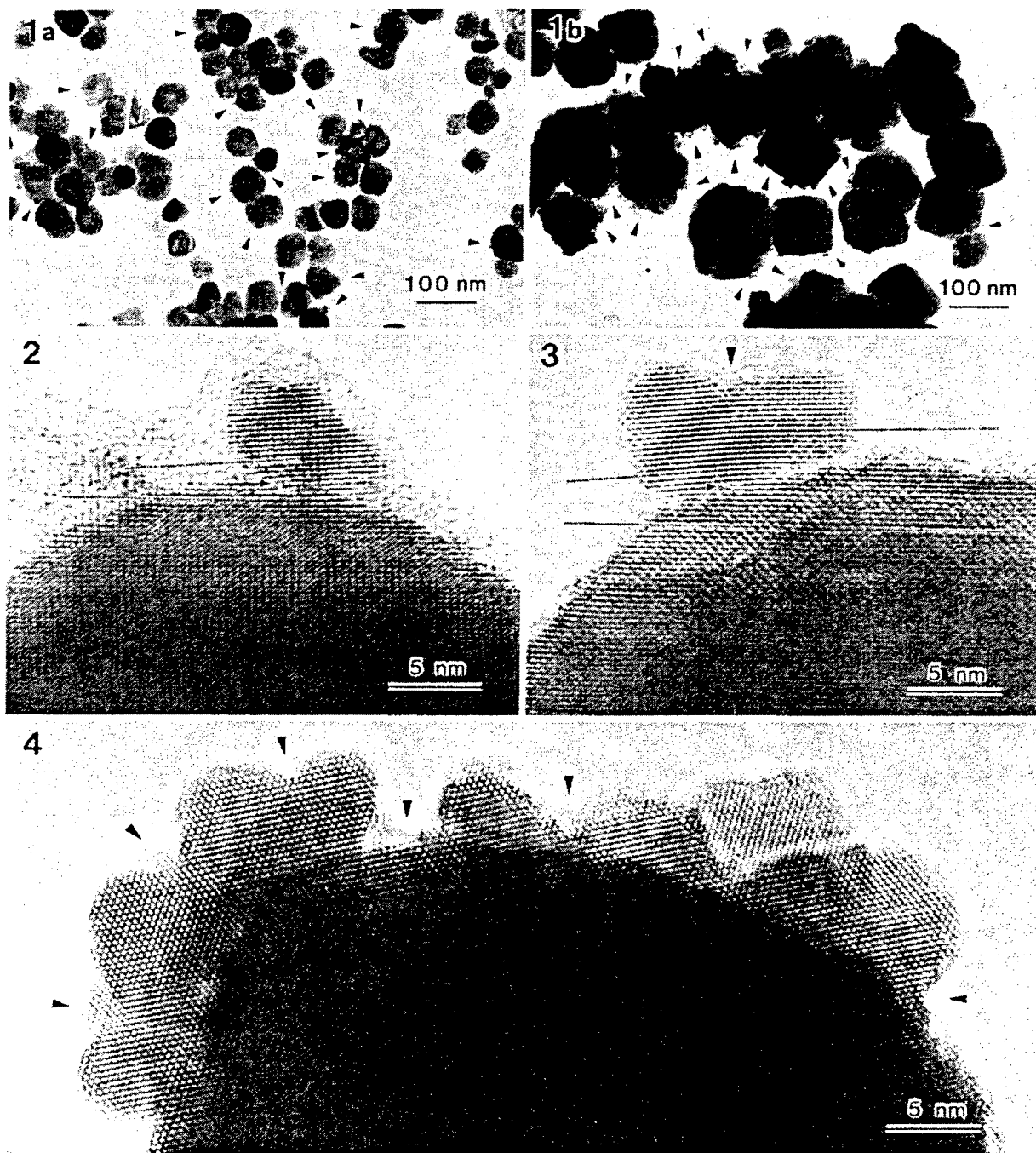
FIG. 1.—TEM images of BaTiO$_3$ particles processed by adding BaTiO$_3$ seeds into a supernatant and aged at 80°C (a) for 30 min, the early stage of growth (b) for 48 hours, the final stage of growth.

FIG. 2.—HREM image of BaTiO$_3$ particles corresponding to the early stage of growth, showing low angle tilt boundary between a primary BaTiO$_3$ nuclei and a seed

FIG. 3.—HREM image of BaTiO$_3$ particles corresponding to the early stage of growth, showing both misfit orientation between primary BaTiO$_3$ nuclei and a seed and kink in lattice fringes between two neighboring nuclei.

FIG. 4.—HREM image of BaTiO$_3$ particles for a seed with relatively many primary nuclei.

AMORPHOUS SILICA COATING ON α-ALUMINA PARTICLES

J. W. Mellowes,[#*] C. M. Chun,[‡*] and I. A. Aksay[#*]

Departments of [#]Chemical Engineering and [‡]Geological and Geophysical Sciences; and
*Princeton Materials Institute, Princeton University, Princeton, New Jersey 08544-5211

Mullite ($3Al_2O_3 \cdot 2SiO_2$) can be fabricated by transient viscous sintering using composite particles which consist of inner cores of α-alumina and outer coatings of amorphous silica.[1,2] Powder compacts prepared with these particles are sintered to almost full density at relatively low temperatures (~1300°C) and converted to dense, fine-grained mullite at higher temperatures (>1500°C) by reaction between the alumina core and the silica coating. In order to achieve complete mullitization, optimal conditions for coating alumina particles with amorphous silica must be achieved. Formation of amorphous silica can occur in solution (homogeneous nucleation) or on the surface of alumina (heterogeneous nucleation) depending on the degree of supersaturation of the solvent in which the particles are immersed. Successful coating of silica on alumina occurs when heterogeneous nucleation is promoted and homogeneous nucleation is suppressed.[3] Therefore, one key to successful coating is an understanding of the factors such as pH and concentration that control silica nucleation in aqueous solutions. In the current work, we use TEM to determine the optimal conditions of this processing.

Silica coated alumina particles were prepared by dispersing α-alumina (AKP-30, Sumitomo Chemical) in 60 ml of ethanol and adding tetraethoxysilane (TEOS). After mixing with a magnetic stir bar for 1 hour, silica is precipitated onto the alumina particles by adding 30 ml ammoniated water. Finally, the suspension of coated particles is filtered after 24 hours of stirring and the particles are dried. TEM images (Figs. 3 and 4) indicate that α-alumina core particles are coated with amorphous silica. From the thickness of a coating and by knowing the surface area of the powder and density of amorphous silica, the mass of the coating is calculated. When the mass of the coating is compared to the amount of TEOS used initially, it is possible to determine whether homogeneous or heterogeneous nucleation is occurring within the solution.

The nucleation of amorphous silica is dependent on both pH and concentration of TEOS. Keeping the concentration of TEOS constant, the effects of altering the pH of the ammoniated water were investigated (Fig. 1). At pH < 10, no coatings were present. With increasing pH, the thickness and fraction of coating increased. At pH > 11, particles were completely coated without silica precipitation out of solution. Because the solubility of silica in water increases at higher pH, coatings without precipitation were promoted. Holding the pH of the ammoniated water constant at 11.5, the effects of changing the concentrations of TEOS added were investigated (Fig. 2). At low concentrations, all the TEOS added coated the alumina and therefore the coating thickness was directly related to the amount added. At higher concentrations, the thickness of the coating decreased. In these situations, the degree of supersaturation was high, thus forming many nucleation sites within the solution, making homogeneous nucleation the favored mechanism. This study illustrates the crucial role of optimization within the pH and concentration regime in order to promote silica coating without any homogeneous nucleation.[4]

References:

1. M. D. Sacks *et al.*, *J. Am. Ceram. Soc.*, **74**(1991)2428.
2. I. A. Aksay *et al.*, *J. Am. Ceram. Soc.*, **74**(1991)2343.
3. B. C. Bunker *et al.*, *Science*, **264**(1994)48.
4. This work was supported by a grant from the U. S. Air Force Office of Scientific Research AFOSR-F49620-93-1-0259 and made use of MRSEC Shared Facilities supported by the NSF under Award Number DMR-940032.
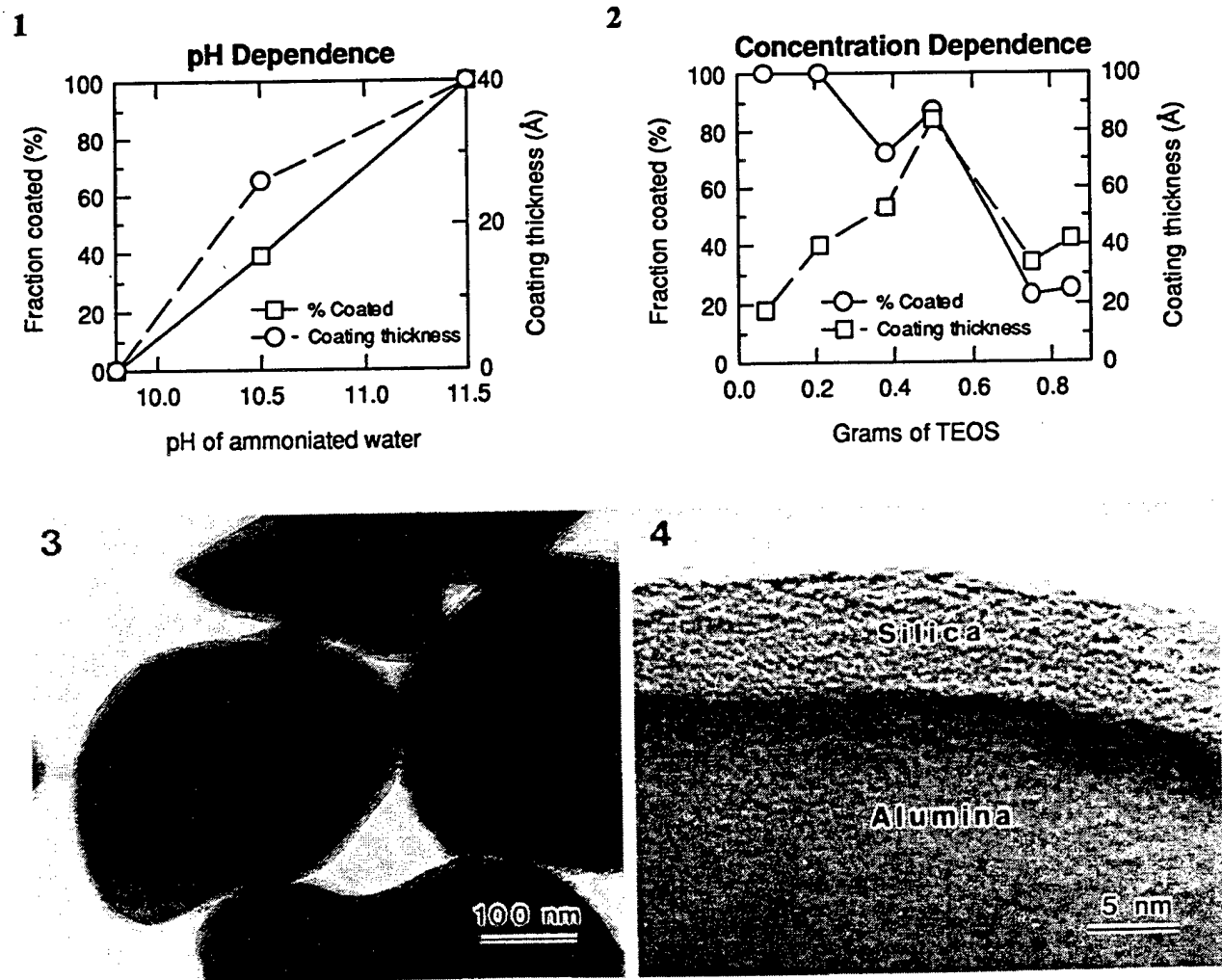
FIG.1.—Coating thickness and coating fraction (mass of silica coating/total silica used in experiment) of composite particles vs. pH of ammoniated water at constant TEOS concentration.

FIG.2.—Coating thickness and coating fraction of composite particles vs. various TEOS concentrations at constant pH of 11.5.

FIG.3.—TEM image of α-alumina core particles coated with amorphous silica.

FIG.4.—HREM image of interface between α-alumina and amorphous silica.

journal

Processing of Silicon Carbide–Mullite–Alumina Nanocomposites

Yoshio Sakka*

National Research Institute for Metals, 2-1, Sengen-1, Tsukuba, Ibaraki 305, Japan

Donald D. Bidinger* and Ilhan A. Aksay*

Department of Chemical Engineering and Princeton Materials Institute, Princeton University,
Princeton, New Jersey 08544-5263

Nanocomposite materials in the form of nanometer-sized second-phase particles dispersed in a ceramic matrix have been shown to display enhanced mechanical properties. In spite of this potential, processing methodologies to produce these nanocomposites are not well established. In this paper, we describe a new method for processing SiC–mullite–Al_2O_3 nanocomposites by the reaction sintering of green compacts prepared by colloidal consolidation of a mixture of SiC and Al_2O_3 powders. In this method, the surface of the SiC particles was first oxidized to produce silicon oxide and to reduce the core of the SiC particles to nanometer size. Next, the surface silicon oxide was reacted with alumina to produce mullite. This process results in particles with two kinds of morphologies: nanometer-sized SiC particles that are distributed in the mullite phase and mullite whiskers in the SiC phase. Both particle types are immersed in an Al_2O_3 matrix.

I. Introduction

CERAMIC-MATRIX nanocomposites have been receiving increasing attention largely due to their significantly enhanced mechanical properties, low-temperature densification, machinability, and superplastic behavior.[1-3] For instance, in the pioneering studies of Niihara and his colleagues, fracture strengths as high as 1.5 GPa and toughnesses as high as 7.5 MPa·m$^{1/2}$ have been reported in systems where nanometer-sized SiC was dispersed in Al_2O_3, MgO, Si_3N_4, and mullite matrices.[3,4] Niihara classified nanocomposites into two general categories.[3] One category consists of composites of only nanometer-sized grains. The other consists of composites where nanosized particles are distributed within the intra- and/or intergrain regions of micrometer-sized grains. The main advantage in using nanocomposites of the first category is that they can be shaped by superplastic deformation, whereas the main advantage of the nanocomposites of the second category is their enhanced high-temperature stability against grain coarsening. In this paper, we deal with the processing of the second type of nanocomposite with a novel reaction sintering method.

Nanocomposites produced by Niihara's group have been formed mainly by using composite powders mixed on the nanometer scale by conventional milling of micrometer-sized powders. Although the mechanisms of size reduction to nanometer scale and the entrapment of particles within each other are not clearly understood, this conventional milling approach has certainly been effective in processing nanocomposites with unique properties despite the fact that milling of powders generally results in contamination or reproducibility problems. Alternatively, chemical vapor deposition (CVD) has also been successfully used to process similar nanocomposites.[3] However, as stated by Niihara,[3] the use of CVD to fabricate large and complex-shape components is not suitable for mass production.

We propose the use of reaction sintering as a more economical and reliable method for producing nanocomposites. In this study, we chose the SiC–mullite–Al_2O_3 system because it has been shown that SiC–mullite, SiC–Al_2O_3, and mullite–SiC systems have excellent mechanical properties.[3-6] Our procedure consists of the three steps shown in Fig. 1.[7] First, we consolidated micrometer-sized SiC and Al_2O_3 powders homogeneously through colloidal consolidation (slip casting), which is known to be an excellent processing route for improved mechanical behavior.[8,9] Second, partial oxidation treatment was conducted to oxidize the surface of the SiC particles to SiO_2 and thus to reduce the size of the SiC particles to nanometer size. Finally, we reacted the surface oxide and Al_2O_3 to produce mullite. As we illustrate in the following sections, the advantages of this method are that (1) the reduction of the inclusion phase to nanoscale can be achieved without milling and (2) because of a volume increase during reaction sintering, the sintering shrinkage is low.

II. Experimental Procedure

The α-Al_2O_3 powder used in this study was Sumitomo Chemical's (AKP-50) high-purity alumina (≥99.995%) with a mean particle diameter of 0.21 μm and a specific surface area of 9.5 m^2/g. Two types of β-SiC powders were used: Superior Graphite's HSC059 containing C (0.85 wt%), Si (0.03), N (0.21), and O (0.80) as major impurities, and Mitsui Toatsu's MSC-20 containing SiO_2 (0.11 wt%) as a major impurity. Figure 2 shows TEM photographs of the two powders. Superior Graphite's powder is relatively coarse (indicated as SiC(C)) with a wide particle size distribution, a mean particle diameter of 0.56 μm, and a specific surface area of 15.0 m^2/g. Mitsui Toatsu's powder is finer (indicated as SiC(F)) with a narrow particle size distribution, a mean particle diameter of 0.15 μm, and a specific surface area of 21.3 m^2/g.
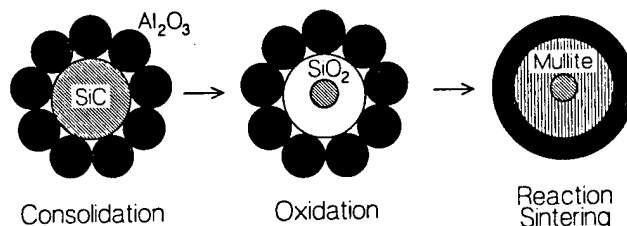
Fig. 1. Schematic illustration of the process steps used to produce nanocomposites by reaction sintering.
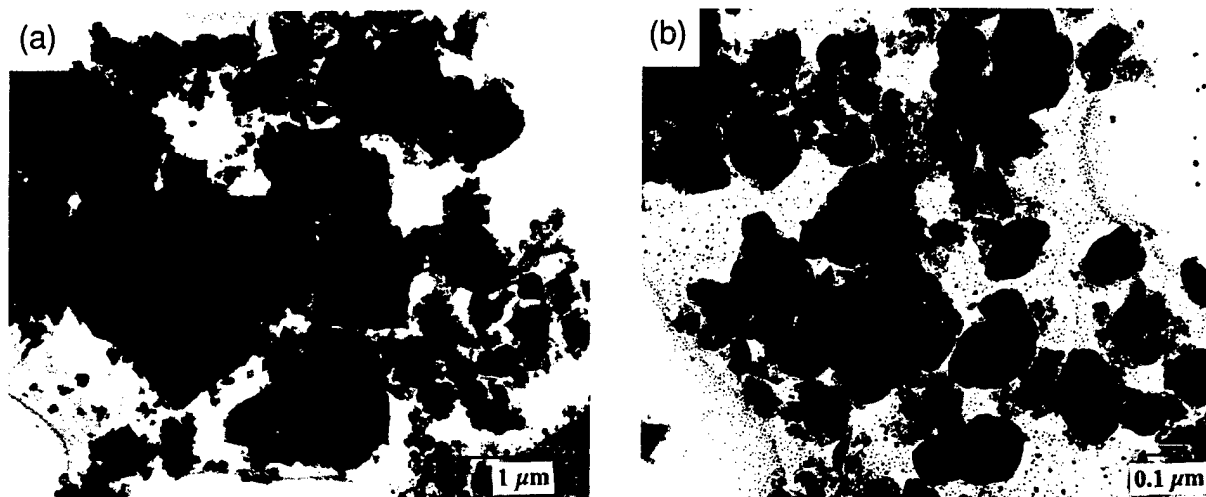
Fig. 2.   TEM photographs of (a) SiC(C) and (b) SiC(F) powders.

The zeta potential of the two SiC powders in suspension was obtained by the Smoluchowski equation[10] from the electrophoretic mobility (Otsuka Electronics ELS-800 and Bel Japan Zetasizer 4) determined on diluted suspensions containing $0.01M$ NaCl (or $0.01M$ KCl) to control ionic strength. The pH was adjusted using NaOH (or KOH) and HCl.

Stable colloidal suspensions with a solid content of 45 vol% were prepared electrosterically in distilled water with an NH_4 salt of poly(methacrylic acid) (PMAA, Darvan C) at pH 10 as described in the next section. NH_4OH was used to adjust the pH. After ultrasonic vibration (Sonic Materials Vibracell 600W Unit, Danbury, CT) was applied for 10 min to facilitate the dispersion of the powder agglomerates, the suspension was stirred using a magnetic stirrer for over 12 h at room temperature. Degassing of the suspension was achieved in a bell jar connected to a vacuum pump. A colloidal consolidation technique employing a gypsum mold was used to consolidate the colloidal particles. The compacts were then dried overnight at 100°C.

Thermogravimetric analysis (TGA; TGA7 thermogravimetric analyzer, Perkin-Elmer, Norwalk, CT) was conducted to determine the oxidation level of SiC by weight increase. The dried compacts were put into a platinum pan and heated to predetermined soak temperatures at a heating rate of 10°C/min in a stream of air.

After partial oxidation treatment in air, reaction sintering was conducted in an alumina crucible in a stream of Ar using a graphite furnace at a heating rate of 25°C/min and a cooling rate of 5°C/min. The densities of the green compacts and the sintered bodies were measured by the Archimedes method using kerosene or distilled water, respectively. The pore channel size distribution of the compacts was determined by mercury porosimetry.[11,12] The pore channel size distribution was obtained using standard values for the mercury surface energy (0.48 N/m) and the contact angle (140°). Phase analysis was conducted by X-ray diffraction (XRD; X-ray diffractometer, Philips Electronic Instruments, Inc, Mahwah, NJ) using Ni-filtered $CuK\alpha$ radiation. Sintered samples were polished down to a 1-μm surface finish with diamond paste and then thermally etched at 1450°C for 20 min in an Ar atmosphere. The resulting microstructures were evaluated by scanning electron microscopy (SEM; Philips 515 scanning electron microscope) and transmission electron microscopy (TEM; Philips 300 transmission electron microscope).

III.   Results and Discussion

(1)   Consolidation Process

In preparing colloidal suspensions, controlling the interactions between particles has a significant influence on the stability of a suspension. In our system, an electrosteric stabilization

approach was preferred over an electrostatic one since it was not possible to disperse both SiC and Al_2O_3 equally well at the same pH level. When only electrostatic dispersion was used, SiC dispersed best under basic conditions since the zeta potential is higher in basic solutions, as seen in Fig. 3, whereas Al_2O_3 dispersed best under acidic conditions.[13-15] Consequently, an NH_4 salt of PMAA was used as an electrosteric stabilizer (0.4 g/m^2)[14,15] to improve the stability of Al_2O_3 under basic conditions so that a low-viscosity composite suspension could be prepared at pH 10.

Figure 4 shows pore channel size distributions of the Al_2O_3–15SiC(C) compacts consolidated by the colloidal consolidation of the suspensions with different values of pH. A green compact with a narrow pore channel size distribution with small pores could be obtained by adjusting the pH.

During colloidal consolidation of binary suspensions, a key problem is the segregation of particles due to either gravitational[11,12,16] or thermodynamic phase separation[17,18] effects. The best solution for minimizing particle segregation is to prepare the suspensions as highly concentrated as possible.[11,12,16-19] In our system, to check if segregation and/or phase separation occurred, the green densities and X-ray intensity ratios along the perpendicular axis of both Al_2O_3–15SiC(C) and Al_2O_3–15SiC(F) compacts (approximately 3.5 cm height) were measured. Because these displayed similar values within experimental error, it was concluded that significant segregation and/or phase separation did not occur while using a 45 vol% solid suspension. As shown in Figs. 5 and 6, relatively
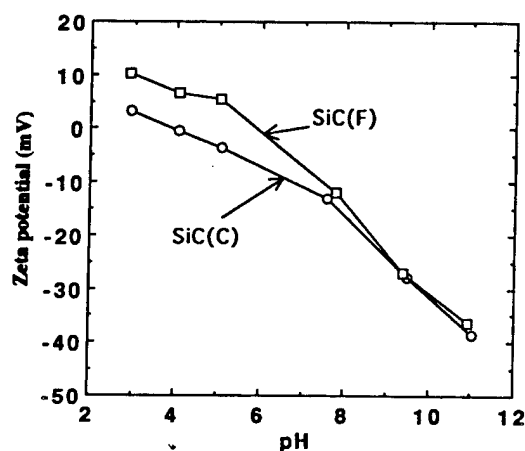
Fig. 3.   Plots of zeta potential vs pH for SiC(C) and SiC(F).
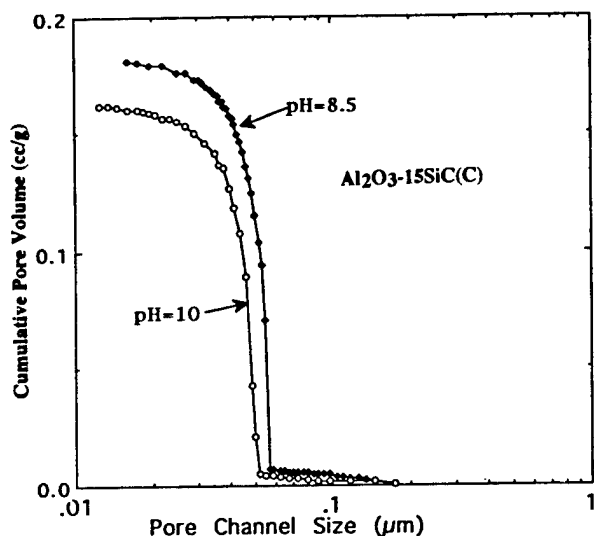
Fig. 4. Pore channel size distributions of the Al_2O_3–15SiC(C) compacts consolidated by the colloidal consolidation of the suspensions with different values of pH.
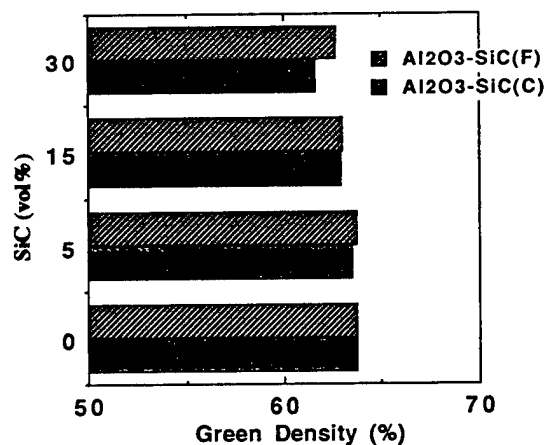
Fig. 5. Green densities of the colloidally consolidated composites with various amounts of SiC(C) and SiC(F) powders.

Fig. 6. Pore channel size distributions of the colloidally consolidated composites with various amounts of SiC(C) and SiC(F) powders.

(2) Oxidation Process

The typical weight losses and/or gains when heating Al_2O_3–15SiC(F) and Al_2O_3–15SiC(C) at a heating rate of 10°C/min are shown in Fig. 7. Upon heating to 700°C weight loss was observed in three regions for the Al_2O_3–15SiC(C) sample: in the first region (up to 300°C), the second (around 350°C), and the third (around 650°C). To determine the origin of the weight loss, a TGA experiment on the Al_2O_3 compact after colloidal consolidation was conducted. By comparison with the weight loss of Al_2O_3–15SiC(C) and Al_2O_3, it is concluded that the first weight loss was due to desorption of water and the second is due to decomposition of the surfactant. Although slight weight loss of Al_2O_3 was observed due to the chemically bonded water (i.e., hydroxy groups) in the temperature range of 400–1000°C, the weight loss was different from that of the third region. Temperature-programmed desorption measurement[20,21] of SiC(C) powder in oxygen atmosphere was conducted, where the evolved gases were monitored with a quadrupole spectrometer. The evolution of CO and CO_2 was observed in the third region. Therefore, in the third region the weight loss was mainly due to the evolution of carbon oxide from carbon impurity. In the case of Al_2O_3–15SiC(F), the third region was not observed because carbon was not a major impurity in the SiC(F). Above 700°C for Al_2O_3–15SiC(C) and above 500°C for Al_2O_3–15SiC(F), the weight loss reached a maximum value

high green densities (Fig. 5) and narrow pore channel size distributions (Fig. 6) obtained with all of these compacts were also an indication of the consolidation of the particles without significant segregation.
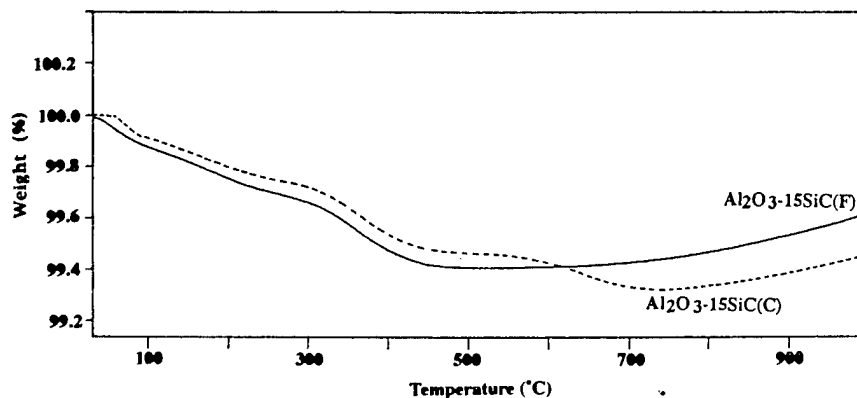
Fig. 7. TGA curves of colloidal consolidated compacts of Al_2O_3–15SiC(C) and Al_2O_3–15SiC(F) at a heating rate of 10°C/min in a stream of air.

and, because of the onset of SiC oxidation, a weight gain was observed at higher temperatures. The plateau value at the maximum weight loss was used as the reference point to approximate the fraction of silica that formed as an oxidation product on the surface of the SiC particles.

The size of the SiC core particles was controlled by determining the fraction of SiC oxidized during heat treatment. Figure 8 shows the weight gain and oxidation fraction. Because of its finer particle size, the oxidation fraction of the SiC(F) system is higher than that of the SiC(C) system. The oxidation behavior of SiC powder in this temperature range is believed to be the following passive oxidation reaction:[22]

$$SiC + 2O_2 \rightarrow SiO_2 + CO_2 \qquad (1)$$
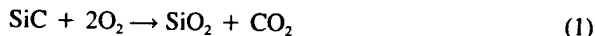
The oxidation reactions at 1400°C are depressed by comparison with those at 1300°C, especially for the SiC(C) system, as seen in Fig. 8. This phenomenon may be due to the significant sintering occurring simultaneously with the oxidation reaction at 1400°C. Therefore, partial oxidation treatments were conducted below 1400°C. Many authors have reported that oxidation of SiC powders in various oxidizing atmospheres follows parabolic reaction rate kinetics.[22-27] The oxidation fraction can be represented by the following Jander's equation:[28]

$$1 - (1 - f)^{1/3} = (kt)^{1/2} \qquad (2)$$

where f is the oxidation fraction, t is the reaction time, and k is the rate constant. As shown in Fig. 9, when $1 - (1 - f)^{1/3}$ is plotted versus the square root of time, a linear variation is observed at low temperatures (1000–1200°C) and also within the initial stages of higher temperature oxidation treatments,
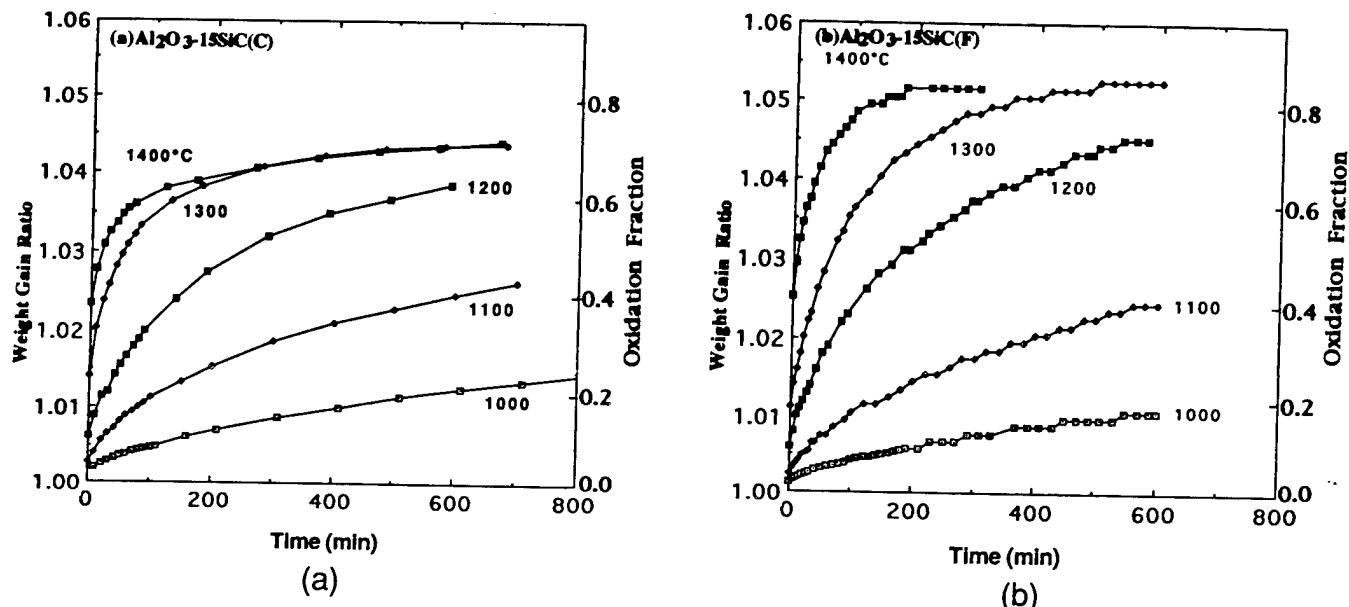
Fig. 8. Weight increase ratio (left-hand side) and oxidation fraction (right-hand side) of (a) Al_2O_3–15SiC(C) and (b) Al_2O_3–15SiC(F) composites during isothermal holding in a stream of air.
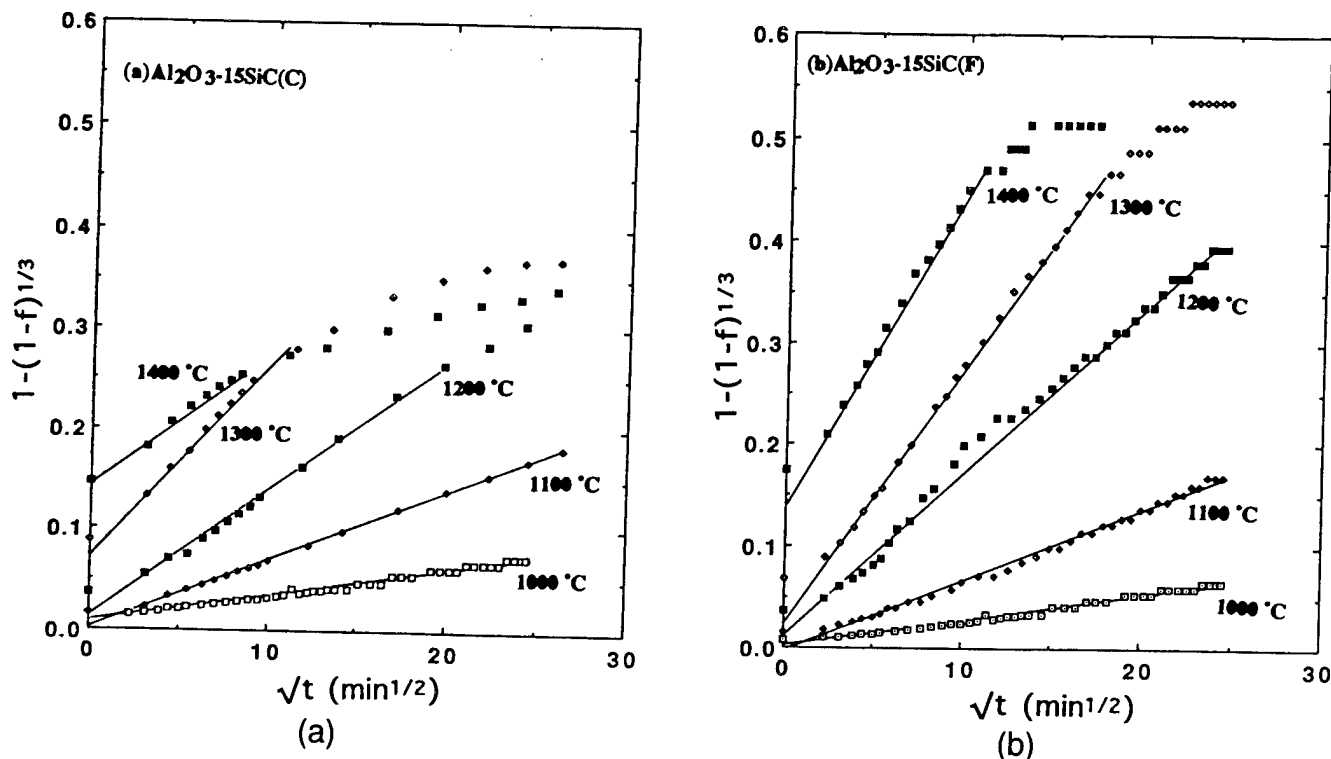
Fig. 9. Relationship between square root of time and $1 - (1 - f)^{1/3}$ for (a) Al_2O_3–15SiC(C) and (b) Al_2O_3–15SiC(F) composites during isothermal holding in a stream of air.

suggesting that oxidation is rate limited by a diffusion process. Using Eq. (2), we can calculate the rate constants at every temperature. Arrhenius plots of the rate constants in the temperature range of 1000–1300°C are shown in Fig. 10. The activation energies of Al_2O_3–SiC(F) and Al_2O_3–15SiC(C) are 256 and 216 kJ/mol, respectively. Activation energies reported in the literature vary from 134 to 498 kJ/mol.[22-27] The large amount of scatter has been attributed to the different types of materials (powder, polycrystal, and single crystal) with varying concentrations of impurities, which can alter the oxidation kinetics significantly. In our case, the activation energies are close to the activation energy of the ionic oxygen diffusion in vitreous silica (298 kJ/mol)[29] but not to that of the molecular oxygen diffusion (113 kJ/mol).[30] Therefore, the present oxidation reaction seems to proceed via ionic oxygen diffusion through a silica film.

Figure 11 shows the X-ray diffraction patterns of Al_2O_3–15SiC oxidized at 1300°C for 5 h in air. The decrease in the amount of SiC and the gain in the amount of SiO_2 (cristobalite and amorphous phase) can be seen from the figure. In the case of Al_2O_3–15SiC(F) (Fig. 11(b)), the SiC peak was broader and
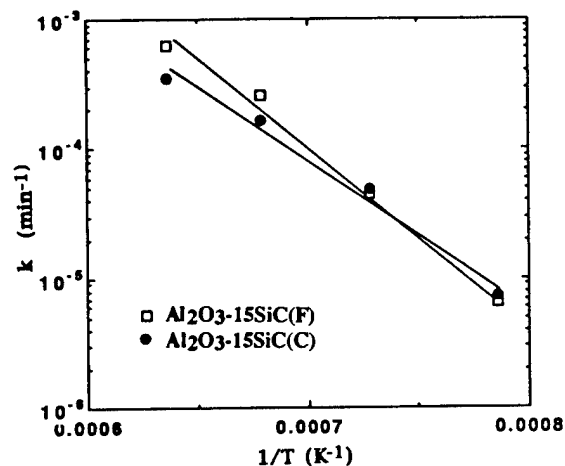
Fig. 10. Arrhenius plots of the rate constants.
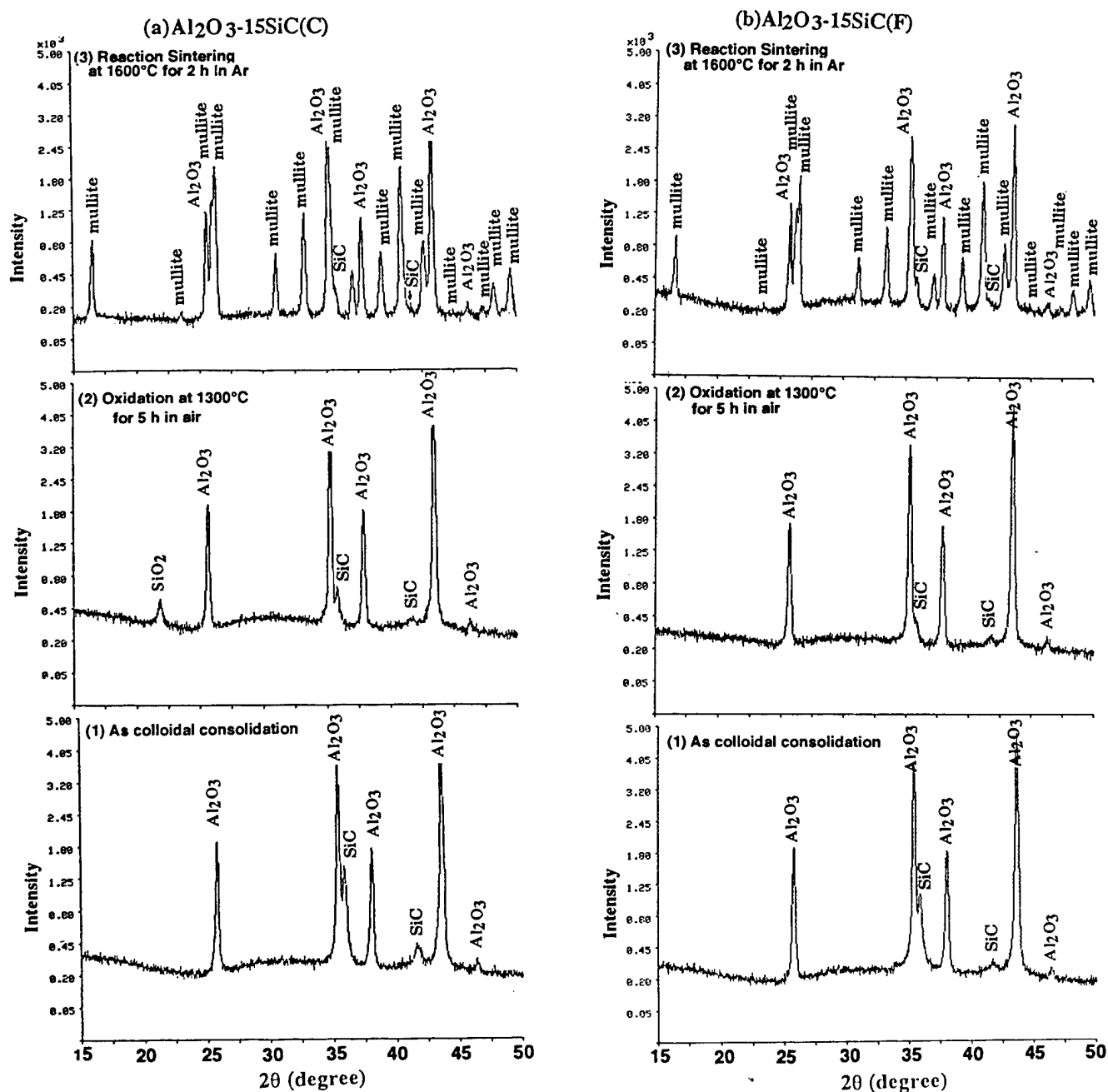
Fig. 11. X-ray diffraction patterns of (a) Al_2O_3–15SiC(C) and (b) Al_2O_3–15SiC(F): (1) as colloidal consolidation, (2) after oxidation at 1300°C for 5 h in air, and (3) after reaction sintering at 1600°C for 2 h in Ar.

the cristobalite phase was not observed after partial oxidation treatment. It is important to note that a large quantity of cristobalite is not preferred since cristobalite causes micro- and macrocracking during its β- to α-cristobalite polymorphic phase transformation during cooling.

(3) Reaction Sintering and Microstructure

Comparison of the X-ray diffraction patterns in Fig. 11 confirms the premise of this study that the SiO_2 phase would form as an oxidation product and be consumed to form mullite during the final stage heat treatment in Ar. In calculating the theoretical densities of the compacts, two types of volume expansion had to be considered.[31] Volume expansion of SiC upon oxidation is 107% and formation of stoichiometric mullite from the reaction of $3Al_2O_3$ and $2SiO_2$ results in a volume increase of ~5% assuming that the densities of Al_2O_3, SiO_2, and mullite are 3.99, 2.33, and 3.16 g/cm^3, respectively. The theoretical densities were determined by the following equation:

$$\rho = [V_s\rho_s + (1 - V_s)\rho_A]W/k \tag{3}$$

where ρ_s and ρ_A are the theoretical densities of SiC and Al_2O_3, respectively. V_s is the volume fraction of SiC, and W is the oxidation weight increase ratio. k is a factor controlled by the composition and the respective volume expansions:

$$k = \frac{fV_s(2.07 \times 1.05 - 1)}{1 + (1 - f)V_s} + 1 \tag{4}$$

where f is the oxidation fraction of SiC.

The effects of the oxidation conditions on the sintered densities are shown in Fig. 12. Note that when the oxidation fraction exceeded 40% (by comparison of Figs. 8 and 12), sintered densities above 95% were obtained by sintering at 1600°C for 2 h in an Ar atmosphere. In contrast, the densities of the samples with no partial oxidation treatment were very low. The presence of amorphous silica after surface oxidation of SiC accelerates the

sintering significantly. A possible explanation for this is the lowering of porosity due to volume expansion during the oxidation of SiC. Although amorphous silica forms only on the SiC particles, the possibility of enhanced densification due to its transient presence needs further investigation.[32,33] As expected, the final composite densities show a slight decrease as the initial SiC content is increased (Fig. 13).

Figure 14 shows a SEM micrograph of a polished and etched Al_2O_3–15SiC(C) sample that was oxidized at 1300°C and sintered at 1600°C. At this resolution, although small second-phase inclusions are observed, it is not obvious whether these inclusions extend to the nanoscale range. In TEM characterization of the composites, two types of nanoscale inclusions were observed (Fig. 15). In the first type (Fig. 15(a)), nanometer-sized SiC particles were observed as inclusions within a mullite matrix as confirmed by energy dispersive X-ray spectroscopy (EDS), where the SiC particles were seen as dark spots. In the second type (Fig. 15(b)), mullite whiskers were observed within the SiC grains, again as confirmed by EDS analysis.

These morphologies are explained as follows. When Mitsui Toatsu's fine SiC is used, the surface of the SiC is oxidized uniformly and nanometer-sized SiC particles remain in the mullite matrix as illustrated in Figs. 1 and 15(a). In contrast, since Superior Graphite's SiC powders are coarser and are produced by milling, the powders may have grain boundaries and cracks
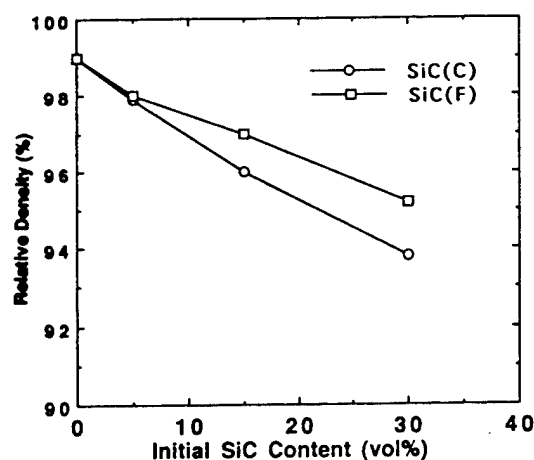
Fig. 13. Effect of initial SiC contents on density after an initial oxidation at 1300°C in air and then a final sintering at 1600°C for 2 h in Ar.

Fig. 12. Effect of oxidation conditions on the densities of the compacts sintered at 1600°C for 2 h in Ar. Calculated compositions of the produced nanocomposites are as follows:

Sample no.	Composition (vol%)		
	Al_2O_3	Mullite	SiC
1	63.5	27.6	8.9
2	61.0	31.0	8.0
3	52.3	42.1	5.6
4	51.3	43.5	5.2
5	48.2	47.3	4.5
6	43.5	53.6	2.9
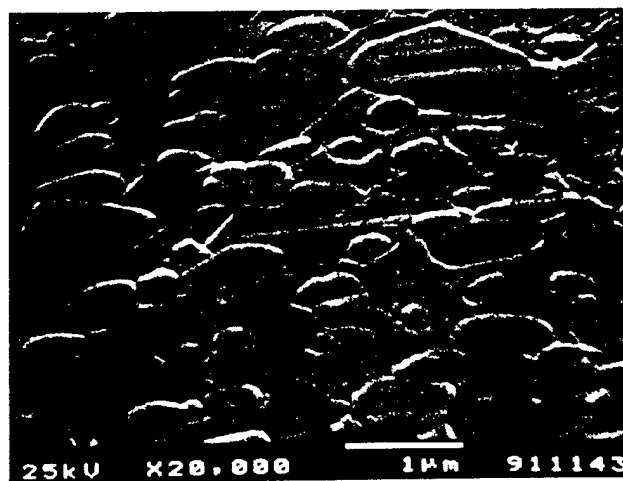
Fig. 14. SEM micrograph of polished and thermally etched Al_2O_3–15SiC(C) composite first oxidized at 1300°C for 5 h and followed by a 1600°C sintering for 2 h in Ar.
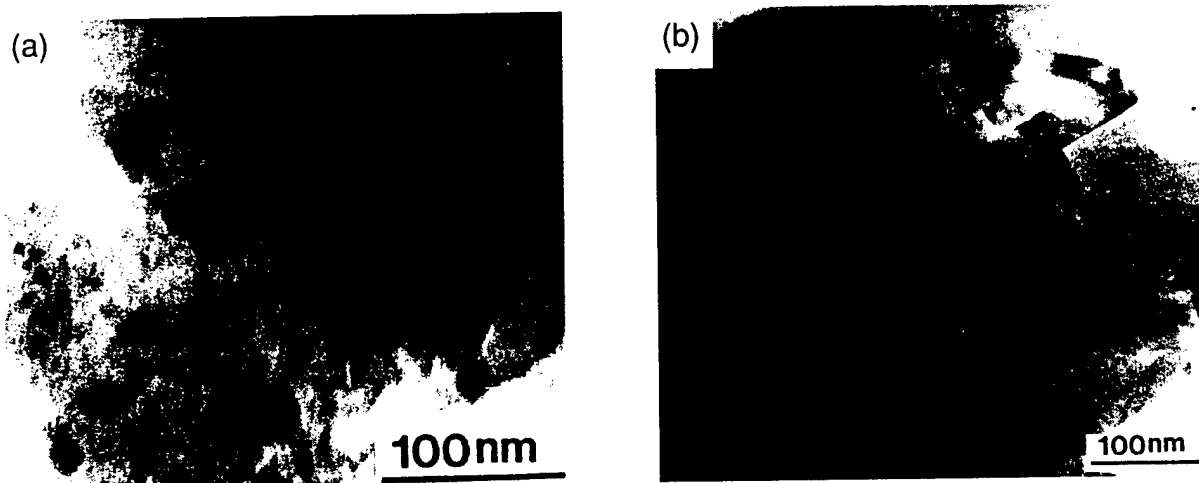
Fig. 15. TEM micrographs of (a) Al_2O_3–15SiC(F) and (b) Al_2O_3–15SiC(C) composites first oxidized at 1300°C for 5 h in air and followed by a final sintering treatment at 1600°C for 2 h in Ar.

that result in preferential oxidation into the SiC grains, producing the type of microstructure observed in Fig. 15(b) by the mechanism summarized below.

Recent studies have shown that in the temperature range <1500°C, mullite forms by a nucleation and growth process within the silica-rich matrix (but not at the alumina interfaces) as the siliceous matrix is saturated with respect to mullite through the dissolution of alumina.[34–36] In this process, first, Al_2O_3 dissolves into the amorphous silica matrix; second, mullite nuclei form within this matrix as the matrix composition exceeds the saturation limit with respect to mullite; and third, mullite crystals grow as more alumina dissolves into the matrix and then is incorporated into the growing mullite grains. The nucleation and growth of mullite within silica-rich fissures on the coarse SiC would then be consistent with the morphology observed in Fig. 15(b).

IV. Conclusions

SiC–mullite–Al_2O_3 nanocomposites were processed through a novel colloidal consolidation and reaction sintering process. First, micrometer-sized SiC and Al_2O_3 particles were colloidally dispersed and consolidated to form uniformly mixed compacts. Second, the SiC particles were partially oxidized to reduce them to nanometer-sized cores. Third, these nanometer-sized core particles were trapped within a mullite matrix as the silica oxidation product reacted with alumina to form mullite.

This process offers several advantages and thereby warrants further research: (1) it eliminates the need to reduce the particle size of the inclusion phase to the nanometer range by milling and thus provides better control in minimizing impurities; and (2) because of a volume increase during reaction sintering, sintering shrinkages are lower.

References

[1]R. P. Andres, R. S. Averback, W. L. Brown, W. A. Goddard III, A. Kaldor, S. G. Louie, M. Moscovits, P. S. Peercy, S. J. Riley, R. W. Siegel, F. Spaepen, and Y. Wang, "Research Opportunities on Cluster and Cluster-Assembled Materials," *J. Mater. Res.,* 4 [3] 705–36 (1989).

[2]R. W. Siegel, R. Ramasamy, H. Hahn, L. Tiang, and R. Gronsky, "Synthesis, Characterization, and Properties of Nanophase TiO_2," *J. Mater. Res.,* 3, 1367–72 (1988).

[3]K. Niihara, "New Design Concepts of Structural Ceramics—Ceramic Nanocomposite," *J. Ceram. Soc. Jpn.,* 99 [10] 974–82 (1991).

[4]H. Takada, A. Nakahira, H. Ohnishi, S. Ueda, and K. Niihara, "Improvement of Mechanical Properties of Natural Mullite/SiC Nanocomposite," *Jpn. J. Powder Powder Met.,* 38, 348–51 (1991).

[5]T. N. Tiegs, P. F. Becher, and P. Angelini, "Microstructure and Properties of SiC Whisker-Reinforced Mullite Composite"; pp. 463–72 in Ceramic Transactions, Vol. 6, *Mullite and Mullite Matrix Composites.* Edited by S. Somiya, R. F. Davis, and J. A. Pask. American Ceramic Society, Westerville, OH, 1990.

[6]B. R. Marple and D. J. Green, "Mullite/Alumina Particulate Composites by Infiltration Processing: III, Mechanical Properties," *J. Am. Ceram. Soc.,* 74 [10] 2453–59 (1991).

[7]Y. Sakka, D. D. Bidinger, J. Liu, M. Sarikaya, and I. A. Aksay, "Processing of SiC–Mullite–Al_2O_3 Nanocomposite"; pp. 15–26 in NASA Conference Publication, Vol. 3175, *The 16th Conference on Metal Matrix, Carbon, and Ceramic Matrix Composites.* Edited by J. D. Buckley. National Aeronautics and Space Administration, Washington, DC, 1992.

[8]I. A. Aksay, F. F. Lange, and B. I. Davis, "Uniformity of Al_2O_3–ZrO_2 Composites by Colloidal Filtration," *J. Am. Ceram. Soc.,* 60 [10] C-190–C-192 (1983).

[9]F. F. Lange, "Powder Processing Science and Technology for Increased Reliability," *J. Am. Ceram. Soc.,* 72 [1] 3–15 (1989).

[10]S. Ross and I. D. Morrion, *Colloidal Systems and Interfaces*; pp. 205–63. Wiley, New York, 1988.

[11]C. Han, "Sintering of Bimodal Powder Compacts"; M.S. Thesis. University of California, Los Angeles, CA, 1985.

[12]C. Han, I. A. Aksay, and O. J. Whittemore, "Characterization of Microstructure Evolution with Mercury Porosimetry"; pp. 339–47 in *Advances in Materials Characterization, II.* Edited by R. L. Snyder, R. A. Condrate, Sr., and P. F. Johnson. Plenum, New York, 1985.

[13]E. Liden, L. Bergstrom, M. Persson, and R. Carlsson, "Surface Modification and Dispersion of Silicon Nitride and Silicon Carbide Powders," *J. Eur. Ceram. Soc.,* 7 [6] 361–68 (1990).

[14]J. Cesarano III, I. A. Aksay, and A. Bleier, "Stability of Aqueous α-Al_2O_3 Suspensions with Poly(methacrylic acid) Polyelectrolyte," *J. Am. Ceram. Soc.,* 71 [4] 250–55 (1988).

[15]J. Cesarano III and I. A. Aksay, "Processing of Highly Concentrated Aqueous α-Al_2O_3 Suspensions Stabilized with Polyelectrolytes," *J. Am. Ceram. Soc.,* 71 [12] 1062–67 (1988).

[16]Y. Hirata and I. A. Aksay, "Particle Segregation during Colloidal Filtration"; pp. 3–15 in *Advances in Materials, Processing and Manufacturing, Proceedings of the Advanced Materials Technology Ceramic Workshop,* No. 4. International Committee for Advanced Materials Technology, Nagoya, Japan, 1988.

[17]J. Liu, W. Y. Shih, R. Kikuchi, and I. A. Aksay, "Clustering of Binary Colloidal Suspensions: Theory," *J. Colloid Interface Sci.,* 142 [2] 369–77 (1991).

[18]M. Yasrebi, W. Y. Shih, and I. A. Aksay, "Clustering of Binary Colloidal Suspensions: Experiment," *J. Colloid Interface Sci.,* 142 [2] 357–68 (1991).

[19]M. D. Sacks and G. W. Scheiffele, "Properties of Silicon Suspensions and Slip-Cast Bodies," *Ceram. Eng. Sci. Proc.,* 6 [7–8] 1109–23 (1985).

[20]Y. Sakka, T. Uchikoshi, and E. Ozawa, "Low-Temperature Sintering and Gas Desorption of Gold Ultrafine Powders," *J. Less-Common Met.,* 147, 89–96 (1989).

[21]Y. Sakka, S. Ohno, and M. Uda, "Oxidation and Degradation of Titanium Nitride Ultrafine Powders Exposed to Air," *J. Am. Ceram. Soc.,* 75 [1] 244–48 (1992).

[22]W. L. Vaughn and H. G. Maahs, "Active-to-Passive Transition in the Oxidation of Silicon Carbide and Silicon Nitride in Air," *J. Am. Ceram. Soc.,* 73 [6] 1540–43 (1990).

[23]G. Ervin, Jr., "Oxidation Behavior of Silicon Carbide," *J. Am. Ceram. Soc.,* 41 [9] 347–52 (1958).

[24]P. J. Jorgensen, M. E. Wadsworth, and I. B. Cutler, "Oxidation of Silicon Carbide," *J. Am. Ceram. Soc.,* 42 [12] 613–16 (1959).

[25]R. F. Adamsky, "Oxidation of Silicon Carbide in the Temperature Range 1200 to 1500°," *J. Phys. Chem.*, **63**, 305–7 (1959).

[26]K. L. Luthra, "Some New Perspectives on Oxidation of Silicon Carbide and Silicon Nitride," *J. Am. Ceram. Soc.*, **74** [5] 1095–103 (1991).

[27]T. Shimoo, "Carbon Removal and Oxidation of SiC Powder Synthesized by Carbothermic Reduction of Silica," *J. Ceram. Soc. Jpn.*, **99** [9] 768–73 (1991).

[28]W. Jander, "Reactions in Solid State at High Temperatures: I," *Z. Anorg. Allg. Chem.*, **163**, 1 (1927).

[29]E. W. Sucov, "Diffusion of Oxygen in Vitreous Silica," *J. Am. Ceram. Soc.*, **46** [1] 14–20 (1963).

[30]F. J. Norton, "Permeation of Gaseous Oxygen Through Vitreous Silica," *Nature (London)*, **191**, 4789 (1961).

[31]S. Wu and N. Claussen, "Fabrication and Properties of Low-Shrinkage Reaction-Bonded Mullite," *J. Am. Ceram. Soc.*, **74** [10] 2460–63 (1991).

[32]M. D. Sacks, N. Bozkurt, and G. W. Scheiffele, "Fabrication of Mullite-Matrix Composites by Transient Viscous Sintering of Composite Powders," *J. Am. Ceram. Soc.*, **74** [10] 2428–37 (1991).

[33]J. E. Webb, "Processing Mullite for Use as a Ceramic–Ceramic Composite Matrix Material"; M.S. Thesis. University of Washington, Seattle, WA, 1991.

[34]S. Sundaresan and I. A. Aksay, "Mullitization of Diphasic Aluminosilicate Gels," *J. Am. Ceram. Soc.*, **74** [10] 2388–92 (1991).

[35]W. Wei and J. W. Halloran, "Transformation Kinetics of Diphasic Aluminosilicate Gels," *J. Am. Ceram. Soc.*, **71** [7] 581–87 (1988).

[36]J. C. Huling and G. L. Messing, "Epitactic Nucleation of Spinel in Aluminosilicate Gels and Its Effect on Mullite Crystallization," *J. Am. Ceram. Soc.*, **74** [10] 2374–81 (1991). □

Elimination of an isolated pore: Effect of grain size

Wan Y. Shih
*Department of Chemical Engineering and Princeton Materials Institute, Princeton University,
Princeton, New Jersey 08544-5263*

Wei-Heng Shih
Department of Materials Engineering, Drexel University, Philadelphia, Pennsylvania 19104

Ilhan A. Aksay
*Department of Chemical Engineering and Princeton Materials Institute, Princeton University,
Princeton, New Jersey 08544-5263*

The effect of grain size on the elimination of an isolated pore was investigated both
by the Monte Carlo simulations and by a scaling analysis. The Monte Carlo statistical
mechanics model for sintering was constructed by mapping microstructures onto domains
of vectors of different orientations as grains and domains of vacancies as pores. The
most distinctive feature of the simulations is that we allow the vacancies to move. By
incorporating the outer surfaces of the sample in the simulations, sintering takes place
via vacancy diffusion from the pores to the outer sample surfaces. The simulations were
performed in two dimensions. The results showed that the model is capable of displaying
various sintering phenomena such as evaporation and condensation, rounding of a sharp
corner, pore coalescence, thermal etching, neck formation, grain growth, and growth of
large pores. For the elimination of an isolated pore, the most salient result is that the
scaling law of the pore elimination time t_p with respect to the pore diameter d_p changes
as pore size changes from larger than the grains to smaller than the grains. For example,
in sample-size-fixed simulations, $t_p \sim d_p^3$ for $d_p < G$ and $t_p \sim d_p^2$ for $d_p > G$ with
the crossover pore diameter d_c increasing linearly with G where G is the average grain
diameter. For sample-size-scaled simulations, $t_p \sim d_p^4$ for $d_p < G$ and $t_p \sim d_p^3$ for
$d_p > G$. That t_p has different scaling laws in different grain-size regimes is a result of
grain boundaries serving as diffusion channels in a fine-grain microstructure such as
those considered in the simulations. A scaling analysis is provided to explain the scaling
relationships among t_p, d_p, and G obtained in the simulations. The scaling analysis also
shows that these scaling relationships are independent of the dimensionality. Thus, the
results of the two-dimensional simulations should also apply in three dimensions.

I. INTRODUCTION

Materials processing by sintering of powder compacts has been a central issue in the field of ceramics and metallurgy. With increasing emphasis on nanostructural design, an aspect of sintering that requires more adequate understanding is the densification of nanometer-sized particles without grain growth beyond 100 nm. This is the size range where the pores and the particles are of similar size and thus the spatial distribution of the porosity plays an increasingly significant role on the evolution of structure. In this size range, due to the formation of particle agglomerates, powder compacts often exhibit hierarchical pore-size distributions and thus while some pores are smaller than or equal to the particles, others are much larger than the particle size.[1] Individual particles can be polycrystalline as well,[2] adding to the complexity of the structure and the densification kinetics. With increasingly complicated structures, it is important to know how sintering is affected by the difference in the structures. For example, a different pore size/grain size ratio can affect the number of grain boundaries intersecting the pore surface. Theories that treated sintering as a diffusion-driven phenomenon have assumed that pores are surrounded by a certain number of grains and thus did not take into account the effect of a different pore size/grain size ratio explicitly. On the other hand, the pore stability argument of Kingery and Francois[4] that addressed the effect of pore size/grain size ratio did so only within the framework of thermodynamics and neglected the diffusional aspects.

In this paper, we study the role of structural features on sintering by means of Monte Carlo simulations of a microscopic model that can take into account both the structural effects and the diffusional aspect simultaneously. Microscopic simulations of structures were first started by Anderson *et al.*[5] who developed a Monte Carlo statistical mechanics model to study the grain growth behavior of a fully dense system, in which

structures were mapped onto domains of vectors of different orientations. A grain is a domain of vectors with the same orientation. Grain growth in this model took place by flipping the orientations of the vectors simulated with a Monte Carlo algorithm. The Monte Carlo simulations of this vector model allowed the statistical mechanics of microstructures to be taken into account and their simulations were capable of showing various desired scenarios of grain growth such as the movement of the grain boundaries in the direction of the concave curvature, the increase of the grain size in a power-law fashion with time with an exponent between 0.3 and 0.5, and a time-independent normalized grain-size distribution during grain growth.

Compared to grain growth of a fully dense system, sintering is a more complicated phenomenon in that it involves not only the orientational changes but also the diffusion of matter (or vacancies) in a powder/pore network. Grain boundaries may act as vacancy pipes or as vacancy sinks depending on the lattice vacancy concentration, the pore size, and the location of the pore with respect to a grain boundary.[6] A microscopic sintering model must take into account both the microstructures and the diffusional aspect. Recently, Chen et al.[7] have incorporated domains of vacancies as pores into the model of Anderson et al.[5] to study the final-stage sintering. However, vacancies in this model did not actually move; but, the densification was accomplished by removing vacancies from pores at their junctions with grain boundaries. The pore-shrinkage probability was obtained from a macroscopic derivation with a presumed pore geometry and therefore, pores in this model can only shrink.[7]

In the present paper, in addition to orientational flipping, we incorporate diffusion of vacancies into the simulations. By allowing the vacancies to move, we are able to examine the microstructural effects on sintering more generally. For the orientational changes, we employ the vector-vacancy model where a domain of vectors of the same orientation is a grain and a domain of vacancies is a pore. By incorporating the outer surfaces of the samples in the simulations and allowing vacancies to move, densification of a sample is a result of the diffusion of vacancies away from the pores to the outer sample surfaces. The movement of a vacancy is achieved by exchanging it with one of its neighboring vectors and is simulated with the Monte Carlo method. The movement of a vacancy may also be viewed as a movement of matter in the opposite direction. As vacancies can move away from a pore, they can also move into a pore. Therefore, in addition to pore shrinkage, our model is also capable of exhibiting pore growth and pore coalescence as in a real system.

Simulations have been carried out in two dimensions and showed that the model is indeed capable of

exhibiting various desired features of sintering such as densification, growth of large pores, pore coalescence, evaporation and condensation, rounding of a sharp corner, grain growth, neck formation, and thermal etching of grain boundaries.

To clearly illustrate the effect of different grain size/pore size ratios, we investigated the sintering behavior of an isolated pore. By single-pore simulations, we exclude the effect of interpore interactions and focus on the effect of different grain size/pore size ratios on pore sintering. The effect of interpore interactions on the sintering of a multipore compact will be addressed in subsequent publications. For the sintering of an isolated pore, the most salient result is that the scaling relationship for the pore elimination time t_p with respect to the pore diameter d_p changes when d_p changes from larger than the grain diameter G to smaller than G. This is a result of the grain boundaries serving as diffusion channels in a fine-grain microstructure such as those considered in the simulations. In the sample-size-fixed simulations where the sample size was kept fixed, we show that for $d_p > G$, the pore shrinkage rate is independent of d_p and proportional to $1/G$ whereas for $d_p < G$, the pore shrinkage rate becomes independent of G but proportional to $1/d_p$ where the pore shrinkage rate is the rate of change in the pore area. Consequently, the pore elimination time t_p shows two distinct power laws with respect to d_p: $t_p \sim d_p^3$ for $d_p < G$ and $t_p \sim d_p^2$ for $d_p > G$ in sample-size-fixed simulations. The crossover pore diameter d_c, i.e., the pore size that signifies the change from one scaling relationship to another, increases roughly linearly with G. In sample-size-scaled simulations where the sample size scales in proportion to the initial pore diameter d_p, $t_p \sim d_p^4$ for $d_p < G$ and $t_p \sim d_p^3$ for $d_p > G$, indicating a linear dependence of t_p on the sample size. A scaling analysis is provided to explain the simulated results relating the pore elimination time to the pore size. The scaling analysis is similar to Herring's scaling theory[8] but is derived for systems with grain-boundary diffusion. We further show that these scaling relations are independent of dimensionality. Thus, the results of the two-dimensional simulations should also hold in three dimensions.

The rest of the paper is organized as follows. Sections II and III describe the model and the simulation procedures, respectively. The results of the simulations are contained in Sec. IV. Sec. V gives the detail of the scaling analysis and Sec. VI, the concluding remarks.

II. MODEL

The statistical mechanics model that we employ in the present study is composed of vectors of different orientations and vacancies.[7] In addition to the application for final-stage sintering, it has also been successfully

applied to study grain-boundary wetting.[9] As in Ref. 7, we map a microstructure onto a discrete lattice, as shown in Fig. 1. A lattice site can be a portion of a grain as denoted by a letter or a portion of a pore as denoted by an empty site. Each letter represents a crystalline orientation. A domain of the same letter represents a grain and a domain of vacancies, a pore. There are N possible crystalline orientations. For simplicity, we take the N crystalline orientations to be N planar vectors uniformly spaced on a circle with the angle of a vector a multiple of $2\pi/N$. The interaction between two vectors depends on the angle difference θ of the two vectors, and, in general, can be any reasonable function. In the present study, we take

$$V(\theta) = E_{gb} \quad \text{if } \theta \neq 0$$
$$= 0 \quad \text{if } \theta = 0. \quad (1)$$

We consider only the nearest-neighbor interactions; i.e., only the interactions between adjacent lattice sites can be non-zero. The interaction between a vector and a vacancy (empty site) is E_s and the interaction between two vacancies is zero. With these definitions, the solid-vapor interfacial energy at $T = 0$ K is proportional to E_s and the grain-boundary energy at $T = 0$ K is proportional to E_{gb}. Therefore, the ratio of E_s/E_{gb} determines the $T = 0$ K dihedral angle Ψ by $\Psi = 2 \cos^{-1}(2E_s/E_{gb})$. For example, $E_s/E_{gb} = 5/3$ gives $\Psi = 145°$.

III. MONTE CARLO SIMULATIONS

Monte Carlo simulations[10] can be a powerful tool for the kinetic study of a statistical mechanics model when an appropriate kinetic procedure is chosen. We include (i) the orientational flipping of vectors to simulate microstructural changes such as grain growth and (ii) vacancy diffusion to give rise to sintering
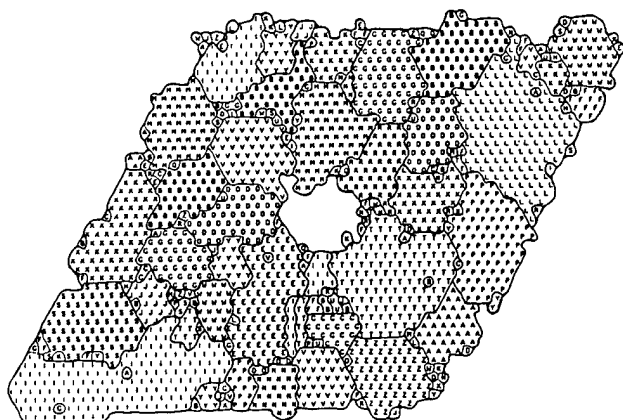
FIG. 1. A lattice representation of a structure. A domain of a same letter is a grain and a domain of empty sites is a pore. Each letter denotes a different crystalline orientation.

A. Orientational flipping

Given a microstructure (with vectors and vacancies), an occupied site, i.e., a vector is randomly chosen. Before the vector is allowed to change its orientation, it first breaks its bonds with its neighboring vectors that have the same orientation as the vector. Breaking each of such bonds costs E_{gb}. Therefore, the total energy cost ΔE to break all such bonds is $\Delta E = nE_{gb}$ where n is the number of neighboring vectors that have the same orientation as the vector, and whether the vector will successfully break its bonds with its neighbors is determined by the transition rate

$$W = (1/\tau_G)e^{-\Delta E/kT} \quad \text{if } \Delta E > 0$$
$$= 1/\tau_G \quad \text{if } \Delta E \leq 0, \quad (2)$$

where $1/\tau_G$ is the attempt frequency associated with orientational flipping, k the Boltzmann constant, and T the sintering temperature. Equation (2) is simulated as follows. In each attempt for bond breaking, the energy cost ΔE is calculated and the Boltzmann factor $e^{-\Delta E/kT}$ will be compared to a random number between 0 and 1. If the Boltzmann factor $e^{-\Delta E/kT}$ is larger than or equal to the random number, the vector breaks its bonds with its neighboring vectors and slips to a new orientation which is picked by another random number. If the Boltzman factor $e^{-\Delta E/kT}$ is smaller than the random number, the orientation of the vector remains unchanged.

B. Vacancy diffusion

Sintering of a porous object requires transporting vacancies out of the object. In order to study sintering from a microscopic perspective, diffusion of vacancies must be incorporated in the simulations. Vacancy diffusion in our simulations is modeled as a sequence of random translational movements of vacancies. When a vacancy is adjacent to at least one vector, it may undergo a random translational movement as follows. First, one of the vacancy's neighboring vectors is chosen at random. The transition rate W_{ex} for exchanging the position of the vacancy with that of the chosen vector is

$$W_{ex} = (1/\tau_D)e^{-\Delta E_{ex}/kT} \quad \text{if } \Delta E_{ex} > 0$$
$$= 1/\tau_D \quad \text{if } \Delta E_{ex} \leq 0, \quad (3)$$

where $1/\tau_D$ is the attempt frequency for vacancy diffusion and ΔE_{ex} is the energy change associated with the exchange, which depends on the parameters E_s and E_{gb} as well as the neighboring configuration of the vector-vacancy pair before and after the exchange. To achieve the transition rate depicted in Eq. (3), the simulation is done as follows. In each trial for a position exchange, the energy change ΔE_{ex} as well as the Boltzmann factor $e^{-\Delta E_{ex}/kT}$ are calculated. If the Boltzmann factor $e^{-\Delta E_{ex}/kT}$ is larger than or equal to a random number between 0 and 1, the position of the vacancy will be

exchanged with that of the chosen neighboring vector. If the Boltzmann factor $e^{-\Delta E_{ex}/kT}$ is smaller than the random number, the position of the vacancy and that of the vector will remain unchanged. An example is shown in Figs. 2(a) and 2(b) to illustrate how ΔE_{ex} is calculated. The movement of a vacancy may also be viewed as a movement of matter in the opposite direction. The attempt frequency $1/\tau_D$ for vacancy diffusion can be different from that for orientational flipping, $1/\tau_G$, depending on the material. The ratio τ_D/τ_G can be used to control the grain growth rate relative to densification in the simulations. A small τ_D/τ_G corresponds to a system with slow grain growth. By allowing vacancies to move and by incorporating the outer surfaces in the simulations, densification of a sample will take place through the diffusion of vacancies away from the pores to the outer surfaces of the sample.

IV. RESULTS

For the present studies, we chose $N = 30$ and $E_s/E_{gb} = 1.67$ (equivalent to a 145° dihedral angle at $T = 0$ K). Simulations were all carried out at $T = 0.8\ T_m$ where $T_m = 0.83\ E_{gb}$ is the melting temperature estimated by mean-field approximations.[9] For a large value of N such as the one we used, the melting temperature estimated by the mean-field approximations should be as good as that estimated by Monte Carlo simulations.[11] For computational ease, the simulations were carried out in two dimensions on a triangular lattice with periodic boundary conditions. All the simulation results shown in this paper were averaged over 100 independent runs. The Monte Carlo cell is such that the sample is located at the center of the cell and is surrounded by three rows of vacancies (open space) around each edge. Due to the periodic boundary conditions, the system may be thought of as an infinite repetition of the Monte Carlo cell in both the x and the y directions with an edge-to-edge sample distance of six rows. Therefore, under suitable conditions, i.e., at higher temperatures, necking may occur between the upper edge and the lower edge of the sample, which are six rows apart due to the periodic
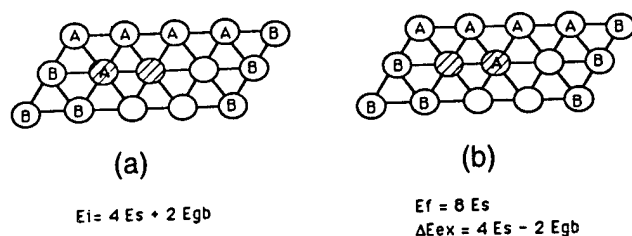
boundary conditions. Likewise, necking may also occur between the left and the right edges.

A. General features of the model

Figures 3(a)–3(d) illustrate the sintering behavior of a multipore compact. We use $\tau_D/\tau_G = 0.1$ to produce Figs. 3(a)–3(d). Figure 3(a) is the initial configuration with 10% porosity. Figure 3(b) is taken at $t = 2000\ \tau_D$. Note that (i) the entire sample is shrinking compared to Fig. 3(a) due to the transportation of vacancies from the interior of the sample to the outer surfaces of the sample, (ii) some pores are coalescing, and (iii) some of the material has evaporated, as indicated by the arrow. Figure 3(c) is at $t = 4000\ \tau_D$. In this snapshot, it can been seen that part of the surface has ruptured, as indicated by arrow α. Also notice than an initially sharp corner has become rounded, as indicated by arrow β. Figure 3(d) is taken at $t = 50,000\ \tau_D$ when the sample is almost fully densified. Note that (i) grains have grown considerably larger, (ii) the material that has evaporated earlier has recondensed (condensation), (iii) necking has already taken place, as indicated by the arrows on the top and at the bottom due to the periodic boundary conditions (initially the upper edge and the lower edge were separated by six rows of vacancies), and (iv) the opening up of a grain boundary at the surface (thermal etching). Note that although the energy parameters we have chosen should, in principle, give a dihedral angle of 145°, the actual dihedral angles displayed in Figs. 3(b)–3(d) are not quite 145° due to the discrete lattice we used in the simulations. It is clear from Figs. 3(a)–3(d) that our sintering model is indeed capable of showing various essential sintering phenomena, e.g., densification, pore coalescence, necking, thermal etching of the outer surface at a grain boundary, evaporation and condensation, rounding of a sharp corner, and grain growth. The incorporation of the vacancy diffusion in our model indeed catches the microscopic essence of sintering.

B. Elimination of an isolated pore

Sintering of a multipore compact involves many factors. Often the interactions between pores inhibit a clear-cut separation of the effect of one factor from another. In order to avoid pore interactions, we study the sintering of an isolated pore first. While studying the sintering of an isolated pore may be difficult experimentally, it is doable with computer simulations. The closest experiments to the sintering of isolated pores are those of Zhao and Harmer[12] in which they studied the sintering of alumina compacts with very low initial porosity so that the initial pore radii were much smaller than the distances between pores. More recently, Slamovich and Lange[13] have done similar experiments

FIG. 2. An example showing how ΔE_{ex} is calculated. (a) and (b) represent the configurations before and after the position exchange of a vector-vacancy pair, respectively. The vector-vacancy pairs under consideration are shaded. E_i and E_f denote the energy of the vector-vacancy pair before and after the move and $\Delta E_{ex} = E_f - E_i$.

$E_i = 4\ E_s + 2\ E_{gb}$

$E_f = 8\ E_s$
$\Delta E_{ex} = 4\ E_s - 2\ E_{gb}$

J. Mater. Res., Vol. 10, No. 4, Apr 1995

1003

(a)

(b)

(c)

(d)

FIG. 3. A typical structural evolution of a multipore compact; (a) $t = 0$, (b) $t = 2000\ \tau_D$, (c) $t = 4000\ \tau_D$, and (d) $t = 50,000\ \tau_D$.

on yttria doped zirconia systems. The sintering of a pore may depend on several factors such as the pore diameter, the pore shape, and the average grain diameter of the surrounding polycrystalline matrix. In the present geometry, there are no other pores around; the only diffusion distance is that from the pore surface to the outer sample surface. Therefore, pore elimination may also depend on the sample size. The results of the simulations showed that with sufficient sintering time, all pores can be eliminated and the pore elimination time, indeed, depends on all of the above factors. In the following, we will examine each of the above factors.

A typical microstructural evolution during the sintering of an isolated pore is shown in Figs. 4(a)–4(c). Figure 4(a) is the initial configuration with a hexagonal pore at the center where the length of an edge equals 4 with the length expressed in units of the lattice

constant of the underlying lattice. Figure 4(b) is at $t = 2000\ \tau_D$. As in Figs. 3(a)–3(d), we used $\tau_D/\tau_G = 0.1$ for Figs. 4(a)–4(c). Notice that not only the pore shrank but the shape of the pore also changed. The pore was not longer hexagonal. In sintering experiments, shape changes were also evident.[12-14] Figure 4(c) is at $t = 5000\ \tau_D$ when the pore is almost completely removed.

The effect of pore diameter and that of pore shape are summarized in Fig. 5 where we plot the pore elimination time t_p as a function of the initial pore area A_p in a double logarithmic scale for various pore shapes. The pore elimination time t_p is the time needed to completely eliminate a pore and is directly obtained from the simulations. To focus on the effect of pore area and pore shape, the result shown in Fig. 5 is obtained at a fixed grain diameter $G = 4.0$ where G is the grain diameter taken as the square root of the average grain area. The

(a)

(b)

(c)
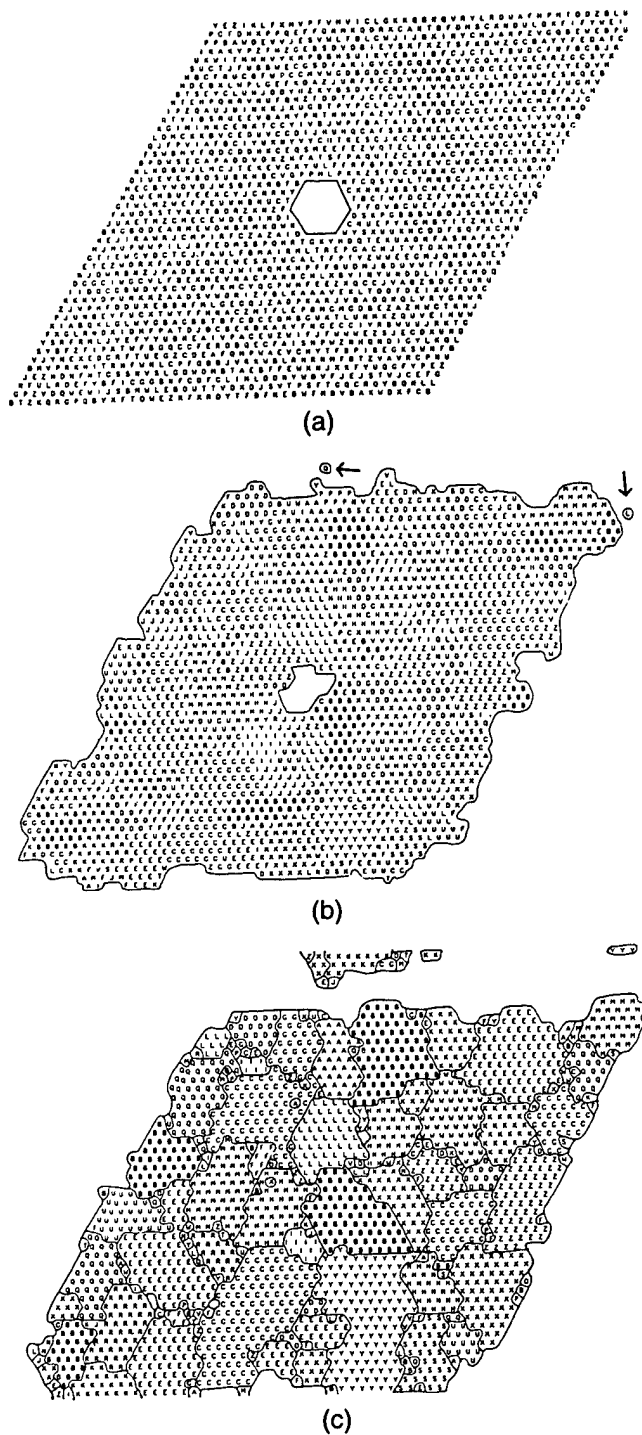
FIG. 4. The structural evolution of an isolated hexagonal pore with edge = 4, at (a) $t = 0$, (b) $t = 2000 \, \tau_D$, and (c) $t = 5000 \, \tau_D$.

FIG. 5. t_p vs A_p at $G = 4.0$ for fixed sample size 45×45 where t_p and A_p are the pore elimination time and the initial pore area, respectively. Full circles and open squares denote initially hexagonally, and rhombically shaped pores. Notice that all data points fall on the same curve, indicating that the pore elimination time is independent of the initial pore shape.

diameter increases with time as a power law $G \sim t^{0.38}$. A typical G-vs-t plot was shown in Fig. 6. Once the desired grain diameter was reached, sintering of the pore began. To separate the effect of grain growth, we did not allow orientational flipping to occur during sintering. The sample size was fixed at 45×45. Examples of how these pores evolve with time under such conditions are shown in Fig. 7 where the pore area as a function
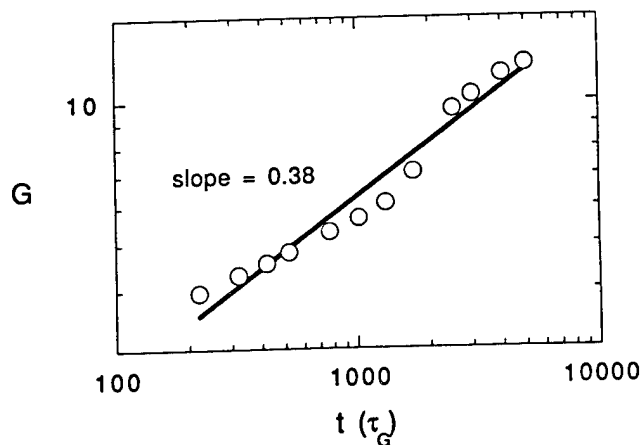
FIG. 6. G vs t where G is the average grain diameter and t is the time in unit of τ_G. The slope of ln G vs t is about 0.38 for the present model.

simulation procedure is as follows. We started with a random grain configuration with a pore of a certain area and a certain shape located at the center of the sample as similar to Fig. 4(a). Before the sintering of the pore began, we allowed the orientational flipping to occur for a certain period of time so that grains could grow to the desired diameter. In the present simulations, the grain

FIG. 7. Pore area versus time for two pores. Arrows α and β indicate the pore elimination time t_p for $A_p = 37$ and 61, respectively.

of time is shown for two pores with $A_p = 37$ and 61, respectively. The simulation conditions for Fig. 7 are identical to those for Fig. 5. From Fig. 7, one can see that overall, the pore area decreases with time while some short-lived increases occurred due to the random nature of the diffusional processes. Eventually, both pores were completely eliminated. The pore elimination times t_p for the two pores shown in Fig. 7 are marked by arrow α and arrow β for $A_p = 37$ and 61, respectively.

From Fig. 5, first, note that the pore elimination time t_p is essentially independent of the initial pore shape. This is conceivable since pores undergo shape change during sintering, as we have shown above. Notice that the pore elimination time t_p follows two distinct power laws with respect to the initial pore area A_p: (i) $t_p \sim A_p^{1.0}$ for large pores and (ii) $t_p \sim A_p^{1.5}$ for small pores. A full account for the scaling behavior of the pore elimination time with respect to the initial pore area will be given in the next section with a scaling analysis. Here we will focus on the difference in the scaling laws of the pore elimination time between large pores and small pores. The difference between the scaling law for large pores and that for small pores is a result of grain boundaries serving as diffusion channels in fine-grained microstructures. When the pores are larger than the grains, the number of diffusion channels is proportional to d_p/G where $d_p = A_p^{0.5}$ is the initial diameter of the pore. On the other hand, when the pore is smaller than the grains, the number of diffusion channels becomes independent of d_p/G. This difference in the pore shrinkage rate gives the additional $A_p^{0.5}$ dependence in the pore elimination time for small pores in Fig. 5. More discussions will be given in the next section concerning the different dependence of the number of the diffusional channels on d_p/G at the pore surface between pores larger than the grains and pores smaller

than the grains. Given that the number of the diffusion channels at the pore surface is proportional to d_p/G for pores larger than the grains and is independent of d_p/G for pores smaller than the grains, one would expect that as the grain diameter increases, the crossover pore area A_c below which the small-pore scaling law prevails and above which the large-pore scaling law dominates increases in proportion to G^2. In Fig. 8, we plot the pore elimination time as a function of A_p for a different grain diameter $G = 8.0$. Also plotted is the pore elimination time for $G = 4.0$ for comparison. Again, like the case of $G = 4.0$, the pore elimination time for $G = 8.0$ is independent of the initial pore shapes and depends only on the initial pore area. One can see that the small-pore sintering behavior, i.e., $t_p \sim A_p^{1.5}$ persists up to about $A_p \cong 40$ above which the large-pore sintering behavior, i.e., $t_p \sim A_p^{1.0}$ takes over. Indeed, the crossover pore area A_c increases roughly in proportion to the square of the grain diameter from about $A_c \cong 12$ for $G = 4.0$ to about $A_c \cong 48$ for $G = 8.0$.

The effect of the grain diameter G is summarized in Fig. 9 where we plot the remaining pore area A_R at $t = 2000 \, \tau_D$ as a function of the grain diameter G for hexagonal pores of three different initial pore
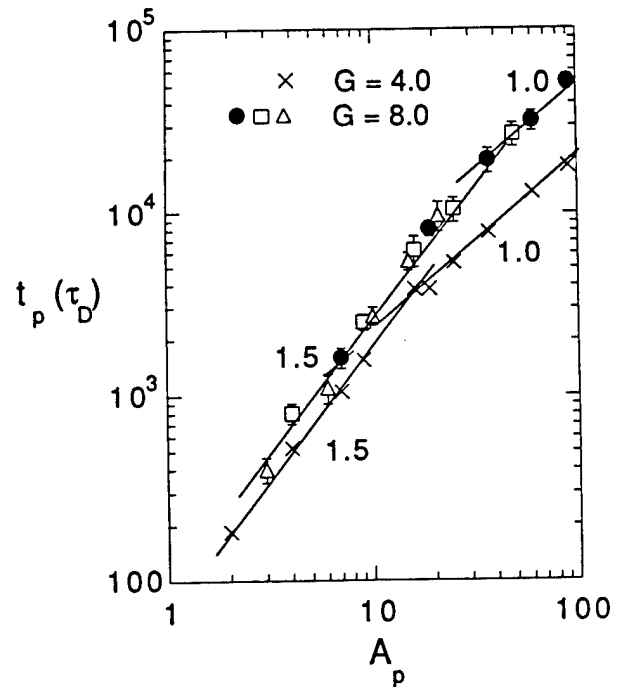
FIG. 8. t_p vs A_p at $G = 8.0$ for fixed sample size 45×45 where t_p and A_p are the same as defined in Fig. 4. Full circles, open squares, and open triangles denote initially hexagonally, rhombically, and triangularly shaped pores. Again, the data points of pores with different initial shapes all fall on the same curve, indicating that the pore elimination time is independent of the initial pore shape. The crosses are the same data points as in Fig. 4 for $G = 4.0$ shown here for comparison.
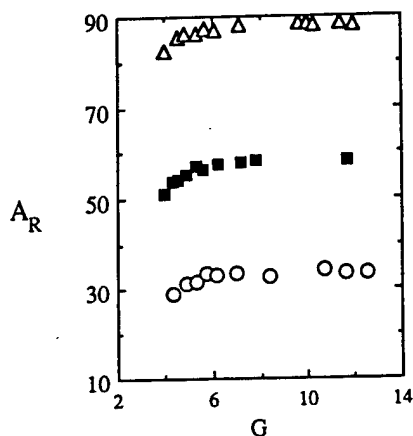
FIG. 9. A_R vs G where A_R is the remaining pore area at $t = 2000 \ \tau_D$ and G is the average grain diameter. Open circles, full squares, and open triangles denote $A_p = 37, 61$, and 91, respectively.

area: open circles, full squares, and open triangles for $A_p = 37$ (edge = 4), 61 (edge = 5), and 91 (edge = 6), respectively. Notice that on the average, pores shrank after 2000 τ_D and there exist two regimes for the pore shrinkage rate. (i) At small G, the shrinkage of pores decreases as G increases and (ii) at large G, A_R flattens out. The boundary between two regimes occurs at about $G \cong d_p$. In order to better illustrate this, we plot ΔA as a function of d_p/G in Fig. 10 where $\Delta A = A_p - A_R$ is the average decreased in the pore area at $t = 2000$ τ_D. Notice that ΔA increases linearly with d_p/G when $d_p > G$ and ΔA becomes a constant when $d_p < G$. The linear dependence of ΔA on d_p/G at $G < d_p$ evidences that grain boundaries serve as diffusion channels in the present simulations. A constant ΔA for large G indicates that the number of diffusion channels becomes

independent of G when grains are larger than the pores. The different slopes of ΔA-vs-(d_p/G) of the three curves in Fig. 10 are due to the different values of A_p. In fact, under the present simulation geometry, the pore shrinkage rate is independent of d_p and only proportional to $1/G$ for $d_p > G$. For $d_p < G$, the shrinkage is independent of G and only proportional to $1/d_p$. In Fig. 11(a), we replot ΔA as a function of $1/G$. Indeed, for large $1/G$ (small G), ΔA vs $1/G$ of $A_p = 37, 61$, and 91 all fall on the same straight line whereas for small $1/G$ (large G), ΔA is independent of G and decreases with increasing d_p. A blow-up for the small $1/G$ region in Fig. 11(a) is shown in Fig. 11(b) with the vertical axis as $\Delta A d_p/d_1$ and the horizontal axis as $1/G$ where d_1 is the initial diameter for $A_p = 37$. Indeed, $\Delta A d_p/d_1$ is a constant, indicating that in the small $1/G$ region, ΔA is independent of G and inversely proportional to d_p. A more detailed explanation will be provided with

FIG. 10. ΔA vs d_p/G for the data shown in Fig. 9. $\Delta A = A_p - A_R$ is the decrease in pore area at $t = 2000$ τ_D and $d_p = A_p^{0.5}$ is the initial pore diameter. Again, open circles, full squares, and open triangles denote $A_p = 37, 61$, and 91, respectively.
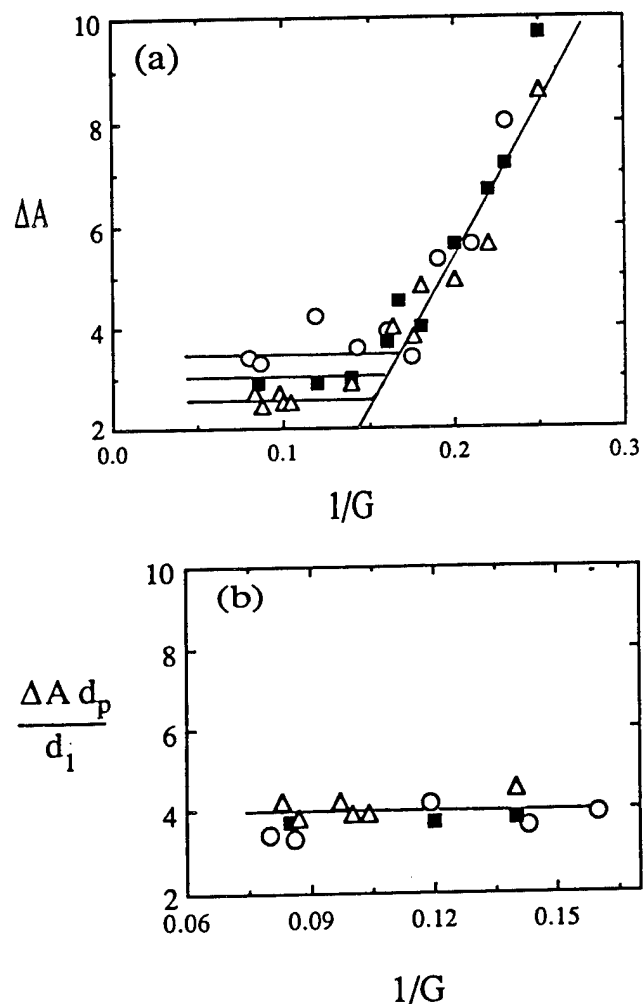
FIG. 11. (a) ΔA vs $1/G$ for the data shown in Fig. 10 and (b) $\Delta A d_p/d_1$ vs $1/G$ for the small $1/G$ region in (a). ΔA and d_p are the same as defined in Fig. 10. d_1 is the initial diameter for $A_p = 37$ and G, the average grain diameter. Again, open circles, full squares, and open triangles denote $A_p = 37, 61$, and 91, respectively.

a scaling theory in the following section. The different scaling laws for the pore elimination time as a function of the initial pore area between pores larger than the grain and pores smaller than the grain shown in Figs. 5 and 8 are reminiscent of the different pore shrinkage rates with respect to grain diameter between pores larger than the grains and pores smaller than the grains, as shown in Figs. 9–11 and are the result of grain boundaries serving as diffusion channels in the present simulations.

Qualitatively, the reason that the grain boundaries serve as diffusion channels in the present model is the following. In order for the pores to shrink, (1) vacancies must first break up with a pore and (2) vacancies must diffuse away. In both processes, vacancies must overcome an energy barrier ΔE_{ex} to exchange their positions with a neighboring vector where the energy barrier ΔE_{ex} is the energy change associated with the exchange, as depicted in Eq. (3). If the vector involved is on a grain boundary, ΔE_{ex} is reduced due to the fact that a vector on a grain boundary has a higher initial energy as depicted by Eq. (1) and hence a smaller ΔE_{ex}. This is illustrated in Figs. 12 and 13. Figures 12(a) and 12(b) illustrate an example when a vacancy breaks up with a pore and moves into a grain, i.e., by exchanging its position with that of a vector that is not

on a grain boundary (not surrounded by vectors with different orientations). Figures 12(c) and 12(d) illustrate an example when the vacancy breaks up with the pore at a grain boundary, i.e., by exchanging its position with that of a vector that is on a grain boundary (surrounded by at least one vector that has a different orientation). Comparing the ΔE_{ex} of the two processes, one can see that the process in which the vacancy moves into a grain boundary has a lower ΔE_{ex}. Figures 13(a) and 13(b) illustrate an example when a vacancy that is initially on a grain boundary moves into a grain, and Figs. 13(c) and 13(d) show an example when a vacancy moves along a grain boundary. It is clear that ΔE_{ex} is lower when a vacancy moves along a grain boundary. Therefore, vacancies tend to break up with a pore at the junction of a grain boundary with the pore surface and also tend to move along a grain boundary in the subsequent movements. Thus, in fine-grained structures such as the ones considered in the simulations, grain boundaries effectively serve as the channels for the transportation of vacancies away from the pores.

The effect of sample size was analyzed by comparing the scaling law of the pore elimination time t_p with A_p of the sample-size-fixed simulations to those obtained with the sample size varying in proportion to
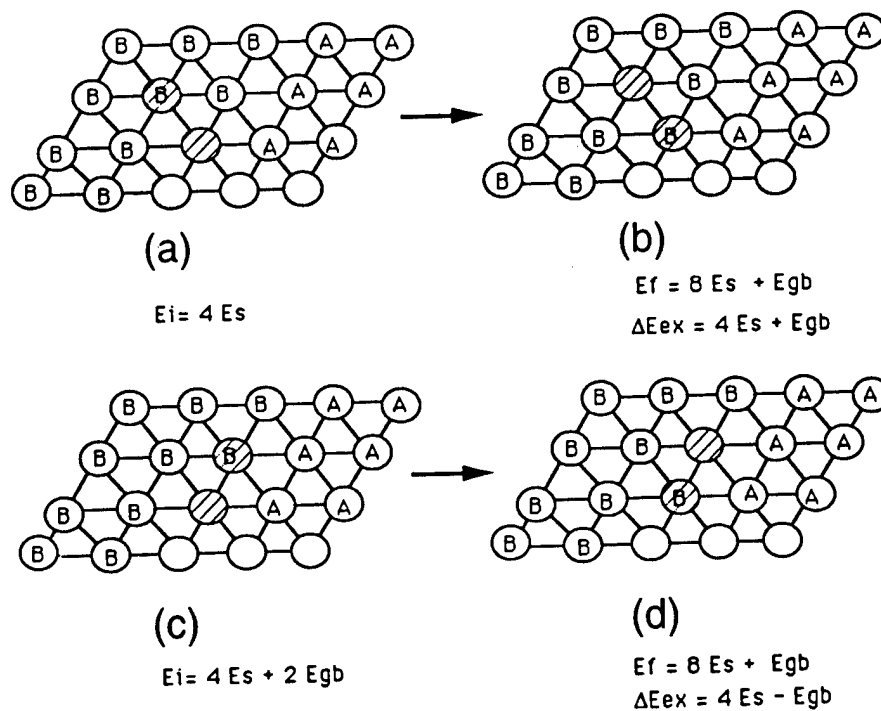
FIG. 12. (a) and (b) show an example when a vacancy breaks up with the pore by moving into a grain where (a) and (b) represent the configuration before and after the move, respectively. Meanwhile, (c) and (d) represent an example when a vacancy breaks up with the pore at a grain boundary where (c) and (d) represent the configuration before and after the move, respectively. The vacancy-vector pairs that are under consideration for the move are shaded in all figures. E_i and E_f denote the energy of the vector-vacancy pair before and after the move and $\Delta E_{ex} = E_f - E_i$. One can see that ΔE_{ex} is lower when a vacancy breaks up with the pore at the junction of a grain boundary [(c) to (d)] than at a grain surface [(a) to (b)].

d_p. The pore elimination time t_p as a function of A_p for sample-size-scaled simulations is shown in Figs. 14(a) and 14(b). Figure 14(a) shows that $t_p \sim A_p^{2.0}$ for small pores and Fig. 14(b) shows $t_p \sim A_p^{1.5}$ for large pores. Also plotted in Figs. 14(a) and 14(b) for comparison are t_p-vs-A_p results for sample-size-fixed simulations. From the comparison of the results of the sample-size-fixed simulations to that of sample-size-scaled simulations, it is clear that changing the sample size in proportion to the pore diameter gives the additional $A_p^{0.5}$ dependence, meaning that the pore elimination time is linearly proportional to the sample size in the present geometry.

It is worth noting that the simulation results indicate that pore sintering is a kinetics-dominated phenomenon rather than one solely governed by thermodynamics[4] since the simulations showed that all pores were eliminated given a sufficient amount of time and that for a given grain size, it takes longer to eliminate larger pores despite their higher pore-grain coordination number. This is in line with the experimental observations of Zhao and Harmer[12] and Slamovich and Lange.[13] However, note that although on the average, pore area decreases with time as shown in Figs. 5, 8–14, some of the larger pores can actually grow at some intermediate time. Examples are shown in Figs. 15(a)–15(d), all of which were taken at $t = 2000 \ \tau_D$. Figures 15(a) and

15(b) evolved from an initial pore area $A_p = 61$ at $G = 5.7$. The remaining pore area $A_R = 48$ in Fig. 15(a) is smaller than the initial pore area whereas the remaining pore area $A_R = 62$ in Fig. 15(b) is larger than the initial pore area. Figures 15(c) and 15(d) evolved from an initial pore area $A_p = 127$ at $G = 16$. The remaining pore area $A_R = 113$ in Fig. 15(c) is smaller than the initial pore area whereas the remaining pore area $A_R = 128$ in Fig. 15(d) is larger than the initial pore area. Note that this pore growth phenomenon is more evident with larger pores. With smaller pores, we see less pore growth. As A_p becomes larger than 60, we begin to observe pore growth and the occurrence of pore growth becomes more frequent as A_p becomes larger. The observed growth of some of the large pores can be explained as follows. The diffusional process involved in sintering is a thermally activated random process. The randomness of the diffusional process allows the possibility of a pore to expand at some finite time. This is especially so for large pores where the macroscopic driving force for shrinkage which is related to the curvature of the pore surface is reduced. It should be noted that the observed pore growth for larger pores is only a temporary phenomenon due to the random nature of the diffusional process. As we have shown above, given a sufficient amount of time, all pores will eventually be eliminated, as the macroscopic driving

(a)

$E_i = 6 E_s + E_{gb}$

(b)

$E_f = 6 E_s + 4 E_{gb}$

$\Delta E_{ex} = 3 E_{gb}$

(c)

$E_i = 6 E_s + 2 E_{gb}$

(d)

$E_f = 6 E_s + 2 E_{gb}$

$\Delta E_{ex} = 0$
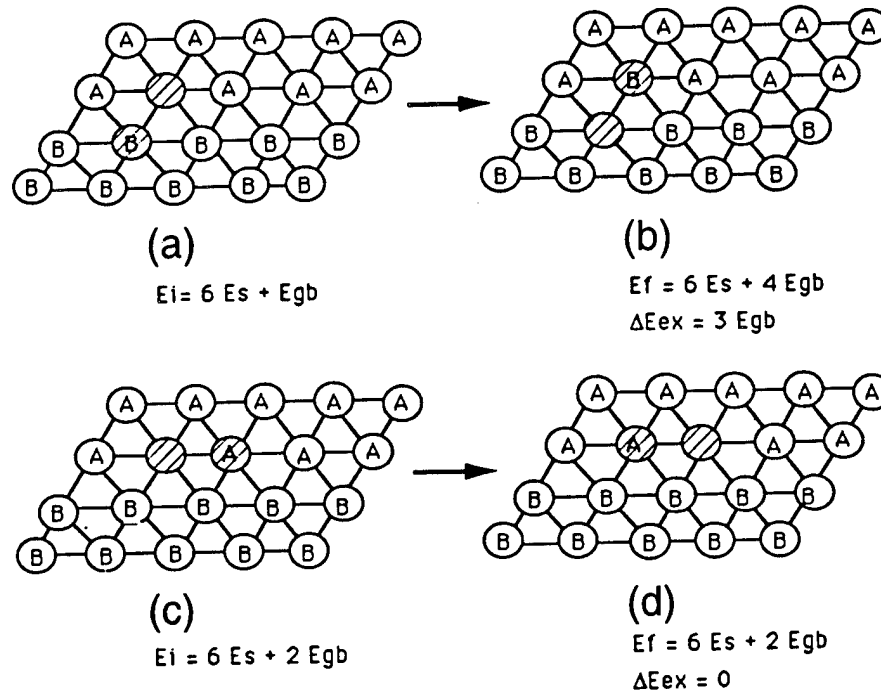
FIG. 13. (a) and (b) show an example when a vacancy that is initially on a grain boundary moves into a grain where (a) and (b) represent the configuration before and after the move, respectively. Meanwhile, (c) and (d) represent an example when a vacancy that is initially on a grain boundary moves along the grain boundary where (c) and (d) represent the configuration before and after the move, respectively. The vacancy-vector pairs that are under consideration for the move are shaded in all figures. E_i and E_f denote the energy of the vector-vacancy pair before and after the move and $\Delta E_{ex} = E_f - E_i$. One can see that ΔE_{ex} is lower when a vacancy moves along a grain boundary [(c) to (d)] than into a grain [(a) to (b)].

force consideration would suggest. This can also be seen clearly in Fig. 7. Owing to the statistical mechanical nature of the diffusional process, care must be taken when comparing simulations (or experiments) with a macroscopic theory. It is essential to do proper averaging with sufficient sampling when comparing the results of simulations or experiments to a macroscopic theory that intrinsically deals with statistically averaged quantities. This is why the results shown in this paper were all averaged over at least 100 independent runs. The scaling behaviors of the pore elimination time and that of the pore shrinkage rate we have shown above would not be clear if we had not had enough independent runs for averaging.

Finally, what drives the vacancies to leave the pore than entering the pore is the curvature (Kelvin) effect. To illustrate the curvature effect in the model, let us compare the energy of a vector right beneath a pore surface to that of a vector right beneath a flat surface. For simplicity, let us consider the solid to be single crystalline. A flat interface is depicted in Fig. 16(a) while Figs. 16(b), 16(c), and 16(d) show the pore surface of a hexagonal pore with $A_p = 1, 7$, and 19, respectively. (The corresponding edge length $L = 1$, 2, and 3, respectively.) Let E_{vet} denote the energy of a vector right beneath a vacancy-vector interface. For pore

surfaces such as those shown in Figs. 16(b)–16(d), E_{vet} is calculated by dividing the sum of the energies of all the vectors that are on the pore surface by the number the vectors on the pore surface. Thus, $E_{vet} = 2.0, 1.0$, 1.5, and 1.67 E_s for Figs. 16(a), 16(b), 16(c), and 16(d), respectively. It can be seen that E_{vet} is lower at a pore surface and that E_{vet} decreases with a decreased pore size, i.e., L. Thus, for a vector, being located right beneath a flat interface on the edges of the sample is less energetically favorable than being located right beneath a pore surface, providing the driving force for vectors on the edges of the sample to diffuse to the pore surface (or for vacancies on the pore surface to diffuse to the sample edge), resulting in pore shrinkage. Moreover, with $E_{vet,0}$ defined as the energy of a vector right beneath a flat surface, the correlation between $\Delta E_{vet} \equiv E_{vet} - E_{vet,0}$ of a hexagonal pore and the length of the pore edge L is also summarized in Table I. It is clear that ΔE_{vet} is inversely proportional to L. Note that the radius r_p of a hexagon is proportional to the length of its edge. Moreover, E_{vet} is essentially the Gibbs free energy per vector at $T = 0$ K. Therefore, that ΔE_{vet} is inversely proportional to L is reminiscent of the Kelvin effect; i.e., the Gibbs free energy difference of an atom beneath a surface with a radius of curvature R with respect to that of an atom beneath a flat surface is inverse proportional
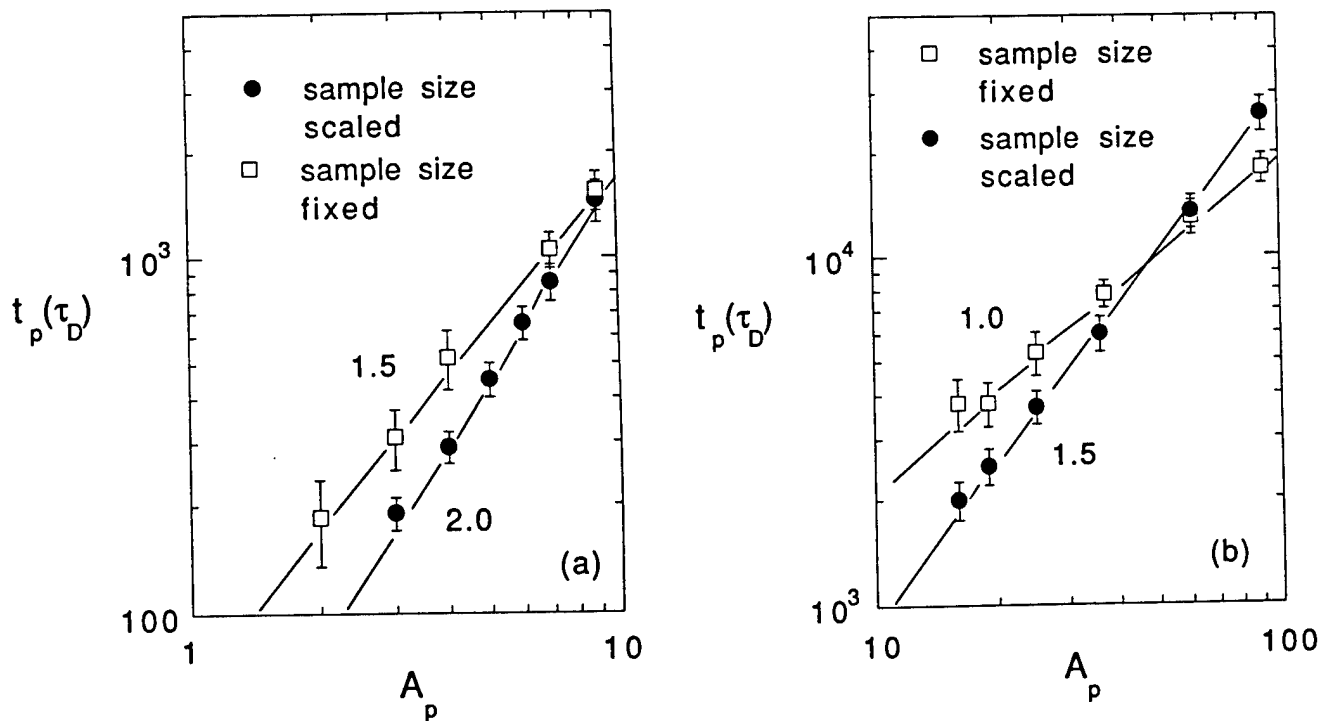
FIG. 14. t_p vs A_p at $G = 4.0$ (a) for small pores and (b) for large pores. t_p and A_p are the same as defined in Fig. 4. Full circles represent data points obtained with sample size scaled in proportion to the initial pore diameter. Also shown are the data points obtained with a fixed sample size 45 × 45 (open squares) for comparison.

TABLE I. E_{vet} represents the energy of a vector right beneath the surface of a hexagonal pore within a single crystal as depicted in Figs. 16(b)–16(d) for $A_p = 1, 7$, and 19. A_p is the pore area and L is the length of an edge of the pore $\Delta E_{vet} \equiv E_{vet} - E_{vet,0}$ with $E_{vet,0}$ as the energy of a vector right beneath a flat surface, as depicted in Fig. 16(a).

A_p	L	E_{vet} (E_s)	ΔE_{vet} (E_s)	$\Delta E_{vet} L$	
1	1	1	−1.0	−1	Fig. 16(b)
7	2	1.5	−0.5	−1	Fig 16(c)
19	3	1.67	−0.33	−1	Fig. 16(d)
37	4	1.75	−0.25	−1	Not shown

to R. The Kelvin (or curvature) effect arises from the pore geometry but not from any artificial constrains. The curvature effect is the essence both in Herring's scaling analysis and in ours that is described in the next section.

V. SCALING ANALYSIS

In order to understand the scaling relations observed in the simulations, we provide in the following a scaling analysis similar to Herring's for systems where diffusion takes place mainly through grain boundaries. Consider a two-dimensional polycrystalline sample with a pore sitting at the center of the sample as in the simulations. The pore elimination time t_p can be written as

$$t_p \sim A_p/J \sim d_p^2/J, \qquad (4)$$

where A_p is the initial pore area, $d_p = A_p^{0.5}$ the initial pore diameter, and J the atomic current flow into the pore, and J can be decomposed as

$$J = j \times S, \qquad (5)$$

(a)

(b)

(c)

(d)
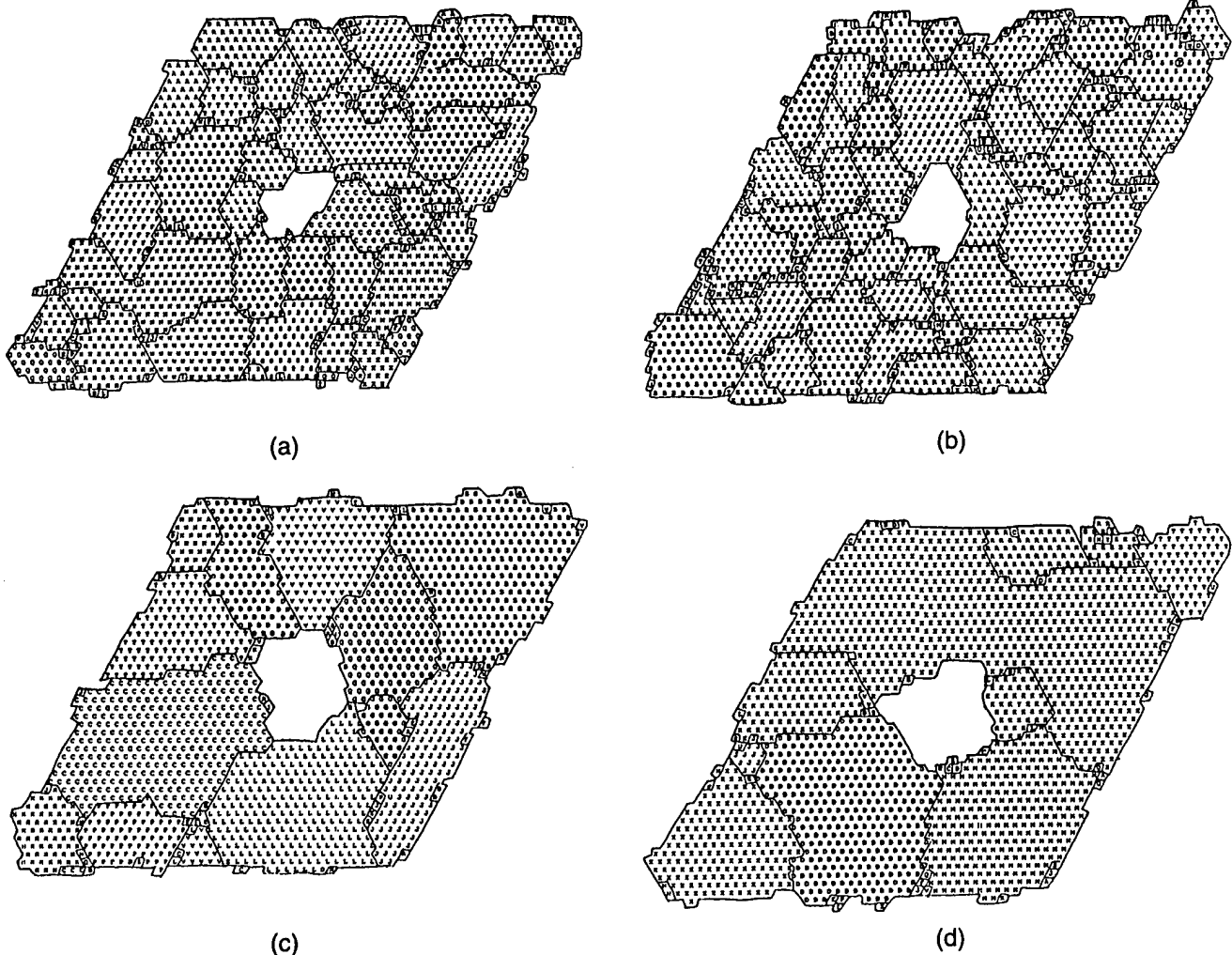
FIG. 15. Structures at $t = 2000\ \tau_D$. (a) and (b) evolved from an initial pore area $A_p = 61$ at $G = 5.7$. The remaining pore area $A_R = 48$ in (a) is smaller than the initial pore area whereas $A_R = 62$ in (b) is larger than the initial pore area. (c) and (d) evolved from an initial pore area $A_p = 127$ at $G = 16$. $A_R = 113$ in (c) is smaller than the initial pore area and $A_R = 128$ in (d) is larger than the initial pore area. Note that the pore growth phenomenon occurs more prominently with larger pores.

J. Mater. Res., Vol. 10, No. 4, Apr 1995

1011

in which j is the current density at the pore surface defined as the current per unit length and S is the total cross-section length of the grain boundaries at the pore surface. For a sample with a given average grain size G, the total cross-section length S of the grain boundaries with the pore surface should be the product of the cross-section length A_{gb} of an individual grain boundary times the number of grain boundaries intersecting the pore surface. Let us assume that the number of grain boundaries intersecting the pore surface is linear in d_p/G for $d_p > G$ and independent of d_p/G for $d_p < G$. In two dimension, A_{gb} is a constant. Therefore,

$$S \sim A_{gb}(d_p/G)^1 \sim (d_p/G)^1 \quad \text{for } d_p > G, \quad (6)$$

and

$$S \sim A_{gb}(d_p/G)^0 \sim (d_p/G)^0 \quad \text{for } d_p < G. \quad (7)$$

Note that the geometry of the present simulations for $d_p < G$ is comparable to that in Coble's pore sintering theory,[3] namely, the pores are smaller than the grains and are located at junctions of grains. In Coble's theory, the number of grain boundaries intersecting the pore surface is fixed. This is equivalent to saying that the number of grain boundaries is independent of d_p/G. Thus, the

assumption that the number of the grain boundaries intersecting the pore surface is independent of d_p/G for $d_p < G$ is consistent with what was assumed in Coble's theory, which was basically based on experimental observations.[3] While the previous sintering theories did not consider situations for pores larger than the grains, the different scaling laws observed in the present simulations between $d_p < G$ and $d_p > G$ revealed that the dependence of the number of the grain boundaries intersecting the pore surface on d_p/G can be different in the two regimes. As we will show below, by taking into account such difference in the dependence of the number of the grain boundaries intersecting the pore surface on d_p/G between $d_p < G$ and $d_p > G$ and with a proper scaling analysis, one can reproduce the scaling relationships observed in the simulations.

The current density j is related to the diffusivity and the chemical potential gradient of atoms as

$$j = -M\nabla\mu, \quad (8)$$

where $M = Dc/kT$ with D as the diffusion coefficient, c the concentration, k the Boltzmann constant, and T the sintering temperature. In the present simulation geometry, the density j at the pore surface can be

(a)

(b)

(c)

(d)
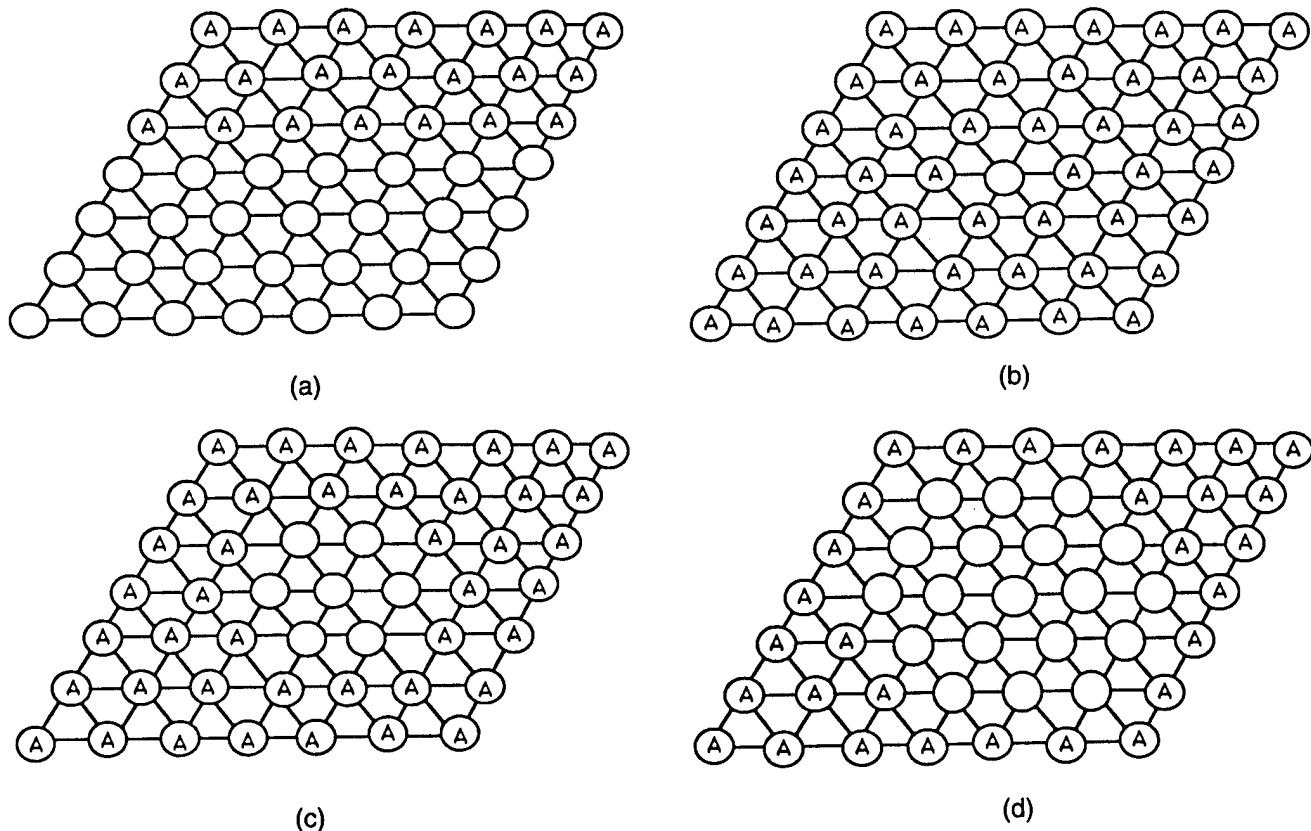
FIG. 16. The interface between a single crystalline solid as represented by vectors A and the vacuum. (a) represents a flat interface; and (b), (c), and (d) depict the pore surface of a hexagonal pore of $A_p = 1$, 7, and 19, respectively.

approximated as

$$j \sim M(\mu_p - \mu_{out})/r,\qquad(9)$$

where r is the distance from the pore surface to the outer surface of the sample and μ_p and μ_{out} are the chemical potentials of atoms at the pore surface and that at the outer surface of the sample, respectively. Using the Kelvin equation, the chemical potential of an atom at a curved surface is related to the radius of curvature r_s of the curved surface and the surface tension σ as

$$\mu = \mu_0 + V\sigma/r_s,\qquad(10)$$

in two dimensions where μ_0 is the chemical potential of an atom in the bulk solid phase with a flat surface and V is the atomic area. Therefore,

$$\mu_p - \mu_{out} \sim 2V\sigma(d_p^{-1} - d_{out}^{-1}),\qquad(11)$$

where d_p and d_{out} are the diameter of curvature of the pore surface and that of the outer surface of the sample, respectively. The current density j at the pore surface can be rewritten as

$$j \sim (d_p^{-1} - d_{out}^{-1})/r.\qquad(12)$$

Combining Eqs. (6), (7), and (12), we obtain

$$J \sim (d_p/G)(d_p^{-1} - d_{out}^{-1})/r \quad \text{for } d_p > G,\qquad(13)$$

and

$$J \sim (d_p^{-1} - d_{out}^{-1})/r \quad \text{for } d_p < G.\qquad(14)$$

The pore elimination time t_p is then

$$t_p \sim d_p^2 r(d_p/G)^{-1}(d_p^{-1} - d_{out}^{-1})^{-1} \quad \text{for } d_p > G,\qquad(15)$$

and

$$t_p \sim d_p^2 r(d_p^{-1} - d_{out}^{-1})^{-1} \quad \text{for } d_p < G.\qquad(16)$$

(i) Size-fixed samples

For size-fixed samples, if the sample size is sufficiently larger than the pore diameter as in the simulations, the outer surfaces can be approximated as flat surfaces, namely, $1/d_{out} \cong 0$ and the distance r from the pore surface to the outer surface can be regarded as a constant. Therefore, the current density j at the pore surface reduces to

$$j \sim d_p^{-1}.\qquad(17)$$

The total current through the pore surface reduces to

$$J \sim G^{-1} \quad \text{for } d_p > G,\qquad(18)$$

and

$$J \sim d_p^{-1} \quad \text{for } d_p < G.\qquad(19)$$

Note that Eqs. (18) and (19) are indeed in agreement with the shrinkage rate result shown in Figs. 11(a) and 11(b). The pore elimination time for sample-size-fixed simulations reduces to

$$t_p \sim d_p^2(d_p/G)^{-1}d_p \sim Gd_p^2 \quad \text{for } d_p > G,\qquad(20)$$

and

$$t_p \sim d_p^2(d_p^0/G^0)^{-1}d_p \sim d_p^3 \quad \text{for } d_p < G.\qquad(21)$$

One can see that Eqs. (20) and (21) indeed describe the scaling relations observed in the simulations shown in Figs. 5 and 8. The crossover pore diameter d_c can be obtained by equating the right-hand side of Eq. (20) to that of Eq. (21),

$$d_c \sim G.\qquad(22)$$

Again, Eq. (22) is in agreement with the result shown in Fig. 8 where the crossover pore area A_c increases in proportion to G^2.

The agreement between the results of the scaling analysis shown in Eqs. (18)–(22) and the simulation results indicates that the number of diffusion channels is indeed linear in d_p/G for $d_p > G$ and independent of d_p/G for $d_p < G$, as depicted in Eqs. (6) and (7).

(ii) Size-scaled samples

In size-scaled samples, r, d_p, d_{out} all change in proportion. Therefore, the current density j at the pore surface for size-scaled samples becomes

$$j \sim d_p^{-2}.\qquad(23)$$

The total flux for size-scaled samples becomes

$$J \sim (Gd_p)^{-1} \quad \text{for } d_p > G,\qquad(24)$$

and

$$J \sim d_p^{-2} \quad \text{for } d_p < G.\qquad(25)$$

The pore elimination time t_p for sample-size-scaled simulations becomes

$$t_p \sim d_p^2(d_p/G)^{-1}d_p^2 \sim Gd_p^3 \quad \text{for } d_p > G,\qquad(26)$$

and

$$t_p \sim d_p^2(d_p^0/G^0)^{-1}d_p^2 \sim d_p^4 \quad \text{for } d_p < G,\qquad(27)$$

in agreement with the result shown in Figs. 12(a) and 12(b). Note that the scaling relations among the pore elimination time t_p, the pore diameter d_p, and the grain diameter G shown in Eqs. (20)–(21) and (26)–(27) are independent of the dimensionality of the system. This can be shown as follows.

Consider a d-dimensional system. The pore area A_p in Eq. (4) is now replaced by the pore "volume"

$$V_p \sim d_p^d,\qquad(28)$$

J. Mater. Res., Vol. 10, No. 4, Apr 1995

1013

where d is the dimension of the system. In two dimensions, the intersections of grain boundaries with the pore surface are an array of dots and the length A_{gb} of each dot is a constant, as depicted in Eqs. (6) and (7). In d dimensions, the intersections of grain boundaries with the pore surface can be approximated as arrays of "lines" and the "area" A_{gb} of each "line" is no longer a constant but dependent on the pore diameter d_p. A_{gb} can be written as

$$A_{gb} \sim w_{gb} d_p^{d-2}, \tag{29}$$

where w_{gb} is the grain-boundary width. Equation (29) satisfies that in two dimensions, these "lines" are actually dots with a constant length A_{gb}, and in three dimensions these "lines" are lines with a width w_{gb} and a length on the order of d_p. For $d_p > G$, there will be an array of d_p/G such "lines" in each of the $d - 1$ dimensions of the pore surface. For $d_p < G$, the number of such "lines" will be constant. Thus, the total cross-section area at the pore surface becomes

$$S \sim (d - 1)(d_p/G)^1 w_{gb} d_p^{d-2} \sim d_p^{d-1} G^{-1}$$
$$\text{for } d_p > G, \tag{30}$$

and

$$S \sim (d_p/G)^0 w_{gb} d_p^{d-2} \sim d_p^{d-2} \quad \text{for } d_p < G. \tag{31}$$

Note that the $(d - 1)$ and G^{-1} dependence in Equation (30) is similar to the relationship[15]

$$S_v = 2/G, \tag{32}$$

between the grain boundary area per unit volume S_v and the average grain diameter G in three dimensions where $d - 1 = 2$ and d_p in Eq. (30) is replaced by unity. Thus, in d dimensions, the total flux becomes

$$J \sim d_p^{d-1} G^{-1}(d_p^{-1} - d_{out}^{-1})/r \quad \text{for } d_p > G, \tag{33}$$

and

$$J \sim d_p^{d-2}(d_p^{-1} - d_{out}^{-1})/r \quad \text{for } d_p < G. \tag{34}$$

The pore elimination time is

$$t_p \sim V_p/J \sim r d_p G(d_p^{-1} - d_{out}^{-1})^{-1} \quad \text{for } d_p > G, \tag{35}$$

and

$$t_p \sim V_p/J \sim r d_p^2 (d_p^{-1} - d_{out}^{-1})^{-1} \quad \text{for } d_p < G. \tag{36}$$

One can see that the d_p^d factor in V_p cancels the d_p^d factor in S. As a result, the scaling relations among t_p, d_p, and G do not depend on the dimensionality of the system. Therefore, Eqs. (20)–(21), and (26)–(27) also hold for three dimensions.

It is interesting to note from Eqs. (30) and (31) that the total cross section S of the diffusion channels at the pore surface has a volume-diffusion-like feature, d_p^{d-2} dependence for small pores. These features give rise to the similarity of the scaling relation $t_p \propto d_p^3$ for large pores in our sample-size-scaled simulations to Herring's scaling for volume diffusion, and the similarity of the scaling $t_p \propto d_p^4$ for small pores in our sample-size-scaled simulations to Herring's scaling for surface diffusion. The similarity between the scaling relations observed in our simulations and those of Herring's scaling theory arises from the curvature effect in the chemical potential as we have discussed above, which is essential both in Herring's theory and in our simulations. However, it must be noted that Herring considered lattice diffusion in his theory and there was no consideration of the grain-size effect, whereas in the present simulations, sintering is governed by grain-boundary diffusion.

VI. CONCLUDING REMARKS

We have investigated the grain-size effect on sintering, in particular, the elimination of an isolated pore both with the Monte Carlo simulations and with a scaling analysis. The Monte Carlo simulations were carried out with a general microscopic statistical mechanics model in which microstructures were mapped onto domains of vectors as grains and domains of vacancies as pores. More importantly, we allow vacancies to move in the simulations. By incorporating the outer surfaces of the sample in the simulations, sintering took place via the diffusion of vacancies from the pores to the outer surfaces. The simulations were carried out in two dimensions. The model was shown capable of displaying various sintering phenomena such as evaporation and condensation, rounding of a sharp corner, pore coalescence, thermal etching, neck-formation, grain growth, and growth of large pores. Because of the fine-grained microstructures considered in the simulations, the transport of vacancies was mainly through grain boundaries. We showed that the pore elimination time is independent of the initial pore shape as consistent with the pore-shape change observed during the course of simulation. Experimental observations also support pore-shape change during sintering.[12-14] For $d_p > G$, the pore shrinkage rate is linear in $1/G$ and independent of d_p and for $d_p < G$, the pore shrinkage rate is independent of G and inversely proportional to $1/d_p$, resulting from grain boundaries serving as diffusion channels. The number of grain boundaries intersecting the pore surface is independent of d_p/G for $d_p < G$ and is proportional to d_p/G for $d_p > G$. Another manifestation of the grain-boundary-diffusion mechanism is that the scaling law of t_p with respect to d_p for $d_p > G$ is different from that for $d_p < G$.

For samples with a fixed sample size much larger than the pore size, $t_p \propto d_p^2$ for $d_p > G$ and $t_p \propto d_p^3$ for $d_p < G$. In sample-size-scaled simulations $t_p \propto d_p^3$ for $d_p > G$ and $t_p \propto d_p^4$ for $d_p < G$. The additional one power of d_p dependence in t_p for $d_p < G$ as compared to that for $d_p > G$ is due to the fact that the number of diffusion channels is independent of d_p/G for $d_p < G$ and is proportional to d_p/G for $d_p > G$. The pore elimination time t_p has one additional power of d_p dependence in the sample-size-scaled simulations as compared to the sample-size-fixed simulations, indicating that t_p is proportional to the sample size. We explained these scaling relationships with a scaling analysis and further showed that the scaling relationships among t_p, d_p, and G should be independent of dimensionality. Therefore, the result of the present simulations should also hold for three dimensions.

The transport of matter (or vacancies) in the present simulations is mainly through grain boundaries due to the fine grain structures considered. In order to compare the results of the present simulations with experiments, the experimental systems must also have fine grains. Although the diffusion coefficient of vacancies is higher along grain boundaries, the cross-section area of grain boundaries may not be comparable to that of grains with large grains. As the ratio of the cross-section area of grain boundaries to that of the grains is increased with a decreasing grain size, the total current through grain boundaries may become larger than that through the grains.

The following is an estimate of the largest grain size of an experimental system for comparing with the present results. Let us assume that the chemical potential gradient at the grain boundaries is the same as that in the grains. For pores larger than the grains, the current through the grain boundaries J_{gb} is proportional to $D_{gb}w_{gb}$ and that through the grains J_g is proportional D_gG where D_{gb}, D_g are the diffusion coefficient in the grain boundaries and that in the grains, respectively. When the ratio $J_{gb}/J_g = (D_{gb}w_{gb})/(D_gG)$ is larger than unity, grain-boundary diffusion becomes more important than lattice diffusion. The largest grain size G_c below which grain boundary diffusion is important is thus given by

$$G_c = D_{gb}w_{gb}/D_g . \qquad (37)$$

The value for G_c will depend on the material. For example, given the width of a grain boundary about 5 Å, if the ratio of the diffusion coefficient along the grain boundaries to that of grains is 10^4, G_c will be 5 μm.

Finally, it is worth mentioning that a similar scaling crossover has also been observed in the neck growth between two nanometer-sized gold particles[16] and in simulations of neck growth between two particles.[17]

ACKNOWLEDGMENTS

REFERENCES

1. For example, see I. A. Aksay, W. Y. Shih, and M. Sarikaya, in *Ultrastructure Processing of Advanced Ceramics*, edited by J. D. Mackenzie and D. R. Ulrich (John Wiley & Sons, New York, 1988), p. 393.
2. E. B. Slamovich and F. F. Lange, J. Am. Ceram. Soc. **73**, 3368–3375 (1990).
3. R. L. Coble, J. Appl. Phys. **32**, 787 (1961).
4. W. D. Kingery and B. Francois, in *Sintering and Related Phenomena*, edited by G. C. Kuczynski, N. A. Hooton, and C. F. Gibbon (Gordon and Breach, New York, 1967), pp. 471–496.
5. M. P. Anderson, D. J. Srolovitz, G. S. Grest, and P. S. Sahni, Acta Metall. **32**, 783 (1984).
6. J. E. Burke, J. Am. Ceram. Soc. **40**, 80 (1957).
7. G. N. Hassold, I-W. Chen, and D. J. Srolovitz, J. Am. Ceram. Soc. **73**, 2857 (1990); I. W. Chen, G. N. Hassold, and D. J. Srolovitz, J. Am. Ceram. Soc. **73**, 2865 (1990).
8. C. Herring, J. Appl. Phys. **21**, 301 (1950).
9. M. Schick and W-H. Shih, Phys. Rev. B **35**, 5030 (1987).
10. *Application of the Monte Carlo Method in Statistical Physics*, edited by K. Binder (Springer-Verlag, 1987).
11. F. Y. Wu, Review of Modern Physics **54**, 235 (1982).
12. J. Zhao and M. P. Harmer, J. Am. Ceram. Soc. **71**, 530 (1988).
13. E. B. Slamovich and F. F. Lange, J. Am. Ceram. Soc. **75**, 2498–2508 (1992).
14. J. Rodel and A. M. Glaeser, J. Am. Ceram. Soc. **73**, 3302 (1990).
15. For example, see p. 219 in L. H. Van Vlack, *Elements of Materials Science and Engineering*, 6th ed., Addison-Wesley, 1989.
16. J. Liu, M. Sarikaya, W. Y. Shih, and I. A. Aksay, unpublished.
17. W. Y. Shih, W-H. Shih, and I. A. Aksay, unpublished.

J. Mater. Res., Vol. 10, No. 4, Apr 1995

1015

NANOCOMPOSITE PROCESSING VIA INFILTRATION OF MESOPOROUS SILICA

U. Srinivasan,[#*] I. Homma,[#*] C. M. Chun,[‡*] D. M. Dabbs,[#*] D. A. Hajduk,[†*] S. M. Gruner,[†*] and I. A. Aksay[#*]

Departments of [#]Chemical Engineering, [‡]Geological and Geophysical Sciences, and [†]Physics; and *Princeton Materials Institute, Princeton University, Princeton, New Jersey 08544-5211

Synthesis of materials with nanoscale (1~100 nm) organization is important in various applications. Recently, scientists at Mobil described a new family of mesoporous molecular sieves.[1] These materials have regular arrays of uniform pore channels ranging from 1.6~10 nm in diameter in contrast to other mesoporous solids such as amorphous silicas and modified layered clays and silicates.[2] A surfactant-silicate co-assembly model has been proposed to explain the formation of these materials.[3] According to this pathway, the matching of the charge density at the organic-inorganic interface controls the assembly of the mesophases and four distinct silica mesophases have been observed, lamellae, hexagonally packed tubes, and two bicontinuous structures of cubic symmetry. Different phases are constructed by varying the synthesis parameters such as the surfactant/silicate ratio and the acidity. Here, we report the synthesis of a new amorphous mesoporous phase with short range order and with no long range crystallinity. Due to its interpenetrating network structure, this amorphous mesoporous silica can be used as a matrix for nanocomposite processing. Here, we use it as a host to process ruby glass.

In order to synthesize this amorphous mesoporous silica (AMS) phase, 1.11 g of $C_{16}TMACl$ (29% aqueous solution, Akzo Chem.), 11.2 g of 10 N HCl, and 400 g of deionized water are stirred for 10 min. Then, 32 g of TEOS (Alpha Chem.) is added and the solution is stirred for 15 min or until the solution becomes transparent. The mixture is poured into a flat dish and is allowed to evaporate in a fume hood until a transparent solid forms. These (AMS) samples were ground and dispersed in methanol using ultrasonication. TEM (Fig. 1) shows no periodic order. XRD (Fig. 2) shows a single broad maximum consistent with disordered pores with ca. 8 nm spacing. The transparent samples were calcined at 600°C for 4 hours to remove the surfactant from the mesopores. After heat treatment, the AMS samples remain transparent and colorless. BET surface area analysis (Micromeritics Flow Sorb II2300) gives surface areas of 680 m^2/g. Since calcined AMS materials are transparent and have high surface areas, they are prime candidates for infiltration with another material to form a nanocomposite.

In order to dope the AMS samples with nanosized metallic gold, calcined AMS pieces were soaked overnight in a 10 wt% aqueous solution of gold (III) chloride (Aldrich Chem.). Next, the pieces were carefully washed with deionized water to remove the excess gold chloride ions adsorbed onto their surfaces. Then, the pieces were soaked in a 1 wt% aqueous solution of citric acid, trisodium salt dihydrate (Aldrich Chem.) to reduce the adsorbed anions to metallic gold inclusions. At this stage, the thick films became purple while maintaining transparency. This color change can be attributed to the plasmon absorption of the nanosized gold particles encapsulated within the mesochannels of the AMS films. TEM (Fig. 3) shows that following reduction, the particles in the mesopores aggregate with those from neighboring channels to form branched clusters approximately 10 nm in diameter. In comparison to physical infiltration techniques which involve ion implantation, high-vacuum evaporation and plasma processing, the low-temperature route to nanocomposite synthesis described in this paper is economical and can be used to create other nanocomposites for electronic and optical applications.

References:

1. J. S. Beck *et al.*, *J. Am. Chem. Soc.*, **114**(1992)10834.
2. C. T. Kresge *et al.*, *Nature*, **359**(1992)710.
3. M. D. McGehee *et al.*, *Proc. Ann MSA Meeting*, **52**(1994)448.
4. This work was supported by a grant from the U. S. Air Force Office of Scientific Research AFOSR-F49620-93-1-0259 and made use of MRSEC Shared Facilities supported by the NSF under Award Number DMR-940032.

1
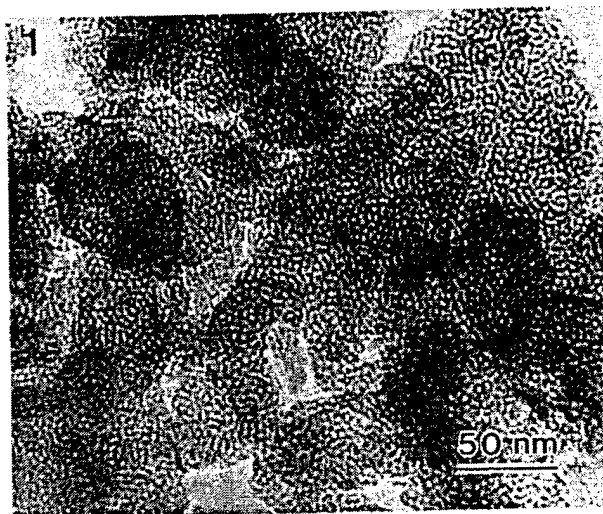
2
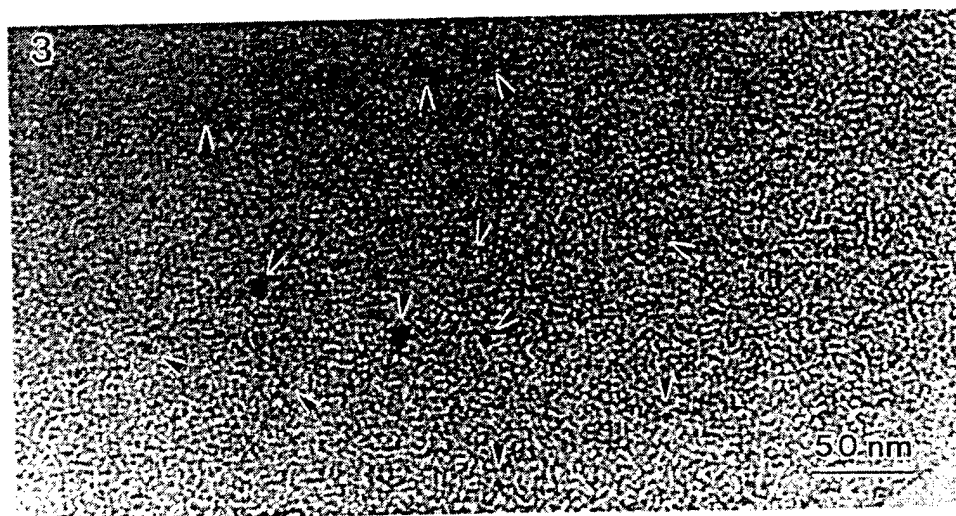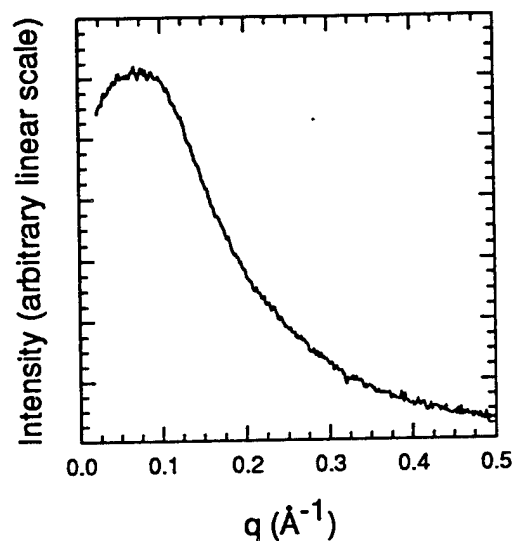
FIG.1.—TEM image of an amorphous mesoporous silicate (AMS) material.

FIG.2.—Low angle XRD spectra for an AMS material.

FIG.3.—TEM image of calcined AMS material infiltrated with nanosized gold inclusions.

Electric-field-induced pattern formation in colloidal dispersions

M. Trau, S. Sankaran, D. A. Saville & I. A. Aksay

Department of Chemical Engineering and
Princeton Materials Institute, Princeton University, Princeton,
New Jersey 08544-5263, USA

THE formation of patterned colloidal structures from dispersions of particles has many potential uses in materials processing[1-3]. Structures such as chains of particles that form in the presence of electric or magnetic fields are also central to the behaviour of electrorheological fluids[4-6] and ferrofluids[7]. Electrohydrodynamic effects in aqueous suspensions have been described by Rhodes *et al.*[8]. Here we show that such effects can be used to create structures within a non-aqueous colloidal dispersion of dielectric particles. When the conductivity of a particle-rich spherical region (bolus) is higher than that of the surrounding fluid, an electric field deforms the bolus into a prolate ellipsoid. If the conductivities are reversed (by adding salt to the surrounding fluid, for example), a disk-like shape results. In this way, we form colloidal columns, disks and more complex structures. Once formed, these could be frozen in place by solidifying the fluid matrix by gelation or polymerization[9].

We work with a simple model system—a spherical bolus containing suspended particles (region 1)—nested inside clear ambient fluid (region 2). The transition between the suspension and the clear fluid is gradual and smooth, without an interfacial tension. Its thickness is determined by a combination of brownian diffusion and sedimentation. Because of the particles, the dielectric constant, ε_1, and conductivity, σ_1, of region 1 differ from those of region 2 (that is, $\varepsilon_1 \neq \varepsilon_2$, $\sigma_1 \neq \sigma_2$). The mismatch between the dielectric constants of the two regions results from intrinsic differences between particles and fluid and polarization of any diffuse double layer (ion cloud) around each charged particle. Differences in conductivity arise from several factors: (1) particles impede ion flow and hence reduce the conductivity; (2) dissolved ions from the particles increase the local conductivity; and (3) σ_1 and σ_2 may be artificially increased by selectively dissolving a soluble salt. Left on its own and given time to come to equilibrium, the system will either become completely mixed via brownian diffusion or form a flat layer of particles owing to sedimentation. When subject to an electric field, the transition layer between regions 1 and 2 (that is, the region where ε and σ vary spatially) experiences an anisotropic electrostatic body force. This sets the suspension in motion and distorts the shape of the bolus. If mismatches in conductivity and dielectric constant are large enough, the electrohydrodynamic force will be dominant. It is this force which we exploit to manipulate the structure of a colloidal dispersion. The effect under study is not an 'electrorheological effect', although it may be present in electrorheological systems. The commonly accepted origin of the electrorheological effect is dipole–dipole interactions between the suspended particles induced by the applied field[4,6], whereas the effects under study result from bulk fluid motion induced by electrical body forces acting on the suspension.

We used 100-nm barium titanate ($BaTiO_3$) particles prepared by a hydrothermal process[10] and dispersed in castor oil. Barium titanate was chosen because it has an extremely high dielectric constant[11], typically between 300 and 10,000, depending on the crystalline form, and is a technologically useful material in both the electronic and optical component industries[12,13]. Castor oil was chosen as the fluid medium because: (1) it has a low conductivity ($\sigma = 1.8 \times 10^{-11}$ S m^{-1}); (2) fatty-acid-based oils are good dispersing media for $BaTiO_3$ particles[14]; and (3) its conductivity may easily be varied over a wide range by doping with small amounts of soluble organic salts (for example, tetrabutyl-ammonium tetraphenylborate, TBATPB). Two experiments were performed to illustrate the importance of the conductivity mismatch in setting the direction of flow for the spherical geometry described above (see Fig. 1). In the first experiment, the conductivity of the dispersion was adjusted to be ~100 times higher than that of the clear fluid by dissolving a trace amount of an organic salt (to give 0.2 mM TBATPB) in the $BaTiO_3$ dispersion before injection. In the second experiment, the conductivity mismatch was reversed by dissolving the organic salt in the clear castor oil before injecting the dispersion. Figure 1 illustrates results from both experiments. In the sequence Fig. 1*a-d* (with higher conductivity on the inside), the spherical bolus deforms in the direction of the applied field and continues to stretch until it collides with the top electrode to form a near-perfect column. The column remains intact for several seconds until the disturbance generated at its top (see Fig. 1*d*) propagates down the entire length. In the sequence Fig. 1*e-h*, a dramatically different flow pattern is engendered by the field. Here the spherical bolus deforms orthogonal to the applied field, forming a disk shape which continues to expand laterally. After some time, a film forms across the bottom electrode. Steady (d.c.) fields were used to generate all of the patterns shown in Fig. 1, but the direction and speed of the motion is insensitive to field polarity. Similar flow patterns are induced by applying low-frequency a.c. fields (~100 Hz), which shows that the particle motions are not the result of electrokinetic phenomena; they can be explained in terms of an electrohydrodynamic flow.

In order to achieve useful pattern formation in these systems, however, the deliberate manipulation of colloidal structure over long periods of time is of much greater interest. For this technique to be useful for any of the applications mentioned earlier,
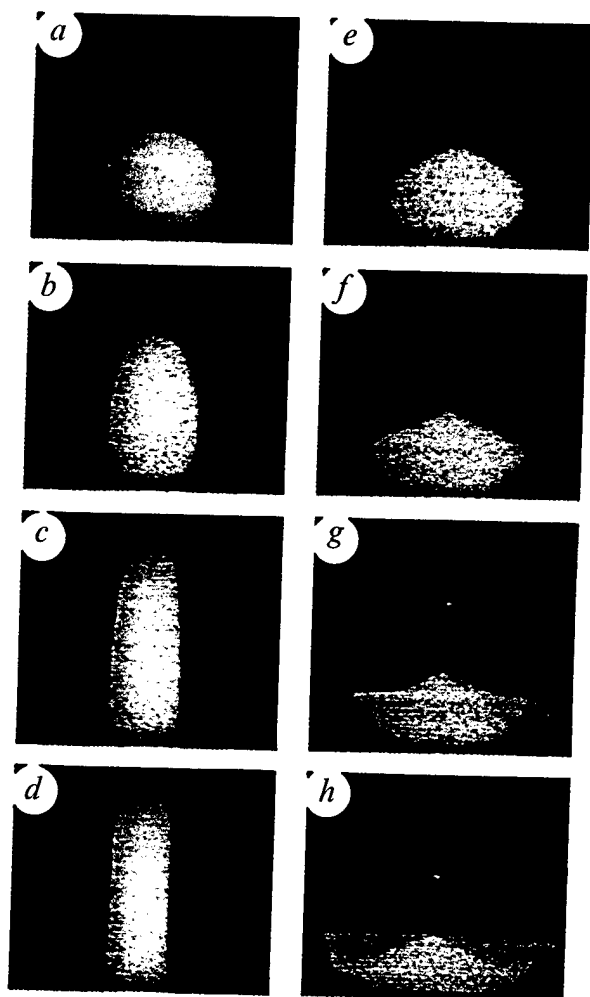
FIG. 1 *a–d* and *e–h*, Two examples of the deformation of a colloidal dispersion by means of an applied electric field. A dilute dispersion of 100-nm diameter $BaTiO_3$ particles (0.025 vol%) in castor oil was injected into clear castor oil fluid through a pinhole in a metal electrode. Slow injection of the dispersion into the clear fluid results in a spherical bolus of the dispersion nested within clear castor oil (*a, e*). The 4×4 cm metal electrodes were 1.5 cm apart; the diameter of the colloidal bolus was ~5 mm. *a–d* And *e–h* are video image sequences taken after a steady d.c. field, $2,000 \, V \, cm^{-1}$, was applied in the vertical direction. The resulting photographs have been electronically coloured to enhance the contrast between particle-containing regions and clear fluid. In the two experiments the conductivity mismatch between the inner and outer bolus region was reversed by selectively dissolving a trace amount of tetrabutylammonium tetraphenylborate (TBATPB) (0.2 mM) either in the inner region (*a–d*) or in the surrounding clear fluid (*e–h*). The measured conductivity of a 0.2 mM solution of TBATPB in castor oil was $2.28 \times 10^{-9} \, S \, m^{-1}$, ~100 times higher than that of pure castor oil. The time interval between panels is ~0.2 s.

the formed colloidal structures must remain stable for a sufficiently long time to enable the surrounding fluid to be solidified by means of (for example) polymerization or gelation techniques. Unfortunately, the long-term evolution of such patterns is extremely difficult to predict for two reasons; (1) any fluid motion will deform the sample and alter the conductivity and dielectric constants from their initial values, and (2) the morphology of the transition layer (that is, both the ion- and particle-concentration profiles) will change as a result of flow induced by electrohydrodynamic, diffusion and sedimentation effects. Generally, the transition layer will become more diffuse with time. Figure 2 shows the simultaneous deformation of eight identical spherical $BaTiO_3$ suspension boli into a ringed columnar structure by the application of a steady d.c. field

$(500 \, V \, cm^{-1})$. This type of slow deformation results in a columnar structure from each bolus. At the tip of each column a sharp spike forms, which continues to sharpen parallel to the field, stretching the column to a gradually thinner diameter (measured by laser diffraction to be $<30 \, \mu m$). By applying a low-frequency a.c. field (for example, $4,000 \, V \, cm^{-1}$, 100 Hz in Fig. 2), colloidal spikes are formed over a much larger time period and remain stable for more than three hours before any evidence of dissipation. This time is sufficient for polymerization of the ambient fluid, as previously described[9]. Obviously, the formation of such structures is not limited to forming eight columns at a time. Multiple thin films may also be formed in this manner.

In the situations just described, motion arises from two sorts of electrical body forces, one stemming from a polarization force arising from gradations in the dielectric constant, the other due to the action of the applied field on induced free charge. Electric
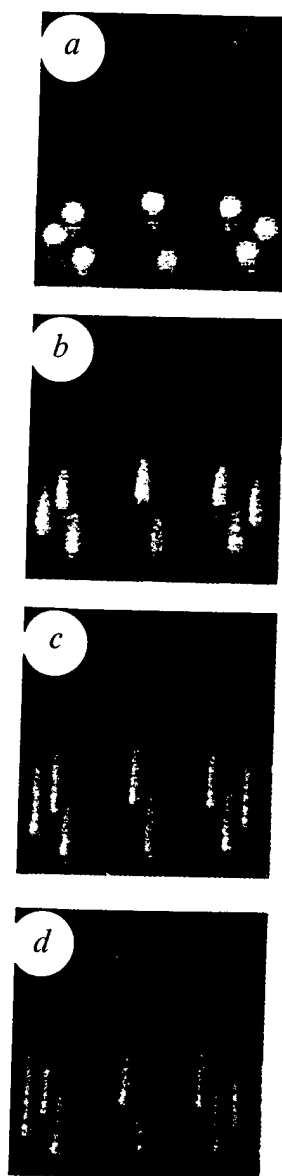
FIG. 2 The formation of multiple colloidal columns/spikes by means of electrohydrodynamic flow. *a–d* represent a sequential series of video images taken after a steady d.c. field ($500 \, V \, cm^{-1}$) was applied to eight identical spherical boli of the $BaTiO_3$ dispersion described in Fig. 1. The separation distance between columns is 7 mm. The slight bow in these columns is thought to be due to a hydrodynamic interaction between the columns and the vessel wall or between adjacent columns.

438

FIG. 3 Streamline pattern for flow engendered by a circular-shaped cloud of dispersion immersed in a clear fluid with a lower conductivity and dielectric constant, calculated from the model described in the text.

forces can be described in terms of Maxwell's stress tensor or as a body force[15,16], that is,

$$f_e = -\tfrac{1}{2}\varepsilon_0 E \cdot E \nabla \varepsilon + \rho_e E$$

where f_e is the electric body force per unit volume, ε_0 is the permittivity of free space, E is the electric field strength, $\nabla\varepsilon$ is the gradient of the local dielectric constant, and ρ_e is the free charge per unit volume. Gradations in the dielectric constant arise from the factors mentioned earlier. Free charge stems from the polarizing action of the applied field on ions that carry the current. To calculate the flow field arising from the action of these electrical body forces, the Stokes equations must be solved; clearly, one must know how the dielectric constant, charge and electric field are distributed to do this[8,17]. In our calculation, we take account of effects due to the polarization force and the force engendered by free charge created by the action of the imposed field in regions where the dielectric constant and conductivity vary smoothly. Accordingly, in addition to the Stokes equations, we employ equations for transport of charge along with the relation between charge and potential, and solve for the flow field numerically.

A qualitative picture of the flow patterns can be obtained from a simple model where the dielectric constant and conductivity distributions are prescribed. This was done for situations where a transverse electric field acts on a circular region with dielectric constant ε_1 and conductivity σ_1, surrounded by a region with properties σ_2 and ε_2; each property varies smoothly in the (thin) transition zone. Figure 3 depicts the situation and shows the streamlines of the velocity field calculated when the dielectric constant and conductivity of the interior exceed those in the exterior. In this case the dispersion would be drawn out into a ribbon-like shape oriented parallel to the field. (In three dimensions the shape would be ellipsoidal.) The flow direction reverses when the conductivity of the interior is less than that of the exterior, and the sample takes up a flat configuration orthogonal to the field. These features are in complete agreement with our experimental observations.

The relation between the direction and strength of the flow is complicated by the large number of parameters involved. Generally, however, if the difference between the dielectric constants of the two regions is not too large, flow will be in the direction of the applied field if the interior conductivity exceeds that of the exterior. The sense of the flow reverses when the conductivities are reversed. For apolar liquids with low conductivities, electrical forces due to free charge and dielectric-constant variations each play a role.

Although the experiments presented here used $BaTiO_3$/castor oil dispersions, the technique is not restricted to this system. Indeed, provided that there exists a sufficient mismatch in conductivi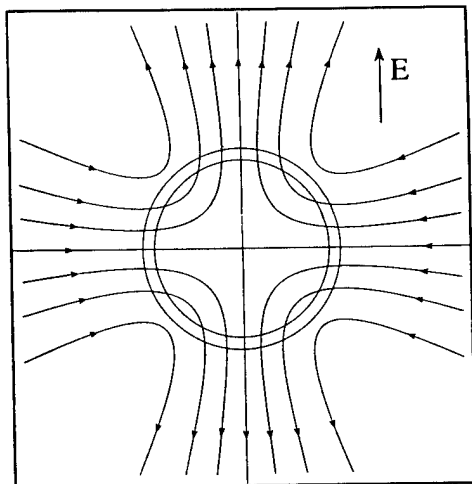ty and/or dielectric constant, any colloidal dispersion nested within any ambient fluid may be manipulated in a similar manner. An example is the observation of dispersion bands during protein electrophoresis. In such experiments, a fluid bolus containing protein molecules is immersed inside a buffer solution and exposed to an electric field. As the protein molecules migrate through the gel, becoming separated on the basis of charge, bands appear to grow in an orthogonal direction to the applied field. The formation of such band structures is suspected of involving electrohydrodynamic processes similar to the ones described here[8,17]. ☐

1. Lachman, I. M., Bagley, R. D. & Lewis, R. M. Ceram. Soc. Bull. **60**, 202–205 (1981).
2. Tummala, R. R. et al. IBM J. Res. Dev. **36**, 889–904 (1992).
3. Newnham, R. & Ruschau, G. R. J. Am. Ceram. Soc. **74**, 463–480 (1991).
4. Gast, A. P. & Zukoski, C. F. Adv. Colloid Interface Sci. **30**, 153–202 (1989).
5. Halsey, T. C. Science **258**, 761–766 (1992).
6. Zukoski, C. F. A. Rev. Mater. Sci. **23**, 45–78 (1993).
7. Rosensweig, R. E. Ferrohydrodynamics (Cambridge Univ. Press, New York, 1985).
8. Rhodes, P. H., Snyder, R. S. & Roberts, G. O. J. Colloid Interface Sci. **129**, 78–90 (1989).
9. Randall, C. A., Miyazaki, S., More, K. L., Bhalla, A. S. & Newnham, R. E. Mater. Lett. **15**, 26–30 (1992).
10. Dogan, F., Liu, J., Sarikaya, M. & Aksay, I. A. in Proc. A. Meeting EMSA Vol. 50 (ed. Bailey, G. W.) 304–305 (San Francisco Press, San Francisco, 1992).
11. Kingery, W. D., Bowen, H. K. & Uhlmann, D. R. Introduction to Ceramics (Wiley, New York, 1976).
12. Scott, J. F. & Paz de Araujo, C. A. Science **246**, 1400–1405 (1989).
13. Glass, A. M. Mater. Res. Soc. Bull. **13**, 16–20 (1988).
14. Hirata, Y. & Kawabata, M. Mater. Lett. **16**, 175–180 (1993).
15. Landau, D. & Lifshitz, E. M. Electrodynamics of Continuous Media (Pergamon, New York, 1960).
16. Russel, W. B., Saville, D. A. & Schowalter, W. R. Colloidal Dispersions (Cambridge Univ. Press, 1989).
17. Saville, D. A. Phys. Rev. Lett. **71**, 2907–2910 (1993).

Pattern Formation in Nonaqueous Colloidal Dispersions via Electrohydrodynamic Flow

M. Trau, S. Sankaran, D. A. Saville, and I. A. Aksay*

Department of Chemical Engineering and Princeton Materials Institute, Princeton University, Princeton, New Jersey 08544-5263

We describe a new electrohydrodynamic phenomenon observed in inhomogeneous, nonaqueous colloidal dispersions with a spatially varying particle number concentration. In the presence of an external electric field, the dielectric constant and conductivity gradients in these systems engender fluid motion which results in the formation of patterned colloidal structures: columns, disks, and other more complicated structures. Other workers found similar effects in high conductivity systems, where the particles are dispersed in water with dissolved electrolyte. Our experimental results with barium titanate dispersed in low conductivity, apolar liquids indicate that electrical forces due to free charge and dielectric constant variations each play a role in inducing flow. This pattern forming phenomenon differs from previously observed field-induced pattern formation in colloidal dispersions (e.g., colloidal string formation in electrorheological and ferrofluids) largely as a result of the induced fluid flow. A mathematical model has been developed which predicts, qualitatively, the initial flow patterns encountered in our system. The theory may also help explain the formation of more complicated field-induced particle morphologies which have been reported in aqueous and nonaqueous media as well as the observation of dispersion band broadening during electrophoresis.

I. Introduction

The formation of patterned colloidal structures has many applications in materials processing. Examples include catalytic support honeycombs produced by extrusion,[1] hierarchical electronic devices made with ceramic multilayers (e.g., computer multichip modules),[2] electrorheological fluids,[3-7] and "smart materials" (e.g., detectors and actuators) formed from patterned composites.[8] Moreover, nested levels of structural hierarchy in composite materials can impart vastly superior properties over a homogeneously structured material.[9-11] This is a design feature which is readily exploited in biological materials (e.g., bone, abalone shell, muscles, and tendons) where subtle differences in structure over various length scales can lead to major differences in the performance characteristics. Indeed, these enhanced performance characteristics have sprouted a new field of materials design known as biomimetics, with the goal of mimicking the hierarchical structures found in biological materials.[12] Due to the intrinsic dimensional limitations of mechanical forming, pattern formation in man-made materials has hitherto been restricted to length scales larger than a few tens of micrometers. We have been investigating the use

of forces which act directly on nonhomogeneous regions in a colloidal dispersion so as to manipulate colloidal structure on smaller length scales.[13] Here we describe a novel example of this approach, to form patterned colloidal dispersions via electrohydrodynamic manipulation, a technique free of many of the limitations of mechanical forming. A brief account of this work recently appeared in a letter to *Nature*.[13] In this paper, we provide a full account of the experimental techniques, the observations, and the underlying theory.

Electrohydrodynamics is the study of fluid motions which arise as a result of an applied electric field. Electrohydrodynamic deformation of liquid/liquid interfaces, in particular, the deformation of liquid droplets surrounded by a second fluid, has been the subject of extensive studies.[14-22] The common feature in these systems is the use of weakly conducting organic fluids and the existence of a liquid/liquid interface. Upon application of an electric field, droplets can be deformed into either an oblate or prolate shape, depending on the ratios of the conductivities and dielectric constants between the inner and outer fluid of the droplet. The currently accepted model for this type of deformation was proposed by Taylor in 1966.[14] In his model, known as the "leaky dielectric" model, the liquids are considered to have small conductivities so, when an electric field is applied, free charge appears at the drop interface. The action of the electric field on this charge sets the fluid in motion and toroidal circulation patterns are formed inside and outside the droplet, resulting in deformation. Measure-

[⊗] Abstract published in *Advance ACS Abstracts,* November 15, 1995.

(1) (a) Bagley, R. D. *Extrusion Method for Forming Thin-walled Honeycomb Structures,* U. S. Patent 3,790,654. (b) Lachman, I. M.; Bagley, R. D.; Lewis, R. M. *Am. Ceram. Soc. Bull.* **1981,** *60,* 202. This original work by Corning has resulted in hundreds of new patents and follow-on papers.
(2) Tummala, R. R. *IBM J. Res. Dev.* **1992,** *36,* 817.
(3) Zukoski, C. F. *Annu. Rev. Mater. Sci.* **1993,** *23,* 45.
(4) Gast, A. P.; Zukoski, C. F. *Adv. Colloid Interface Sci.* **1989,** *30,* 153.
(5) Fermigier, M.; Gast, A. P. *J. Colloid Interface Sci.* **1992,** *154,* 522.
(6) (a) Halsey, T. C. *Science* **1992,** *258,* 761. (b) Halsey, T. C.; Martin, J. E. *Sci. Am.* **1993,** October, 58.
(7) (a) Halsey, T. C.; Toor, W. *Phys. Rev. Lett.* **1990,** *65,* 2820. (b) Martin, J. E.; Odinek, J.; Halsey, T. C. *Phys. Rev. Lett.* **1992,** *69,* 1524. (c) Toor, W. R.; Halsey, T. C. *Phys. Rev. A* **1992,** *45,* 8617.
(8) Newnham, R.; Ruschau, G. R. *J. Am. Ceram. Soc.* **1991,** *74,* 463.
(9) Lakes, R. *Nature* **1993,** *361,* 511.
(10) Lurie, K. A.; Cherkaev, A. V. *Proc. R. Soc. Edinburgh* **1984,** *99A,* 71.
(11) Torquato, S. *Appl. Mech. Rev.* **1991,** *44,* 37.
(12) Aksay, I. A.; et al. Eds. *Hierarchically Structured Materials;* MRS Proc. 255; Materials Research Society: New York, 1992.

(13) Trau, M.; Sankaran, S.; Saville, D. A.; Aksay, I. A. *Nature* **1995,** *374,* 437.
(14) Taylor, G. I. *Proc. R. Soc. London* **1966,** *A291,* 159.
(15) Allan, R. S.; Mason, S. G. *Proc. R. Soc. London* **1962,** *A267,* 45.
(16) Melcher, J. R.; Taylor; G. I. *Annu. Rev. Fluid Mech.* **1969,** *1,* 111.
(17) Torza, S.; Cox, R. G.; Mason, S. G. *Philos. Trans. R. Soc. London* **1971,** *269,* 259.
(18) Melcher, J. R. *J. Electrostat.* **1976,** *2,* 121.
(19) Arp, P. A.; Foister, R. T.; Mason, S. G. *Adv. Colloid Interface Sci.* **1980,** *12,* 295.
(20) Melcher, J. R. *Continuum Electromechanics;* MIT Press: Cambridge, MA, 1981.
(21) Baygents, J. C.; Saville, D. A. In *Drops & Bubbles: Third Intl. Colloq.;* Wang, T., Ed.; American Institute of Physics: New York, 1989; p 7.
(22) Vizika, O.; Saville, D. A. *J. Fluid Mech.* **1992,** *239,* 1.
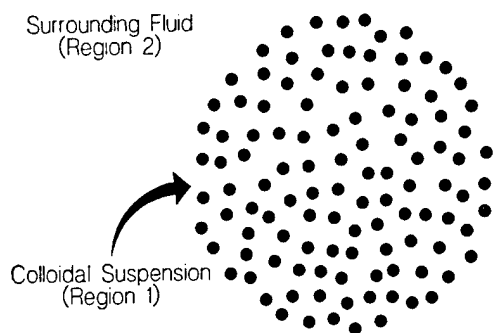
Figure 1. Schematic diagram of our model system. A spherical particle-containing bolus (region 1) nested inside clear ambient fluid (region 2).

ments of the extent of this deformation conform with the Taylor model.[22] Electrohydrodynamic motions have also been observed in aqueous colloidal dispersions and our work has been informed by the work of Rhodes *et al.*[23] on polystyrene particles suspended in electrolytes.

We are interested in the electrohydrodynamic deformation of inhomogeneous colloidal dispersions. The simplest example of such a system is that of a spherical, particle containing region (bolus)—region 1—nested inside clear ambient fluid—region 2 (Figure 1). This system differs from droplets suspended in a second phase in that the boundary layer between regions 1 and 2 is a gradual transition between the suspension and the clear fluid and is devoid of interfacial tension. The thickness of this transition region is determined by a combination of Brownian diffusion and sedimentation. Because of the particles (or the composition of the fluids), the dielectric constant and conductivity of region 1 differ from those of region 2. The mismatch between the dielectric constants of the two regions results from intrinsic differences between particles and fluid and polarization of any diffuse double layer (ion cloud) around each charged particle. Differences in conductivity arise from the following factors: (i) particles impede ion flow and hence reduce the conductivity; (ii) dissolved ions from the particle surfaces increase the local conductivity; (iii) the conductivity of region 1 or 2 may be artificially increased by selectively dissolving a soluble salt. Left on its own and given time to come to equilibrium, the system will become completely mixed via Brownian motion or form a flat layer of particles due to sedimentation. When subject to an electric field, the transition layer between regions 1 and 2 (i.e., the region where ϵ and σ vary spatially) experiences an anisotropic electrostatic body force. This sets the suspension in motion and distorts the shape of the bolus. If the mismatch in conductivity and dielectric constant is large enough, the electrohydrodynamic force will be dominant. It is this force that we exploit to manipulate the structure of a colloidal dispersion. Once colloidal patterns are formed, these structures can be "frozen" in place by solidifying the fluid matrix via gelation or polymerization.[24,25] Moreover, using electrohydrodynamic flows to manipulate colloid structures prior to solidification offers a new route to advanced ceramic manufacture.

The electrohydrodynamic patterning phenomenon under study here differs significantly from previously observed field-induced pattern formation in homogeneous colloidal dispersions (e.g., colloidal string formation in electrorheological and ferrofluids).[3-7,24-28] The commonly accepted patterning mechanism in such systems is via dipole—dipole interactions between suspended particles induced by the presence of either an electric or magnetic field. This is not the mechanism which operates here. Our phenomenon derives from bulk motion brought on by electrical body forces lodged in the suspension, not forces on individual particles. This motion carries particles along with it irrespective of small scale structure, although this structure may affect the details. Bulk motion cannot be explained solely by dipole—dipole interactions between suspended particles.

II. Experimental Section and Discussion

We worked with 100 nm barium titanate ($BaTiO_3$) particles prepared via a hydrothermal process[29,30] and dispersed in castor oil (Aldrich). Barium titanate was chosen because it has an extremely high dielectric constant,[31] typically between 300 and 10 000, depending on its crystalline form, and is a technologically useful material in both the electronic and optical component industries.[32,33] Castor oil was chosen as the fluid medium because (i) it has a low conductivity ($\sigma = 1.8 \times 10^{-11}$ S m^{-1}), (ii) fatty-acid based oils are good dispersing media for barium titanate particles,[34] (iii) its conductivity may easily be varied over a wide range by doping with small amounts of soluble organic salts (e.g., tetrabutylammonium tetraphenylborate, TBATPB), and (iv) its viscosity is similar to those of polymerizable silicone oils used to prepare colloidal barium titanate structures within a solid silicone polymer matrix.[24,25] To form a system similar to that depicted in Figure 1, a dilute dispersion of barium titanate particles (0.025 vol %) in castor oil was injected into clear castor oil fluid via a pinhole in a metal electrode. Slow injection of the dispersion into the clear fluid results in a spherical bolus of the dispersion nested within clear castor oil (cf. parts a and e of Figure 2). The 4 × 4 cm metal electrodes were 1.5 cm apart; the diameter of the colloidal bolus was approximately 5 mm.

Two experiments were performed to illustrate the importance of the conductivity mismatch in setting the direction of flow. In the first experiment, the conductivity of the dispersion was artificially adjusted to be higher than the conductivity of the clear fluid by dissolving a trace amount of an organic salt (0.2 mM of TBATPB) in the $BaTiO_3$ dispersion prior to injection. In the second experiment, the conductivity mismatch was reversed by dissolving the organic salt in the clear castor oil prior to injecting the dispersion. The measured conductivity of a 0.2 mM solution of TBATPB in castor oil was 2.28 × 10^{-9} S m^{-1}, approximately 100 times higher than that of neat castor oil. Figure 2 illustrates the results for both experiments as two series of video images taken after the application of a 2000 V cm^{-1} electric field and separated by a time interval of approximately 0.2 s. In sequence a–d (with higher conductivity on the inside), the spherical bolus deforms immediately in the direction of the applied

(23) Rhodes, P. M.; Snyder, R. S.; Roberts, G. O. *J. Colloid Interface Sci.* **1989**, *129*, 78.

(24) Randall, C. A.; Miyazaki, S.; More, K. L.; Bhalla, A. S.; Newnham, R. E. *Mater. Lett.* **1992**, *15*, 26.

(25) Bowen, C. P.; Bhalla, A. S.; Newnham, R.; Randall, C. A. *J. Mater. Res.* **1994**, *9*, 781.

(26) Rosensweig, R. *Ferrohydrodynamics*; Cambridge University Press: Cambridge, MA, 1985.

(27) Dickstein, A. J.; Erramilli, S.; Goldstein, R. E.; Jackson, D. P.; Langer, S. A. *Science* **1993**, *261*, 1012.

(28) Hu, Y.; Glass, J. L.; Griffith, A. E.; Fraden, S. *J. Chem. Phys.* **1994**, *100*, 4674.

(29) Lilley, T.; Wusirika, R. R. *Method for the Production of Mono-Size Powders of Barium Titanate*, U. S. Patent 4,764,493, 1988.

(30) Dogan, F.; et al. *Proc. Ann. Meeting EMSA* **1992**, *50*, 304.

(31) Kingery, W. D.; Bowen, H. K.; Uhlmann, D. R. *Introduction to Ceramics*; John Wiley and Sons: New York, 1976.

(32) Scott, J. F.; Paz De Araujo, C. A. *Science* **1989**, *246*, 1400.

(33) Glass, A. M. *Mater. Res. Soc. Bull.* **1988**, *13*, 16.

(34) Hirata Y.; Kawabata, M. *Mater. Lett.* **1993**, *16*, 175.

Figure 2. Two examples of the deformation of a colloidal dispersion via an applied electric field. Panels a–d (left) and e–h (right) are video image sequences taken after a steady dc field was applied to a spherical cloud of $BaTiO_3$ dispersion nested inside clear castor oil fluid. The $BaTiO_3$ dispersion was comprised of 100 nm $BaTiO_3$ particles dispersed in castor oil at 0.025% volume fraction. The resulting photographs have been artificially colorized to enhance the contrast between particle containing regions and clear fluid. In the two experiments the conductivity mismatch between the inner and outer bolus region was reversed by selectively dissolving a trace amount of tetrabutylammonium tetraphenylborate (0.2×10^{-3} mol dm^{-3}) either in the inner region, sequence a–d, or in the surrounding clear fluid, sequence e–f. In both cases the magnitude of the applied field was 2000 V cm^{-1}, applied in a vertical direction. The time interval between panels is approximately 0.2 s.

field and continues to stretch out until it collides with the top electrode to form a near-perfect column. The column remains intact for several seconds until the disturbance

generated at the top of the column (see Figure 2d) propagates down the entire length of the column. In the part e–h sequence, a dramatically different flow pattern

is engendered by the field. Here the spherical bolus deforms orthogonal to the applied field, forming a disklike shape which continues to expand laterally. After some time, a film forms across the bottom electrode. Steady (dc) fields were used to generate all of the patterns shown in Figure 2 but the direction and speed of the motion are insensitive to field polarity. Similar flow patterns are induced by applying low frequency ac fields (approximately 100 Hz) which shows that the particle motions are not the result of electrokinetic phenomena.

Similar flow patterns are also induced if the effective dielectric constant of the dispersion is made to be less than that of the surrounding fluid. This is done by dispersing silica particles (100 nm in diameter with $\epsilon \sim$ 2, Bangs Laboratories) in castor oil ($\epsilon = 4.43$) and injecting this mixture into clear castor oil fluid as before. The conductivity of the inner region of the resulting spherical dispersion bolus can be adjusted to be higher or lower than the surrounding clear fluid in an identical manner to that of the previous experiment. Upon application of the electric field the spherical bolus undergoes a deformation identical with that observed with the barium titanate dispersion (i.e., prolate for higher and oblate for lower inner conductivity). This result suggests that the dielectric constant mismatch in these systems is overwhelmed by effects due to the conductivity contrast. This differs from behavior predicted for nonuniform colloidal dispersions subject only to the dipole force.[35] There the bolus flow pattern should *reverse* direction when the dielectric constant mismatch is reversed. To explain the observed behavior, we postulate the influence of an additional electrical force which results from the accumulation of free charge in the transition layer between the suspension and clear fluid. A theory which takes this effect into account is presented in the next section. To further test this hypothesis, an experiment was performed with no colloidal particles present in the spherical bolus (i.e., no dielectric constant mismatch between the inner and outer region). The inner region contained only dissolved salt (tetrabutylammonium tetraphenylborate) and an inert dye ("Oil Red", Aldrich) used to visualize the flow. Application of the electric field in this experiment resulted in a flow pattern identical with that shown in Figure 2. The combination of all three experiments demonstrates that the electrical body force resulting from gradations in dielectric constant is not the only force responsible for the observed electrohydrodynamic flow in these systems.

These results illustrate how the flow pattern around a bolus can be manipulated by adjusting the conductivity mismatch between the inner and outer regions. To achieve useful pattern formation in these systems, however, the deliberate manipulation of colloidal structure over long periods of time is of much greater interest. For this technique to be useful for any of the applications mentioned earlier, it must be capable of two functions: first, colloidal patterning must be achieved on small (mesoscopic) length scales; second, these colloidal structures must remain stable for a sufficiently long time to enable the surrounding fluid to be solidified via, for example, polymerization or gelation techniques. Unfortunately, the long-time evolution of such patterns is extremely difficult to predict for a number of reasons: (i) any fluid motion will deform the sample and alter the conductivity and dielectric constants from their initial values; (ii) the morphology of the transition layer (i.e., both the ion and particle concentration profiles) will change as a result of electrohydrodynamic, diffusion, and sedimentation induced flow. Gen-

(35) Saville, D. A. *Phys. Rev. Lett.* **1993**, *71*, 2907.
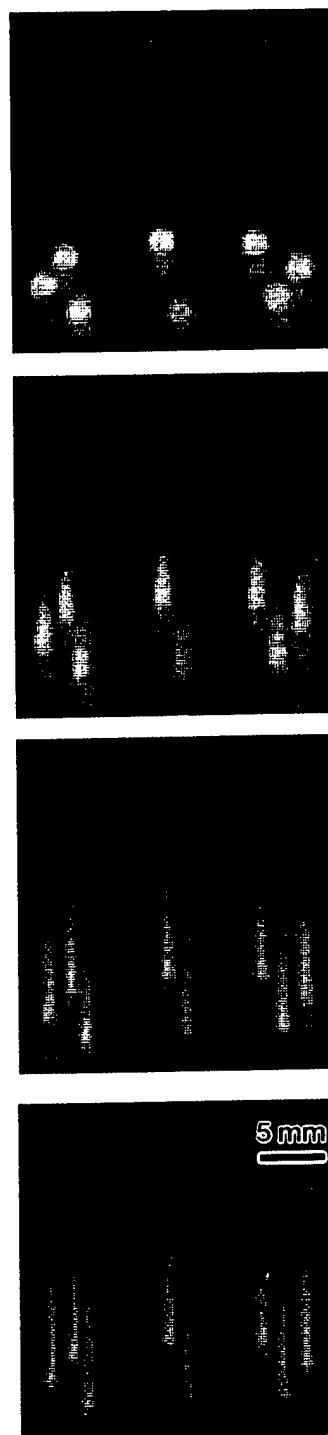
Figure 3. Formation of multiple colloidal columns/spikes via electrohydrodynamic flow. Parts a–d (top to bottom) represent a sequential series of video images taken after a steady dc field (500 V cm^{-1}) was applied to eight identical spherical boli of the BaTiO$_3$ dispersion described in Figure 2. The separation distance between columns is 7 mm. The slight bow in these columns is thought to be due to a hydrodynamic interaction between the columns and the vessel wall or between adjacent columns.

erally, the transition layer will become more diffuse with time. Given these difficulties, a detailed theoretical analysis for long-time pattern evolution has not yet been attempted. Preliminary experiments, however, look promising in view of the above application requirements. Figure 3 shows the simultaneous deformation of eight identical spherical BaTiO$_3$ suspension boli into a ringed columnar structure via the application of a steady dc field (500 V cm^{-1}). This type of slow deformation results in a

columnar structure from each individual bolus. At the tip of each column a sharp spike forms, which continues to sharpen parallel to the direction of the field, stretching the column to a gradually finer diameter. Shortly after the formation, the sharpness of this spike is beyond the resolution of the human eye. An attempt to measure the thickness of the colloidal spike was made by focusing a green argon-ion laser beam ($\lambda = 488$ nm, approximately 200 mW, Lexel, Inc.) onto the spike tip and recording the resulting diffraction line spacings, projected onto a screen 4 m from the sample. Laser diffraction is a standard method used for the determination of fiber thicknesses in the diameter range of $1-100$ μm.[36] The sensitivity of the method is limited by the refractive index mismatch between the fiber, in this case the colloidal column, and the surrounding medium. Given the low volume fraction of particles in our suspension, this mismatch is expected to be quite small and hence limit the sensitivity of the measurement. In our samples, the thinnest part of the colloidal fiber which gave rise to a detectable diffraction pattern corresponded to a thickness of 30 μm. We concluded that the thicknesses of the colloidal spikes produced in this manner were less than 30 μm. By applying a low frequency ac field (e.g., 4000 V cm^{-1}, 100 Hz), the colloidal spikes shown in Figure 3 are formed over a much larger time period and remain stable for periods greater than 3 h before any evidence of dissipation. This time is sufficient to enable polymerization of the ambient fluid, as previously described,[24,25] so as to permanently retain the colloidal structure formed via the electrohydrodynamic flow. Obviously, the formation of such structures is not limited to forming only eight columns at a time. Since each of the columns shown in Figure 3 is similar, it should be easy to extrapolate this process to form large numbers of colloidal columns/fibers simultaneously. Multiple thin films may also be formed in this manner.

Another simple approach to forming complicated colloidal patterns is to change the initial shape of the colloidal region nested within the clear fluid. The structures formed by the electrohydrodynamic flow depend on the initial configuration of the dispersion, and with other arrangements complex, sometimes disordered, structures ensue. This is illustrated in Figure 4, which shows the plan view of a flat layer of a 0.025 vol % BaTiO$_3$ dispersion in castor oil covered with clear castor oil fluid. Glass electrodes are used so as to view the colloidal dispersion. Upon application of a steady dc field (500 V cm^{-1}, directed out of the page) a regular cellular structure forms, which evolves into a more complex pattern as a result of the electrohydrodynamic flow. This experiment clearly illustrates the complex nature of the process and more detailed analysis of this situation is needed in order to predict the evolution of such structures with time.

We believe that the "pancake" experiment displayed in Figure 4 may be similar to the Rayleigh–Bernard instability,[37,38] where an unstable stratification of liquid density is set up in a fluid by heating uniformly from below. In such systems, patterned convective flow is observed, usually with a hexagonal cellular structure, once a critical temperature gradient is established. In Figure 4b, similar "hexagon-like" convection patterns are observed at the initial stages of the electrohydrodynamic flow once a field is applied. The motion in this case results from electrostatic (i.e., Coulombic and polarization) rather than gravitational body forces acting on the fluid. In this

(36) Li, C. T.; Tietz, J. V. *J. Mater. Sci.* **1990**, *25*, 4694.
(37) Bernard, H. *Rev. Gen. Sci. Pure Appl.* **1900**, *11*, 1261.
(38) Chandrasekhar, S. *Hydrodynamic and Hydromagnetic Stability*; Oxford University Press: London, 1961.
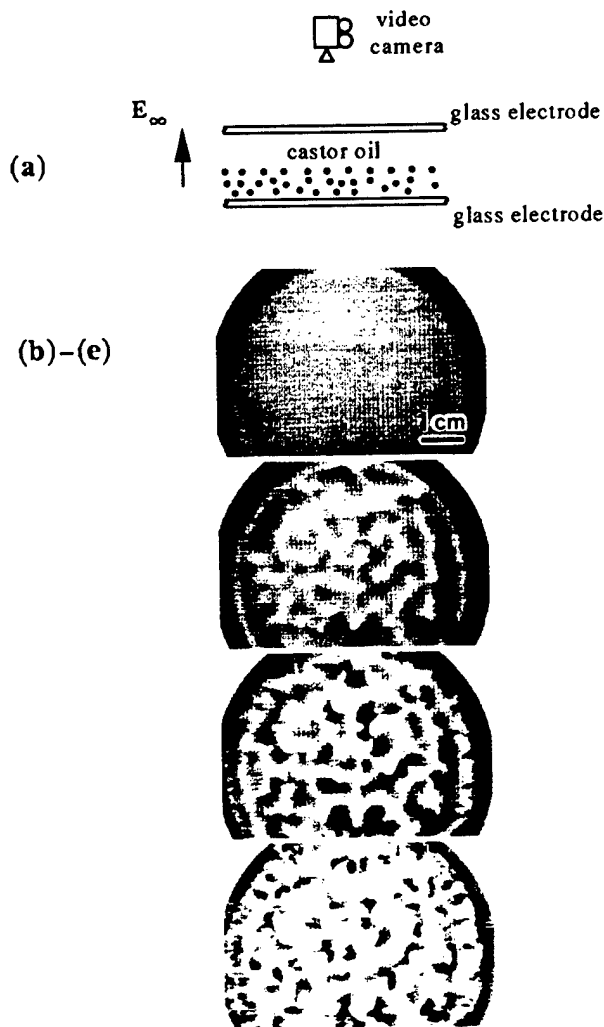
Figure 4. (a) Schematic representation of the apparatus used to obtain a plan view of the BaTiO$_3$ dispersion layer. (b) Sequential video images of the dispersion layer after the application of a steady dc field (500 V cm^{-1}).

problem there may be a critical value for the electrostatic field strength, rather than the temperature gradient, which sets the fluid in motion. Nevertheless, much of the similarity between these two systems ends here, because as soon as the liquid is set into motion, the evolution of the conductivity and dielectric constant distributions differs from that of the density distribution in the Rayleigh–Bernard problem.

III. Electrohydrodynamic Theory

In the situations just described, motion arises from two sorts of electrical body forces, one stemming from a polarization force derived from gradations in the dielectric constant and the other due to the action of the applied field on induced free charge. To synthesize a theoretical description, we link Maxwell's theory for electrical phenomena to the equations describing the mechanics of the flow. Our analysis builds on those of Rhodes et al., who considered the deformation of a cylinder with a sharp interface,[23] and Saville,[35] who analyzed an object with a diffuse interface. Differences with these two approaches arise from (i) considering a diffuse interface and (ii) accounting for the generation of a volumetric free charge whenever there is a gradation in conductivity *and* dielectric constant. Electric forces can be described in

terms of Maxwell's stress tensor or as a body force,[39] i.e.

$$\mathbf{f}_e = -\frac{1}{2}\epsilon_0 \mathbf{E}\cdot\mathbf{E}\nabla\epsilon + \rho_e\mathbf{E} \qquad (1)$$

The symbols are $\mathbf{f}_e$, the electric body force per unit volume, ϵ_0, the permittivity of free space, $\mathbf{E}$, the electric field strength, $\nabla\epsilon$, the gradient of the local dielectric constant, and ρ_e, the free charge per unit volume. Gradations in the dielectric constant arise from the factors mentioned earlier. Free charge stems from the action of the applied field on ions that carry the current. To calculate the flow field arising from these electrical body forces when the flow is slow, the Stokes equations must be solved for the velocity, $\mathbf{u}$, and pressure, p, in a fluid with viscosity, μ, viz.

$$\mathbf{0} = -\nabla p + \mathbf{f}_e + \mu\nabla^2\mathbf{u} \qquad \nabla\cdot\mathbf{u} = 0 \qquad (2)$$

Clearly, one must know how the electric field is distributed to solve these equations. The field is governed by

$$\nabla\cdot\epsilon\epsilon_0\mathbf{E} = \rho_e \qquad (3)$$

and the charge density is related to the ion concentrations by

$$\rho_e \equiv \sum_{k=1}^{N} ez^k n^k \qquad (4)$$

Here e is the charge on a proton and z^k is the valence of the kth ionic species whose concentration is n^k. Ions are carried by the flow and move in response to gradients in the electrochemical potential, so if we denote the mobility of the kth ionic species by ω^k, the conservation equation is

$$\mathbf{u}\cdot\nabla n^k = \nabla\cdot[-\omega^k ez^k n^k \mathbf{E} + \omega^k k_B T \nabla n^k] \qquad (5)$$
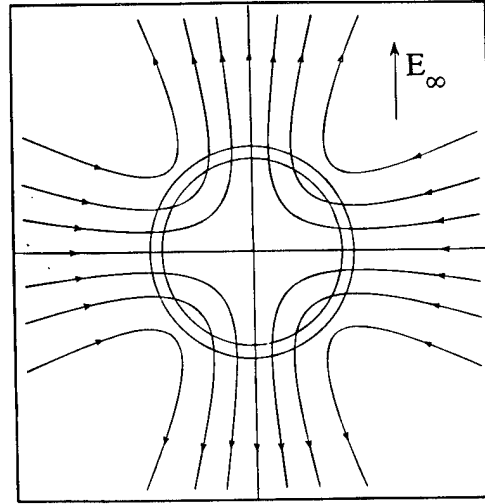
$$k = 1, \cdots, N$$

Here k_B is Boltzmann's constant and T is the absolute temperature. Since magnetic effects are small, the electric field is irrotational and we can write the field as the gradient of a potential, ϕ

$$-\nabla\phi = \mathbf{E} \qquad (6)$$

These equations are too complex to solve in any general sense but useful insight can be gained by studying simplified forms. Our objective is to decide how a nonuniform dispersion will deform so tractability is important. To help decide on the elements of the simplified model, we analyze an equation for charge conservation and restrict attention to situations where the mobilities of all ions are the same, as denoted by ω, and the dielectric constant distribution is known. Upon multiplying eq 5 by ez^k and adding the equations for each ion species, we obtain the charge conservation equation as

$$\mathbf{u}\cdot\nabla\rho_e = \nabla\cdot[\sigma\nabla\phi + D\nabla\rho_e] \qquad (7)$$

where $\sigma \equiv \sum_{k=1}^{N}(ez^k)^2\omega n^k$ is the conductivity and D is the ion diffusivity, $\omega k_B T$. Now if the contributions from convective transport, $\mathbf{u}\cdot\nabla\rho_e$, and diffusive transport, $\nabla\cdot[D\nabla\rho_e]$, are small compared to conduction, $\nabla\cdot[\sigma\nabla\phi]$, then the structure of the electric field will be determined by conduction and the charge distribution follows from Gauss'

(39) Landau, D.; Lifshitz, E. M. *Electrodynamics of Continuous Media*; Pergamon Press: New York, 1960.

Figure 5. Streamline pattern for flow engendered by a circular shaped cloud of a dispersion immersed in a clear fluid with a lower conductivity and dielectric constant calculated from the model set here.

law, eq 3. An order-of-magnitude analysis can be used to assess the relative magnitudes.

The situation under study differs from those commonly encountered in electrokinetics where free charge exists in the equilibrium state due to the presence of charged interfaces. Here we study systems on a length scale where, in the absence of an external field, there is no free charge; free charge is induced in the bulk by the field as it adjusts itself to ensure conservation of charge. Denoting the magnitude of the applied field as E_∞ and the length scale as l, it follows from eq 3 that the charge density is $\mathcal{O}(\epsilon_0 E_\infty/l)$. From the Stokes equation we see that the velocity is $\mathcal{O}(\epsilon_0 E_\infty^2 l/\mu)$ so that the convective term in eq 7 is $\mathcal{O}(\epsilon_0^2 E_\infty^2/\sigma\mu)$ relative to the term representing current carried by conduction. The diffusive term is $\mathcal{O}(\epsilon_0 D/\sigma l^2)$ compared to conduction. To estimate the orders-of-magnitude we choose $l \approx 1$ mm, $E_\infty \approx 10^5$ V/m, $D \approx 10^{-10}$ m²/s, $\sigma \approx 10^{-9}$ S/m, and $\mu \approx 10^{-2}$ kg/ms, typical values for the phenomena under study in low dielectric constant liquids. Thus $(\epsilon_0^2 E_\infty^2/\sigma\mu) \approx 10^{-1}$ and $(\epsilon_0 D/\sigma l^2) \approx 10^{-6}$. Accordingly, we can approximate the electric potential by solutions of

$$\nabla\cdot[\sigma\nabla\phi] = 0. \qquad (8)$$

In a general model one would need to track the ion densities to calculate the local electric conductivity and have an evolution equation for the dielectric constant. In situations involving dispersions, the particle distribution must be calculated as it evolves due to electrical and hydrodynamic forces. However, a qualitative picture can be obtained from a simple model where the dielectric constant and conductivity distributions are prescribed. This has been done for situations where a uniform transverse electric field, E_∞, acts on a circular region of radius a with dielectric constant ϵ_s and conductivity σ_s, surrounded by a region with properties σ_∞ and ϵ_∞. Each property varies smoothly in the transition zone of thickness δ (see Figure 5). Since the situation is two-dimensional, the solution is relatively straightforward. First, eq 8 can be converted to an ordinary differential equation for the potential since the field varies as cos ϑ for one that is uniform at infinity; here ϑ is the angle measured from the direction of the field. Thus

$$\phi = R(r)\cos\vartheta \qquad (9)$$

and the differential equation for $R(r)$ is

$$R'' + [r^{-1} + S(r)]R' - r^{-2}R = 0 \qquad (10)$$

with

$$S(r) \equiv \frac{1}{\sigma(r)}\frac{d\sigma}{dr} \qquad (11)$$

To represent the conductivity distribution we choose

$$\sigma = \sigma_s \qquad 0 < r < a$$

$$\sigma = \frac{1}{2}\Big[\bar{\sigma} + \Delta\sigma\,\cos\Big[\frac{\pi(r-a)}{\delta}\Big]\Big] \qquad a < r < a+\delta \quad (12)$$

$$\sigma = \sigma_\infty \qquad a+\delta < r < \infty$$

with $\bar{\sigma} \equiv \sigma_s + \sigma_\infty$ and $\Delta\sigma \equiv \sigma_s - \sigma_\infty$. Accordingly, the potential can be seen to depend on the independent and parametric variables as

$$\phi = aE_\infty\Phi\Big[\frac{r}{a}, \vartheta, \frac{\Delta\sigma}{\bar{\sigma}}, \frac{\delta}{a}\Big] \qquad (13)$$

Equation 10 can be solved numerically to obtain the potential and field strength for a given conductivity distribution.

To obtain the flow field, the known potential distribution is used to solve eq 2 numerically for situations where the dielectric constant is distributed as

$$\epsilon = \epsilon_s \qquad 0 < r < a$$

$$\epsilon = \frac{1}{2}\Big[\bar{\epsilon} + \Delta\epsilon\,\cos\Big[\frac{\pi(r-a)}{\delta}\Big]\Big] \qquad a < r < a+\delta \quad (14)$$

$$\epsilon = \epsilon_\infty \qquad a+\delta < r < \infty$$

with $\bar{\epsilon} \equiv \epsilon_s + \epsilon_\infty$ and $\Delta\epsilon \equiv \epsilon_s - \epsilon_\infty$. Since the gradient in the dielectric constant is radial, the Stokes' equation becomes

$$0 = -\nabla p - \frac{1}{2}\epsilon_0\mathbf{E}\cdot\mathbf{E}\frac{d\epsilon}{dr}\mathbf{e}_r + \rho_e\mathbf{E} + \mu\nabla^2\mathbf{u} \qquad (15)$$

with $\mathbf{e}_r$ representing a unit vector in the radial direction. From eq 3, the charge density is calculated as

$$\rho_e = -\epsilon\epsilon_0\nabla^2\phi - \epsilon_0\frac{d\epsilon}{dr}\frac{\partial\phi}{\partial r} = \epsilon_0\epsilon\Big[\frac{1}{\sigma}\frac{d\sigma}{dr} - \frac{1}{\epsilon}\frac{d\epsilon}{dr}\Big]\frac{\partial\phi}{\partial r} \quad (16)$$

Note that the sense of the free charge force is controlled by the relative magnitudes of the conductivity and dielectric constant variations and one may outweigh the other. On the other hand, the sense of the body force arising from dielectric constant variations is set by the difference between the dielectric constant inside of and outside of the cylindrical region.

Since the problem is two-dimensional, a stream function, ψ, can be used to represent the flow field, viz.

$$u_r = \frac{1}{r}\frac{\partial\psi}{\partial\vartheta}, \qquad u_\vartheta = -\frac{\partial\psi}{\partial r} \qquad (17)$$

$$\psi(r,\vartheta) = \frac{a^2\epsilon_0\epsilon_\infty E_\infty^2}{\mu}\, G\Big[\frac{r}{a}, \frac{\delta}{a}, \frac{\Delta\sigma}{\bar{\sigma}}, \frac{\Delta\epsilon}{\bar{\epsilon}}\Big]\sin(2\vartheta) \quad (18)$$

This leads to a fourth order ordinary differential equation for the G function. Note that here the scaling for the velocity has been modified slightly to reduce the number of parameters.

Table 1. Deformation in the Absence of Free Charge Effects

$\Delta\epsilon$	$\Delta\sigma$	deformation
>0	>0	prolate
<0	<0	prolate
>0	<0	oblate
<0	>0	oblate

Table 2. Fluid Speed at the Edge of the Transition Region[a]

δ/a	u	δ/a	u
0.001	13.3	0.5	1.36
0.01	2.83	1.0	1.93
0.1	1.11	2.0	3.38

[a] Calculations for $\sigma_s/\sigma_\infty = 100$ and $\epsilon_s/\epsilon_\infty = 1$; the scale factor is $a\epsilon_0 E_\infty^2/\mu$.

The equations for the potential and stream functions have been solved for several choices of σ_s, σ_∞, ϵ_s, and ϵ_∞. Figure 5 depicts the situation and shows the streamlines of the velocity field calculated when the dielectric constant and conductivity of the interior exceed those in the exterior. In this case the dispersion would be drawn out into a prolate ellipsoidal shape with its major axis parallel to the field. According to the theory, and in agreement with our experimental observations, the flow direction reverses when the conductivity of the interior is less than that of the exterior. Here the sample takes up the shape of an oblate ellipsoid with its axis orthogonal to the field. In our experiments with barium titanate the conductivity ratio, σ_s/σ_∞, is $\approx 10^2$ when the dispersion is doped with TBATPB and $\approx 10^{-2}$ when the TBATPB is added to the suspending oil. Under these conditions, the effects of conductivity contrast overwhelm the relatively small effects of dielectric constant variation. In the previous section, we described experiments with a silica dispersion and an organic dye bolus in clear fluid. These experiments confirmed the negligible effects of dielectric constant variation in the above experiment. Once again theory and experiment were in qualitative agreement; prolate deformations for a high conductivity bolus and an oblate deformation when the suspending fluid had the higher conductivity. No deformation was observed when the dyed bolus had the same conductivity as the suspending oil.

The relation between the direction and strength of the flow is complicated by the large number of parameters involved. Most of the results discussed below are for $\delta/a = 0.1$. Changing this ratio does not seem to affect matters qualitatively. First, if free charge effects are suppressed, i.e., $\rho_e = 0$, then the sense of the deformation depends on $\Delta\sigma$ and $\Delta\epsilon$ as shown in Table 1.[35] Two other special cases are of interest. When $\Delta\epsilon = 0$ but $\Delta\sigma \neq 0$, the deformation is due to free charge effects and it is prolate when $\Delta\sigma > 0$ and oblate when $\Delta\sigma < 0$. On the other hand, when $\Delta\epsilon \neq 0$ but $\Delta\sigma = 0$, the deformation is oblate when $\Delta\epsilon > 0$ and prolate when $\Delta\epsilon < 0$. Rhodes et al.[23] derived an analytical *discriminating function* for a sharp interface, viz.

$$\Big[\frac{\sigma_s}{\sigma_\infty}\Big]^2 + \frac{\sigma_s}{\sigma_\infty} + 1 - 3\frac{\epsilon_s}{\epsilon_\infty}\begin{cases} > 0 \text{ prolate deformation} \\ < 0 \text{ oblate deformation} \end{cases}$$

which gives the sense of the deformation when $\delta = 0$; our numerical results agree with this expression when δ/a is small.

The speed of the deformation is strongly dependent on the δ/a ratio, as Table 2 illustrates. Note that with the characteristic values quoted earlier, the deformation speed is several millimeters per second. The nonmonotonic

change of velocity with δ/a reflects the complex interplay between the body forces and the transition layer thickness.

Finally, we note that the effects of a variable frequency can be obtained by including the Maxwell current, $\partial \mathbf{P}/\partial t$, where $\mathbf{P}$ is the polarization.[40] Although the general case is complicated, the high frequency limit offers some insight. Here, free charge effects are negligible and the expression for the conductivity in eq 11 contains only effects from dielectric constant variations across the transition region, viz.

$$S(r) \equiv \frac{1}{\sigma(r)} \frac{d\sigma}{dr} = -\frac{\pi}{\delta} \frac{\Delta\epsilon/\bar\epsilon \, \sin[\pi(r-a)/\delta]}{1 + \Delta\epsilon/\bar\epsilon \, \cos[\pi(r-a)/\delta]} \tag{19}$$

Accordingly, at high frequencies the fluid behaves as a perfect dielectric and solution of the equations shows that the deformation is always prolate. However, for this approximation to hold, the oscillation frequency must be substantially larger than the highest relaxation frequency, $\sigma/\epsilon\epsilon_0$; for the oily systems studied here this frequency ranges from (roughly) 1 Hz for the neat castor oil to 50 Hz for the doped fluid. The highest frequency used in our experiments with dispersions was 100 Hz, probably not large enough to produce perfect dielectric behavior. However, we did carry out experiments with a dyed, particle-free bolus. Here effects due to dielectric constant variations should be negligible. There was no deformation when the frequency was above 300 Hz, indicating that free charge effects had been nullified because the free charge force was unable to keep pace with the field. At lower frequencies, deformations gradually appeared and conformed with the sense dictated by the conductivity contrast.

IV. Conclusions

We have demonstrated a new phenomenon in inhomogeneous, nonaqueous colloidal dispersions. In such systems, the intrinsic difference in dielectric constant and conductivity ($\Delta\epsilon$ and $\Delta\sigma$) between regions of differing particle number concentration engenders fluid motion upon the application of an external electric field. For apolar fluids, with low conductivity, electrical forces due to free charge and dielectric constant variation each play a role in inducing flow. By tailoring $\Delta\epsilon$, $\Delta\sigma$, and the initial configuration of the dispersed particles, many intricate colloidal patterns and shapes can be produced in a controlled manner. With appropriate choice of suspending fluid, these patterns can be made to remain stable for sufficient periods to enable solidification of the fluid matrix by conventional means (e.g., gelation or polymerization). Although the experiments presented here have been performed solely on $BaTiO_3$/castor oil and SiO_2/castor oil dispersions, this technique is in no way restricted to these system. Indeed, provided that $\Delta\epsilon$ and/or $\Delta\sigma$ is large enough, any colloidal dispersion nested within any ambient fluid may be manipulated in a similar manner. Another example of such an effect is the observation of dispersion bands during protein electrophoresis.[23] In such experiments, protein solution is initially injected as a fluid bolus and subsequently separated electrophoretically via the application of an external electric field. During separation, the protein bands are observed to broaden in a direction orthogonal to the electric field. The formation of such bands can be explained by similar electrohydrodynamic processes to the ones considered here. Analysis of the phenomenon may also provide insight into the formation of complicated field-induced particle morphologies which have been reported in aqueous[28] and nonaqueous[6,7,24,25] systems. More fully understood, the electrohydrodynamic manipulation of colloids may be put to use in the manufacture of materials with patterns that cannot be formed by mechanical means.

(40) Russel, W. B.; Saville, D. A.; Schowalter, W. R. *Colloidal Dispersions*; Cambridge University Press: Cambridge, MA, 1989.

THE BREAKUP OF THE INTERMEDIATE GOLD AGGREGATES

Nan Yao,[1] Wan Y. Shih,[1,2] Daniel M. Dabbs,[1,2] and Ilhan A. Aksay[1,2]

[1]Princeton Materials Institute, and the
[2]Department of Chemical Engineering, Princeton University, New Jersey 08540-5211

The synthesis of nanometer scale gold particles is well known historically.[1,2] Stable and highly colored suspensions result from the reduction of gold cations in solution. But the formation of the gold particles is not monotonic, that is, the mechanism is not simply nucleation and growth. Rather, the pronounced color changes in the evolving suspension indicate that the mechanism is nucleation, aggregation, deaggregation, and growth.[3,4] Until recently, the structure of the intermediate aggregate had been assumed to be an aggregation of primary particles, each 4-7 nm in diameter.[4] HRTEM studies have shown that the intermediates are continuous ramified structures (Figure 1) which undergo a desintering process to form the final particles (~24-26 nm diameter).[3,5] In this paper, we discuss a model which explains the role of the surfactant on the gold intermediate in the breakup of the intermediate structure.

Gold colloids were prepared by reducing $Au^{III}Cl_3$ (aq) with sodium citrate as in previous studies:[3-5] $Au^{III}Cl_3$ (aq) + Cit^{3-} (aq) $\rightarrow$ Au^0. For the present study, 95mL of an aqueous solution of $AuCl_3$ (50 mg Au/L) was heated to 95°C and 5 mL of 1 wt% sodium citrate (aq) added to yield a solution of $C_{Au} = 2.54 \times 10^{-4}$ M and $C_c = 1.9 \times 10^{-3}$ M. TEM samples were prepared by dipping holey carbon support grids into the suspension followed by drying on filter paper. HREM studies were conducted with a Philips CM-20 ST TEM operated at 200 keV. The electron dose was about 10-20 A/cm^2 under moderate vacuum of 10^{-6}-10^{-7} Torr. Figure 1 shows three TEM micrographs for samples collected at various times: (a) at t = 5 min when the suspension color was purple and D ~ 90 nm, (b) at t = 15 min when the suspension started to redden and D ~ 50 nm, and (c) at t = 35 min when the suspension was ruby red and D stabilized at ~ 20 nm. The aggregates shown in Figure 1(a) are not clusters of well-separated particles. A detailed structure is shown in Figure 2. The aggregates appear continuous with a high population of twin boundaries in the intermediate sausage-like structure. The high density of nanometer-sized twin boundaries in the gold structure is due to the minimization of the total interfacial free energy of the gold particles.[6] Also, due to the small diameter in the sausage structure, the surface area of the intermediate is orders of magnitude larger than in bulk material. It is known that diffusion coefficients can be orders of magnitude higher at grain boundaries than inside grains. The surfaces and twin boundaries may then provide transport paths, allowing much faster redistribution of matter within the aggregates.

Mass transport is first facilitated by the movement of the adsorbed citrate ions on the conductive gold surface under a constant potential. In a corner of angle β between the two faces of the corner (Figure 3), the electrical field normal to the surface, $E_\phi(\rho)$, varies with ρ as $E_\phi(\rho) = -(\alpha_1/\beta)\rho^{(\pi/\beta)-1}$, where ρ is the radial distance from the origin and α_1 a constant related to the surface potential.[7] The repulsive force diminishes near the origin and the area over which the repulsive force diminishes increases with decreasing angle β. The breakup mechanism can be explained as follows: (1) The repulsive electric force on the adsorbed charges diminishes near the corner of a cusp and (2) the surface area with a diminishing electric force increases as the cusp gets sharper. So the aggregate surface is unstable against a cusp-like perturbation. Once a cusp is formed, the cusp will sharpen to allow more adsorbed charges around the cusp, leading eventually to breakup. The formation and sharpening of the cusps are facilitated by the high diffusivity of gold atoms.[8]

References:

1. M. Faraday, *Phil. Trans.*, **147**(1857)145.
2. For example, see P. C. Hiemenz, *Principles of Colloid and Surface Chemistry*, 2nd edition, Marcel Dekker (1986).
3. J. Liu, M. Sarikaya, and I. A. Aksay, *Proc. Ann. MSA,* **46**(1988)716.
4. M. K. Chow and C. F. Zukoski, *J. Colloid and Interf. Sci.*, **165**(1994) 97.
5. D. M. Dabbs, N. Yao, and I. A. Aksay, *Proc. Ann. MSA,* **52**(1994)446.
6. L. Marks and A. Howie, *Philos. Mag.* **A49**(1984)81.
7. J. D. Jackson, *Classical Electrodynamics* John Wiley & Sons (1975)77.
8. This work made use of MRSEC Shared Facilities supported by the NSF under Award Number DMR-940032 and was supported by a grant from the U. S. Air Force Office of Scientific Research AFOSR-F49620-93-1-0259.
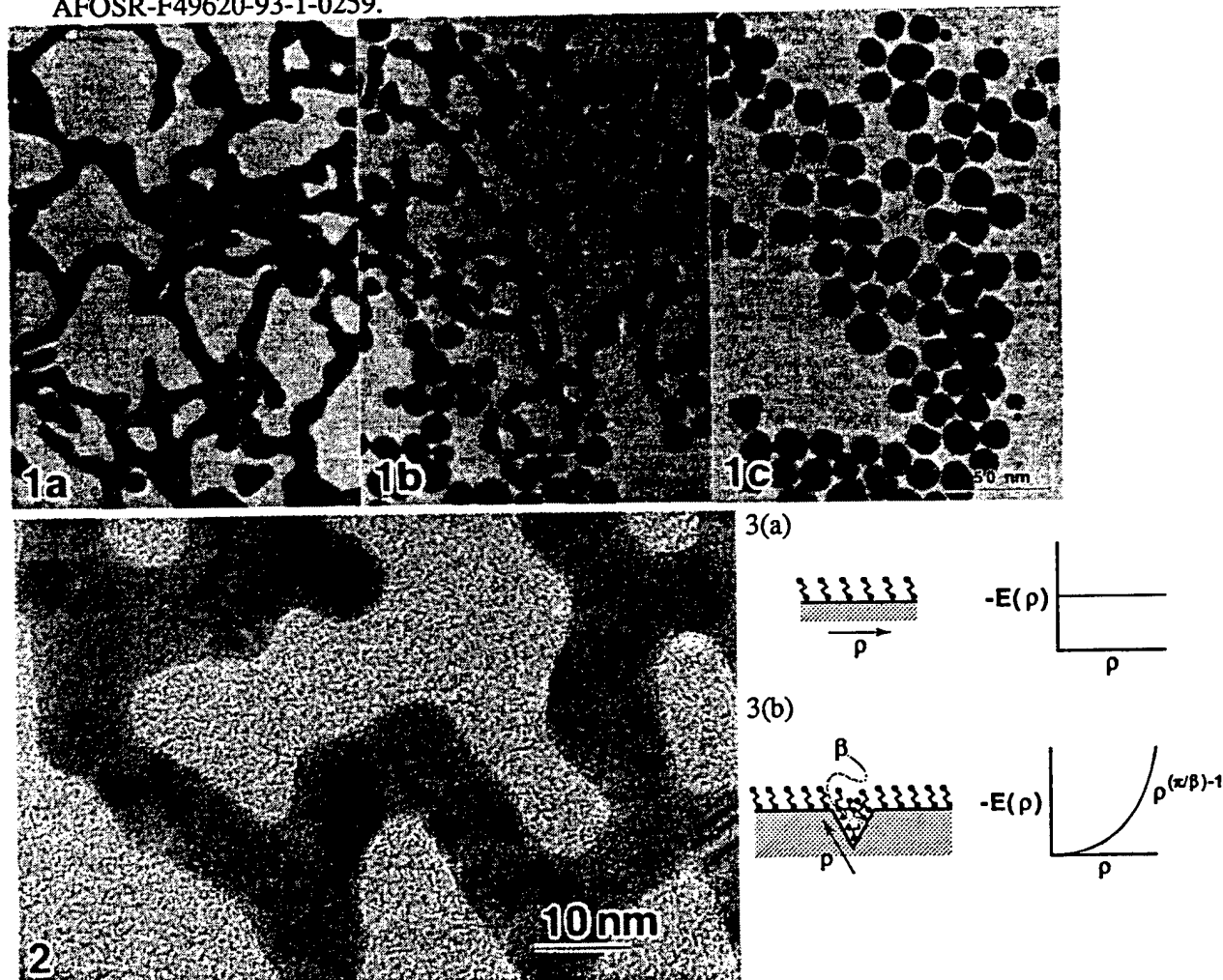
FIG. 1.—Electron microscope images showing the morphology of gold particles collected at various times: (a) t=5 min., (b) t=15 min., and (c) t=30 min. Note the sausage-like structure at t=5 min.

FIG. 2.—TEM image showing the high density of twin boundaries within sausage-like gold structure.

FIG. 3.—Schematic diagram of a gold surface under (a) a constant potential and (b) with the presence of a cusp on the surface of angle β.

Field-Induced Layering of Colloidal Crystals

M. Trau, D. A. Saville, and I. A. Aksay*

Field-Induced Layering of Colloidal Crystals

M. Trau, D. A. Saville, I. A. Aksay*

An electrohydrodynamic methodology has been developed that makes possible the precise assembly of two- and three-dimensional colloidal crystals on electrode surfaces. Electrophoretically deposited colloidal particles were observed to move toward one another over very large distances (greater than five particle diameters) to form two-dimensional colloidal crystals for both micrometer- and nanometer-size particles. This coalescence of particles with the same charge is opposite to what is expected from electrostatic considerations and appears to result from electrohydrodynamic fluid flow arising from an ionic current flowing through the solution. The ability to modulate this "lateral attraction" between particles, by adjusting field strength or frequency, facilitates the reversible formation of two-dimensional fluid and crystalline colloidal states on the electrode surface. Further manipulation allows controlled structures to be assembled.

The controlled assembly of materials with patterned structural features on submicrometer length scales, "nanostructured materials," is a rapidly expanding area in materials science (1). In particular, multilayered nanocomposites, typically formed by molecular vapor deposition, exhibit macroscopic properties that are remarkably different from those of more conventional engineering materials, whose structural features lie in the micrometer-size range or greater (2). Although nanostructured materials display considerable potential, their development is currently hindered by an inability to conveniently and economically form such materials in large quantities, preferably under ambient conditions. As an alternative to molecular vapor deposition, which uses individual molecules as building blocks, we propose the assembly of macromolecular building blocks (such as colloids and proteins) to form designed structures on larger length scales by electrophoretic deposition. The assembly of colloids into patterned structures has heretofore been achieved by dispersing monosized colloidal particles in a solvent and allowing crystalline regions to form as a result of specific particle-particle interaction forces or entropic effects (3). The formation of such colloidal crystals is difficult to regulate externally and is cumbersome to confine to two dimensions so as to process "designed" multilayers (4). For similar reasons, protein crystallization is difficult to regulate and is currently the rate-determining step in the determination of the structure of biologically important proteins (5). Here we report on a method that allows layer-by-layer deposition of colloidal crystals through electrohydrodynamic manipulation.

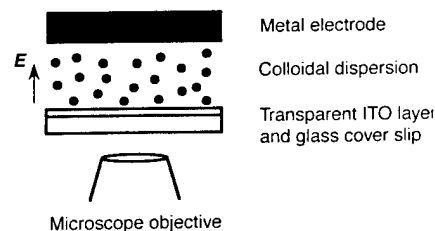To observe the deposition mechanism in detail, we used an optically transparent in-

dium tin oxide (ITO) electrode coupled to an optical microscope (Fig. 1). To illustrate the phenomenon by optical microscopy, we used large particles. Similar results were obtained with nanometer-size particles (see below). Examples of electrophoretic deposition onto an ITO anode with our technique are shown in Fig. 2 for submonolayer, electrophoretically deposited films of silica [Fig. 2A; 900 nm in diameter (Bangs Laboratories)] and polystyrene [(PS) Fig. 2D; size standards 2 μm in diameter (Duke Scientific)] particles from a dilute suspension. With silica, the suspending fluid was triply distilled water (pH = 5.8 with a conductivity of <1 μS cm⁻¹); for PS the ambient fluid contained a mixture of ionic and nonionic surfactants (Duke Scientific) added to provide the colloidal stability. Two-dimensional (2D) "gaseous" structures (Fig. 2, A and D) form upon application of a weak electric field (for example, 0.5 V) across the dilute suspension or when the particles settle onto the electrode. In neither case do the particles adhere to the electrode surface; instead, they continue to move in two dimensions through Brownian agitation.

The 2D mobility of these particles in the presence of an electric field is surprising, given the large electrostatic attraction between negatively charged particles and a positively charged electrode. This effect appears to be a consequence of steric stabilization. For our PS particles, stabilization was provided by an adsorbed surfactant layer on the surface of the particles. With the silica particles, no surfactant was added to the solution, and it is probable that the particles remain stable because of the presence of polysilicate moieties at the silica-aqueous solution interface. The existence of such polysilicate moieties, "stubble hair," on the silica surface has been shown to cause a short-range repulsive force between silica surfaces (6, 7).

Increasing the applied voltage (for example, from 0.5 to 1.5 V) caused surprising

responses (see Fig. 2, B, C, E, and F). With a sufficiently strong current, the particles move toward one another across the electrode surface. This "lateral attraction," first observed by Richetti et al. (8), acts normal to the applied field and is strong enough to bring particles together to form stable, 2D colloidal crystals. However, no detailed understanding of the underlying mechanism was achieved. At field strengths of 50 to 100 V cm⁻¹ (1 to 2 V applied, ~100 μA cm⁻²), crystal formation is reversible. When the field is removed, particles are stirred by Brownian motion to form 2D "gaseous" structures similar to the ones shown in Fig. 2, A and D. One can adjust the strength of the lateral attraction between particles by changing the magnitude of the current. Modulation of the strength of the particle-particle interaction allows the formation of different 2D "gas," "liquid," and crystalline colloidal phases on the electrode. Phase transitions can be easily induced by varying the current. The lateral attraction also acts when an ac voltage is applied, as long as the frequency is not too high. The 2D colloidal phase transitions are observed when the amplitude of the applied ac or dc voltage is gradually increased. Above a frequency of 1 MHz, the attraction disappears.

To investigate the deposition mechanism of nanometer-size particles too small to be imaged by optical microscopy, we performed deposition experiments with 16-nm gold particles, following the method reported by Giersig and Mulvaney (9). Gold particles synthesized according to the method of Turkevich et al. (10) were electrophoretically deposited onto a carbon-coated electron microscope grid. After deposition, the films were removed from solution, dried, and imaged with transmission electron microscopy (TEM). A typical example of a submonolayer film of particles formed

Metal electrode

Colloidal dispersion

Transparent ITO layer and glass cover slip

Microscope objective

Fig. 1. Diagram of the apparatus. An ITO-coated microscope cover slip (resistivity, 60 ohms per square) forms the anode, and a piece of polished brass (2 cm by 2 cm) forms the cathode of an electrolytic cell. These are separated by an insulating Teflon spacer 0.2 mm thick, and the thin cavity is filled with a colloidal dispersion. Upon application of an electric field E, particles are observed through the transparent electrode by means of an optical microscope (Leitz Metallovert). Particle motion is recorded on video tape.

Department of Chemical Engineering and Princeton Materials Institute, Princeton University, Princeton, NJ 08544, USA.

*To whom correspondence should be addressed.

in this way is shown in Fig. 3. The formation of 2D clusters, similar to those shown in Fig. 2, reveals the existence of a lateral attraction operating in a manner similar to that observed for larger particles (11). Lateral attraction during electrophoretic deposition is a general phenomenon that operates for any colloidal material that remains colloidally stable at the electrode-solution interface.

Attraction between electrophoretically deposited particles at the electrode interface is surprising, given the strong repulsion expected from purely electrostatic forces. All of the particles are similarly charged and have a diffuse ion cloud (double layer) that is polarized by the electric field. Accordingly, some electrostatic repulsion from monopole and dipole interactions is present as particles approach each other, so the observed attraction is clearly not the result of a simple electrostatic interaction. Whatever the attractive interaction, it must be strong enough to overcome electrostatic repulsion.

The attractive interaction appears to result from electrohydrodynamic effects arising from charge accumulation near the electrodes due to the passage of ionic current. The currents in our system are between 1 and 500 μA cm^{-2}, depending on the applied voltage and the time required to reach steady state, and they result from the electrolysis of water. Bubble formation was not observed under our experimental conditions because current densities were low, <1 mA cm^{-2}, which allowed H$_2$ and O$_2$ reaction products to be solubilized in the bulk solution and transported away from the electrode surface (12). Electrolysis produces H$_3$O$^+$ ions at the anode and OH$^-$ ions at the cathode, and, with background electrolyte concentration present (for ex-

ample, due to dissolved CO$_2$), ionic conduction occurs primarily through electromigration of the electrolyte species. Provided the fluid remains motionless, the passage of current leads to a buildup of ions in the vicinity of the electrodes, a process known in electrochemistry as "concentration polarization" (13). The accumulation of ions near the electrode sets up a pressure gradient in the fluid because coulombic forces, which act on regions of fluid near the electrode where there is an ionic space charge, are balanced by pressure gradients so as to maintain equilibrium. Given the planar symmetry of the two-electrode system, the induced pressure-gradient is uniform in directions parallel to the electrodes. However, the planar symmetry is interrupted by the presence of particles. Our model of the phenomenon of attraction is as follows.

Concentration polarization occurs on a length scale that is directly proportional to the ionic strength and ion mobility and inversely proportional to the current. At conditions representative of our work, this length scale is a few micrometers. However, the thickness of the concentration polarization layer varies laterally because of the alteration of the current arising from particles near the cathode. Lateral variations in the amount of concentration polarization induce a spatially varying "free charge," and the action of the electric field on the free charge induces fluid motion. This electrohydrodynamic motion and the associated pressure field cause the particles to move toward one another. Because the induced charge is proportional to the applied field (or current), motion can be induced by either dc or ac fields, as long as the frequency is not too high. Hydrodynamic calculations based on this model show that, al-

though the convection cells fill the space between the electrodes, they are weak outside the polarization layer. To check the quantitative features of our electrohydrodynamic model, we performed experiments with a patterned electrode. The flows observed were in accord with our model (14).

Another example of this phenomenon is
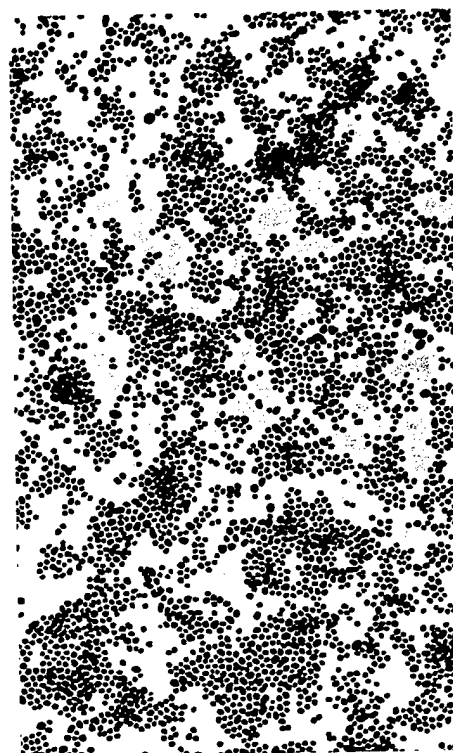
Fig. 3. TEM image of a submonolayer of gold particles (mean particle diameter, 16 nm) electrophoretically deposited onto a carbon-coated copper grid by application of a field of 0.3 V cm^{-1} for 300 s. The extensive clustering of particles reveals the existence of a lateral attraction operating in a manner similar to that observed for larger particles (Fig. 2).

Fig. 2. Two examples of the long-range "lateral attraction force" that acts during electrophoretic deposition. (A to C) Silica particles 900 nm in diameter electrophoretically deposited onto the transparent anode with the applied voltage controlled (from 0 to 2 V) to maintain a constant current of 40 μA cm^{-2}. The applied electric field restricts the particle motion to two dimensions on the surface of the electrode, whereupon a long-range (>five particle diameters) attractive force pulls the particles together to form 2D crystals. (D to F) PS particles 2 μm in diameter deposited by application of a constant voltage (2 V). Long-range lateral attraction forces cause the larger polystyrene particles to aggregate into 2D crystals. The time elapsed between successive frames is ~15 s. No field was applied in (A) and (D). Manipulating the current density changes the magnitude of the lateral attraction, allowing the formation of different 2D colloidal phases, such as gas, liquid, and solid, on the surface of the electrode.
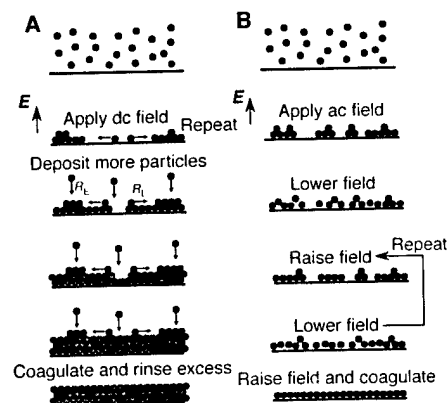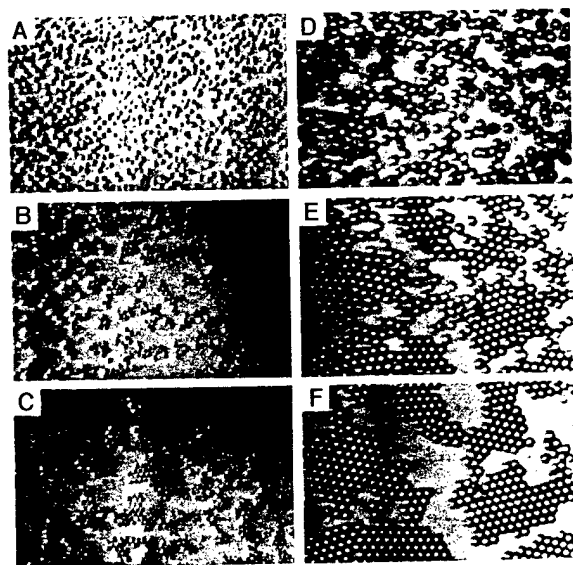
Fig. 4. Two methods of assembling colloidal particles into ordered multilayers: (A) particle assembly with a dc field, and (B) particle assembly with a low-frequency ac field. Both techniques deliberately use the lateral attraction force displayed in Fig. 2 to form highly ordered structures.

707

seen during electroplating reactions, where convective currents are frequently observed and result in patterned blemishes on the plated surface (15). Once fluid is set in motion, the situation becomes more complex because the space charge distribution is affected by this motion. This electrohydrodynamic mechanism fits qualitatively with the observed long-range nature of the lateral attractive force. It also conforms with another of our experimental observations: the migration of particles toward macroscopic scratches and defects in an ITO electrode (14).
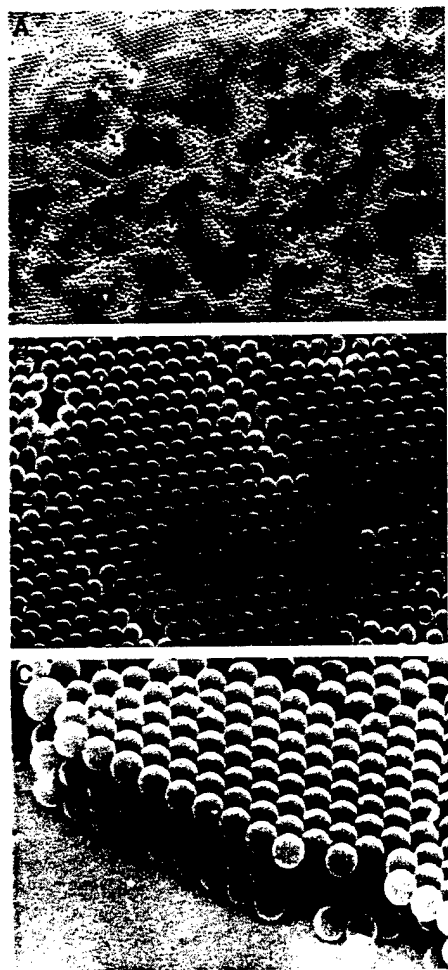
Fig. 5. Scanning electron microscope images of a multilayered colloidal crystalline film made by assembling and coagulating 2-μm PS colloidal particles according to the scheme shown in Fig. 4A. The particles were deposited by the application of an electric field of 40 V cm^{-1} (2 V applied) for 40 min with a dispersion of the PS particles. The current density during most of this period was ~100 μA cm^{-2}. To coagulate the first three layers, we left the field on for 12 hours after the assembly process was complete. Then, particles not coagulated by the field (that is, particles in the fourth or higher layers) were rinsed away with distilled water. (**A** and **B**) The surface of the film at two different magnifications. (**C**) A cross-sectional view revealed by scratching a portion of the film with a sharp needle.

External control of the magnitude of the lateral attraction force between electrophoretically deposited particles allows the controlled assembly of highly ordered mono- and multilayers of colloidal particles. We used two assembly procedures which use the lateral attraction force (Fig. 4). With the dc-field assembly the total number of dispersed particles was far greater than that required to form a monolayer (Fig. 4A). The dc electric field was adjusted so that the rate of arrival of particles through electrophoretic deposition, R_E, was slow relative to the rate of lateral motion of particles toward other particles on the surface, R_L, due to the lateral attraction force. The quantity R_E depends mainly on the particle charge and the magnitude of the electric field in the bulk solution; R_L depends mostly on the current density passing through the particle layer. When $R_L \geq R_E$, highly ordered multilayered films may be grown with large ordered domains. A three-layer film of PS particles, assembled in ~40 min at 2 V, is shown in Fig. 5. Manipulation of the R_L/R_E ratio, that is, changing the "quenching rate" of the assembly process, controls the size of the domains, thereby allowing formation of a variety of packing geometries, from amorphous to highly crystalline. Similar multilayered structures have been formed with the silica particles shown in Fig. 2.

Once the crystalline structures have been assembled, they may be permanently "frozen" if one induces controlled coagulation with the applied field. For example, a strong dc voltage (>2 V) compresses the particles in the direction of the field and they coagulate or adhere to the electrode surface. When a large-amplitude ac voltage (for example, 1 kHz, 5 V) is applied, the particles experience no net electrostatic force pulling them toward the electrode, but they are pushed together by electrohydrodynamic effects. With the ac field, particles coagulate, with little or no adhesion to the electrode. This method of controlled coagulation allows the removal of a coagulated sheet of colloidal material, either electrophoretically, by reversing the polarity of the electrodes, or by flow. We caused the layered structure shown in Fig. 5 to coagulate by leaving the applied voltage at 2 V for 12 hours after the multilayer had assembled. Coagulation of the first layer onto the electrode surface is achieved relatively quickly (<1 min for voltages >2 V); however, coagulation of higher layers is more difficult and requires higher applied voltages and longer coagulation times.

Another method of monolayer assembly is shown in Fig. 4B. This method is particularly suited for the sequential assembly of multilayered colloidal structures with alternating composition. Here, the exact num-

ber of particles required to form a fully dense monolayer on the surface is dispersed in the suspension and electrophoretically deposited onto the electrode in a random arrangement similar to that shown in the first step of Fig. 4A. Next, the applied field strength is lowered until Brownian agitation begins to fluidize the colloidal layer, that is, until the 2D crystal structures in the first layer begin to melt and form liquid or gaseous phases. After the particles randomize by Brownian motion, the applied voltage is raised until the particles in the first layer crystallize. At this point, a certain number of particles previously in the second layer have been transferred to the first layer, and a new crystal structure is formed. This process is repeated until all of the particles in the second, or higher layers, have been transferred to the first layer. For our 2-μm PS particles, this is usually achieved by the application of a low-frequency ac offset voltage (for example, 0.02 Hz at 0.2 to 2 V peak to peak) for ~20 min. These monolayers have packing geometries similar to the surface layer shown in Fig. 5, but the domain sizes are smaller because of the many randomization steps. The procedure, "field-induced annealing," has the effect of sequentially melting ("shaking") and freezing the crystallized colloidal layer until all of the particles are present in the required packing arrangement. The kinetics of the process, that is, the duration of the shaking step compared with the duration of the freezing step, determines the domain size of the 2D crystals in the monolayer.

The controlled assembly and coagulation of colloidal particles into patterned structures through electrophoretic deposition offers a simple method for the construction of materials with designed microscopic architectures. The simplicity of this technique as compared to molecular vapor deposition methods makes it very attractive as a route to economically manufactured nanostructured materials. Furthermore, this method may also be suitable to assemble macromolecules such as proteins into 2D crystals and other patterned structures.

REFERENCES AND NOTES

1. G. M. Whitesides, J. P. Mathias, C. T. Seto, *Science* **254**, 1312 (1991); J. M. Schnur, *ibid.* **262**, 1669 (1993); R. W. Siegel, *Phys. Today* **64**, 64 (1993); H. Masuda and K. Fukuda, *Science* **268**, 1466 (1995); E. Kim, Y. Xia, G. M. Whitesides, *Nature* **376**, 581 (1995).
2. T. Tsakalakos and J. E. Hilliard, *J. Appl. Phys.* **54**, 734 (1983); A. F. Jankowski, *Nanostructured Mater.* **6**, 179 (1995); M. Gell, *J. Min. Met. Mater. Soc.* **46**, 30 (1994).
3. P. Pieranski, *Contemp. Phys.* **24**, 25 (1983); P. N. Pusey and W. van Megan, *Nature* **320**, 340 (1986); D. J. W. Aastuen, N. A. Clark, L. K. Cotter, B. J. Ackerson, *Phys. Rev. Lett.* **57**, 1733 (1986); K. Schatzel and B. J. Ackerson, *ibid.* **68**, 337 (1992); W. van Megan and S. M. Underwood, *Nature* **362**, 616

(1993); T. Okubo, *Langmuir* **10**, 1695 (1994).

4. G. Y. Onoda, *Phys. Rev. Lett.* **55**, 226 (1985); D. H. Van Winkle and C. A. Murray, *Phys. Rev. A* **34**, 562 (1986); R. G. Freeman *et al.*, *Science* **267**, 1629 (1995).

5. A. McPherson, *Preparation and Analysis of Protein Crystals* (Wiley, New York, 1982); G. Kolata, *Science* **229**, 370 (1985); F. Rosenberger, *J. Cryst. Growth* **76**, 618 (1986).

6. T. W. Healy, *Adv. Chem. Ser.* **234**, 146 (1994).

7. G. Vigil, Z. Xu, S. Steinberg, J. Israelachvili, *J. Colloid Interface Sci.* **165**, 367 (1994).

8. P. Richetti, J. Prost, P. Barois, *J. Phys. Lett.* **45**, L-1137 (1984); F. Richetti, J. Prost, N. A. Clark, in *Physics of Complex and Supermolecular Fluids*, S. A. Safran and N. A. Clark, Eds. (Wiley, New York, 1987), p. 387.

9. M. Giersig and P. Mulvaney, *J. Phys. Chem.* **97**, 6334 (1993); *Langmuir* **9**, 3408 (1993). These researchers observed the formation of 2D colloidal clusters and monolayers; however, they did not postulate a mechanism for the lateral attraction of particles on the electrode surface.

10. J. Turkevich, P. C. Stevenson, J. Hillier, *Discuss. Faraday Soc.* **11**, 55 (1951).

11. Extensive 2D clustering of these gold particles is not possible through capillary aggregation mechanisms that occur during drying. These mechanisms always result in patchy, more irregular structures, as has been demonstrated by J. Liu, W. Y. Shih, M. Sarikaya, and I. A. Aksay [*Phys. Rev. A* **41**, 3206 (1990)] and control experiments performed by us.

12. J. O. Bockris and S. U. M. Khan, *Surface Electrochemistry: A Molecular Level Approach* (Plenum, New York, 1993).

13. V. G. Levich, *Physicochemical Hydrodynamics* (Prentice-Hall, Englewood Cliffs, NJ, 1962).

14. Our results on a quantitative calculation of the flow field resulting from lateral current gradients that exist on the surface of the electrode as a result of either electrodeposited colloidal particles or scratches or defects in the ITO layer will be published elsewhere (M. Trau, D. A. Saville, I. A. Aksay, unpublished results).

15. V. Fleury, J. H. Kaufman, D. B. Hibbert, *Nature* **367**, 435 (1994); M. Wang, W. J. P. van Enkevort, N. Ming, P. Bennema, *ibid.*, p. 438; C. Livermore and P. Wong, *Phys. Rev. Lett.* **72**, 3847 (1994).

16. This work was supported by the U.S. Air Force Office of Scientific Research and the Microgravity Science and Applications Division of the National Aeronautics and Space Administration. Partial support for M.T. was provided by the Fulbright Commission. We acknowledge discussions with A. B. Bocarsly.

Mullite (3Al$_2$O$_3$-2SiO$_2$) Synthesis With Aluminosiloxanes

D. R. Treadwell,[†][*] D. M. Dabbs,[‡] and I. A. Aksay[‡]

[†]Department of Materials Science and Engineering and
Washington Technology Center
University of Washington, Seattle, WA 98195

[‡]Department of Chemical Engineering and
Princeton Materials Institute,
Princeton University, Princeton NJ 08544-5263

High yield mullite (3Al$_2$O$_3$-2SiO$_2$) precursors consist of aluminosiloxanes synthesized from mixtures of aluminum and silicon alkoxides. Atomic level mixing of the aluminum and silicon oxides is demonstrated by the low temperature conversion (<1000°C) of the aluminosiloxanes to phase-pure mullite. The proper selection of monomeric sidegroups serves several functions: (i) controlling reactivity of the silicon and aluminum monomers, thereby favoring atomic-level mixing; (ii) maintaining the tractability of the resulting aluminosiloxane; and (iii) improving the yield during mullitization of the aluminosiloxane through easy thermolytic removal. The tractability of the aluminosiloxane compounds permits these materials to be used in fiber spinning, the casting of thin films and monoliths, and as impregnants to powder compacts.

I. Introduction

Interest in mullite (3Al$_2$O$_3$-2SiO$_2$) spans a wide range of technologies due to its unique thermal, chemical, dielectric, and optical properties.[1-7] The type of precursors used for the synthesis and processing of mullite play a key role on the shape forming characteristics, sinterability, and the final properties of the product. While particulate or macromolecular colloids are preferred in fiber processing, powders are the most common form used in the fabrication of bulk objects. In all cases, the spatial scale at which the components (e.g., aluminum and silicon oxides or their precursors) are mixed determines

---

[*]Now at the Department of Materials Science and Engineering, University of Michigan, Ann Arbor, MI 48109-2125.

the reaction sequence leading to the formation of mullite. Mixing at the atomic scale is useful for producing mullite at temperatures below 1000°C; however, powders produced by this approach do not easily sinter and temperatures higher than 1500°C are required for full densification. Precursors composed of segregated phases are better suited for low temperature densification (1250°C to 1500°C) due to the formation of a silica-rich viscous phase which aids densification. This phase segregation is usually retained to some degree in the final product, which will contain amorphous inclusions that deleteriously affect mechanical and optical properties.[1]

In this study, we sought to synthesize mullite from *tractable* aluminosiloxanes mixed at the atomic scale. Prior studies have shown that these precursors can yield phase-pure mullite at temperatures below 1000°C and are suitable for fiber spinning or film forming applications.[8,9,10] Our specific goal was to increase the high conversion yields of the precursors to mullite to minimize cracking due to excessive shrinkage and thus to expand the range of applications to include the processing of bulk shapes. The precursors that we have synthesized have been shown to maintain chemical homogeneity throughout mullitization, evidenced by the low temperature of conversion (~980°C), and to completely convert to mullite. The precursors remain tractable due to the presence of stable organic sidegroups, and can be used in forming tapes, fibers, and coatings of extremely high purity, and as effective impregnants to porous powder compacts.

The methods for synthesizing high purity mullite range across several length scales, with shorter scales indicating higher precursor homogeneity. At the macroscopic end of the range (~μm scale), mixtures of colloidal powders (e.g., aluminosilicate clays mixed with alumina powders) are reaction sintered to form mullite.[1,2,11] In these systems, the scale of homogeneity is set by the size of the component powders and mullitization is delayed to high temperatures (>1650°C). Mullitization on this length scale proceeds by reaction at the interface between the respective phases.[1,2]

Near atomic scale mixing has used metal salts and/or metal alkoxides to prepare homogeneous precursors at the nanometer scale.[12–24] Small scale mullitization is driven by the diffusion of the aluminum moiety into a siliceous matrix until the critical

concentration required for mullite nucleation is achieved. The transformation of a molecularly homogeneous precursor is signaled by an exothermic reaction at ~980°C.[22,23] It has been shown that mullitization, spinel formation, and silica segregation can occur simultaneously at 980°C, with mullitization favored over spinel formation as the degree of homogeneity increases (also marked by a reduced temperature of mullitization).[25,26] Although extremely slow hydrolysis (≥ 4 weeks[19]) of a sol-gel mixture results in a viscous precursor with short diffusional lengths,[19,22,25,26] phase segregation remains a significant problem as the control parameters, pH and ambient conditions, while effective, require long processing times (up to several weeks) and the exclusion of excessive water for the synthesis of homogeneous materials.[27] Even slight inheterogeneities in the structure of precursors that otherwise appear to be homogeneous at longer length scales are sufficient to cause phase separation within the precursor at temperatures near 980°C.[14,23,28]

Many sol-gels are not atomically homogeneous because the base structure is that of a collection of clusters composed of substituted macromolecular alumoxanes, in which silicon is segregated to the pendant groups around an alumoxane core.[29,30] The core consists of fused Al_2O_2 rings, analogous in structure to the aluminum-centered octahedron found in boehmite and diaspore, encapsulated by terminal triethylsiloxyl ($\equiv O-SiEt_3$) groups.[29] If sufficient care is taken, the size of the alumina core can be reduced, lowering the diffusional length scale and enhancing mullitization. Also, segregation can be avoided by synthesizing an aluminosiloxane with the appropriate stoichiometry as a precursor to mullite, putting the scale of homogeneity at the atomic level.[8-10,28-31] A polymeric structure consisting of alternating alumoxane and siloxane groups would represent an ideal arrangement for a mullite precursor. Molecular weights and the tractability of such a macromolecule can be controlled by controlling the nature of the sidechains and/or the chemistry of the solvent carrier.[10,28] By controlling viscosity, spinnable solutions have been used to prepare dense fibers,[10] but the low conversion yields of these systems (<35% ceramic yield)[8-10] prevent application to the fabrication of films or bulk monoliths, where the large material losses during conversion would result in cracking.

In the work reported in this paper, we have carefully matched the reactivity of the selected monomers to minimize segregation near the atomic level, using selected sidegroups that serve to prevent crosslinking between the growing oligomers yet are easily removed by thermolysis. It was necessary to ensure that the silicon moieties were not prematurely volatized before condensing with the aluminum compounds.

II. Experimental

We approached the formation of mullite precursors with the intent of first achieving homogeneous polymerization between the silicon and aluminum monomers by matching the relative reactivity of the respective monomers, and, second, preventing the premature loss of silicon by using less volatile silicon monomers. Systematic characterization of the growing polymer and of the final product were necessary to control the quality of the product. The monomers used in this study are listed in Table 1; schematics of the monomeric structures are shown in Figure 1. As we were seeking to prepare a poly(aluminosiloxane), the selected monomers had to satisfy two criteria: (i) both aluminum and silicon monomers had to have equivalent reactivities with respect to condensation while (ii) cross-linking between the growing polymers was reduced or avoided (e.g., condensation should preferentially result in linear co-polymers containing both aluminum and silicon atoms in the molecular backbone) and (iii) organic side groups should be minimized to reduce the amount of material to be removed by subsequent processing.

The sensitivity of the reactants to contaminants required that all synthesis glassware was scrupulously clean and that all reactions be run using standard Schlenk line techniques or in a nitrogen glove box. The procedure involved soaking the glassware in KOH/ethanol solution for 12h followed by soaking in 2N HNO_3 (aq) for three hours. The glassware was removed from the cleaning solution, doubly rinsed with deionized water, and dried at 80°C for three hours. The dry glassware was transferred into a glove box under a nitrogen atmosphere where the reagents were loaded into the distillation apparatus. The apparatus were removed to a fume hood and fitted (because of the high

temperatures involved and the potential for highly exothermic reactions) with an explosion shield during reaction.

Prior to use, tetrahydrofuran (THF) was distilled over sodium/benzophenone ketyl under nitrogen and ethanol was distilled from magnesium ethoxide. Other reagents* were used as received. Sufficient amounts of the respective silicon and aluminum compounds were used in each mixture to set the Al/Si ratio in solution to 3.

For precursors **I-VI**, the monomers were placed in a flask and heated to 160°C under dry nitrogen, at which temperature all were clear homogeneous liquids. Volatile components were then removed by heating the solutions to temperatures between 260–270°C. The solubility of removed aliquots of the mixture in THF was monitored at every 10°C increase in temperature to avoid converting the reaction mixture into an intractable and insoluble material. The use of a resin flask is particularly helpful for this reaction, easing removal of the product in the event intractable precursors are formed. THF was chosen as a good, non-hydroxylic solvent for the non-crosslinked materials, but was a poor solvent for any crosslinked materials. Tractable intermediates were subsequently converted to oxide in standard air furnaces. Conversion heat treatments were a simple two-step procedure: (i) initial heating to 800°C at 1°/minute followed by (ii) heating above 800°C at 10°/minute.

A high ceramic yield precursor, **VII**, was formed by hydrolyzing 2.14g of tetra-methylcyclotetrasiloxane (TMCTS) with one equivalent of water in ethanol using one drop of methanesulfonic acid as a catalyst. The mixture was stirred until the heat of reaction had dissipated (30 min). Meanwhile, sufficient aluminum *iso*-propoxide to give a 3:1 aluminum to silicon ratio was melted (150°C) in a separate flask and then supercooled to 60°C (this must be done carefully to avoid boiling the TMCTS mixture). The hydrolyzed TMCTS was added to the aluminum *iso*-propoxide and the resulting precipitate redissolved upon stirring the mixture overnight. The mixture was heated as

---

*Aluminum compounds: Alfa Products, Danvers, MA.
Silanes and siloxanes: Huls America, Bristol, PA.
Tetraethoxysilane: Aldrich

before to drive off first the solvent, then the volatile byproducts of the condensation reaction.

The extent of polymerization during heating was monitored by collecting distillates at timed intervals for analysis by Fourier transform infrared spectrometry** (FTIR). Spectra of the liquid samples were obtained as neat thin films placed between KBr support plates. For solids, spectra were obtained by DRIFTS as dispersions in KBr powder. Separation and analysis of the distillate components was done using in-tandem gas chromatography/mass spectrometry[†] (GC/MS).

X-ray powder diffraction[‡] (XRD) scans were run on dried and ground samples heat treated at 800°, 1000°, and 1350°C to monitor the extent of crystallization and the phase composition of the precursors. Resident software diagnostics were used to estimate the percentages of the various phases present after the final heat treatment at 1350°C. Differential thermal analysis[§] (DTA) studies were performed in air at heating rates of 1°, 2°, 5°, and 10°C/min respectively to confirm mullitization. Thermogravimetric analysis[§§] (TGA) was used to characterize the weight loss of the precursor compounds during heating and to determine the amount of ceramic remaining after burnout.

The chemistry of the synthesized polymers was determined using FTIR and TGA. Small samples of the polymeric mixtures were removed from the reaction chamber during refluxing. It was observed that while the polymeric samples were slightly hygroscopic the apparent rate of hydrolysis was slow enough to preclude special sampling techniques. Calcined samples were also characterized using FTIR and XRD.

[**]Model 5DXB, Nicolet, Madison, WI.

[†]Model 5890A, Hewlett Packard, Palo Alto, CA.

[‡]APD 3720, Philips Electronic Instruments, Mount Vernon, NY.

[§]E. I. Du Pont de Nemours & Co., Wilmington, DE.

[§§]Model TAS 7, thermal analysis system, Perkin-Elmer, Hartford, CT.

III. Results and Discussion

The results of the phase analysis of precursors heated to high temperature are shown in Table 2. In the formation of the precursors, three stages of reaction were observed, delimited by the temperature of the reactant solution: (i) T<250°C, (ii) 250°<T<300°C, and (iii) T>300°C. The first stage of reaction involved the evolution of alcohols and acetates, evidence that condensation was occurring between the monomers. In all aluminum-centered molecules, chelates were invariably found to be stable at lower temperatures, remaining bonded to the metal centers during condensation. At higher temperatures, traces of aluminum compounds appeared in the distillates in some cases, evidenced by the rapid formation of precipitates when the distillates were exposed to the atmosphere.

In mixtures of aluminum di-*iso*-propoxide acetoacetic ester chelate (APAE) with dimethyl-diacetoxy silane (DMAS) (**II**) and APAE with octamethyl cyclotetrasiloxane (OMTS) (**III**), silicate esters containing random alkyl groups were detected in the distillate by GC/MS. Also present were ethers formed by the non-hydrolytic condensation of alkoxy groups, esters from the acetoxy ligands, and alcohols when hydroxyls (diphenylsilanediol and hydrolyzed TMCTS) were present. The production of silicate esters during low temperature refluxing indicated that the reactivity of the chosen silicon monomer was too high, favoring reaction with alcohols or other byproducts of the reaction process present in the reaction vessel. The products of these unwanted reactions were volatile and evaporated from the reaction vessel, removing silicon from the reaction mixture, and ultimately lowering the reaction yields and preventing mullitization of the precursor. In mixtures **I** and **IV - VII**, no silicon was detected in the distillate during this reaction step.

The onset of the second stage of the reaction process for mixtures **I-VII** was indicated by the increase in the temperature in the reaction vessel to temperatures above 250°C. Above this temperature, chelate molecules and/or larger pendant groups (e.g., phenols) were detected in the distillate and silanol groups were detected in the reaction mixtures. The loss of the larger side groups from the reaction vessel was visible as the

mixture became first colored and then darkened concomitant with a steady rise in the temperature of the reaction mixture. The deepening color accompanied a steady rise in the temperature of the reaction mixture as the sidegroups continued to be removed from the reaction vessel. TGA of the polymeric mixture revealed that most of the weight loss in the reaction vessel occurred between 250° and 300°C, consistent with the loss of the protective sidegroups.

At temperatures above 300°C a third stage of reaction was reached when the reaction mixture set and solidified due to extensive cross-linking (bridging) between the unprotected metal centers. A simple model of the ideal process can be described using the major chemical changes occurring in the reaction vessel: (i) In the first stage, condensation between the monomers releases the more volatile components from the monomer mixture. Meanwhile, the more tightly held chelates and phenyl groups protect the emerging oligomer from side reactions and prevent premature hydrolysis (and volatilization) of silicon compounds. (ii) The more protective sidegroups begin to come off at elevated temperatures, exposing the oligomer to cross-linking reactions. (iii) Finally, a critical amount of the remaining sidegroups is removed from solution, at which point the material sets.

Since one of our primary goals was the synthesis of *tractable* mullite precursors, tractibility in the reactant mixture was maintained by cooling the reaction vessel once the temperature was observed to rise above 250°C. Subsequent studies (described in the following paragraphs) used only the tractable portion of the reaction mixture.

In Table 2 we show the evolving crystalline phase composition of the initially tractable precursors when calcined to 800°, 1000°, and 1350°C, respectively. No further changes in composition were seen to occur above 1350°C. Five of the mixtures in our study produced single-phase mullite by 1350°C. As noted above, the two that did not convert completely to mullite (**II** and **III**) had suffered premature and substantial loss of silicon due to the volatility of silicon compounds formed during low temperature reflux, evidenced by the low mullite content of the calcined solid. Where pure mullite was the final product (**I, IV-VII**), the lack of any detectable alumina indicated that the

concentration of free silica was below 0.3% by weight (the detection limit of the spectrometer). Thus, the degree of mixing in the reaction vessel was very high and was retained during the condensation and cross-linking stages of the reaction.

We sought to prevent elemental segregation during the polymerization reactions in order to control the nucleation and growth of mullite at lower temperatures. Mixtures **I** and **IV-VII** all satisfied the first condition as the silicon content was maintained throughout the reaction. It was assumed that the stoichiometry of the mixture was fixed at the appropriate 3:1 Al/Si ratio since all eventually and completely converted to mullite. Evidence for satisfying the second condition was indirect: Mixture **I** obviously failed to maintain phase purity shown by the growth of γ-alumina in the matrix at 1000°C. Further heat treatment completed the process to full mullite by 1350°C, indicating that diffusion lengths remained fairly moderate after phase separation. Mixture **IV** remained amorphous up to 1000°C, at which point mullitization was rapid and complete. Mixtures **V** and **VI** showed traces of mullite at 800°C and were completely converted at 1000°C. It was believed that the reactivity of the aluminum tri-*sec*-butoxide, used in both systems, closely matched that of the silicon compounds with respect to condensation. As a result, the precursors formed were chemically stable. However, both systems had low conversion yields, based on the starting materials.

These results also demonstrate that if sufficient care is given to the differences in reaction rates between the silicon and aluminum monomers, it is not necessary to use bulky ligands or chelating agents to ensure homogeneity. In the case of the high-ceramic-yield precursor, good homogeneity (evidenced by the mullitization temperature) can be obtained by the prehydrolysis of the silicon species, creating the more reactive Si–OH moieties. Again, maintaining a suitable reaction atmosphere obviates the need to protect aluminum with chelating agents as the aluminum monomer will be reasonably stable in the absence of water.

In earlier work we have described the presence of an infrared absorbance at ~2340 cm^{-1} in mullite caused by the retention of a silicon-rich phase after complete conversion of the matrix.[19] This absorption band provides a method for characterizing

the extent of chemical homogeneity in the precursor, being absent in truly chemically homogeneous systems (e.g., in mullite made using chemical vapor deposition). It is likely that this absorption arises from the constrained vibrations of CO_2 trapped within an amorphous phase present in the mullite matrix.[32] The CO_2 remains from the thermolytic decomposition of the organic moieties in the original material. Better (e.g., smaller scale) mixing of the precursor chemicals reduces the amount of amorphous phase and thereby decreases the retention of CO_2.

In Figure 2 we show representative spectra of mullite formed by CVD and from two of our polymeric precursors. In the case of both CVD mullite and mullite formed from the homogeneous precursor mixtures **I** and **IV**, the 2340 cm^{-1} band either does not appear or is greatly attenuated in the final product. For contrast, a high purity mullite formed from a sol-gel precursor shows that, at this degree of homogeneity, a second, amorphous phase is retained after mullitization is complete.[19] Phase separation during the mullitization process can be observed using this same absorption band. In Figure 3, we can see that at 800°C, a mullite stoichiometry is present in precursor **IV** and that phase separation exists to some extent (evidenced by silica absorption bands as well as the band at 2340cm^{-1}). After mullitization is completed at 1000°C, only a trace of the second phase remains, indicating the high degree of homogeneity achieved from the original precursor.

IV. Summary and Conclusions

Tractable aluminosiloxane precursors have been made that convert to mullite at ~1000°C. Homogeneity was controlled by the use of appropriate monomers, shown in Table 2. Crystalline mullite nucleation was not required for low temperature conversion; in our observations, better yields were achieved using materials that remained amorphous up to ~1000°C (**I, IV**). Although low temperature (<1000°C) phase separation was observed by XRD in one of the amorphous systems (**I**), the diffusion lengths remained short and full mullitization was achieved by 1350°C. In the second amorphous system (**IV**), mullitization was completed at 1000°C, and XRD characterization indicated that the matrix was single phase throughout mullitization. However, infrared analysis of this

system indicated that while the material had mullite stoichiometry at 800°C, the presence of an absorption band near 2340cm^{-1} was evidence that some degree of phase separation existed in this compound at 800°C. In this case, the diffusional lengths were apparently very small as the material fully converted to mullite by 1000°C. In mixture **VII**, a high-ceramic yield, tractable polymer was obtained without the need for the higher reaction temperatures by choosing starting materials with low organic content and utilizing a pre-hydrolysis step to match the reactivity of the silicon and aluminum monomers.

Precursors with high ceramic conversion yields are important particularly for the impregnation of powder compacts to make monolithic ceramics and/or ceramic/ceramic composites. Because of shrinkage due to solvent loss and organic burnout, a single impregnation step is likely to fill less than 10% of the void space in a compact. More efficient filling of the void space reduces the number of necessary impregnations. Reducing the void volume within a porous ceramic compact speeds the densification of the monolith while preventing deleterious shrinkage, thus these new materials provide effective processing aids for the production of films and monoliths from powder compacts.

Acknowledgments

References

(1)   Aksay, I. A.; Dabbs, D. M.; Sarikaya, M. *J. Am. Cer. Soc.* **1991** *74 [10]*, 2343.

(2)   Schneider, H.; Okada, K.; Pask, J. A. *Mullite and Mullite Ceramics*; J. Wiley and Sons: New York, 1994.

(3)   Becher, P. F.; *J. Am. Ceram. Soc.* **1991**, *74 [2]*, 255.

(4)   Somiya, S.; Hirata, Y. *Am. Ceram. Soc. Bull.* **1991** *70 [10]*, 1624.

(5)   Nixon, R. D.; Chevacharoenkul, S.; Davis, R. F.; and Tiegs, T. N., in *Ceram. Trans. 6: Mullite and Mullite Matrix Composites*, S. Somiya, R. F. Davis, and J. A. Pask, eds.; American Ceramic Society: Westerville OH, 1990.

(6)   Tummala, R. R. *J. Am. Ceram. Soc.* **1991**, *74 [5]*, 895.

(7)   Prochazka, S.; Klug, F. J. *J. Am. Ceram. Soc.* **1983**, *66 [12]*, 874.

(8)   Lannutti, J. J. *Inorganic Polymers in Ceramic Processing*; University of Washington: Seattle, WA, 1990.

(9)   Lannutti, J. J.; Schilling, C. H.; Aksay, I. A., in *Processing Science of Advanced Ceramics, MRS Symp. Proc.*, *155*, I. A. Aksay, G. L. McVay, and D. R. Ulrich, eds., Materials Research Society: Pittsburgh, PA, 1990.

(10) Yogo, T.; Aksay, I. A. *J. Mater. Chem.* **1994**, *4 [2]*, 353.

(11) Rodrigo, P. D. D.; Boch, P. *Int. J. High Technol. Ceram.*, **1985**, *1*, 3.

(12) Roy, R. *J. Am. Ceram. Soc.* **1956**, *39 [4]*, 145.

(13) McGee T. D.; Wirkus, C. D. *Ceram. Bull.* **1972**, *51 [7]*, 577.

(14) Mazdiyasni, K. S.; Brown, L. M. *J. Am. Ceram. Soc.* **1972**, *55 [11]*, 548.

(15) Metcalfe, B. L.; Sant, J. H. *Trans. Brit. Ceram. Soc.* **1975**, *74*, 193.

(16) Yoldas, B. E. *J. Mater. Sci.* **1977**, *12*, 1203.

(17) Yoldas, B. E. *Ceram. Bull.* **1980**, *59 [4]*, 479.

(18) Hirata, Y.; Minamizono, H.; Shimada, K. *Yogyo-Kyokai-Shi* **1985**, *93 [1]*, 46.

(19) Shinohara, N.; Dabbs, D. M.; Aksay, I. A. *Infrared and Optical Transmitting Materials*, SPIE **1986**, *683*, 19.

(20) Komarneni, S.; Suwa, Y.; Roy, R. *J. Am. Cer. Soc.* **1986**, *69 [7]*, C-155.

(21) Wei, W.-C.; Halloran, J. W. *J. Am. Cer. Soc.* **1988**, *71 [3]*, 166.

(22) Okada, K.; Otsuka, N. in *Mullite and Mullite Matrix Composites*, S. Somiya, R. F. Davis, and J. A. Pask, eds., American Ceramic Society: Westerville, OH, 1990.

(23) Huling, J. C.; Messing, G. L. *J. Non-Cryst. Sol.* **1992**, *147-148*, 213.

(24) Laine, R. M.; Treadwell, D. R.; Mueller, B. L.; Bickmore, C. R.; Waldner, K. F.; Hinklin, T. R. *J. Mat. Chem.*, **1996**, in press.

(25) Taylor, A.; Holland, D. *J. Non-Cryst. Sol.* **1993**, *152*, 1.

(26) Gerardin, C.; Sundaresan, S.; Benziger, J.; Navrotsky, A. *Chem. Mater.* **1994**, *6 [2]*, 160.

(27) Chakraborty, A. K. *J. Mater. Sci.*, **1994**, *29*, 6131.

(28) Interrante, L. V.; Williams, A. G. *Polym. Prep.* **1984**, *25 [1]*, 13.

(29) Apblett, A. W.; Warren, A. C.; Barron, A. R. *Chem. Mat.* **1992**, *4*, 167.

(30) Landry, C. C.; Davis, J. A.; Apblett, A. W.; Barron, A. R. *J. Mater. Chem.* **1993**, *3 [6]*, 597.

(31) Morgan, P. E. D.; Bump, H. A.; Pugar, E. A.; Ratto, J. J. *Science of Ceramic Chemical Processing*, L. L. Hench and D. R. Ulrich, eds., J. Wiley and Sons: New York, NY, 1986.

(32) McGovern, S. J. *An Infrared Photoacoustic Study of Metal Oxide Catalysts*; Princeton University: Princeton, NJ, 1985.

Figures

Aluminum diisopropoxide
acetoacetic ester chelate

Diphenyl silanediol

Aluminum sec-butoxide

Octamethylcyclotetrasiloxane
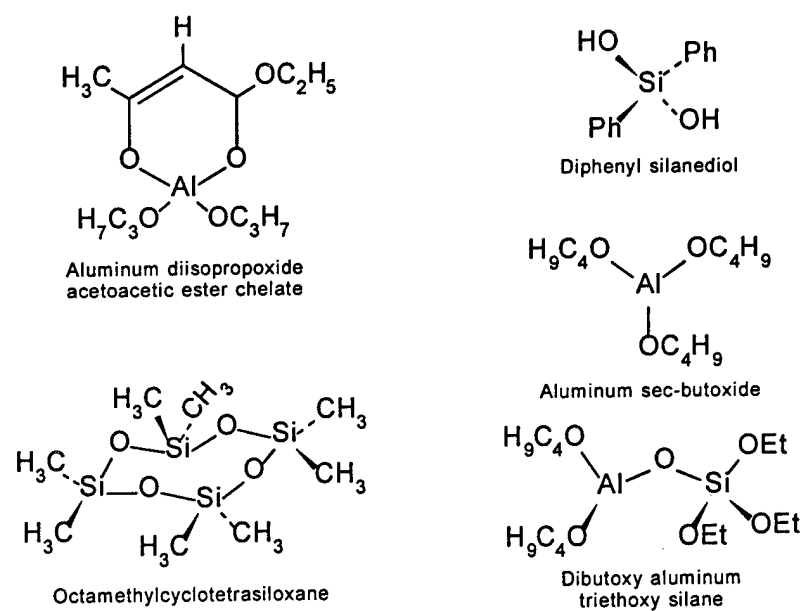
Dibutoxy aluminum
triethoxy silane

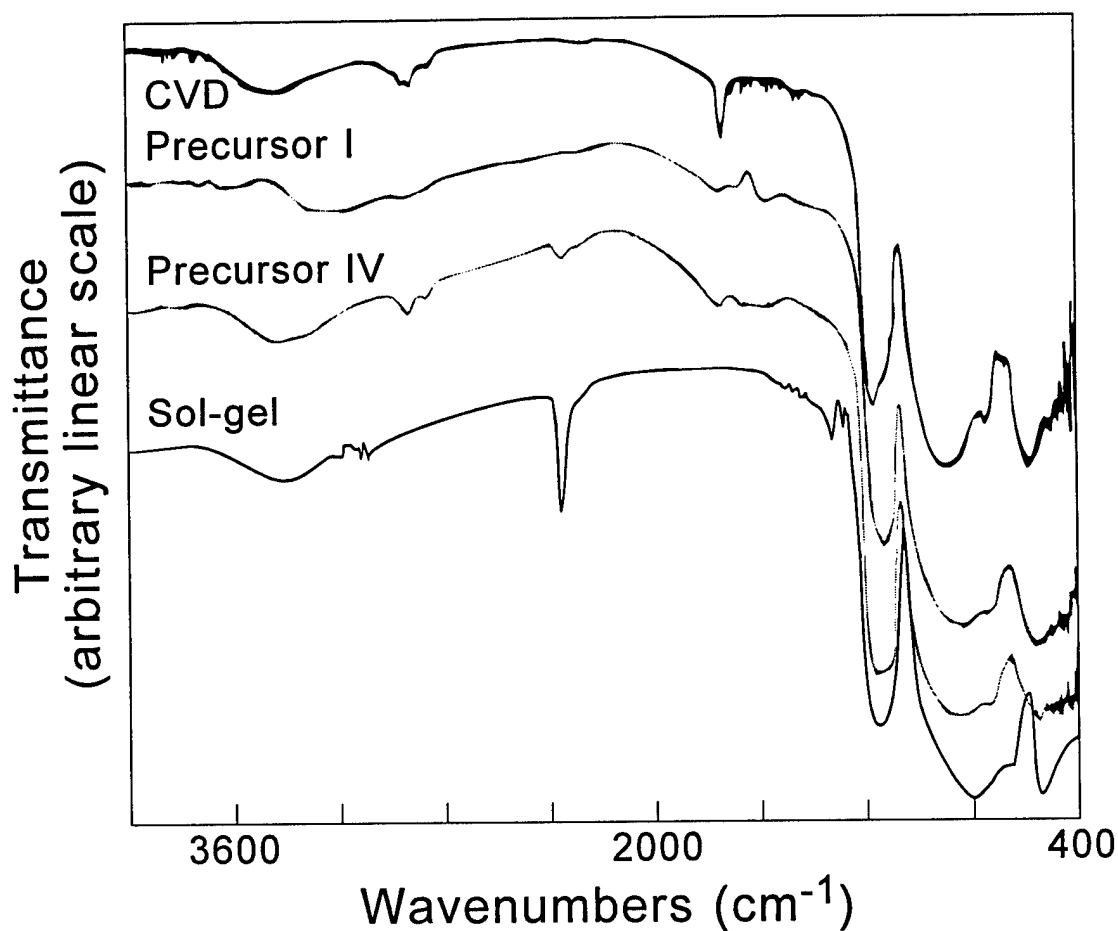Figure 1: Monomeric schematics of the chemicals used in this study.

Figure 2: Chemical homogeneity in mullite prepared from polymeric precursors can be observed using FTIR. The above spectra show that mullite prepared from the precursors **I** and **IV** resemble the spectrum of mullite made by chemical vapor deposition. In contrast, a retained phase in mullite prepared from sol-gel is revealed by the presence of an infrared absorption band at ~2340cm^{-1}, probably due to the presence of constrained CO_2 in an amorphous phase.[32] (All samples but CVD mullite were heat treated to sufficiently high temperatures to ensure complete mullitization: 1000°C for **IV**, and 1350°C for **I** and sol-gel mullite.)
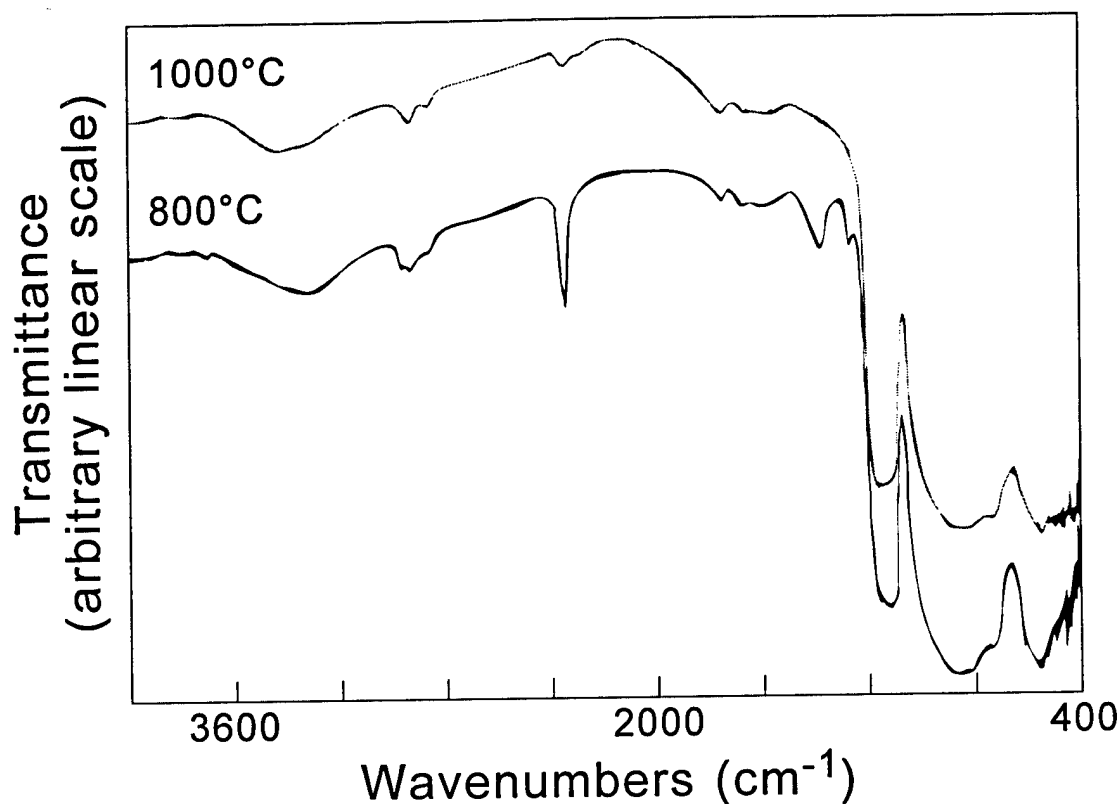
Figure 3: Transient phase separation in a mullite precursor can be observed using the absorption band at ~2340cm^{-1}. At 800°C, the precursor mixture **IV** is amorphous by X-ray diffraction (Table 2) but IR analysis shows a mullite stoichiometry already exists in the matrix. Phase separation is also apparent in the presence of the 2340cm^{-1} band and silica absorbances. When heated to 1000°C, mixture **IV** completely transforms to mullite with little remaining phase segregation.

Tables

Table 1. Aluminum and silicon monomers used in this study (schematic structures of the monomeric units are shown in Figure 1).

Aluminum only monomers	Silicon only monomers	Silicon-aluminum monomer
Aluminum di-*iso*-propoxide acetoacetic ester chelate	Diphenylsilanediol	Dibutoxy aluminoxy triethoxy silane
Aluminum tri-*sec*-butoxide	Octamethyl cyclotetrasiloxane	
Aluminum tri-*iso*-propoxide	Dimethyl-diacetoxy silane	
	Tetramethyl cyclotetrasiloxane	

Table 2. Mullite formation from pure precursors.

	Aluminum source	Silicon source	Phases present			%Mullite at process end
			800°C	1000°C	1350°C	
I	chelate	Al–O–Si	amorphous	γ–alumina and mullite	mullite	100
II	chelate	acetoxy	γ–alumina	γ–alumina	α–alumina and mullite	7.3
III	chelate	octamethylcy-clotetrasiloxane	γ–alumina (trace)	γ–alumina	α–alumina and mullite	6.4
IV	chelate	diphenyl-silanediol	amorphous	mullite	mullite	100
V	*sec*-butoxide	octamethylcy-clotetrasiloxane	mullite (trace)	mullite	mullite	100
VI	*sec*-butoxide	acetoxy	mullite (trace)	mullite	mullite	100
VII	iso-propoxide	tetramethylcy-clotetrasiloxane		mullite	mullite	100